THE UNIVERSITY OF CHICAGO

MATERIAL AND DEVICE DESIGN STRATEGIES FOR SUPPRESSING THE FOREIGN BODY RESPONSE TO IMPLANTABLE ELECTRONICS

A DISSERTATION SUBMITTED TO
THE FACULTY OF THE PRITZKER SCHOOL OF MOLECULAR ENGINEERING
IN CANDIDACY FOR THE DEGREE OF
DOCTOR OF PHILOSOPHY

BY
SHINYA WAI

CHICAGO, ILLINOIS
AUGUST 2026

TABLE OF CONTENTS

LIST OF FIGURES

LIST OF TABLES

ACKNOWLEDGMENTS

If I told my high school self that I will be getting a PhD, my high school self would probably tell me that that was not a smart move, to which I would disagree. To this day, I am not quite sure how I got to where I am now. To be clear, I definitely know based on memory, but at the same time, I have trouble comprehending. Without a doubt, a major reason I got here is because many people have supported me and guided me in the right direction, allowing me to explore directions that I found interesting and were good for my career. My PhD advisors, Professors Sihong Wang and Matthew Tirrell, were instrumental in this process. Not only did they give me their trust, guidance, and support, they also gave me the freedom to explore various scientific avenues that I would have never imagined that I would have the opportunity to explore before joining their research groups. I believe my PhD experience was unique, and I am not sure if I would have gotten anything approaching my PhD experience anywhere else except in the labs of Professors Sihong Wang and Matthew Tirrell at The University of Chicago. Sihong created the conditions necessary for me to pursue seemingly unrelated scientific fields that converged to give rise to a coherent scientific narrative. Matt usually had interesting and useful insights that I would not have gotten anywhere else, which sometimes was the catalyst for breaking me out of a thought loop. Sihong and Matt also believed in me and my success, supporting me in my career development as much as they can. They taught me what mentorship means, and how mentorship can have a significant impact on someone's life. I truly feel grateful and lucky to have received their mentorship throughout my PhD.

Next, I would like to thank my fellow colleagues who gave me social and scientific support. From the Wang lab, Qi and Ping have put a substantial amount of effort to make me feel welcomed when I first joined the Wang lab. I appreciate their sincere effort to be welcoming during the COVID-19 pandemic. From the Wang lab, Nan and Yahao have helped me situate myself scientifically in a field that I was completely familiar with prior to joining.

Nan and Yahao also ran GIWAXS on my samples at the Advanced Photon Source (APS) at the Argonne National Laboratory (ANL) with the help of Dr. Joseph Strzalka, who I also would like to thank. Yahao ran conductive AFM on my samples too, which became a key part of a manuscript figure. When trying to figure out how to conduct electrophysiological recordings in mice, all the questions that Tianda answered with regards to circuit design was instrumental in elevating one of my manuscripts to another level, and I would like to thank him for that. I would like to thank Sean S. and Max for showing me how to do photolithography and microfabrication in general. You two also were very helpful in bouncing off ideas and helping me come up with troubleshooting steps. I also appreciate all the non-science-related, conversations we had. All topics, ranging from dumb to intellectual ones, were on the table, and I was highly entertained by them. Sean L., despite being pretty vanilla, you are a good hang, and I will surely remember all the restaurant explorations that we did over the years; and thanks for the water contact angle data.

From the Tirrell lab, I appreciated the company of Angelika, Carlos, Yan, and Ed when I first joined. Helping me situate myself at The University of Chicago during the COVID-19 pandemic was invaluable. I would like to thank Angelika for answering all my questions on polyelectrolytes. I would like to thank Angelika and Carlos for being good company when running SAXS at the APS at ANL. And of course, I would like to thank the beamline scientists, Dr. Xiaobing Zuo and Dr. Soenke Seifert, for making SAXS possible. Regardless of Carlos' angry chihuahua tendencies, he made a good companion throughout my time here. If I ignore Kaden's flaws of playing fake drums on benches too much, he has been helpful with providing polyelectrolytes that he synthesized and helping me troubleshoot RAFT polymerization. I appreciate you keeping in touch with me after becoming a professor.

I received quite a bit of help from the Hubbell and Swartz lab with regards to *in vivo* experiments. I would like to thank Seounghun from the Hubbell lab for teaching me how to handle mice and conducting subcutaneous implantation surgeries. He guided me through

various other biological techniques. I would like to thank Emiliano from the Hubbell and Swartz lab for giving me helpful tips with techniques, such as histology and RNA isolation. I would like to thank Trevin from the Swartz lab for giving me very useful advice on flow cytometry. Trevor from the Swartz lab, who also happens to be my roommate, helped me learn a variety of biological techniques. There were many nights, during which I cornered him in our apartment and inhumanely bombarded him with a million questions. My other roommate, Mohit from Physics, has served me faithfully well by machining a variety of metal components for me and answering physics questions that were tangentially related to my research. Having roommates from immunoengineering and physics was a valuable experience, and I learned a lot from it. I feel lucky to have you two as roommates.

In addition, I would like to thank the many staff scientists, who have made equipment usage and services at various core facilities a smooth experience. I would like to thank Dr. Tera Lavoie for taking quality cryo-TEM images of my samples. I would like to thank Dr. Phil Griffin for patiently training me on many instruments at the Soft Matter Characterization Facility. I would like to thank Dr. Terri Li, Christy Schmel, Xin Jiang, and Haiqing Luo at the Human Tissue Resource Center for embedding and sectioning all the tissue samples I generated for histology. It must have been hours and hours of work, and it would not have been possible to obtain central pieces of data for some of my projects if it wasn't for you all.

Last and not least, I would like to thank my parents, Futami Wai and Wing-Kin Wai, for supporting me throughout my life and encouraging me to have personal agency in deciding what I want to do. Thank you both for believing in me even when I was going through a long problematic phase, during which I refused to study. I cannot imagine what kind of life I would be leading right now had I not been raised by you two.

ABSTRACT

Implantable medical devices (IMDs) are playing an increasingly important role due to an aging population and the associated increasing prevalence of chronic diseases. However, the foreign body response (FBR) has limited IMDs from realizing their full potential. The FBR is characterized by inflammatory and fibrotic processes that surround the implanted material. Degradative chemicals enzymes produced in the process can damage the implant. Fibrotic encapsulation is particularly detrimental for biosensors and electrophysiological devices because it would impede the diffusion of analytes and ions. Despite this, there seem to be few strategies for suppressing the FBR in the long term. As electronic materials for IMDs, poly(3,4-ethylenedioxythiophene):poly(styrene sulfonate) (PEDOT:PSS) is of interest because it is chemically stable, highly processable, non-cytotoxic, and has good mixed ion-electron conducting properties. Furthermore, PEDOT:PSS can be chemically modified and physically blended with a variety of materials which makes it interesting for generating new strategies for suppressing the FBR to electronic materials. Nonetheless, previous work addressing the FBR against PEDOT:PSS did not place their focus on long-term solutions or did not carry out FBR-specific characterization methods. In Chapter 1 of this dissertation, we introduce FBR and the problems that it causes for IMDs. We will go into the in-depth mechanism of the FBR, at the molecular, cellular, and cellular network level. Then, we will explore the reported material strategies for suppressing the FBR. An overview on conjugated polymers, including PEDOT:PSS, and its role in IMDs will also be discussed.

In Chapter 2, we introduce the zwitterionic PEDOT:PSS hydrogel (ZIPH) which was found to have both good electrical conductivity and good FBR-suppressing properties. Zwitterionic polymers are a class of materials with promising FBR suppressing properties which have been shown to nearly eliminate the FBR for at least a year in mice. We hypothesized that by combining PEDOT:PSS and a zwitterionic polymer into a double-network hydrogel and carefully tuning its phase separation morphology, the conductivity can be increased

and the FBR can be suppressed indefinitely. In this chapter, we demonstrate a process for inducing PEDOT:PSS network formation in situ in a zwitterionic hydrogel matrix, which significantly improves its conductivity and reduces FBR-associated fibrosis. Investigation of the mechanism of the FBR suppression revealed that ZIPH is associated with a unique immune response that diverged significantly from its parent materials, PEDOT:PSS and zwitterionic polymer.

In Chapter 3, we sought to demonstrate that the high electrical conductivity and FBR-suppressing properties of ZIPH are advantageous in electrophysiological applications via electrocardiography (ECG) in mice. Device design and a new surface functionalization strategy for substantially enhancing adhesion of ZIPH on plastic substrates are explored. We also discuss the (ECG) recording setup and amplifier design. Finally, we show that ZIPH ECG electrodes have less signal degradation compared to PEDOT:PSS ECG electrodes. Furthermore, ZIPH ECG electrodes have similar signal degradation compared to PEDOT:PSS ECG electrodes with dexamethasone-eluting silicone backings without the side effects associated with dexamethasone. We have successfully demonstrated that the novel approach for designing ZIPH can lead to long-lasting implantable electrophysiological devices.

In Chapter 4, we take a different approach from previous chapters and confer antifouling properties to PEDOT:PSS by assembling zwitterionic polymer brushes. Because PEDOT:PSS has no useful functional groups for chemical modification and swells easily in water, conventional coating strategies do not work as well. In addition, maintaining a low interfacial impedance is desirable. To solve this, we devised a new coating strategy that involves the electrostatic interaction between PSS and other polyelectrolytes. The coating terminates with a polyzwitterion-polyelectrolyte block copolymer, which demonstrated good antifouling properties. We also use this strategy to coat PEDOT:PSS ECG electrodes, which are implanted in mice for 12 weeks, and demonstrate the strategy can lead to almost no signal loss.

CHAPTER 1

INTRODUCTION

1.1 Introduction to The Foreign Body Response

1.1.1 Implantable Medical Devices and The Foreign Body Response

The first implantable medical device (IMD) entered a patient's body in the form of a cardiac pacemaker in 1958 in Stockholm.[1] Since then, many types of IMDs have been introduced to the market ranging from cochlear implants to glucose sensors. More recently, the increasing prevalence of chronic diseases as the global population ages[2] and advancements in brain-computer-interfaces[3] are expected to become key IMD market drivers. In 2020, the global IMD market was valued at $84.10 billion and is projected to grow to $141.08 billion by 2028.[4] Despite this continuous growth, there is one major obstacle known as the "foreign body response (FBR)" that has limited IMDs from realizing their full potential. The FBR is characterized by inflammatory and fibrotic processes that surround the implant once it enters the body, which can lead to degradation and mechanical failure of the devices within several weeks.[5–8] Furthermore, fibrotic encapsulation of the implant leads to the isolation of the IMD from the rest of the body, which is detrimental for IMDs with sensing and interfacing functionalities.[6,8] Thus, there is a substantial need for materials and devices that can carry out its function in the body without eliciting a significant amount of FBR.

IMDs can broadly be divided into two categories: active IMDs and passive IMDs. Active IMDs require an external power supply to support its functions, while passive IMDs do not, since in many cases, they only have structural functions.[9] All discussions from this point on will be from the perspective of electronic materials and devices, so active IMDs will simply be referred to as IMDs unless explicitly mentioned otherwise. While the FBR does not necessarily prevent established active IMDs, such as cardiac pacemakers, continuous glucose monitors, and cochlear implants from functioning properly in the majority of cases, it still

presents with obstacles and complications that cannot be disregarded.[10–12] For emerging implantable technologies, such as brain-computer-interfaces and various implantable biochemical sensors, the effects of the FBR can vary from unclear long-term influences due to the lack of systematic studies to causing overwhelmingly detrimental hurdles for clinical translation. To provide context for the role of the FBR in IMDs, which is a diverse class of devices, how the FBR affects cardiac pacemakers, continuous glucose monitors, cochlear implants, and emerging implantable technologies will be discussed in the following sections.

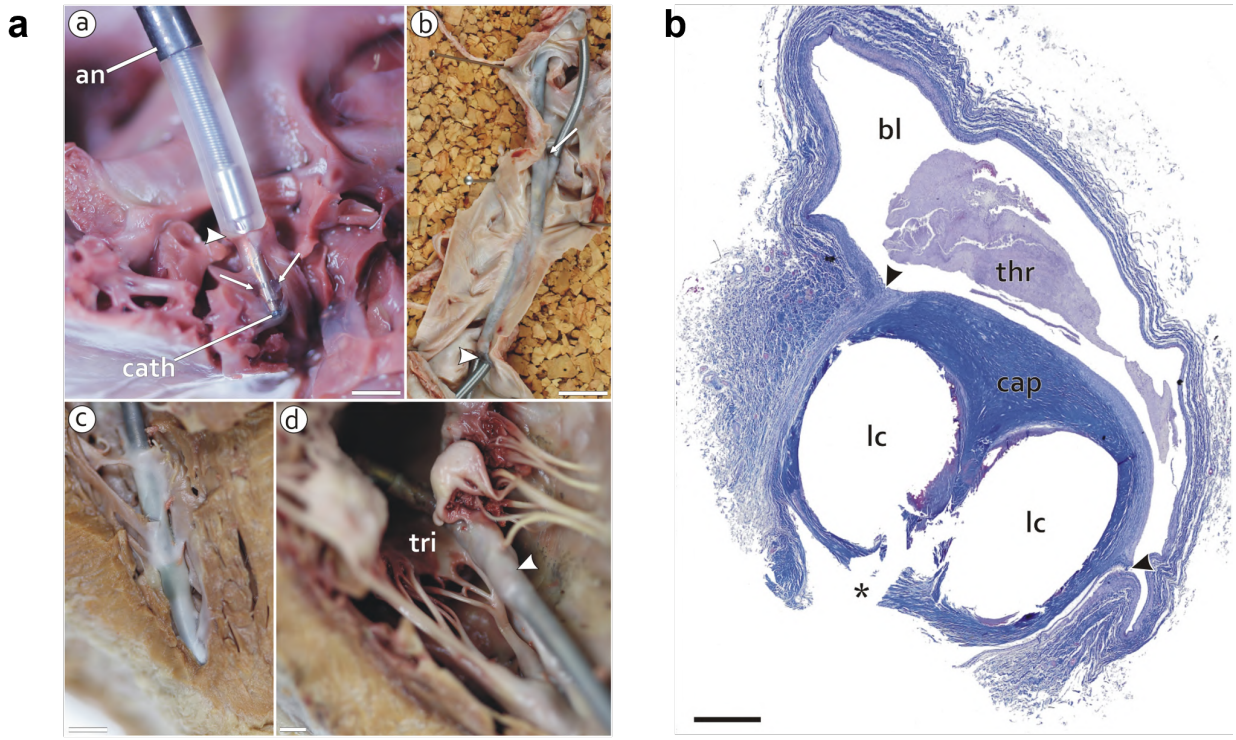

Figure 1.1. Fibrotic encapsulation of cardiac pacemaker leads. **a**, Photographs of fibrosis and tissue encapsulated pacemaker leads from formaldehyde-ethanol fixed body donors. an, anode; cath, cathode; tri, tricuspid valve; scale bar, 3 mm. **b**, Azan stained tissue section of a subclavian vein with two side-by-side pacemaker leads. bl, blood-side lumen; thr, thrombus; cap, fibrotic encapsulation; lc, lead-side lumen; scale bar, 1 mm. Adapted with permission from Ref.[12]. Copyright 2017 Elsevier.

1.1.2 Effects of The FBR on Cardiac Pacemakers

There are an estimated 3 million people worldwide with cardiac pacemakers and 600,000 pacemakers implanted each year.[13,14] Cardiac pacemakers are used to treat bradycardia, an abnormally slow heart rate, and consist of electrodes that both sense cardiac electrical signals and deliver electrical stimulation to the myocardium.[13] Pacemaker electrodes are usually inserted into the subclavian vein and guided to the inner atrial wall, where they are fixed.[12,13] In the early days, the FBR-induced fibrotic insulation of electrodes (Fig. 1.1a) would cause pacemakers to experience a large initial increase in stimulation threshold. After plateauing, the stimulation threshold would constantly fluctuate, requiring automatic or manual threshold adjustments.[14,15] Enzyme-catalyzed degradation via reactive oxygen species of lead insulation was also observed to cause issues due to current leakages.[16–18] Improved understanding of the failure modes of pacemakers eventually led to the introduction of dexamethasone-eluting silicone collars placed in the vicinity of the electrodes to suppress fibrotic tissue overgrowth and cellular accumulation.[14,15] Early formulations of polyurethane insulation were replaced with either newer formulations of polyurethane or different materials to resist chemical degradation.[18]

Despite these advancements, pacemakers still suffer from non-negligible increases and fluctuations in stimulation thresholds.[15,19,20] An increase in stimulation threshold leads to higher power consumption, decreasing battery longevity. Furthermore, 1 to 6% of people with cardiac pacemakers develop some type of implant-related complications at some point in their lifetimes, ranging in severity from high lead impedances to thromboembolisms triggered by the FBR.[11] Arguably, the largest issue that the FBR causes for pacemakers is the fibrotic encapsulation of leads (Fig. 1.1) that makes surgical retrieval of defective leads extremely difficult.[12] In Germany, for example, around 50% of defective leads are never extracted, and extraction procedures can have mortality rates that are as high as 2.6%.[12]

1.1.3 Effects of The FBR on Continuous Glucose Monitors

Diabetes affects hundreds of millions of people around the world and is continuing to increase in prevalence.[21,22] Because maintaining physiological blood glucose levels is the only way diabetes patients can maintain a healthy lifestyle, it is no surprise that, since it's commercial introduction in 1999,[23] the number of continuous glucose monitor (CGMs) users have increased to more than 9 million worldwide.[22] Conventional CGMs consist of a needle with sensing electrodes, enabling minimally invasive biomarker detection through skin penetration.[24]

Most CGMs are approved to be worn for only 10-14 days. One of the major factors that limit the wear time of CGMs to 10-14 days is the FBR to the implanted sensors.[25] FBR-related fibrosis reduces the availability of glucose to the sensors by slowing its diffusion at the implantation site.[25–27] As a result, sensor noise and inaccuracies become issues, necessitating frequent blood glucose calibrations to correct signal trend.[25,28] In 2024, the Food and Drug Administration (FDA) approved Eversense, the first and only CGM with a 365-day wear time. Eversense can be worn for 365 days due to the device-integrated dexamethasone-releasing drug depot. Even though this is a significant improvement in wear time over conventional devices, the wear time of Eversense is still limited because the FBR will resume when dexamethasone in the drug depot is depleted. In addition, Eversense still requires regular finger prick for sensor calibration.[29]

1.1.4 Effects of The FBR on Cochlear Implants

Cochlear implants (CI) are neuroprostheses that provide auditory perception to individuals with moderate to severe sensorineural hearing loss. There are over 1 million CI users around the world.[30] CI electrodes are inserted into the scala tympani, one of the cavities of the spiral-shaped cochlea. External microphones wirelessly send auditory signals to the implanted internal receiver, which electrically stimulates the cochlear nerve with the inserted

electrodes. FBR after surgery is reported in 90% of CIs, leading to the formation of a fibrous capsule surrounding the electrode, resulting in increased impedance at the electrode-tissue interface.[31–33] This elevates the stimulation thresholds required for effective function, which negatively affects signal transmission and leads to progressive residual hearing loss.[32,33]

Similarly to cardiac pacemakers, local delivery of dexamethasone with dexamethasone-loaded silicone has been reported to stabilize and prevent increases in CI stimulation threshold.[34–36] Clinical trials of the first dexamethasone-eluting CIs are underway,[37,38] and it is yet to be found if dexamethasone-eluting CIs will still have still have fluctuations and increases in stimulation threshold, similar to what is seen in pacemakers,[15,19,20] or will have limits on the length of time dexamethasone elution can stay effective, similar to what is seen in Eversense CGMs.[29]

1.1.5 Effects of The FBR on Emerging Implantable Technologies

Beyond the established IMDs on the market today, there are many emerging implantable technologies that appear to be on the verge of commercialization. A few of these technologies will be discussed in this section.

A prominent emerging class of IMDs today are brain-computer-interfaces (BCIs), a well known example of which is Neuralink.[39] By interfacing with the brain, BCIs can restore sensory and motor functions in individuals with neurological disorders or missing body parts by allowing individuals to control external devices with their brains.[40–42] This is a diverse class of IMDs, ranging from Neuralink's intracortical fiber electrodes[39] to Synchron's endovascular electrocorticograpic thin film stentrodes.[43] A class of IMDs with significant overlap with BCIs are neural prosthetics, which place emphasis on restoring sensory and motor functions in individuals with missing body parts. Neural prostheses often interface with the peripheral nervous system instead of the brain, and an established example of this is cochlear implants.[40] In either case, the FBR has been observed to degrade signal quality as fibro-

sis progresses and the tissues surrounding the electrodes remodel.[40–42,44] However, despite initial setbacks,[45] the first patient to receive Neuralink's BCI still has functional electrodes over 18 months after surgical implantation.[46] Even though this is promising, data on more patients are needed to draw conclusions on whether the FBR is solved for this application area.

Another emerging class of IMDs are biochemical sensors. Implantable biochemical sensors can potentially provide continuous health monitoring to catch early onsets of diseases and enable continuous closed-loop therapies. Even though commercial continuous glucose monitors have been around since 1999, commercial diversification of sensors into other types of analytes have been virtually non-existent.[47] This may be due to the myriad of difficult problems that plague continuous biochemical sensors in addition to the FBR.[48,49] Due to the complexity of such devices, systematic investigations into the contributions of the FBR to device stability has been limited, but biochemical sensors as a whole are expected to face the same diffusion barrier problem that FBR-induced fibrosis causes for continuous glucose monitors.[25–27]

1.1.6 Limitations of Dexamethasone in Suppressing the FBR

So far, commercial IMDs, including cardiac pacemakers and CGMs, have demonstrated that dexamethasone elution can be an effective strategy to prolong the functionality of implanted devices in humans.[15,29] However, issues, such as negative influences on device function from incomplete elimination of fibrotic overgrowth,[15,19,20] interference of remaining fibrotic overgrowth in IMD retrieval,[12] and depletion of the drug over time,[29,50] could be fundamental limits of the strategy when it comes to further increasing the reliability and expanding the application area of IMDs. Furthermore, atrophy of various tissues is a major side effect of glucocorticoids, which is a class of anti-inflammatory steroids that dexamethasone belongs to,[51–54] and could limit the use case of the strategy for more sensitive applications, as is the

case for neural interfacing devices.[55–58] To move beyond dexamethasone, we must understand the mechanism of the FBR at a much deeper level and design materials and devices that can suppress the FBR without any side effects.

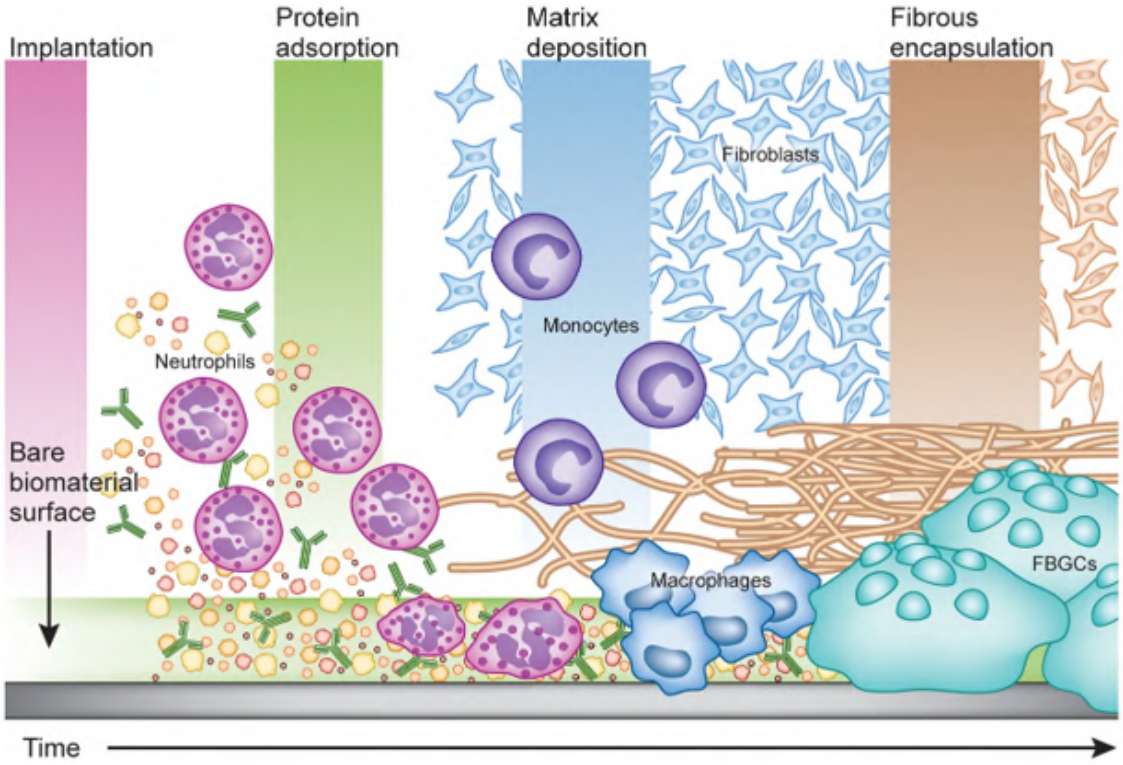

Figure 1.2. Schematic depiction of the simplified mechanism of the foreign body response. Immediately after implantation, macromolecules adsorb onto the implant surface. Neutrophils are the first cells to arrive at the implant surface, followed by monocytes that differentiate into macrophages. Macrophages recruit fibroblasts that deposit collagen on the implant surface. Finally, macrophages fuse to form foreign body giant cells (FBGCs). Adapted with permission from Ref.[59]. Copyright 2013 Springer Nature.

1.2 Mechanism of The Foreign Body Response

1.2.1 General Mechanism of The FBR

The FBR is a complex process, involving non-specifically interacting proteins and cells across timescales of months to years. Experimentally, there are many potential confounding factors that can obscure causal relationships.[5,7] For example, in the harsh environment of the peri-

implant space, degradation and abrasion can lead to the implant surface shedding molecules and particles that can be taken up by immune cells, which can cause the FBR process to deviate from what would be expected from pure surface effects.[60–63] Despite this, based on mechanistic and empirical findings, we know with considerable certainty that the FBR is largely governed by surface effects.

To understand the FBR, one must take a few steps back from device level observations and shift their focus to how the human body recognizes something that is foreign, which naturally leads to the conceptual frameworks of immunology. There are four well accepted theories: the self non-self theory,[64] the infectious non-self theory,[65] the danger theory,[66] and the discontinuity theory.[67] The self non-self theory, proposed by Nobel prize laureate, MacFarlane Burnet, posits that clonal selection of antibody-producing lymphocytes allow the immune system to discriminate between what is self and what is foreign and explains how the adaptive immune system produces pathogen-specific antibodies.[64,68] The infectious non-self theory, conceived by Charles Janeway, proposes that the immune system recognizes foreign dangers by detecting pathogen associated molecular patterns (PAMPs), conserved molecular structures carried by all known human pathogens.[65] This is largely supported by the discovery of many pattern recognition receptors (PRRs) that bind to PAMPs.[69] Polly Matzinger proposed the danger theory, which posits that cell death, distressed cells, and tissue damage release damage associated molecular patterns (DAMPs) into the extracellular space, signaling the immune system to engage.[66] This theory is also supported by the discovery of the many PRRs that bind to DAMPs.[70] Lastly, the discontinuity theory states that the immune system responds to changes in composition and abundance of antigens or molecular patterns over time and is consistent with how the immune system can become tolerized to persistent antigenic expression.[67] All of these models are useful for explaining experimental observations, either by itself or in combination with other models.

A natural question to ask, then, is: which of these theories most accurately explains

the FBR? Since the FBR is also observed in synthetic materials that lack biochemical motifs,[5,7] the self non-self theory, which requires foreign peptides to be presented on major histocompatbility complexes (MHCs) on antigen presenting cells,[68] would not make sense. By extension, the infectious non-self theory[65] would also not make sense because PAMPs are not present in many of these synthetic materials. On the other hand, the danger theory is an excellent fit because whenever an implant enters a living body, it inevitably leads to tissue damage, releasing DAMPs. Even if, hypothetically, an implant was able to be surgically inserted without causing any tissue damage, endogenous proteins will non-specifically adsorb onto the surface of the implant. The adsorbed proteins change conformations, externalizing their hydrophobic domains, which become DAMPs and become accessible to PRRs.[71] The discontinuity theory only makes sense in conjunction with the danger theory because the temporal change in composition of molecular patterns is a result of the release of DAMPs.

Using the danger theory, it can be appreciated that the experimentally supported current understanding of the FBR (Fig. 1.2) has fundamental immnological roots. The first phase of the FBR can be thought of as analogous to the first phase of sterile injury and is marked by the release of DAMPs into the extracellular space.[5,72,73] Tissue damage, cell death, and distressed cells caused by the damaging effects of inserting an implant into a living body triggers the release of DAMPs. DAMPs can either be (1) intracellular molecules that are released by necrotic cells, such as high-mobility group box 1 (HMGB1), heat shock proteins (HSPs), adenosine triphosphate (ATP), and histones or (2) molecules that are actively secreted by distressed cells, such as defensins, IL-1α, and IL-33, as shown in Table 1.1.[70] The release of DAMPs act as inflammatory and chemoattractant agents that recruit and activate immune cells.[70] However, the presence of an implant causes the FBR to deviate from a normal sterile injury response.[5,72,73] Within seconds to minutes of implantation, DAMPs non-specifically adsorb onto the implant surface, in a process commonly known as fouling.[5,7] In addition to cellular DAMPs, blood plasma, consisting of over 300 distinct types

Table 1.1. List of damage-associated molecular patterns (DAMPs), their receptors, and their origins.

Origin		Major DAMPs	Receptors
Extracellular matrix		Biglycan	TLR2, TLR4, NLRP3
		Decorin	TLR2, TLR4
		Versican	TLR2, TLR6, CD14
		LMW hyaluronan	TLR2, TLR4, NLRP3
		Heparan sulfate	TLR4
		Fibronectin (EDA domain)	TLR4
		Fibrinogen	TLR4
		Tenascin C	TLR4
Intracellular compartments	Cytosol	Uric acid	NLRP3, P2X7
		S100 proteins	TLR2, TLR4, RAGE
		Heat shock proteins	TLR2, TLR4, CD91
		ATP	P2X7, P2Y2
		F-actin	DNGR-1
		Cyclophilin A	CD147
		Aβ	TLR2, NLRP1, NLRP3, CD36, RAGE
	Nuclear	Histones	TLR2, TLR4
		HMGB1	TLR2, TLR4, RAGE
		HMGN1	TLR4
		IL-1α	IL-1R
		IL-33	ST2
		SAP130	Mincle
		DNA	TLR9, AIM2
		RNA	TLR3, TLR7, TLR8, RIG-I, MDA5
	Mitochondria	mtDNA	TLR9
		TFAM	RAGE
		Formyl peptide	FPR1
		mROS	NLRP3
	ER	Calreticulin	CD91
	Granule	Defensins	TLR4
		Cathelicidin (LL37)	P2X7, FPR2
		EDN	TLR2
		Granulysin	TLR4
	Plasma membrane	Syndecans	TLR4
		Glypicans	TLR4

ER, endoplasmic reticulum; EDC, eosinophil-derived neurotoxin
Adapted with permission from Ref.[70]. Copyright 2018 Korean Association of Immunologists.

of proteins, become a major source of fouling, with some acting as DAMPs. The adsorption process denatures blood plasma proteins on the implant surface, externalizing chemical motifs that are normally not accessible to PRRs in their native states. Although technically not considered to be DAMPs, complement proteins, such as C3b, can opsonize and adsorb onto the implant surface and facilitate the formation of potent chemoattractants, C3a and C5b.[5,74,75] The significance of biofouling in the FBR is that synthetic materials, which often have no native cognate receptors, suddenly acquire numerous, diverse "cognate receptors" that indirectly recognizes the synthetic material through the adosrbed DAMPs, allowing the immune system to recognize and attack the implant.

In the second, acute inflammation phase of the FBR, freely soluble extracellular DAMPS activate and recruit immune cells through PRRs.[5,7] Within minutes of implantaion, DAMPs activate mast cells. Mast cells act as rapid-response sentinels, releasing histamines, which act as chemoattractants and vasodilators.[76,77] Within hours, neutrophils, detecting the release of DAMPs and other chemoattractants, arrive at the implantation site. Within hours to days, DAMPs and other chemoattractants recruit monocytes to the implantation site. Monocytes differentiate into macrophages, which play a key role in the evolution of the FBR, upon arrival. Neutrophils and macrophages recognize the implant through cell surface PRRs, such as toll-like receptors (TLRs), NOD-like receptors, and scavenger receptors.[5,70,78] The acute inflammatory phase lasts several days.[5,6]

The infiltration of lymphocytes marks the start of the third, chronic inflammation phase of the FBR, which lasts 2-3 weeks.[5–8] During the chronic inflammation phase, macrophages continue to arrive at the implantation site, and macrophages and various other cells produce platelet derived growth factors (PDGFs), vascular endothelial growth factors (VEGF), and TGF-β. These growth factors facilitate the recruitment of fibroblasts and endothelial cells and the initiation of fibrosis, ending the chronic inflammation phase and beginning the process of insulating the implant from the rest of the body.[5] TGF-β induces the differentiation

of fibroblasts to myofibroblasts which produce contractile actin filaments and causes mechanical stress on the implant.[5,8] In addition to producing growth factors, macrophages produce matrix metalloproteinases (MMPs) which promote the remodeling of the tissue surrounding the implant.[5,7] Depending on the intended function of the implant, tissue remodeling may be unfavorable because it may compromise the quality of contact between the implant and the tissue.[79] The fourth and final process of the FBR is characterized by a mature, collagenous fibrotic capsule that segregates the implant from the rest of the body.[5–8]

1.2.2 Role of Non-Specific Binding in the FBR

Non-specific binding, or fouling, is central to the initiation of the FBR. To further understand non-specific binding, one must first understand the difference between specific and non-specific binding. Specific binding occurs when molecules bind at defined interfaces, at defined orientations, with stereospecificity, and with shape complementarity. Non-specific binding lacks all of these qualities, and the molecules bind at multiple, ill-defined interfaces.[80] Thermodynamically, specific binding occurs when two binding partners, molecules or solid surfaces, explore multiple conformational states until they fall into a well-defined global minimum. Non-specific binding occurs when two binding partners fall into one of the many local minima as they explore multiple conformational states.[80] One important distinction here is that reversibility of a binding event is not the same as the specificity of the binding event. Reversibility is determined by the depth and steepness of the thermodynamic well that the binding partners have found themselves in. Both specific and non-specific binding can be either reversible or irreversible (Fig. 1.3).[80]

The blood plasma is composed of 8-9% solids, with the majority of the solids being proteins.[81] Because specific interactions scale linearly with concentration while non-specific interactions scale quadratically with concentration,[82] the high concentration of proteins in blood plasma means non-specific binding is very prevalent in biological systems. Due to this

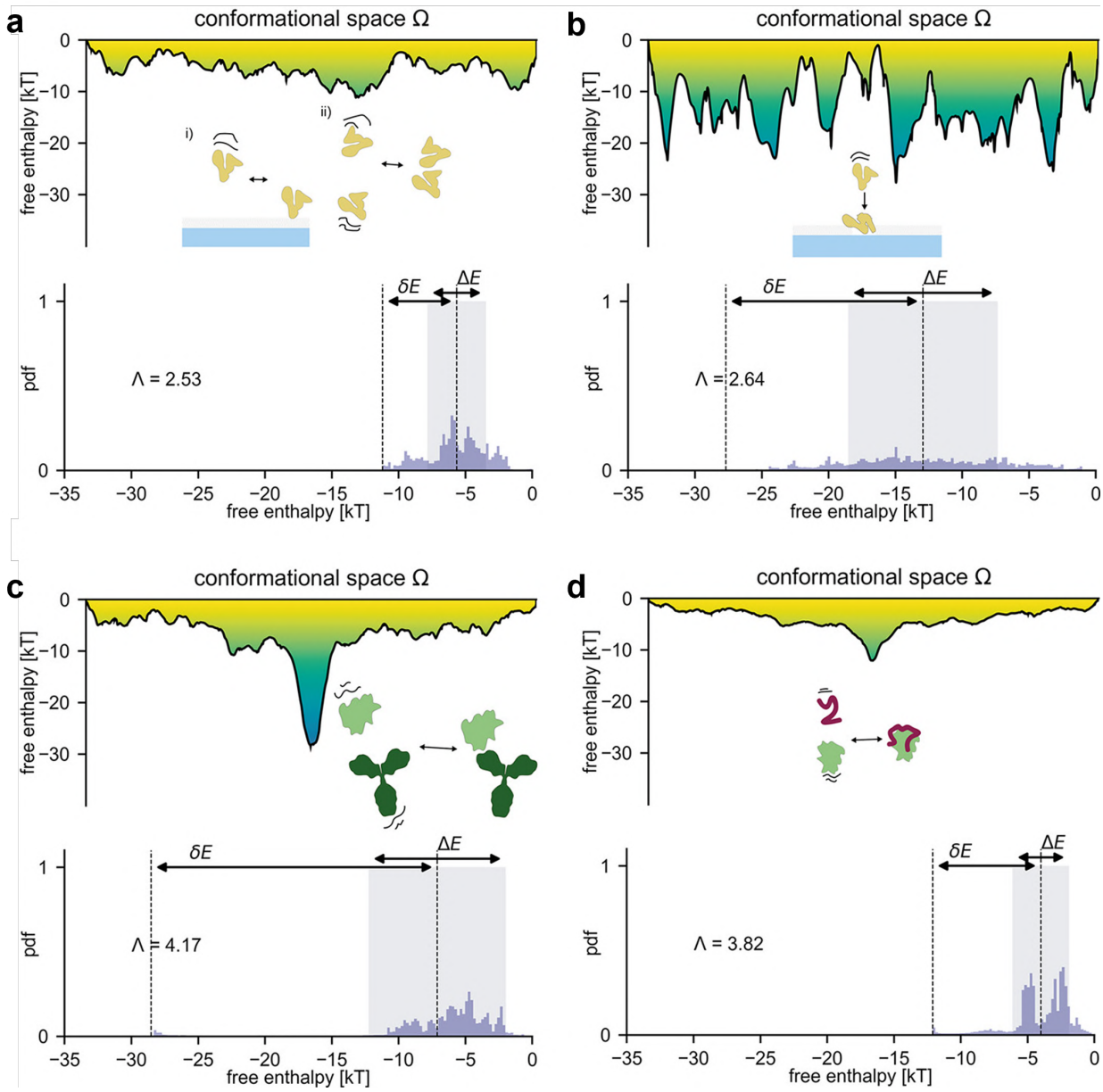

Figure 1.3. Qualitative intrinsic energy landscapes between two interaction partners of various conformational states. **a**, Energy landscape of reversible non-specific binding. **b**, Energy landscape of irreversible non-specific binding. **c**, Energy landscape of irreversible specific binding. **d**, Energy landscape of reversible specific binding. pdf, probability density function. Adapted with permission from Ref.[80]. Copyright 2021 American Chemical Society.

and thermodynamic limitations, some speculate that it will always be physically impossible to eliminate non-specific binding completely.[80]

In the FBR, the Vroman effect is believed to play a major role. The Vroman effect describes the continuous non-specific binding and de-binding of proteins on solid surfaces, usually in blood plasma.[83–85] At early time points during the protein adsorption process, kinetics dominate, leading to the adsorption of high mobility, high concentration proteins, such as albumin. Because many of the kinetically governed binding events are reversible, the initially bound proteins are gradually replaced by more thermodynamically favorably bound proteins, such as fibrinogen, kininogen, fibronectin, and vitronectin. Some of these proteins become irreversibly bound.[83–87] The kinetics argument is supported by studies that have found that bovine serum albumin undergoes a single step adsorption process, whereas fibrinogen undergoes a complex, multi-stage adsorption process.[88,89] These thermodynamically favorably bound proteins are thought to be the major mediators of the subsequent FBR processes.

Fibrinogen adsorption has been of particular interest among researchers investigating the FBR and, more broadly, fouling.[8,90] As little as 7 ng/cm^2 of fibrinogen has been shown to induce platelet adhesion and thrombosis.[75,91] The initiation of thrombosis leads to further fouling via fibrin and platelets. Surface-adsorbed fibrinogen mediates the adhesion of leukocytes to the implant surface via CD11b/CD18 (Mac-1), a complement receptor.[75,92] In addition, TLR4 recognizes fibrinogen, and the recognition of fibrinogen by TLR4 has been found to stimulate macrophages to secrete chemokines, such as MIP-1α and MCP-1.[70,78,93] It would make sense that intracellular DAMPs would be recognized by PRRs since under homeostatic conditions, intracellular DAMPs would not be accessible to PRRs. Yet, fibrinogen, which is a plasma protein that is always present extracellularly, is recognized by receptors. One potential explanation for this is that when the native conformational state of fibrinogen is perturbed, regions in the protein that were not normally accessible become

externalized. This is partially supported by studies that show that regions of fibrinogen that are buried in its native state get recognized by Mac-1 receptors when fibrinogen is adsorbed onto surfaces.[94,95] This is teleologically consistent with what has been proposed by Polly Matzinger — exposed hydrophobic regions that are normally buried in proteins become alarm signals for the immune system when externalized because the existence of denatured proteins is a potential sign for trauma, infection, or disease.[71]

In addition to fibrinogen, TLR4 recognizes a variety of DAMPs. In fact, the bulk of known DAMPs are recognized by TLR2 and TLR4.[70] In the context of the FBR, it has been shown that DAMPs bound to implant surfaces are a major drivers of fibrosis[96,97] and that TLR2 and TLR4 are responsible for orchestrating the subsequent events by binding to the surface-adsorbed DAMPs.[97,98] Knocking out either TLR2 or TLR4 led to partial decreases in the number of inflammatory cells and fibrotic capsule thicknesses in mice,[97–99] and a TLR2-TLR4 double knockout led to even larger decreases, with a 60% or more decrease in fibrotic capsule thickness depending on material type.[97,98]

1.2.3 Role of Macrophages in The FBR

Macrophages are believed to play a central role in the progression of the FBR. Macrophage depletion studies that observed a significant decrease in fibrotic encapsulation support this notion.[100–104] It is logical to think, then, that understanding the behavior of macrophages is key to understanding the FBR. However, because macrophages are highly heterogeneous and complex, there is limited consensus on the specifics of what factors affect macrophage behavior in the context of the FBR.[73]

Different researchers have claimed that either of the polarization states of macrophages, M1 and M2 macrophages, are responsible for the exacerbation of the FBR. However, a review on the matter[73] discovered that there were just as many articles claiming that M1 macrophages exacerbate the FBR as there are articles claiming that M2 macrophages exac-

erbate the FBR. How could this be? To understand the origins of the M1-M2 dichotomy, one must look into when the M1-M2 nomenclature was first proposed. The idea of a dichotomous classification system for macrophages first appeared in 1992 when it was proposed that macrophages can be classified as classically-activated and alternatively-activated macrophages.[105] Classically-activated macrophages reflected the IFN-γ dependent type 1 immune response driven by T helper 1 (T_h1) cells, and alternatively-activated macrophages reflected the IL-4 and IL-13 dependent type 2 immune response driven by T helper 2 (T_h2) cells.[105] Later, a different group proposed that classically-activated macrophages be referred to as M1 and alternatively-activated macrophages as M2.[106] This initial dichotomous framing of macrophages was wholly based on the limited knowledge at the time that there were only T_h1 and T_h2 driven responses.[107] However, in 1995, the anti-inflammatory T regulatory (T_{reg}) cells were discovered.[108] The following decade culminated in the discovery of T helper 17 (T_h17) cells.[109–111] By the end of the first decade of the 21st century, it was clear that there were four distinct types of immune responses: type 1, type 2, type 17, and regulatory.[112] Unfortunately, the M1-M2 classification system endured in various fields. There have been efforts to overhaul the macrophage classification system. One proposal was to subdivide M2 macrophages into M2a, M2b, and M2c macrophages.[113] Another proposal was to classify macrophages based on the agents that activates them, e.g., M(IFN-γ), M(IL-4), M(IL-10), and M(LPS) (Fig. 1.4).[114] Nontheless, because research on the role of macrophages in various contexts typically describes macrophages to fall on the M1-M2 dichotomy or continuum, subsequent discussions on the role of macrophage polarization in the FBR will operate under this framework.[73,115–117]

The acute phase of the FBR is thought to roughly mirror the wound healing process.[5,72] At the beginning of the wound healing process, macrophages primarily take on an M1-leaning polarization state, releasing pro-inflammatory cytokines, phagocytosing cellular and tissue debris, and releasing reactive oxygen species (ROS) to eliminate pathogens. The M1-

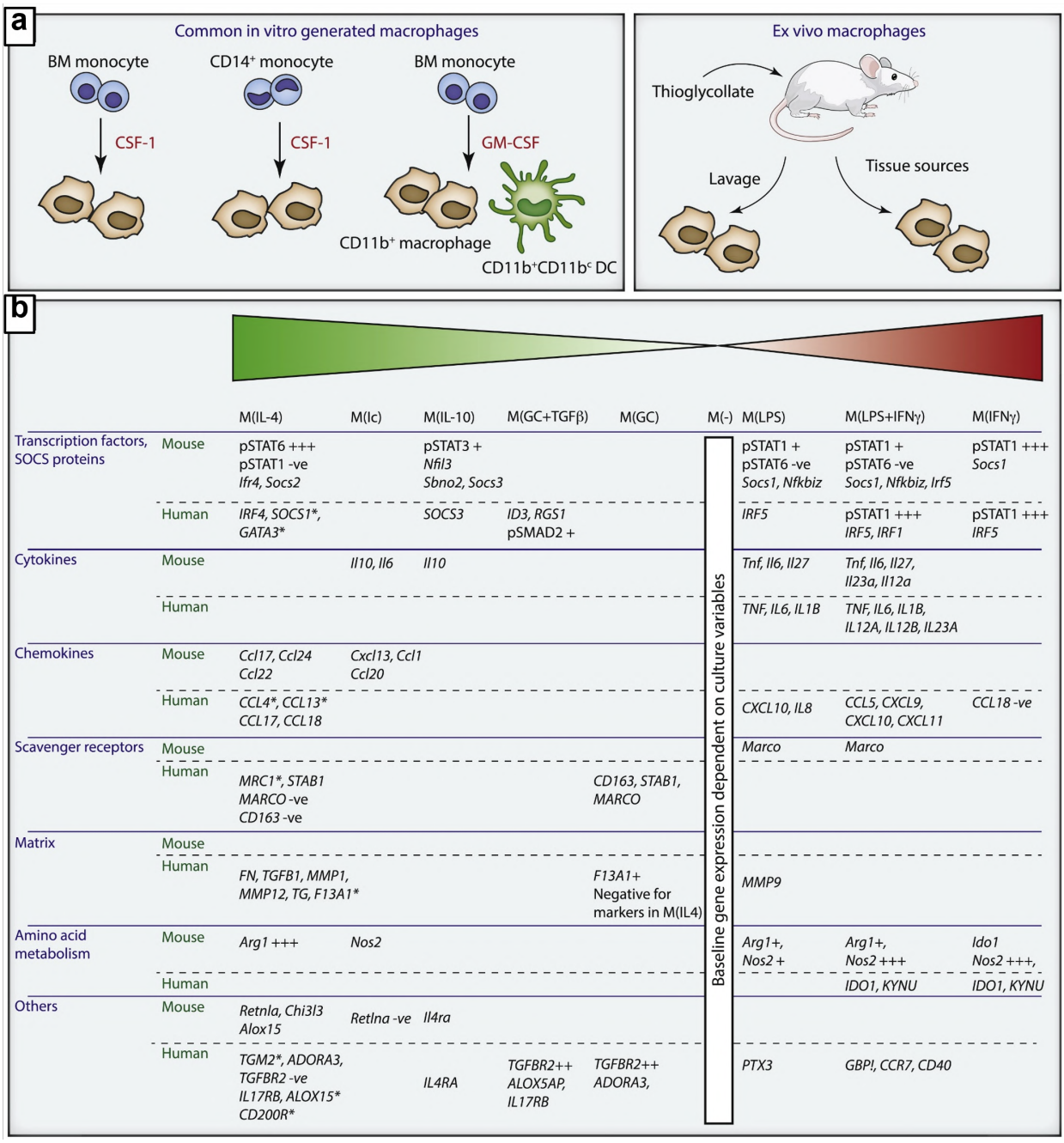

Figure 1.4. Framework for classifying macrophages based on stimulation conditions. **a**, Examples of commonly used macrophage preparation methods. CSF-1-cultured macrophages remain the predominant *in vitro* systems used for generating macrophages and is used as references for this classification system **b**, Markers for identifying different macrophage polarization states. With the M1-M2 classification system, M(IFN-γ) would correspond to M1 and M(IL-4) would correspond to M2. Adapted with permission from Ref.[114]. Copyright 2014 Elsevier.

dominant macrophage population gradually transitions to M2-like polarization states, and by around 1-week post-injury, the wound becomes M2-dominant. M2-leaning macrophages release anti-inflammatory cytokines and act to remodel the tissue surrounding the implant.[5,116,118,119] In the FBR, this M1-to-M2 transition is disrupted and enters a chronically inflammatory state because the implant prevents the wound from healing normally. Because, in many cases, the implant is too large to be phagocytosed by macrophages, the macrophages become "frustrated" and fuse into multinucleated foreign body giant cells (FBGCs) in order to become large enough to phagocytose the implant.[5] FBGCs are considered to be undesirable in the long term because they become a continuous source of enzymes and ROS that can degrade the implant.[5–8] It has been reported that the transition from the M1 to the M2 phenotypes is associated with the formation of FBGCs. However, other studies have challenged this dichotomy, suggesting that the FBGC macrophage polarization states may be on a continuum in between M1 and M2 polarization.[120–122] The role of FBGCs is recognized in humans, but the main animal model for the FBR, C57BL/6 mice, generates FBGCs very sparingly.[123] Therefore, conclusions drawn from animal models regarding FBGCs' role in the FBR should be interpreted with caution.

Because M2-like macrophages resolve the wound healing process, several studies have claimed that M2 macrophages are responsible for lower FBR severity and are anti-inflammatory.[124,125] This may need re-examination. First, as discussed earlier, the M1-M2 dichotomy is based on T_h1 and T_h2 cells. The T_h2-mediated type 2 immune response is inflammatory and is the main driver of allergies — far from being anti-inflammatory. The idea that T_h2-mediated responses are anti-inflammatory has been put to rest with the discovery of T_{reg}s, the true mediator of anti-inflammatory processes, in 1995.[108] Second, a series of studies have found that the type 2 immune response, along with M2-like macrophages, are the main drivers of fibrotic diseases.[126–131] Teleologically, this makes sense because the purpose of the type 2 immune response is to expel multi-cellular parasites

through responses such as tissue remodeling. If the expulsion is unsuccessful, the type 2 immune response facilitates fibrotic encapsulation for isolating the parasites, regardless of whether they are dead or alive.[132] The body seems to treat implants similarly to the way it treats multi-cellular parasites. In addition, key type 2 immunity cytokines, IL-4 and IL-13, have been found to directly stimulate collagen production in fibroblasts.[133–136]

1.2.4 Role of Fibroblasts in the FBR

Fibroblasts are responsible for the deposition of collagen, which is the main component of the fibrotic capsule. All connective tissues in the body consist of fibroblasts that are embedded in extracellular matrices. When fibroblasts transdifferentiate into myofibroblasts, collagen production substantially increases and becomes pathogenic when myofibroblast activation is prolonged, leading to fibrotic capsule formation in the FBR.[73] In normal wound healing, myofibroblasts undergo apoptosis after the wound is healed. Although, in the FBR, macrophages are known to originate from circulating monocytes and tissue resident macrophages,[104] the progenitor source of myofibroblasts is somewhat controversial.[137–139] Myofibroblasts are a highly heterogeneous population with diverse cellular origins, such as tissue resident fibroblasts, pericytes, fibrocytes, myoblasts, and adipocytes.[137–139] Because of this, other than the well known fact that the proximity of α-SMA$^+$ myofibroblast is associated with more severe FBR,[73,100,103,140] there is limited consensus on if there are other relevant phenotypes.

Fibroblasts from different organs all exhibit specialized functions. Dermal fibroblasts, for example, consist of subpopulations including but not limited to reticular, papillary, dermal papilla, and preadipocyte.[72] In the skin, it was shown that dermal fibroblasts expressing *Engrailed-1* in its embryonic progenitors was the predominant lineage, from which myofibroblasts are derived, and was responsible for fibrotic wound healing. The deletion of the gene led to a significant reduction in fibrosis in mouse wound healing models.[141] Interestingly, it was also found that adipocytes derived from *Engrailed-1* lineage fibroblasts was a

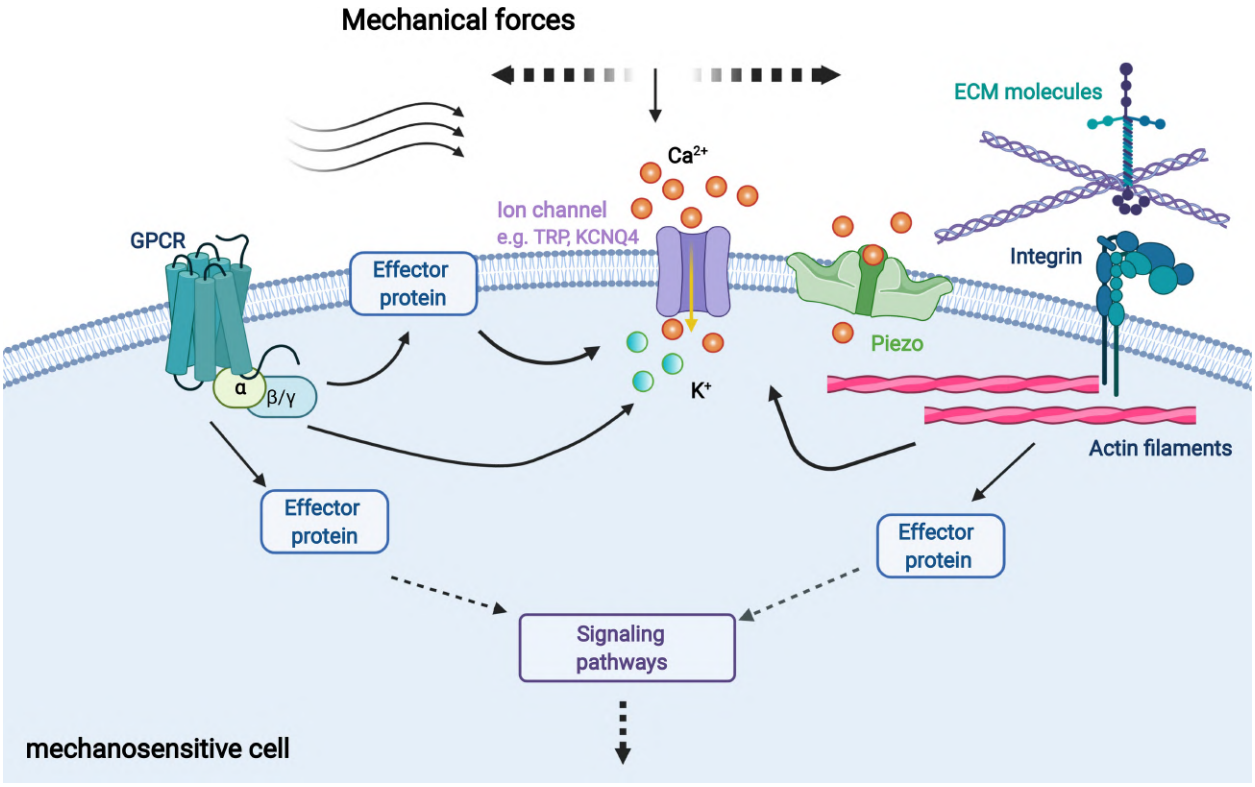

Figure 1.5. Overview of mechanosensitive receptors. Mechanosensitive GPCRs, Mechanosensitive ion channels, and integrins are known to transduce mechanical signals. ECM, extracellular matrix; GPCR, G protein-coupled receptor; TRP, transient receptor potential. Adapted with permission from Ref.[146]. Copyright 2022 American Physiological Society.

major contributor to fibrosis.[142] It was also found in the FBR that *Engrailed-1*$^+$ cells were prevalent in the fibrotic capsules.[143] Unfortunately, given the diverse and varied sources of myofibroblasts in other parts of the body,[144,145] the findings on *Engrailed-1* may not apply to fibrosis and the FBR in other parts of the body and requires more investigation.

1.2.5 Role of Mechanotransduction in The FBR

It has been known that lower Young's modulus is associated with thinner and less dense collagen capsules and lower cell infiltration in the FBR.[55,147,148] In the context of the FBR, there are two general mechanisms with which cells interact with implants mechanically. They are force transduction through the cytoskeleton via receptor-mediated cellular anchoring on

implant surfaces, such as integrins,[149,150] and force transduction through deformation of cell membranes via stretch-activated mechanosensitive proteins (SMPs), such as Piezo1, TRPV4, and most mechanosensitive GPCRs (Fig. 1.5).[150,151]

For integrins to bind to implant surfaces, RGD peptide sequences need to be present at the surface of implants, which is usually not the case.[5,152] The introduction of RGD peptide sequences require protein adsorption. Specifically, fibronectin, vitronectin, collagen, fibrinogen, and laminin are known to mediate integrin adhesion with the implant surface.[5,152] When cells come in contact with stiff surfaces, integrins bind to the RGD peptide sequences and multiproteins complexes called focal adhesions (FAs) form under the cell membrane. FAs transfer the mechanical stimuli from the integrins to the cytoskeleton. The cytoskeleton is coupled to the nucleus, allowing mechanical information to be translated to genetic expression.[150]

SMPs are thought to be activated by stretching, shear stress, and vibrations.[146] Given that the cell membrane needs to be deformed for force to be transduced[146] and there are reports of crosstalk between Piezo1 and FAs,[151] it is likely that cell spreading on substrates as a result of integrin binding is contributing to the activation of SMPs. Another possibility is that the displacement of tissues as a result of the insertion of the implant leads to the induction of compressive forces to its surroundings, which translates to the stretching of cell membranes.

1.3 Material Strategies for Suppressing The FBR

1.3.1 Antifouling Strategies for Suppressing The FBR

Antifouling materials are a class of materials that prevent non-specific binding and can vary in chemical structures. Zwitterionic polymers, a type of antifouling material, was one of the first materials to demonstrate FBR suppressing properties.[124] Zwitterionic polymers

consist of neutral monomers with two oppositely charged functional groups. Some examples of zwitterionic polymers are poly(2-methacryloyloxyethyl phosphorylcholine) (PMPC), poly(carboxybetaine methacrylate) (PCB), poly(sulfobetaine methacrylate) (PSB), and poly(trimethylamine *N*-oxide) (PTMAO) (Fig. 1.6).[153–156] Because the FBR is initiated by the surface adsorption of proteins, zwitterionic polymers potently suppress the FBR.[153,157] There are two theories for the origins of the antifouling properties of zwitterionic polymers. The first theory is that the electrostatically mediated strong hydration of zwitterionic polymers is responsible for repelling protein adsorption.[153,154] The second theory is that the closely located opposite charges on the polymer backbone allow the water molecules to form an unperturbed hydrogen bonding network, which eliminates the thermodynamics driving force for protein adsorption.[154]

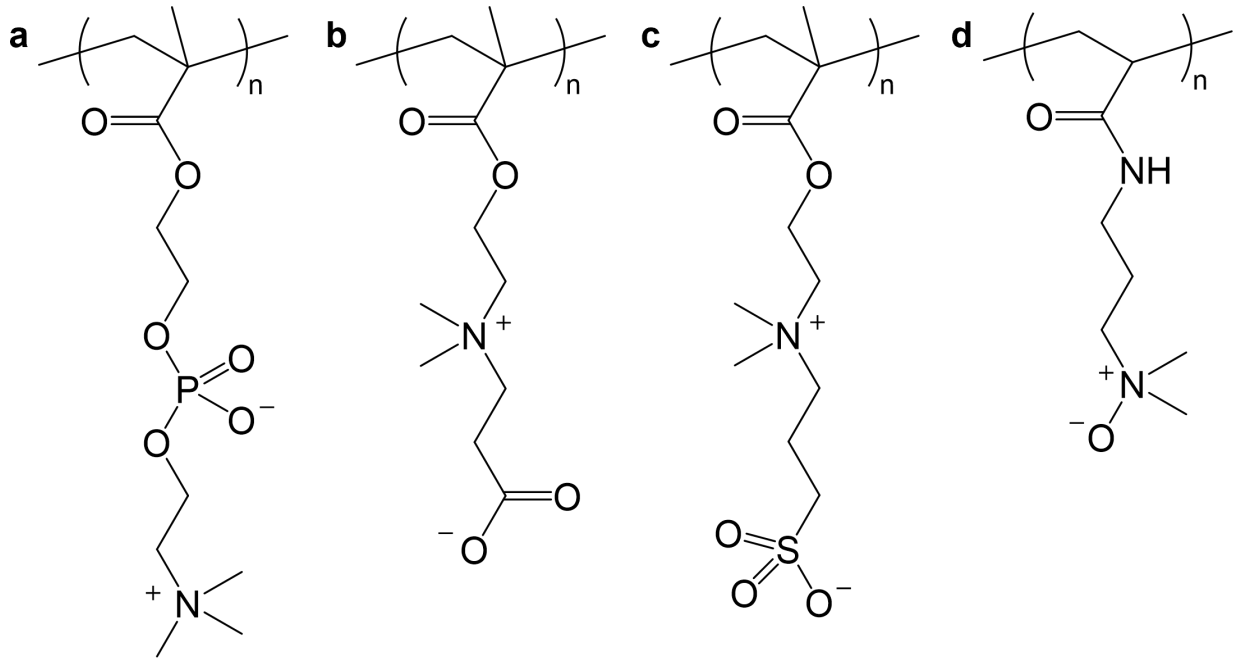

Figure 1.6. Chemical structures of zwitterionic polymers. **a**, Structure of poly(2-methacryloyloxyethyl phosphorylcholine) (PMPC). **b**, Structure of poly(carboxybetaine methacrylate) (PCB). **c**, Structure of poly(sulfobetaine methacrylate) (PSB). **d**, Structure of poly(trimethylamine *N*-oxide) (PTMAO).

The strong hydration make it possible for zwitterionic polymers to be prepared into

hydrogels, which are characterized by high water content and low mechanical moduli.[153,158] Low mechanical moduli further help the suppression of the FBR.[5] Jiang and co-workers showed that zwitterionic hydrogel implants can nearly eliminate the FBR for up to a year in mice due to a combination of their antifouling properties and low mechanical moduli. This is the longest duration of FBR suppression that has ever been reported.[159] Despite being exposed to about 300 distinct proteins in the blood plasma, zwitterionic polymer brushes consistently achieve a total protein adsorption of less than 10 ng/cm^2.[75,153] In comparison, the exposure of polymer brushes of poly(ethylene glycol) (PEG), a commonly used biocompatible and antifouling polymer, to blood plasma leads to a protein adsorption of over 600 ng/cm2.[160] Moreover, less than 5 ng/cm^2 of fibrinogen adsorption was consistently observed on pSB polymer brushes.[153,161]

Other reported antifouling approaches for suppressing the FBR include charged balanced polyelectrolyte complexes[162] and poly(β-homoserine).[163] Polyelectrolyte complexes are formed when oppositely charged polymers bind electrostatically. Charge balanced polyelectrolyte complexes made from negatively charged alginate and positively charged polyethyleneimine have been shown to suppress the FBR in mice for up to 3 months.[162] Poly(β-homoserine) is a silk-inspired material with marginal antifouling properties. Despite having similar antifouling properties as PEG-based materials, it showed suppressed FBR compared to PEG.[163]

1.3.2 Immunomodulatory Strategies for Suppressing The FBR

Here, immunomodulatory properties of a material will be defined as properties that allow materials to shape the immune response to the materials by directly or indirectly acting on cells. This is in contrast with antifouling properties, which indirectly act on immune cells by limiting the amount of endogenous molecules that adsorb onto the surface upon implantation. In other words, immunomodulatory materials direct the FBR with the presence

of immunological signaling while antifouling materials does so with the absence or lack of immunological signaling. Out of the immunomodulatory materials, the most numerous type are the ones discovered via high throughput screens.[140,164–166] Other types are derived from naturally occurring biological ligands.

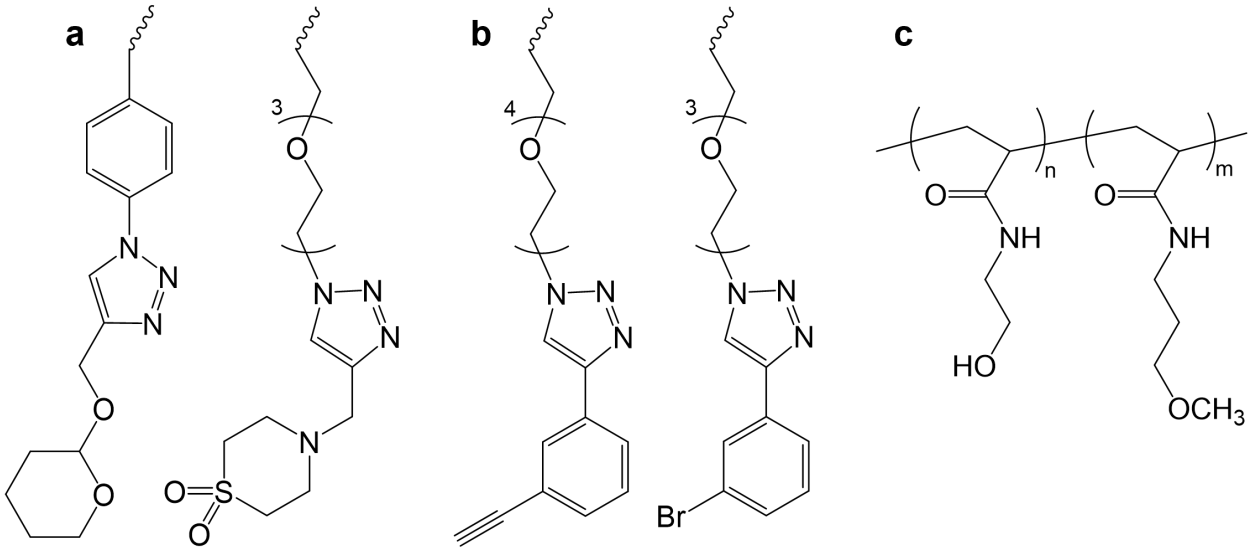

Figure 1.7. Immunomodulatory chemical structures for suppressing the FBR. **a**, Top performing side chain structures of alginate found in a high throughput screen in Ref.[140]. **b**, Top performing side chain structures of alginate found in a high throughput screen in Ref.[164]. **c**, Top performing polyacrylamide-based copolymer found in a high throughput screen in Ref.[166].

As it implies, high throughput screens involve synthesizing a library of molecules. The molecules are tethered on a material, and the library of materials is tested for FBR-suppressing effects *in vivo*. The top candidates of the screen have been found to perform extraoridinarily well with only trace amounts of fibrosis.[140,164–166] Because of this, the mechanism of FBR-suppression is largely unknown, and it is assumed that these materials are immunomodulatory because of empirical biological observations. For example, follow up studies on a combinatorial screening work showed that the top performing material had a high ratio of phospholipid to fatty acid adsorption. The authors reasoned that since phospholipids are anti-inflammatory and fatty acids are pro-inflammatory, the lipid

deposition profile is responsible for the FBR suppression.[167,168]

Out of the naturally occurring biological ligands, sialic acid and CD47 have been tested for FBR suppression. Sialic acid is an anti-inflammatory saccharide that is usually tethered on the *N*-glycans of proteins on the cell membrane surface. It is often found in its polymeric form, polysialic acid.[169] Polysialic acid has been found to suppress the FBR and the associated fibrosis to a limited extent.[170] CD47, also known as the "don't eat me" signal, is an innate immune checkpoint molecule responsible for preventing healthy and native cells from being phagocytosed. CD47 peptides have been coated on bare metal stents and have been shown to significantly reduce neointimal hyperplasia in rats. Although not tested under conditions that are not traditional FBR models, the fact that CD47 peptides were able to be effective under the harsh, highly fouling conditions in the blood filled vasculature shows significant promise for FBR suppression in other regions in the body. In addition, bare metal stents were used, and stiff materials — stainless steel in this case — are known to exacerbate the FBR, which makes the approach even more convincing.[171]

1.3.3 Targeting Mechanotransduction Pathways for Suppressing The FBR

The simplest way to inhibit the mechanotransduction pathway for suppressing the FBR is to make the Young's modulus of the implant as low as possible.[55,147,148] However, given that collagen deposition is observed at Young's moduli as low as 2 kPa[55] and given that materials become fragile at such a low Young's modulus, it is not entirely certain how viable the strategy is. A potential reported solution is to create a layered structure, consisting of ultra-soft tissue-facing layers and a tough, stiff layer to mechanically support the ultra-soft layers.[55,172]

Other than lowering the Young's modulus of the implant, there has been efforts to identify and inhibit targets in the mechanotranduction pathway.[173–176] Currently, the only known way to inhibit these targets is the administration of drugs, such as CWHM-12 to

suppress TGF-β signaling[173] and verteporfin to inhibit yes-associated protein (YAP).[174] Drug-mediated approaches require a continuous local delivery of the drug to stay effective, making long-term FBR-suppression challenging. The drug may run out over time and lose its effectiveness.

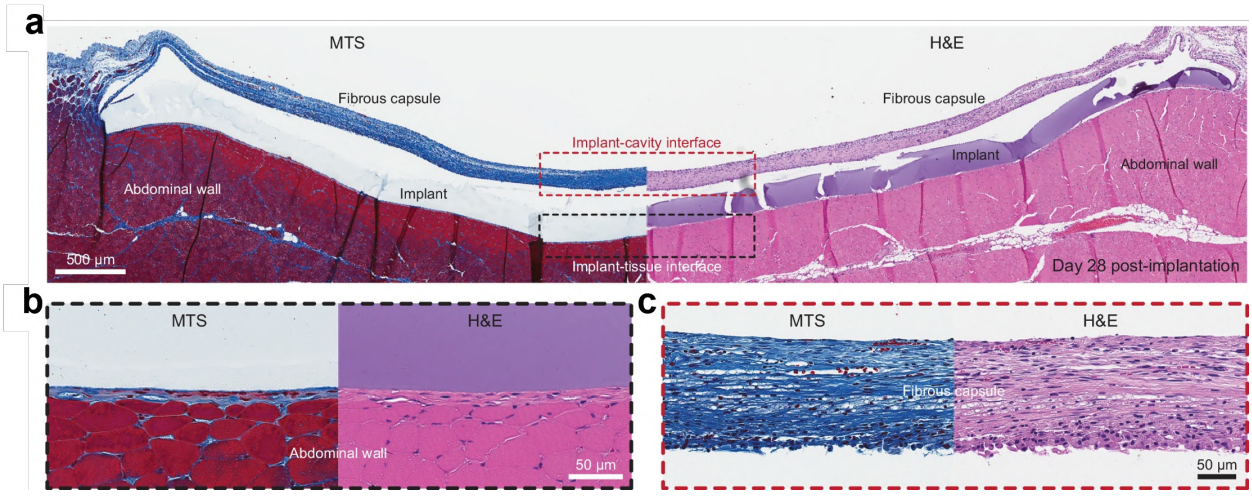

Figure 1.8. Tissue adhesive eliminates fibrosis at adhesion interface. **a**, Side-by-side Masson's trichrome stained and H&E stained tissue sections of tissue adhesive fixed on the abdominal wall 28 days post-implantation. **b**, Magnified image of (**a**) at the adahesion interface. **c**, Magnified images of (**a**) at the cavity interface. Adapted with permission from Ref.[177]. Copyright 2024 Springer Nature.

1.3.4 Tissue Adhesion for Suppressing The FBR

Recently, an approach to completely eliminate fibrotic capsules have been reported.[177–179] The approach involves preparing a tissue adhesive, comprised of poly(acrylic acid), poly(N-succinimidyl acrylate), and a polymer for endowing the tissue adhesive mechanical toughness. The fibrotic capsule is eliminated at the adhesion interface but is present at typical levels on all the other sides of the implant that is not adhered to tissue. Because of this, it is expected to be an excellent solution for electrophysiological interfaces, in which the implant electrodes are not required to be exposed to biofluids. So far, the tissue adhesive strategy has been reported to work on a variety of organs, including the abdominal wall, colon, stomach, lung,

and heart,[177,178] in addition to peripheral nerves[179]. Both electrophysiological stimulation and recording have been demonstrated.[177–179]

1.4 Conjugated Polymers for Implantable Electronics

1.4.1 Introduction to Conjugated Polymers

Conjugated polymers (CPs) consist of alternating double and single bonds, which give rise to overlapping p-orbitals and delocalized π-electrons that facilitate electron transport. Compared to inorganic electronic materials, CPs are promising candidates due to their mixed electronic/ionic conducting properties, broad chemical design space, low mechanical moduli, and solution-processability at low temperatures.[180,181] Charge transport in biological systems are predominantly mediated by ions as opposed to conventional electronics, for which electron transport is the primary charge transport mechanism.[182,183] Unlike inorganic materials, CP materials contain a large fraction of free volume due to their weak inter-chain van der Waals interactions. As a result, ions can readily diffuse through CP materials. Unlike inorganic materials, CP materials also lack an oxide layer, which would act as a barrier to ion transport. Additionally, the hydrophilicity of CPs can be chemically tuned so that the CP material can swell when exposed to water, further improving ion transport properties.[181] Charge transport at the interface between extracellular media and CPs occur through faradaic and capacitive mechanisms, giving CPs its mixed electronic/ionic conducting properties and its ability to effectively bridge the gap between biological and electronic systems.[180,184] As a result, CP-coated platinum electrodes in biological environments can achieve lower electrochemical impedances, higher charge storage capacities, and higher charge injection limit compared to bare platinum electrodes.[185]

The relatively weak van der Waals interactions between polymer chains also give CPs their low Young's moduli on the order of kPa to MPa. Inorganic electronic materials have

rigid three-dimensional networks of chemical bonds, which give them Young's moduli on the order of GPa.[186] Due to their softness, CPs offer better immunocompatibility than their inorganic counterparts.[5,180,181] Moreover, the weak intermolecular interactions allow low-temperature solution processing, allowing CPs to be processed into a variety of form factors during device fabrication.[181] The property of CPs to be solution processed at low temperatures also translates to greater flexibility during the process of incorporating biological moieties in the device when compared to the harsh conditions the biological molecules would potentially be exposed to during the processing step of inorganic materials.[180,181]

CPs in their pristine states are semiconducting as opposed to being conducting, due to the relatively large gap between the HOMO and LUMO energy levels, which is commonly referred to as the band gap. To make CPs conductive, the band gap needs to be reduced. This is achieved by oxidizing or reducing CPs in a process known as doping. P-type doping refers to the oxidative process in which the CPs gain positive charges along their backbones, and n-type doping refers to the reductive process in which the CPs gain negatives charges. There is greater academic interest for p-doped CPs because of their higher chemical stability.[187] Several p-doped CPs have been reported, including polyacetylene, polyaniline, polyaniline, poly(p-phenylene), poly(p-phenylene vinylene), and polythiophene. Among CPs, polythiophene and its derivatives, such as poly(3,4-ethylenedioxythiophene) (PEDOT), have attracted significant attention because of its high chemical stability under ambient conditions. Through the 3,4-disubstitution of thiophene monomers with oxygen, the stability can be further improved. PEDOT is one such polythiophene synthesized from 3,4-disubstituted thiophene monomers.[187] However, PEDOT suffer from poor solubility in most solvents both in its pristine and doped states.[180,188] To overcome this issue, p-doped PEDOT can be polymerized in the presence of poly(styrene sulfonic acid) (PSS). PSS serves as a dopant and counterion for PEDOT. The result are PEDOT:PSS polyelectrolyte complex nanoparticles with PEDOT-rich cores and PSS-rich outer shells that can be dispersed in water (Fig. 5).

PEDOT:PSS is highly conductive, highly processable, and non-cytotoxic.[188–191] As such, PEDOT:PSS has already been used as an electrode coating in a FDA-approved medical device, Amplicoat®, for improving the signal transduction at the electrode-tissue interface.[192] Additionally, PEDOT:PSS aqueous dispersions are widely available through the commercial vendors Heraeus and Agfa, further contributing to its popularity in the bioelectronics field.[188,189]

Since its introduction in the 1990s, the method with which PEDOT:PSS is processed has been an active area of research because processing conditions greatly influences its electrical and mechanical properties.[190] Because PEDOT:PSS exists as nanoparticles with an insulating PSS outer shell, it exhibits conductivities less than 1 S/cm in its pristine form. Hence, connecting the PEDOT domains increases conductivity of PEDOT:PSS.[190] Both as a cosolvent and as a post-treatment solvent, polar organic solvents, such as ethylene glycol and dimethyl sulfoxide (DMSO), have been used to increase the conductivity of PEDOT:PSS by one to three orders of magnitude. Treatment of PEDOT:PSS films with different types of acids also leads to conductivity enhancements.[190,191] PEDOT:PSS films with the highest conductivity of over 4000 S/cm was achieved through a sulfuric acid post-treatment process, making its conductivity comparable to indium tin oxide.[193] Other examples of additives are ionic liquids which can increase the conductivity and stretchability of PEDOT:PSS films from less than 1 S/cm to over 1000 S/cm and from less than 20% to over 100%, respectively.[194] Along with its high conductivity, high stability in ambient conditions, high processability, and low cytotoxicity, the vast parameter space available for processing makes PEDOT:PSS a promising material for implantable electronics applications.

1.4.2 PEDOT:PSS Hydrogels and Its Derivatives for Implantable Electronics

An attractive aspect of PEDOT:PSS for bioelectronics applications is that it can be readily prepared into hydrogels, due to its hydrophilic PSS component. PEDOT:PSS hydrogels

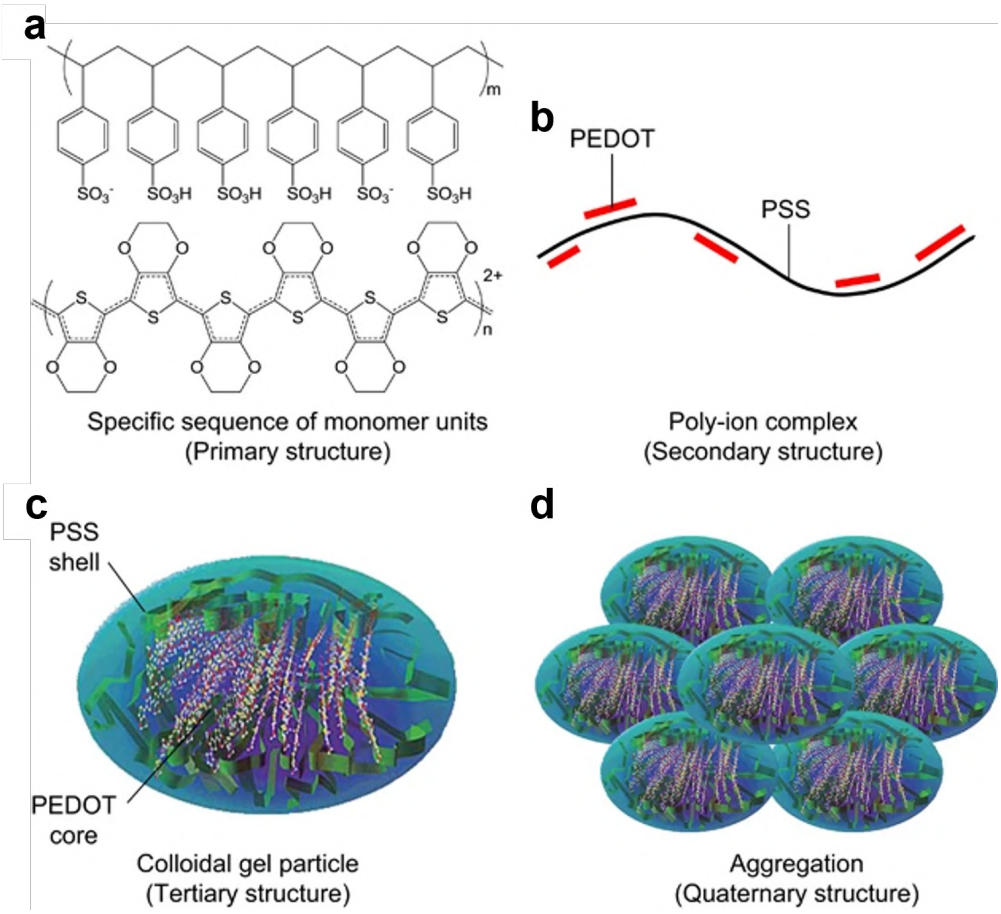

Figure 1.9. Hierarchical structure of PEDOT:PSS. **a**, Chemical structures of PEDOT and PSS. **b**, Secondary structure formed from the polyelectrolyte complexation between PEDOT and PSS. **c**, Colloidal gel particle formed from the micellization of PEDOT and PSS. **d**, Aggregation of the particles cause PEDOT:PSS to form into continuous bulk materials. Adapted with permission from Ref.[191]. Copyright 2015 Springer Nature.

can broadly be divided into single component PEDOT:PSS hydrogels and interpenetrating network (IPN) PEDOT:PSS hydrogels. Single component PEDOT:PSS hydrogels can be prepared through the addition of DMSO or an ionic liquid, the subsequent removal of water, and the re-swelling of PEDOT:PSS in water, resulting in conductivities between 40 and 50 S/cm.[195,196] IPN PEDOT:PSS hydrogels consisting of PEDOT:PSS and a second hydrogel component can be prepared to give rise to a unique combination of properties. The most conductive PEDOT:PSS-based IPN hydrogel reported was prepared by soaking a single component PEDOT:PSS hydrogel with an acrylic acid monomer solution, followed by the

polymerization of the monomers. The resultant hydrogel achieved a conductivity of 0.23 S/cm, and the mechanical properties could be tuned by adjusting the composition.[197]

Despite its widespread use and its ability to form IPN hydrogels, No PEDOT:PSS-based materials to date have the intrinsic ability to suppress the FBR. The most relevant but fundamentally different group of studies so far focused on combining biocompatible materials, such as silk fibroin, gelatin, and poly(ethylene glycol) (PEG), with a PEDOT:PSS hydrogel, but all these studies focus on improving cytotoxicity and cell adhesion of the hydrogel.[198–200] In the field of biomaterials, it has long been known that the long-term implantation of biocompatible and bioinert materials, such as PEG and titanium, leads to an immune response and a FBR.[7,201,202] It is clear from past studies that low cytotoxicity and bioinertness, while beneficial, is not sufficient to suppress the FBR. Therefore, PEDOT:PSS has great potential for giving rise to the first immune compatible electronic material by combining the electrically conductive property of PEDOT:PSS with an immunocompatible material.

1.5 Aim of This Research

Even though incomplete, the fundamental understanding of the FBR has advanced significantly over the past few decades, Advances in the fundamental understanding of immunology, wound healing, and fibrosis have provided context and filled gaps in the understanding of the FBR. However, there are few reported methods for suppressing the FBR, and out of the reported ones, the methods seem to be not broadly applicable and/or lead to incomplete FBR suppression. Tissue adhesion appears to be very promising,[177–179] but fibrotic encapsulation on non-adhesive interfaces could be an issue if free diffusion of molecules is desired. Screening studies have led to the discovery of highly promising antifibrotic chemical structures,[140,164–166] but questions remain on whether they can be used on bulk electronic devices and whether they will perform just as well in humans.

In addition to their excellent tissue interfacing properties, PEDOT:PSS is a versatile

material for testing the effects of incremental changes to material properties, a property shared by organic materials in general. PEDOT:PSS can be chemically modified and easily be made into physically blended composite materials. However, chemical modification is difficult because PEDOT:PSS lacks useful functional groups and harsh conditions are required for useful chemical modifications, which can degrade the electrical properties. To explore new strategies for FBR suppression and to address the difficulty of chemically modifying PEDOT:PSS, we studied how chemical heterogeneity, achieved by physically blending two different materials, affects the FBR and how the findings can be used in working bioelectronic devices. Chemical heterogeneity is an important property to study because electronic IMDs rarely have chemically homogeneous surfaces. Even in relatively simple electrophysiological devices, there are multiple channels on the surface composed of an electronic material, and the channels are separated by insulators at the surface of the device. To more directly address the difficulty of chemically modifying PEDOT:PSS, we also explore a new way to achieve stable antifouling coatings on the surface of PEDOT:PSS. For the first time, we report how chemical heterogeneity could be a parameter that can be tuned to suppress the FBR and how stable zwitterionic antifouling coatings can be deposited on PEDOT:PSS.

1.6 References

1. Jeffrey, K. & Parsonnet, V. Cardiac Pacing, 1960–1985: A Quarter Century of Medical and Industrial Innovation. *Circulation* **97,** 1978–1991. (2026) (1998).
2. Bazaka, K. & Jacob, M. V. Implantable Devices: Issues and Challenges. en. *Electronics* **2,** 1–34. ISSN: 2079-9292. (2026) (Dec. 2012).
3. Saha, S. *et al.* Progress in Brain Computer Interface: Challenges and Opportunities. English. *Frontiers in Systems Neuroscience* **15.** ISSN: 1662-5137. (2026) (Feb. 2021).
4. *Global Implantable Medical Devices Market Size By Product Type (Cardiovascular Implants, Orthopedic Implants, Breast Implants), By Material Type (Metallic, Ceramic), By End- User (Hospitals, Ambulatory Surgical Centers), By Geographic Scope And Forecast* en. (2026).
5. Klopfleisch, R. & Jung, F. The pathology of the foreign body reaction against biomaterials. en. *Journal of Biomedical Materials Research Part A* **105,** 927–940. ISSN: 1552-4965. (2026) (2017).
6. Morais, J. M., Papadimitrakopoulos, F. & Burgess, D. J. Biomaterials/Tissue Interactions: Possible Solutions to Overcome Foreign Body Response. en. *The AAPS Journal* **12,** 188–196. ISSN: 1550-7416. (2026) (June 2010).
7. Anderson, J. M., Rodriguez, A. & Chang, D. T. Foreign body reaction to biomaterials. *Seminars in Immunology. Innate and Adaptive Immune Responses in Tissue Engineering* **20,** 86–100. ISSN: 1044-5323. (2026) (Apr. 2008).
8. Ward, W. K. A Review of the Foreign-body Response to Subcutaneously-implanted Devices: The Role of Macrophages and Cytokines in Biofouling and Fibrosis. EN. *Journal of Diabetes Science and Technology* **2,** 768–777. ISSN: 1932-2968. (2026) (Sept. 2008).
9. Wei, X. & Liu, J. Power sources and electrical recharging strategies for implantable medical devices. en. *Frontiers of Energy and Power Engineering in China* **2,** 1–13. ISSN: 1673-7504. (2026) (Mar. 2008).
10. Kronenberg, J. *et al.* Foreign Body Reaction to Cochlear Implant. *Oto-Rhino-Laryngologia Nova* **11,** 207–209. ISSN: 1014-8221. (2026) (Sept. 2002).
11. Mulpuru, S. K., Madhavan, M., McLeod, C. J., Cha, Y.-M. & Friedman, P. A. Cardiac Pacemakers: Function, Troubleshooting, and Management. *JACC* **69,** 189–210. (2026) (Jan. 2017).
12. Keiler, J. *et al.* Neointimal fibrotic lead encapsulation – Clinical challenges and demands for implantable cardiac electronic devices. *Journal of Cardiology. Topics in implantable medical devices* **70,** 7–17. ISSN: 0914-5087. (2026) (July 2017).
13. DeForge, W. F. Cardiac pacemakers: a basic review of the history and current technology. *Journal of Veterinary Cardiology. Cardiac Pacing* **22,** 40–50. ISSN: 1760-2734. (2026) (Apr. 2019).

14. Radovsky, A., Van Vleet, J., Stokes, K. & Tacker Jr., W. Paired Comparisons of Steroid-Eluting and Nonsteroid Endocardial Pacemaker Leads in Dogs: Electrical Performance and Morphologic Alterations. en. *Pacing and Clinical Electrophysiology* **11,** 1085–1094. ISSN: 1540-8159. (2026) (1988).

15. Mond, H. G., Helland, J. R., Stokes, K., Bornzin, G. A. & McVENES, R. The Electrode-Tissue Interface: The Revolutionary Role of Steroid-Elution. en. *Pacing and Clinical Electrophysiology* **37,** 1232–1249. ISSN: 1540-8159. (2026) (2014).

16. Zhao, Q. H. *et al.* Human plasma 2-macroglobulin promotes in vitro oxidative stress cracking of pellethane 2363-80A: In vivo and in vitro correlations. en. *Journal of Biomedical Materials Research* **27,** 379–388. ISSN: 1097-4636. (2026) (1993).

17. Anderson, J. M. en. in *Biological Interactions on Materials Surfaces: Understanding and Controlling Protein, Cell, and Tissue Responses* (eds Puleo, D. A. & Bizios, R.) 225–244 (Springer US, New York, NY, 2009). ISBN: 978-0-387-98161-1. (2026).

18. De Voogt, W. G. Pacemaker leads: performance and progress. *The American Journal of Cardiology* **83,** 187–191. ISSN: 0002-9149. (2026) (Mar. 1999).

19. Rhoden, W. E., Llewellyn, M. J., Schofield, S. W. & Bennett, D. H. Acute and chronic performance of a steroid eluting electrode for ventricular pacing. English. *International Journal of Cardiology* **37,** 209–212. ISSN: 0167-5273, 1874-1754. (2026) (Nov. 1992).

20. Peng, H., Sun, Z., Zhang, H. & Ma, W. Long-term performance of right ventricular pacing leads: risk factors associated with permanent right ventricular pacing threshold increase. en. *Journal of Interventional Cardiac Electrophysiology* **55,** 349–357. ISSN: 1572-8595. (2026) (Sept. 2019).

21. Vashist, S. K. Continuous Glucose Monitoring Systems: A Review. en. *Diagnostics* **3,** 385–412. ISSN: 2075-4418. (2026) (Oct. 2013).

22. Garg, S. K. Past, Present, and Future of Continuous Glucose Monitors. EN. *Diabetes Technology & Therapeutics* **25.** Num Pages: S-4, S–1. ISSN: 1520-9156. (2026) (June 2023).

23. Gross, T. M. *et al.* Performance Evaluation of the MiniMed® Continuous Glucose Monitoring System During Patient Home Use. EN. *Diabetes Technology & Therapeutics* **2,** 49–56. ISSN: 1520-9156. (2026) (May 2000).

24. Ribet, F., Stemme, G. & Roxhed, N. Real-time intradermal continuous glucose monitoring using a minimally invasive microneedle-based system. en. *Biomedical Microdevices* **20,** 101. ISSN: 1572-8781. (2026) (Dec. 2018).

25. Klueh, U. Analysis: On the Path to Overcoming Glucose-Sensor-Induced Foreign Body Reactions. EN. *Journal of Diabetes Science and Technology* **7,** 452–454. ISSN: 1932-2968. (2026) (Mar. 2013).

26. Sharkawy, A. A., Klitzman, B., Truskey, G. A. & Reichert, W. M. Engineering the tissue which encapsulates subcutaneous implants. I. Diffusion properties. en. *Journal of Biomedical Materials Research* **37,** 401–412. ISSN: 1097-4636. (2026) (1997).

27. Onuki, Y., Bhardwaj, U., Papadimitrakopoulos, F. & Burgess, D. J. A Review of the Biocompatibility of Implantable Devices: Current Challenges to Overcome Foreign Body Response. en. *Journal of Diabetes Science and Technology* **2,** 1003–1015. (2026) (Nov. 2008).

28. Xie, X. *et al.* Reduction of measurement noise in a continuous glucose monitor by coating the sensor with a zwitterionic polymer. en. *Nature Biomedical Engineering* **2,** 894–906. ISSN: 2157-846X. (2026) (Dec. 2018).

29. Bailey, T. S. *et al.* Evaluation of Accuracy and Safety of the 365-Day Implantable Eversense Continuous Glucose Monitoring System: The ENHANCE Study. EN. *Diabetes Technology & Therapeutics* **27,** 407–411. ISSN: 1520-9156. (2026) (May 2025).

30. Zeng, F.-G. Celebrating the one millionth cochlear implant. *JASA Express Letters* **2,** 077201. ISSN: 2691-1191. (2026) (July 2022).

31. Rahman, M. T. *et al.* Cochlear implants: Causes, effects and mitigation strategies for the foreign body response and inflammation. *Hearing Research* **422,** 108536. ISSN: 0378-5955. (2026) (Sept. 2022).

32. Tykocinski, M., Cohen, L. T. & Cowan, R. S. Measurement and Analysis of Access Resistance and Polarization Impedance in Cochlear Implant Recipients. en-US. *Otology & Neurotology* **26,** 948. ISSN: 1531-7129. (2026) (Sept. 2005).

33. Scheperle, R. A. *et al.* Delayed changes in auditory status in cochlear implant users with preserved acoustic hearing. *Hearing Research* **350,** 45–57. ISSN: 0378-5955. (2026) (July 2017).

34. Bohl, A. *et al.* Development of a specially tailored local drug delivery system for the prevention of fibrosis after insertion of cochlear implants into the inner ear. en. *Journal of Materials Science: Materials in Medicine* **23,** 2151–2162. ISSN: 0957-4530, 1573-4838. (2026) (Sept. 2012).

35. Wrzeszcz, A. *et al.* Hydrogel coated and dexamethasone releasing cochlear implants: Quantification of fibrosis in guinea pigs and evaluation of insertion forces in a human cochlea model. en. *Journal of Biomedical Materials Research Part B: Applied Biomaterials* **103,** 169–178. ISSN: 1552-4981. (2026) (2015).

36. Vormelcher, S. *et al.* Dexamethasone abolishes intra-day fluctuations of electrode impedance in cochlear implant users. *Hearing Research* **474,** 109615. ISSN: 0378-5955. (2026) (Apr. 2026).

37. MED-EL Elektromedizinische Geräte GesmbH. *Dexamethasone-Eluting Cochlear Implant Electrode (CIDEXEL): A First in Human Study* Clinical trial registration NCT04450290. submitted: 2020-06-16 (clinicaltrials.gov, May 2022). (2026).

38. MED-EL Elektromedizinische Geräte GesmbH. *Dexamethasone-Eluting Cochlear Implant Electrode (CIDEXEL): Pivotal Study* Clinical trial registration NCT06142682. submitted: 2023-11-07 (clinicaltrials.gov, Aug. 2025). (2026).

39. Fiani, B., Reardon, T., Ayres, B., Cline, D. & Sitto, S. R. An Examination of Prospective Uses and Future Directions of Neuralink: The Brain-Machine Interface. en. *Cureus.* ISSN: 2168-8184. (2026) (Mar. 2021).

40. Lotti, F., Ranieri, F., Vadalà, G., Zollo, L. & Di Pino, G. Invasive Intraneural Interfaces: Foreign Body Reaction Issues. English. *Frontiers in Neuroscience* **11.** ISSN: 1662-453X. (2026) (Sept. 2017).

41. Carnicer-Lombarte, A., Chen, S.-T., Malliaras, G. G. & Barone, D. G. Foreign Body Reaction to Implanted Biomaterials and Its Impact in Nerve Neuroprosthetics. English. *Frontiers in Bioengineering and Biotechnology* **9.** ISSN: 2296-4185. (2026) (Apr. 2021).

42. Mian, S. Y., Honey, J. R., Carnicer-Lombarte, A. & Barone, D. G. Large Animal Studies to Reduce the Foreign Body Reaction in Brain–Computer Interfaces: A Systematic Review. en. *Biosensors* **11.** ISSN: 2079-6374. (2026) (Aug. 2021).

43. Han, J. J. Synchron receives FDA approval to begin early feasibility study of their endovascular, brain-computer interface device. en. *Artificial Organs* **45,** 1134–1135. ISSN: 1525-1594. (2026) (2021).

44. Salatino, J. W., Ludwig, K. A., Kozai, T. D. Y. & Purcell, E. K. Glial responses to implanted electrodes in the brain. en. *Nature Biomedical Engineering* **1,** 862–877. ISSN: 2157-846X. (2026) (Nov. 2017).

45. Paul, A. *85% of Neuralink implant wires are already detached, says patient* en-US. May 2024. (2026).

46. Mathews, J. *Neuralink's first study participant says his whole life has changed* en. (2026).

47. Olczuk, D. & Priefer, R. A history of continuous glucose monitors (CGMs) in self-monitoring of diabetes mellitus. *Diabetes & Metabolic Syndrome: Clinical Research & Reviews* **12,** 181–187. ISSN: 1871-4021. (2026) (Apr. 2018).

48. Ming Li, C., Dong, H., Cao, X., T. Luong, J. H. & Zhang, X. Implantable Electrochemical Sensors for Biomedical and Clinical Applications: Progress, Problems, and Future Possibilities. *Current Medicinal Chemistry* **14,** 937–951 (Apr. 2007).

49. D'Alton, L. *et al.* A holistic pathway to biosensor translation. en. *Sensors & Diagnostics* **3,** 1234–1246. (2026) (2024).

50. Chandorkar, Y., K, R. & Basu, B. The Foreign Body Response Demystified. *ACS Biomaterials Science & Engineering* **5,** 19–44. (2026) (Jan. 2019).

51. Schakman, O., Kalista, S., Barbé, C., Loumaye, A. & Thissen, J. P. Glucocorticoid-induced skeletal muscle atrophy. *The International Journal of Biochemistry & Cell Biology. Molecular Basis of Muscle Wasting* **45,** 2163–2172. ISSN: 1357-2725. (2026) (Oct. 2013).

52. Schoepe, S., Schäcke, H., May, E. & Asadullah, K. Glucocorticoid therapy-induced skin atrophy. en. *Experimental Dermatology* **15,** 406–420. ISSN: 1600-0625. (2026) (2006).

53. LoCascio, V. *et al.* Bone loss in response to long-term glucocorticoid therapy. *Bone and Mineral* **8,** 39–51. ISSN: 0169-6009. (2026) (Jan. 1990).

54. Briot, K. & Roux, C. Glucocorticoid-induced osteoporosis. en. *RMD Open* **1.** ISSN: 2056-5933. (2026) (Apr. 2015).

55. Carnicer-Lombarte, A. *et al. Foreign body reaction is triggered in vivo by cellular mechanosensing of implants stiffer than host tissue* en. Pages: 829648 Section: New Results. Dec. 2022. (2026).

56. Sapolsky, R. M., Krey, L. C. & McEwen, B. S. Prolonged glucocorticoid exposure reduces hippocampal neuron number: implications for aging. en. *Journal of Neuroscience* **5,** 1222–1227. ISSN: 0270-6474, 1529-2401. (2026) (May 1985).

57. Lanshakov, D. A., Sukhareva, E. V., Kalinina, T. S. & Dygalo, N. N. Dexamethasone-induced acute excitotoxic cell death in the developing brain. *Neurobiology of Disease* **91,** 1–9. ISSN: 0969-9961. (2026) (July 2016).

58. Kim, J. B. *et al.* Dexamethasone inhibits proliferation of adult hippocampal neurogenesis in vivo and in vitro. *Brain Research* **1027,** 1–10. ISSN: 0006-8993. (2026) (Nov. 2004).

59. Grainger, D. W. All charged up about implanted biomaterials. en. *Nature Biotechnology* **31,** 507–509. ISSN: 1546-1696. (2026) (June 2013).

60. Maduka, C. V. *et al.* Glycolytic reprogramming underlies immune cell activation by polyethylene wear particles. *Biomaterials Advances* **152,** 213495. ISSN: 2772-9508. (2026) (Sept. 2023).

61. Maduka, C. V. *et al.* Elevated oxidative phosphorylation is critical for immune cell activation by polyethylene wear particles. *Journal of Immunology and Regenerative Medicine* **19,** 100069. ISSN: 2468-4988. (2026) (Feb. 2023).

62. Maduka, C. V. *et al.* Polylactide Degradation Activates Immune Cells by Metabolic Reprogramming. en. *Advanced Science* **10.** _eprint: https://advanced.onlinelibrary.wiley.com/doi/pdf/
2304632. ISSN: 2198-3844. (2026) (2023).

63. Maduka, C. V. *et al.* Role of Mitochondrial Complex I in the Proinflammatory Response to Polylactide Implants. *ACS Applied Engineering Materials* **2,** 2815–2826. (2026) (Dec. 2024).

64. Burnet, S. F. M. & Fenner, F. *The Production of Antibodies* en. Google-Books-ID: fl1BAAAAYAAJ. ISBN: 978-0-598-54712-5 (Macmillan, 1949).

65. Janeway, C. A. Approaching the Asymptote? Evolution and Revolution in Immunology. en. *Cold Spring Harbor Symposia on Quantitative Biology* **54,** 1–13. ISSN: 0091-7451, 1943-4456. (2026) (Jan. 1989).

66. Matzinger, P. TOLERANCE, DANGER, AND THE EXTENDED FAMILY. en. *Annual review of immunology* **12,** 991–1045 (Apr. 1994).

67. Pradeu, T., Jaeger, S. & Vivier, E. The speed of change: towards a discontinuity theory of immunity? en. *Nature Reviews Immunology* **13,** 764–769. ISSN: 1474-1741. (2026) (Oct. 2013).

68. Pradeu, T. *The Limits of the Self: Immunology and Biological Identity* en. Google-Books-ID: VwVpAgAAQBAJ. ISBN: 978-0-19-977749-5 (Oxford University Press, Sept. 2011).

69. Li, D. & Wu, M. Pattern recognition receptors in health and diseases. en. *Signal Transduction and Targeted Therapy* **6,** 291. ISSN: 2059-3635. (2026) (Aug. 2021).

70. Roh, J. S. & Sohn, D. H. Damage-Associated Molecular Patterns in Inflammatory Diseases. *Immune Network* **18,** e27. ISSN: 1598-2629. (2026) (Aug. 2018).

71. Seong, S.-Y. & Matzinger, P. Hydrophobicity: an ancient damage-associated molecular pattern that initiates innate immune responses. en. *Nature Reviews Immunology* **4,** 469–478. ISSN: 1474-1741. (2026) (June 2004).

72. Parker, J. B., Griffin, M. F., Spielman, A. F., Wan, D. C. & Longaker. Exploring the Overlooked Roles and Mechanisms of Fibroblasts in the Foreign Body Response. en. *Advances in Wound Care* **12.** (2026) (July 2022).

73. Witherel, C. E., Abebayehu, D., Barker, T. H. & Spiller, K. L. Macrophage and Fibroblast Interactions in Biomaterial-Mediated Fibrosis. en. *Advanced Healthcare Materials* **8,** 1801451. ISSN: 2192-2659. (2026) (2019).

74. Gorbet, M. B. & Sefton, M. V. Biomaterial-associated thrombosis: roles of coagulation factors, complement, platelets and leukocytes. en. *Biomaterials* **25,** 5681–5703. ISSN: 01429612. (2026) (Nov. 2004).

75. Jaffer, I. H., Fredenburgh, J. C., Hirsh, J. & Weitz, J. I. Medical device-induced thrombosis: what causes it and how can we prevent it? en. *Journal of Thrombosis and Haemostasis* **13,** S72–S81. ISSN: 1538-7836. (2026) (2015).

76. Tang, L., Jennings, T. A. & Eaton, J. W. Mast cells mediate acute inflammatory responses to implanted biomaterials. *Proceedings of the National Academy of Sciences of the United States of America* **95,** 8841–8846. ISSN: 0027-8424. (2026) (July 1998).

77. Zdolsek, J., Eaton, J. W. & Tang, L. Histamine release and fibrinogen adsorption mediate acute inflammatory responses to biomaterial implants in humans. en. *Journal of Translational Medicine* **5,** 31. ISSN: 1479-5876. (2026) (July 2007).

78. McKiel, L. A., Woodhouse, K. A. & Fitzpatrick, L. E. The role of Toll-like receptor signaling in the macrophage response to implanted materials. en. *MRS Communications* **10,** 55–68. ISSN: 2159-6859, 2159-6867. (2026) (Mar. 2020).

79. Polikov, V. S., Tresco, P. A. & Reichert, W. M. Response of brain tissue to chronically implanted neural electrodes. *Journal of Neuroscience Methods* **148,** 1–18. ISSN: 0165-0270. (2026) (Oct. 2005).

80. Frutiger, A. *et al.* Nonspecific Binding—Fundamental Concepts and Consequences for Biosensing Applications. *Chemical Reviews* **121,** 8095–8160. ISSN: 0009-2665. (2026) (July 2021).

81. Mathew, J., Sankar, P. & Varacallo, M. A. eng. in *StatPearls* (StatPearls Publishing, Treasure Island (FL), 2026). (2026).

82. Johnson, M. E. & Hummer, G. Nonspecific binding limits the number of proteins in a cell and shapes their interaction networks. *Proceedings of the National Academy of Sciences* **108,** 603–608. (2026) (Jan. 2011).

83. Vroman, L. & Adams, A. L. Findings with the recording ellipsometer suggesting rapid exchange of specific plasma proteins at liquid/solid interfaces. *Surface Science* **16,** 438–446. ISSN: 0039-6028. (2026) (Aug. 1969).

84. Vroman, L. & Adams, A. L. Identification of rapid changes at plasma–solid interfaces. en. *Journal of Biomedical Materials Research* **3,** 43–67. ISSN: 1097-4636. (2026) (1969).

85. Vroman, L., Adams, A., Fischer, G. & Munoz, P. Interaction of high molecular weight kininogen, factor XII, and fibrinogen in plasma at interfaces. *Blood* **55,** 156–159. ISSN: 0006-4971. (2026) (Jan. 1980).

86. Jung, S.-Y. *et al.* The Vroman Effect: A Molecular Level Description of Fibrinogen Displacement. *Journal of the American Chemical Society* **125,** 12782–12786. ISSN: 0002-7863. (2026) (Oct. 2003).

87. Krishnan, A., Siedlecki, C. A. & Vogler, E. A. Mixology of Protein Solutions and the Vroman Effect. *Langmuir* **20,** 5071–5078. ISSN: 0743-7463. (2026) (June 2004).

88. Wertz, C. F. & Santore, M. M. Fibrinogen Adsorption on Hydrophilic and Hydrophobic Surfaces: Geometrical and Energetic Aspects of Interfacial Relaxations. *Langmuir* **18,** 706–715. ISSN: 0743-7463. (2026) (Feb. 2002).

89. Roach, P., Farrar, D. & Perry, C. C. Interpretation of Protein Adsorption: Surface-Induced Conformational Changes. *Journal of the American Chemical Society* **127,** 8168–8173. ISSN: 0002-7863. (2026) (June 2005).

90. Horbett, T. A. Fibrinogen adsorption to biomaterials. en. *Journal of Biomedical Materials Research Part A* **106.** _eprint: https://onlinelibrary.wiley.com/doi/pdf/10.1002/jbm.a.36460, 2777–2788. ISSN: 1552-4965. (2026) (2018).

91. Tsai, W.-B., Grunkemeier, J. M. & Horbett, T. A. Human plasma fibrinogen adsorption and platelet adhesion to polystyrene. en. *Journal of Biomedical Materials Research* **44.** _eprint: https://onlinelibrary.wiley.com/doi/pdf/10.1002/%28SICI%291097-4636%28199902%2944%3A2%3C130%3A%3AAID-JBM2%3E3.0.CO%3B2-9, 130–139. ISSN: 1097-4636. (2026) (1999).

92. Hu, W.-J., Eaton, J. W., Ugarova, T. P. & Tang, L. Molecular basis of biomaterial-mediated foreign body reactions. *Blood* **98,** 1231–1238. ISSN: 0006-4971. (2026) (Aug. 2001).

93. Smiley, S. T., King, J. A. & Hancock, W. W. Fibrinogen Stimulates Macrophage Chemokine Secretion Through Toll-Like Receptor 4. *The Journal of Immunology* **167,** 2887–2894. ISSN: 0022-1767. (2026) (Sept. 2001).

94. Lishko, V. K., Kudryk, B., Yakubenko, V. P., Yee, V. C. & Ugarova, T. P. Regulated Unmasking of the Cryptic Binding Site for Integrin M2 in the C-Domain of Fibrinogen. *Biochemistry* **41,** 12942–12951. ISSN: 0006-2960. (2026) (Oct. 2002).

95. Deng, Z. J., Liang, M., Monteiro, M., Toth, I. & Minchin, R. F. Nanoparticle-induced unfolding of fibrinogen promotes Mac-1 receptor activation and inflammation. en. *Nature Nanotechnology* **6,** 39–44. ISSN: 1748-3395. (2026) (Jan. 2011).

96. Blackman, S. A., Miles, D., Suresh, J., Calve, S. & Bryant, S. J. Cell- and Serum-Derived Proteins Act as DAMPs to Activate RAW 264.7 Macrophage-like Cells on Silicone Implants. *ACS Biomaterials Science & Engineering* **10,** 1418–1434. (2026) (Mar. 2024).

97. Thompson, B. J., Saleh, L. S., Carillion, E. L., Alper, S. & Bryant, S. J. Damage Associated Molecular Patterns (DAMPs) Mediate the Foreign Body Response to Poly(ethylene glycol) Diacrylate Hydrogels via Toll like Receptors. *ACS Biomaterials Science & Engineering* **11,** 4128–4138. (2026) (July 2025).

98. Thompson, B. J., Carillion, E. L., Alper, S. & Bryant, S. J. The foreign body response to biomaterial implants is reduced by co-inhibition of TLR2 and TLR4. *Acta Biomaterialia* **201,** 320–335. ISSN: 1742-7061. (2026) (July 2025).

99. Auquit-Auckbur, I. *et al.* Role of Toll-like receptor 4 in the inflammation reaction surrounding silicone prosthesis. *Acta Biomaterialia* **7,** 2047–2052. ISSN: 1742-7061. (2026) (May 2011).

100. Veiseh, O. *et al.* Size- and shape-dependent foreign body immune response to materials implanted in rodents and non-human primates. en. *Nature Materials* **14,** 643–651. ISSN: 1476-4660. (2026) (June 2015).

101. Doloff, J. C. *et al.* Colony stimulating factor-1 receptor is a central component of the foreign body response to biomaterial implants in rodents and non-human primates. en. *Nature Materials* **16,** 671–680. ISSN: 1476-4660. (2026) (June 2017).

102. Dondossola, E. *et al.* Examination of the foreign body response to biomaterials by nonlinear intravital microscopy. en. *Nature Biomedical Engineering* **1,** 0007. ISSN: 2157-846X. (2026) (Dec. 2016).

103. Parlani, M., Bedell, M. L., Mikos, A. G., Friedl, P. & Dondossola, E. Dissecting the recruitment and self-organization of SMA-positive fibroblasts in the foreign body response. *Science Advances* **8,** eadd0014. (2026) (Dec. 2022).

104. Saleh, L. S. *et al.* Mapping Macrophage Polarization and Origin during the Progression of the Foreign Body Response to a Poly(ethylene glycol) Hydrogel Implant. en. *Advanced Healthcare Materials* **11,** 2102209. ISSN: 2192-2659. (2026) (2022).

105. Stein, M., Keshav, S., Harris, N. & Gordon, S. Interleukin 4 potently enhances murine macrophage mannose receptor activity: a marker of alternative immunologic macrophage activation. *Journal of Experimental Medicine* **176,** 287–292. ISSN: 0022-1007. (2026) (July 1992).

106. Mills, C. D., Kincaid, K., Alt, J. M., Heilman, M. J. & Hill, A. M. M-1/M-2 Macrophages and the Th1/Th2 Paradigm. *The Journal of Immunology* **164,** 6166–6173. ISSN: 0022-1767. (2026) (June 2000).

107. Mosmann, T. R. & Coffman, R. L. TH1 and TH2 Cells: Different Patterns of Lymphokine Secretion Lead to Different Functional Properties. en. *Annual Review of Immunology* **7,** 145–173. ISSN: 0732-0582, 1545-3278. (2026) (Apr. 1989).

108. Sakaguchi, S., Sakaguchi, N., Asano, M., Itoh, M. & Toda, M. Immunologic self-tolerance maintained by activated T cells expressing IL-2 receptor -chains (CD25). Breakdown of a single mechanism of self-tolerance causes various autoimmune diseases. *The Journal of Immunology* **155,** 1151–1164. ISSN: 0022-1767. (2026) (Aug. 1995).

109. Langrish, C. L. *et al.* IL-23 drives a pathogenic T cell population that induces autoimmune inflammation. *Journal of Experimental Medicine* **201,** 233–240. ISSN: 0022-1007. (2026) (Jan. 2005).

110. Harrington, L. E. *et al.* Interleukin 17–producing CD4+ effector T cells develop via a lineage distinct from the T helper type 1 and 2 lineages. en. *Nature Immunology* **6,** 1123–1132. ISSN: 1529-2916. (2026) (Nov. 2005).

111. Park, H. *et al.* A distinct lineage of CD4 T cells regulates tissue inflammation by producing interleukin 17. en. *Nature Immunology* **6,** 1133–1141. ISSN: 1529-2916. (2026) (Nov. 2005).

112. Wan, Y. Y. & Flavell, R. A. How Diverse—CD4 Effector T Cells and their Functions. *Journal of Molecular Cell Biology* **1,** 20–36. ISSN: 1674-2788. (2026) (Oct. 2009).

113. Mantovani, A. *et al.* The chemokine system in diverse forms of macrophage activation and polarization. English. *Trends in Immunology* **25,** 677–686. ISSN: 1471-4906, 1471-4981. (2026) (Dec. 2004).

114. Murray, P. J. *et al.* Macrophage Activation and Polarization: Nomenclature and Experimental Guidelines. English. *Immunity* **41,** 14–20. ISSN: 1074-7613. (2026) (July 2014).

115. Mills, C. D. Anatomy of a Discovery: M1 and M2 Macrophages. English. *Frontiers in Immunology* **6.** ISSN: 1664-3224. (2026) (May 2015).

116. Wang, N., Liang, H. & Zen, K. Molecular Mechanisms That Influence the Macrophage M1–M2 Polarization Balance. English. *Frontiers in Immunology* **5.** ISSN: 1664-3224. (2026) (Nov. 2014).

117. Yunna, C., Mengru, H., Lei, W. & Weidong, C. Macrophage M1/M2 polarization. *European Journal of Pharmacology* **877,** 173090. ISSN: 0014-2999. (2026) (June 2020).

118. Italiani, P. & Boraschi, D. From Monocytes to M1/M2 Macrophages: Phenotypical vs. Functional Differentiation. English. *Frontiers in Immunology* **5.** ISSN: 1664-3224. (2026) (Oct. 2014).

119. Martinez, F. O. & Gordon, S. The M1 and M2 paradigm of macrophage activation: time for reassessment. *F1000Prime Reports* **6,** 13. ISSN: 2051-7599. (2026) (Mar. 2014).

120. Klopfleisch, R. Macrophage reaction against biomaterials in the mouse model – Phenotypes, functions and markers. *Acta Biomaterialia* **43,** 3–13. ISSN: 1742-7061. (2026) (Oct. 2016).

121. Mosser, D. M. & Edwards, J. P. Exploring the full spectrum of macrophage activation. en. *Nature Reviews Immunology* **8,** 958–969. ISSN: 1474-1741. (2026) (Dec. 2008).

122. Xue, J. *et al.* Transcriptome-Based Network Analysis Reveals a Spectrum Model of Human Macrophage Activation. en. *Immunity* **40,** 274–288. ISSN: 10747613. (2026) (Feb. 2014).

123. Doloff, J. C. *et al.* Identification of a humanized mouse model for functional testing of immune-mediated biomaterial foreign body response. *Science Advances* **9,** eade9488. (2026) (June 2023).

124. Zhang, L. *et al.* Zwitterionic hydrogels implanted in mice resist the foreign-body reaction. en. *Nature Biotechnology* **31,** 553–556. ISSN: 1546-1696. (2026) (June 2013).

125. Sussman, E. M., Halpin, M. C., Muster, J., Moon, R. T. & Ratner, B. D. Porous Implants Modulate Healing and Induce Shifts in Local Macrophage Polarization in the Foreign Body Reaction. en. *Annals of Biomedical Engineering* **42,** 1508–1516. ISSN: 1573-9686. (2026) (July 2014).

126. Song, E. *et al.* Influence of Alternatively and Classically Activated Macrophages on Fibrogenic Activities of Human Fibroblasts. *Cellular Immunology* **204,** 19–28. ISSN: 0008-8749. (2026) (Aug. 2000).

127. Wynn, T. A. Fibrotic disease and the TH1/TH2 paradigm. en. *Nature Reviews Immunology* **4,** 583–594. ISSN: 1474-1741. (2026) (Aug. 2004).

128. Wynn, T. A. & Barron, L. Macrophages: Master Regulators of Inflammation and Fibrosis. en. *Seminars in Liver Disease* **30,** 245–257. ISSN: 0272-8087, 1098-8971. (2026) (Aug. 2010).

129. Wynn, T. A. & Ramalingam, T. R. Mechanisms of fibrosis: therapeutic translation for fibrotic disease. en. *Nature Medicine* **18,** 1028–1040. ISSN: 1546-170X. (2026) (July 2012).

130. Braga, T. T., Agudelo, J. S. H. & Camara, N. O. S. Macrophages During the Fibrotic Process: M2 as Friend and Foe. English. *Frontiers in Immunology* **6.** ISSN: 1664-3224. (2026) (Nov. 2015).

131. Zhang, L. *et al.* Macrophages: friend or foe in idiopathic pulmonary fibrosis? en. *Respiratory Research* **19,** 170. ISSN: 1465-993X. (2026) (Sept. 2018).

132. Murphy, K. & Weaver, C. *Janeway's Immunobiology* en. Google-Books-ID: GmPLCwAAQBAJ. ISBN: 978-1-315-53324-7 (Garland Science, Mar. 2016).

133. Jakubzick, C., Kunkel, S. L., Puri, R. K. & Hogaboam, C. M. Therapeutic targeting of IL-4-and IL-13-responsive cells in pulmonary fibrosis. en. *Immunologic Research* **30,** 339–349. ISSN: 1559-0755. (2026) (Nov. 2004).

134. Chiaramonte, M. G., Donaldson, D. D., Cheever, A. W. & Wynn, T. A. An IL-13 inhibitor blocks the development of hepatic fibrosis during a T-helper type 2–dominated inflammatory response. en. *The Journal of Clinical Investigation* **104,** 777–785. ISSN: 0021-9738. (2026) (Sept. 1999).

135. Kaviratne, M. *et al.* IL-13 Activates a Mechanism of Tissue Fibrosis That Is Completely TGF- Independent. *The Journal of Immunology* **173,** 4020–4029. ISSN: 0022-1767. (2026) (Sept. 2004).

136. Nguyen, J. K., Austin, E., Huang, A., Mamalis, A. & Jagdeo, J. The IL-4/IL-13 axis in skin fibrosis and scarring: mechanistic concepts and therapeutic targets. en. *Archives of Dermatological Research* **312,** 81–92. ISSN: 1432-069X. (2026) (Mar. 2020).

137. Lama, V. N. & Phan, S. H. The Extrapulmonary Origin of Fibroblasts: Stem/Progenitor Cells and Beyond. *Proceedings of the American Thoracic Society* **3,** 373–376. ISSN: 1546-3222. (2026) (June 2006).

138. Szabo, E. *et al.* Direct conversion of human fibroblasts to multilineage blood progenitors. en. *Nature* **468,** 521–526. ISSN: 1476-4687. (2026) (Nov. 2010).

139. Plikus, M. V. *et al.* Fibroblasts: Origins, definitions, and functions in health and disease. English. *Cell* **184,** 3852–3872. ISSN: 0092-8674, 1097-4172. (2026) (July 2021).

140. Vegas, A. J. *et al.* Combinatorial hydrogel library enables identification of materials that mitigate the foreign body response in primates. en. *Nature Biotechnology* **34,** 345–352. ISSN: 1546-1696. (2026) (Mar. 2016).

141. Rinkevich, Y. *et al.* Identification and isolation of a dermal lineage with intrinsic fibrogenic potential. *Science* **348,** aaa2151. (2026) (Apr. 2015).

142. Shook, B. A. *et al.* Myofibroblast proliferation and heterogeneity are supported by macrophages during skin repair. *Science* **362,** eaar2971. (2026) (Nov. 2018).

143. Parker, J. B. *et al.* Engrailed-Positive Fibroblasts: The Primary Cell Type Present in Fibrotic Capsules During Foreign Body Response. en-US. *Journal of the American College of Surgeons* **235,** S68. ISSN: 1879-1190. (2026) (Nov. 2022).

144. Habiel, D. M. & Hogaboam, C. M. Heterogeneity of Fibroblasts and Myofibroblasts in Pulmonary Fibrosis. *Current pathobiology reports* **5,** 101–110. ISSN: 2167-485X. (2026) (June 2017).

145. Mack, M. & Yanagita, M. Origin of myofibroblasts and cellular events triggering fibrosis. *Kidney International* **87,** 297–307. ISSN: 0085-2538. (2026) (Feb. 2015).

146. Wilde, C., Mitgau, J., Suchy, T., Schoneberg, T. & Liebscher, I. Translating the force—mechano-sensing GPCRs. en. *American Journal of Physiology-Cell Physiology.* (2026) (Apr. 2022).

147. Blakney, A. K., Swartzlander, M. D. & Bryant, S. J. The effects of substrate stiffness on the in vitro activation of macrophages and in vivo host response to poly(ethylene glycol)-based hydrogels. *Journal of Biomedical Materials Research. Part a* **100,** 1375–1386. ISSN: 1549-3296. (2026) (June 2012).

148. Jansen, L. E. *et al.* Zwitterionic PEG-PC Hydrogels Modulate the Foreign Body Response in a Modulus-Dependent Manner. *Biomacromolecules* **19,** 2880–2888. ISSN: 1525-7797. (2026) (July 2018).

149. Martino, F., Perestrelo, A. R., Vinarský, V., Pagliari, S. & Forte, G. Cellular Mechanotransduction: From Tension to Function. English. *Frontiers in Physiology* **9.** ISSN: 1664-042X. (2026) (July 2018).

150. Jaalouk, D. E. & Lammerding, J. Mechanotransduction gone awry. en. *Nature Reviews Molecular Cell Biology* **10,** 63–73. ISSN: 1471-0080. (2026) (Jan. 2009).

151. Xia, K. *et al.* Roles of mechanosensitive ion channels in immune cells. English. *Heliyon* **10.** ISSN: 2405-8440. (2026) (Jan. 2024).

152. Anderson, J. M. & McNally, A. K. Biocompatibility of implants: lymphocyte/macrophage interactions. en. *Seminars in Immunopathology* **33,** 221–233. ISSN: 1863-2300. (2026) (May 2011).

153. Jiang, S. & Cao, Z. Ultralow-Fouling, Functionalizable, and Hydrolyzable Zwitterionic Materials and Their Derivatives for Biological Applications. en. *Advanced Materials* **22,** 920–932. ISSN: 1521-4095. (2026) (2010).

154. Schlenoff, J. B. Zwitteration: Coating Surfaces with Zwitterionic Functionality to Reduce Nonspecific Adsorption. *Langmuir* **30,** 9625–9636. ISSN: 0743-7463. (2026) (Aug. 2014).

155. Ishihara, K. Biomimetic materials based on zwitterionic polymers toward human-friendly medical devices. *Science and Technology of Advanced Materials* **23,** 498–524. ISSN: 1468-6996. (2026) (Dec. 2022).

156. Li, B. *et al.* Trimethylamine N-oxide–derived zwitterionic polymers: A new class of ultralow fouling bioinspired materials. *Science Advances* **5,** eaaw9562. (2026) (June 2019).

157. Zhang, D. *et al.* Dealing with the Foreign-Body Response to Implanted Biomaterials: Strategies and Applications of New Materials. en. *Advanced Functional Materials* **31,** 2007226. ISSN: 1616-3028. (2026) (2021).

158. *Polymeric Hydrogels as Smart Biomaterials* (ed Kalia, S.) ISBN: 978-3-319-25320-6 978-3-319-25322-0. (2026) (Springer International Publishing, Cham, 2016).

159. Dong, D. *et al.* High-strength and fibrous capsule–resistant zwitterionic elastomers. *Science Advances* **7,** eabc5442. (2026) (Jan. 2021).

160. Ladd, J., Zhang, Z., Chen, S., Hower, J. C. & Jiang, S. Zwitterionic Polymers Exhibiting High Resistance to Nonspecific Protein Adsorption from Human Serum and Plasma. *Biomacromolecules* **9,** 1357–1361. ISSN: 1525-7797. (2026) (May 2008).

161. Yang, W. *et al.* Film Thickness Dependence of Protein Adsorption from Blood Serum and Plasma onto Poly(sulfobetaine)-Grafted Surfaces. *Langmuir* **24,** 9211–9214. ISSN: 0743-7463. (2026) (Sept. 2008).

162. Zhang, J. *et al.* Novel Balanced Charged Alginate/PEI Polyelectrolyte Hydrogel that Resists Foreign-Body Reaction. *ACS Applied Materials & Interfaces* **10,** 6879–6886. ISSN: 1944-8244. (2026) (Feb. 2018).

163. Zhang, D. *et al.* Silk-Inspired -Peptide Materials Resist Fouling and the Foreign-Body Response. en. *Angewandte Chemie* **132,** 9673–9680. ISSN: 1521-3757. (2026) (2020).

164. Mukherjee, S. *et al.* Screening hydrogels for antifibrotic properties by implanting cellularly barcoded alginates in mice and a non-human primate. en. *Nature Biomedical Engineering* **7,** 867–886. ISSN: 2157-846X. (2026) (July 2023).

165. Rostam, H. M. *et al.* Immune-Instructive Polymers Control Macrophage Phenotype and Modulate the Foreign Body Response In Vivo. English. *Matter* **2,** 1564–1581. ISSN: 2590-2393, 2590-2385. (2026) (June 2020).

166. Chan, D. *et al.* Polyacrylamide-based hydrogel coatings improve biocompatibility of implanted pump devices. en. *Journal of Biomedical Materials Research Part A* **111,** 910–920. ISSN: 1552-4965. (2026) (2023).

167. Schreib, C. C. *et al.* Lipid Deposition Profiles Influence Foreign Body Responses. en. *Advanced Materials* **35,** 2205709. ISSN: 1521-4095. (2026) (2023).

168. Jeang, W. J. *et al.* Antifouling Immunomodulatory Copolymer Architectures That Inhibit the Fibrosis of Implants. en. *Advanced Materials* **37,** 2414743. ISSN: 1521-4095. (2026) (2025).

169. Schauer, R. Sialic acids as regulators of molecular and cellular interactions. *Current Opinion in Structural Biology. Carbohydradtes and glycoconjugates / Biophysical methods* **19,** 507–514. ISSN: 0959-440X. (2026) (Oct. 2009).

170. Hu, D., Wu, G., Zhang, P. & Boukind, A. Polysialic Acid Hydrogel for Reducing Foreign Body Reactions in Implanted Polyurethane Materials. en. *Macromolecular Rapid Communications* **n/a,** e70283. ISSN: 1521-3927. (2026).

171. Slee, J. B. *et al.* Enhanced biocompatibility of CD47-functionalized vascular stents. *Biomaterials* **87,** 82–92. ISSN: 0142-9612. (2026) (May 2016).

172. Li, Y. *et al.* Achieving tissue-level softness on stretchable electronics through a generalizable soft interlayer design. en. *Nature Communications* **14,** 4488. ISSN: 2041-1723. (2026) (July 2023).

173. Noskovicova, N. *et al.* Suppression of the fibrotic encapsulation of silicone implants by inhibiting the mechanical activation of pro-fibrotic TGF-. en. *Nature Biomedical Engineering* **5,** 1437–1456. ISSN: 2157-846X. (2026) (Dec. 2021).

174. Trotsyuk, A. A. *et al.* Inhibiting Fibroblast Mechanotransduction Modulates Severity of Idiopathic Pulmonary Fibrosis. EN. *Advances in Wound Care* **11,** 511–523. ISSN: 2162-1918. (2026) (Oct. 2022).

175. Padmanabhan, J. *et al.* Allometrically scaling tissue forces drive pathological foreign-body responses to implants via Rac2-activated myeloid cells. en. *Nature Biomedical Engineering* **7,** 1419–1436. ISSN: 2157-846X. (2026) (Nov. 2023).

176. Chen, K. *et al.* Targeting circulating mechanoresponsive monocytes and macrophages to reduce fibrosis. en. *Nature Biomedical Engineering,* 1–16. ISSN: 2157-846X. (2026) (Oct. 2025).

177. Wu, J. *et al.* Adhesive anti-fibrotic interfaces on diverse organs. en. *Nature* **630,** 360–367. ISSN: 1476-4687. (2026) (June 2024).

178. Deng, J. *et al.* A bioadhesive pacing lead for atraumatic cardiac monitoring and stimulation in rodent and porcine models. *Science Translational Medicine* **16,** eado9003. (2026) (June 2024).

179. Moon, H. *et al.* Adhesive nonfibrotic bioelectronic interfaces on diverse peripheral nerves for long-term functional neuromodulation. *Science Advances* **11,** eadz3668. (2026) (Nov. 2025).

180. Inal, S., Rivnay, J., Suiu, A.-O., Malliaras, G. G. & McCulloch, I. Conjugated Polymers in Bioelectronics. *Accounts of Chemical Research* **51,** 1368–1376. ISSN: 0001-4842. (2026) (June 2018).

181. Rivnay, J., Owens, R. M. & Malliaras, G. G. The Rise of Organic Bioelectronics. *Chemistry of Materials* **26,** 679–685. ISSN: 0897-4756. (2026) (Jan. 2014).

182. Llinás, R. & Jahnsen, H. Electrophysiology of mammalian thalamic neurones in vitro. en. *Nature* **297,** 406–408. ISSN: 1476-4687. (2026) (June 1982).

183. Sundelacruz, S., Levin, M. & Kaplan, D. L. Role of Membrane Potential in the Regulation of Cell Proliferation and Differentiation. en. *Stem Cell Reviews and Reports* **5,** 231–246. ISSN: 1558-6804. (2026) (Sept. 2009).

184. Yang, W., Xue, H., Carr, L. R., Wang, J. & Jiang, S. Zwitterionic poly(carboxybetaine) hydrogels for glucose biosensors in complex media. *Biosensors and Bioelectronics* **26,** 2454–2459. ISSN: 0956-5663. (2026) (Jan. 2011).

185. Aregueta-Robles, U. A., Woolley, A. J., Poole-Warren, L. A., Lovell, N. H. & Green, R. A. Organic electrode coatings for next-generation neural interfaces. English. *Frontiers in Neuroengineering* **7.** ISSN: 1662-6443. (2026) (May 2014).

186. Yuk, H., Lu, B. & Zhao, X. Hydrogel bioelectronics. en. *Chemical Society Reviews* **48,** 1642–1667. (2026) (2019).

187. K, N. & Sekhar Rout, C. Conducting polymers: a comprehensive review on recent advances in synthesis, properties and applications. en. *RSC Advances* **11,** 5659–5697. (2026) (2021).

188. Kayser, L. V. & Lipomi, D. J. Stretchable Conductive Polymers and Composites Based on PEDOT and PEDOT:PSS. en. *Advanced Materials* **31,** 1806133. ISSN: 1521-4095. (2026) (2019).

189. Donahue, M. J. *et al.* Tailoring PEDOT properties for applications in bioelectronics. *Materials Science and Engineering: R: Reports* **140,** 100546. ISSN: 0927-796X. (2026) (Apr. 2020).

190. Shi, H., Liu, C., Jiang, Q. & Xu, J. Effective Approaches to Improve the Electrical Conductivity of PEDOT:PSS: A Review. en. *Advanced Electronic Materials* **1,** 1500017. ISSN: 2199-160X. (2026) (2015).

191. Horii, T., Li, Y., Mori, Y. & Okuzaki, H. Correlation between the hierarchical structure and electrical conductivity of PEDOT/PSS. en. *Polymer Journal* **47,** 695–699. ISSN: 1349-0540. (2026) (Oct. 2015).

192. Narayan, S., Stoica, L., Liess, A. & Reisinger, A. *Amplicoat® – Conductive Polymer Coating with Enhanced Durability and Performance for Chronic Implants* en. in (American Society of Mechanical Engineers Digital Collection, May 2021). (2026).

193. Kim, N. *et al.* Highly Conductive PEDOT:PSS Nanofibrils Induced by Solution-Processed Crystallization. *Advanced Materials* **26,** 2268–2272. ISSN: 1521-4095. (2026) (2014).

194. Wang, Y. *et al.* A highly stretchable, transparent, and conductive polymer. *Science Advances* **3,** e1602076. (2026) (Mar. 2017).

195. Lu, B. *et al.* Pure PEDOT:PSS hydrogels. en. *Nature Communications* **10,** 1043. ISSN: 2041-1723. (2026) (Mar. 2019).

196. Liu, Y. *et al.* Soft and elastic hydrogel-based microelectronics for localized low-voltage neuromodulation. en. *Nature Biomedical Engineering* **3,** 58–68. ISSN: 2157-846X. (2026) (Jan. 2019).

197. Feig, V. R., Tran, H., Lee, M. & Bao, Z. Mechanically tunable conductive interpenetrating network hydrogels that mimic the elastic moduli of biological tissue. en. *Nature Communications* **9,** 2740. ISSN: 2041-1723. (2026) (July 2018).

198. Magaz, A. *et al.* Modulation of Neuronal Cell Affinity on PEDOT–PSS Nonwoven Silk Scaffolds for Neural Tissue Engineering. *ACS Biomaterials Science & Engineering* **6,** 6906–6916. (2026) (Dec. 2020).

199. Spencer, A. R. *et al.* Electroconductive Gelatin Methacryloyl-PEDOT:PSS Composite Hydrogels: Design, Synthesis, and Properties. *ACS Biomaterials Science & Engineering* **4,** 1558–1567. (2026) (May 2018).

200. Solazzo, M. *et al.* PEDOT:PSS interfaces stabilised using a PEGylated crosslinker yield improved conductivity and biocompatibility. en. *Journal of Materials Chemistry B* **7,** 4811–4820. ISSN: 2050-7518. (2026) (Aug. 2019).

201. Lee, H. C. *et al.* Foreign Body Response to Intracortical Microelectrodes Is Not Altered with Dip-Coating of Polyethylene Glycol (PEG). English. *Frontiers in Neuroscience* **11.** ISSN: 1662-453X. (2026) (Sept. 2017).

202. Trindade, R., Albrektsson, T., Tengvall, P. & Wennerberg, A. Foreign Body Reaction to Biomaterials: On Mechanisms for Buildup and Breakdown of Osseointegration. en. *Clinical Implant Dentistry and Related Research* **18,** 192–203. ISSN: 1708-8208. (2026) (2016).

CHAPTER 2

ZWITTERIONIC HYDROGEL DESIGNS FOR CONDUCTING POLYMERS WITH SUPPRESSED FOREIGN BODY RESPONSES

2.1 Introduction

Strategies to suppress the foreign body response (FBR) in implantable medical devices (IMDs) generally fall into three categories: (i) mechanical matching to tissue[1,2]; (ii) controlled release of immunomodulatory drugs like dexamethasone8; and (iii) surface coatings and modifications to provide antibiofouling[3–5] or tissue adhesive effects[6,7]. While each has shown some success, they also face key limitations. Mechanical matching, even at tissue-level stiffness at a few kPa, can still trigger fibrosis[1,2]. Drug release strategies may cause systemic side effects[8,9] and complicate fabrication, as many drugs are sensitive to heat and UV[10,11]. Surface coatings often suffer from long-term instability due to mechanical wear or chemical degradation and may hinder the transport of chemical species. Among coatings, zwitterionic polymers and hydrogels are particularly promising due to their super-hydrophilic, antifouling nature[12–14] and established clinical use in various IMDs[15]. Studies have shown that zwitterionic hydrogels can nearly eliminate the FBR for up to three months in mice, due to their antifouling properties20. However, these coatings are electronically inactive, which may hinder the transport of analytes and ions for biosensors and electrophysiological devices. In such applications[16–19], having conductive or semiconductive materials directly interfacing with tissue is often more desirable to preserve device function.

As electronic materials for IMDs, conjugated polymers are promising candidates due to their low mechanical moduli, broad chemical design space, and lower interfacial impedance[20]. Specifically, poly(3,4-ethylenedioxythiophene):poly(styrene sulfonate) (PEDOT:PSS) has attracted the most attention because it is chemically stable, highly conductive, highly process-

able, and non-cytotoxic[21,22]. PEDOT:PSS has demonstrated its usefulness in applications ranging from biosensors to electrophysiological recording and stimulation[23–28]. Although PEDOT:PSS has been shown to be biocompatible in terms of cytotoxicity, there is still a lack of understanding of the FBR against PEDOT:PSS and PEDOT derivatives. Most prior studies assessing the FBR to PEDOT:PSS have relied on immunofluorescence (IF) to measure the infiltration of immune cells (e.g., macrophages)[24,28–32]. However, the specific ways that IF was used in these studies may have limitations in giving complete and accurate information about the FBR for the following reasons. First, IF has been used to detect a limited number of markers, leading to an incomplete picture of the FBR. Second, using IF to compare the number of infiltrating immune cells without information about specific phenotypes (e.g., M1 and M2 for macrophage, etc.) does not necessarily reflect FBR severity[33–35]. For example, it has been shown that tissue-resident macrophages, rather than recruited macrophages, are responsible for FBR-related fibrosis[36].

In fact, negatively charged polymers have been reported to lead to poor FBR outcomes[38–42]. As such, it is reasonable to speculate that the negatively charged PSS in PEDOT:PSS follows this observation. In this work, through comprehensive histological analysis involving multiple controls and timepoints, we show that PEDOT:PSS is indeed associated with fibrosis (Fig. 2.1a,c). Therefore, design strategies for improving the intrinsic immunocompatibility of PEDOT:PSS are highly desirable, yet remain a major challenge. To date, the realization of immunocompatible properties in polymers has dominantly relied on the design and synthesis of new chemical structures incorporating immune-compatible components[4,5,14,43], including a recent report on immune-compatible semiconducting polymers[44]. However, because PEDOT:PSS is typically formulated as an aqueous colloidal dispersion, this conventional molecular design strategy—based on synthesis in organic solutions—is not technically feasible.

We hypothesize that creating double-network morphologies between PEDOT:PSS and an

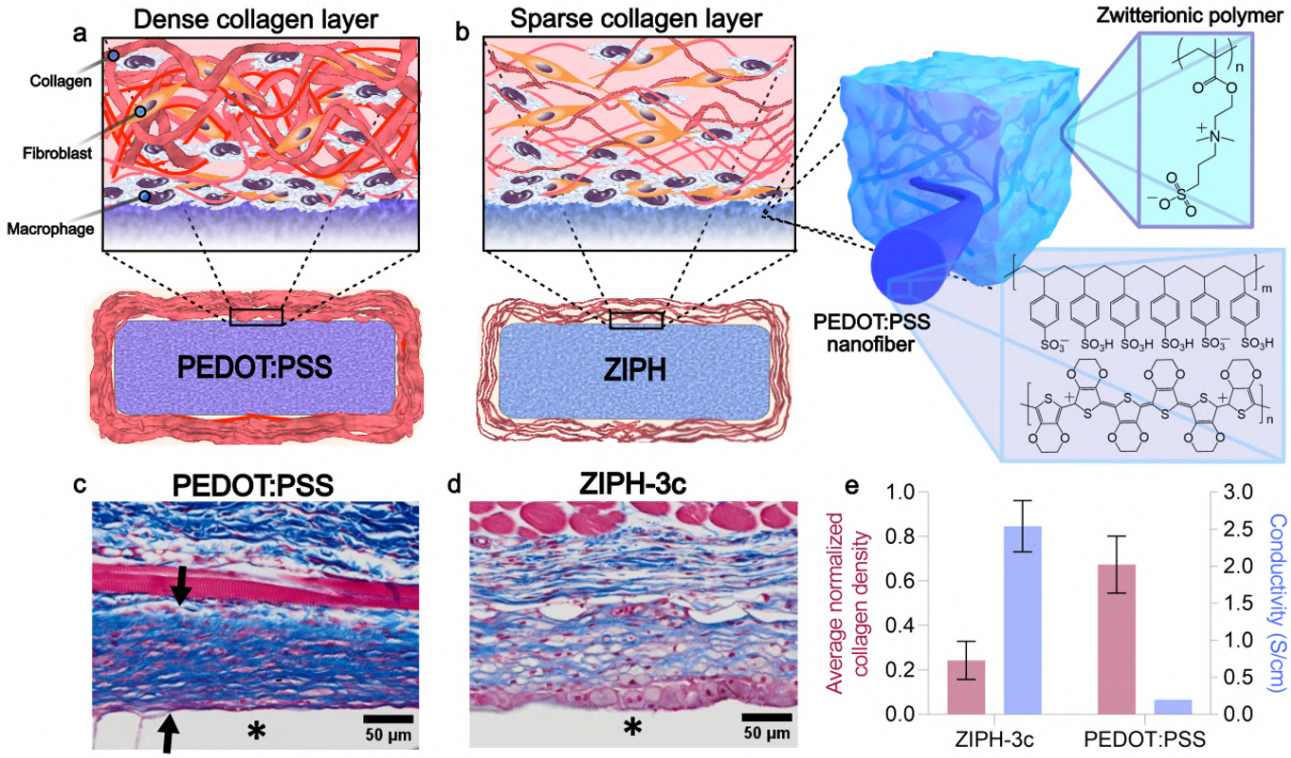

Figure 2.1. Design of zwitterionic PEDOT:PSS hydrogel (ZIPH) achieves superior immunocompatibility and conductivity compared to PEDOT:PSS. **a**, Schematic illustration of the FBR against PEDOT:PSS. **b**, Schematic illustration of the FBR against ZIPH and its nanoscale morphology, which has much less collagen deposition compared to PEDOT:PSS. **c**, Representative MTS-stained tissue sections of explanted PEDOT:PSS. The collagen layer is marked with arrows, and the locations of implants appear clear and are indicated by asterisks. **d**, Representative MTS-stained tissue sections of explanted ZIPH-3c, which show a much less dense collagen layer. **e**, Average normalized collagen density and conductivity value of ZIPH-3c compared to PEDOT:PSS. The PEDOT:PSS conductivity value was taken from the literature[37] for pristine spin-coated PEDOT:PSS films, to illustrate the effect of the ZIPH-3c processing conditions on conductivity.

immune-compatible polymer, with a sufficiently small phase separation length scale, could represent a viable yet unexplored strategy to impart immune-compatible properties to PEDOT:PSS. To this end, we introduce a design and processing method that promotes PEDOT:PSS to form nanofiber networks embedded in a zwitterionic hydrogel matrix (Fig. 2.1b). Although zwitterionic chemistry has been incorporated into PEDOT:PSS-based systems[28,45], substantial room remains for improving FBR suppression, particularly through rational control of phase separation morphology, which can critically influence both immune response and charge transport. Here, we show that such morphology engineering provides a powerful route to simultaneously enhance the immunocompatibility and electrical performance of PEDOT:PSS-based biointerfaces. Compared to unmodified PEDOT:PSS hydrogels, our zwitterionic PEDOT:PSS hydrogel (ZIPH) exhibits a reduction of FBR-associated fibrotic severity by 64% (Fig. 2.1d,e), in addition to an increase in electrical conductivity by more than one order of magnitude (Fig. 2.1e). Surprisingly, the FBR-associated fibrotic severity is even markedly lower than that of the zwitterionic hydrogel (by 53%) utilized in this design, which could come from certain previously unknown effects from the phase separation morphology. Improved chronic electrophysiological recordings obtained with ZIPH electrodes have further validated the benefits provided by the decreased fibrotic severity for practical applications and demonstrates that such material designs can be stable under harsh in vivo conditions. To our knowledge, no studies for implantable biomaterials have explored double-network morphologies as a design strategy for suppressing FBR-mediated fibrosis. As such, the design strategy presented in this work could provide unique insights for other types of biomaterials to achieve suppressed FBR.

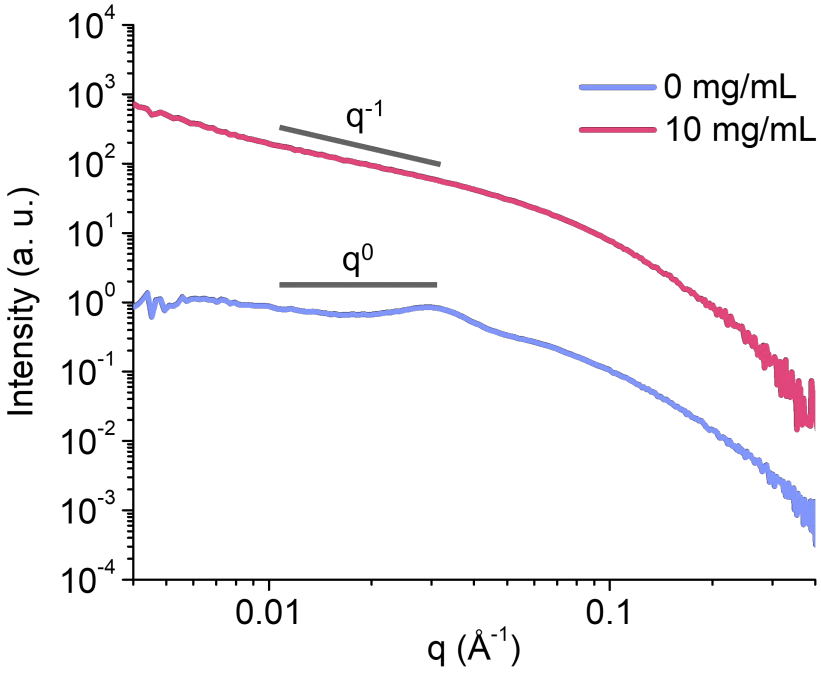

Figure 2.2. Small-angle X-ray scattering (SAXS) of PEDOT:PSS with 0 or 10 mg/mL of 4-ethylbenzenesulfonic acid (EBSA). The transition of the slopes at low- to mid-q from q0 to q-1 signifies that the PEDOT:PSS nanoparticles transition from spheroidal to rod-like particles after the addition of EBSA.

2.2 Results and Discussions

2.2.1 Design of immunocompatible, conductive hydrogels

For combining PEDOT:PSS and zwitterionic polymers for implantable electronics, there are three major criteria that need to be satisfied. First, the double-network morphology should have the zwitterionic matrix dominate the overall immunocompatibility. For this, nanoscale phase separation is preferred so that PEDOT:PSS phases are smaller than the length scales (tens to hundreds of nm) that can be recognized by cells[46]. Second, to achieve high conductivity, the PEDOT:PSS domain needs to be interconnected to facilitate charge transport[47]. Third, to keep stable electrical performance in implantable environments, the

design must not have severe swelling in water.

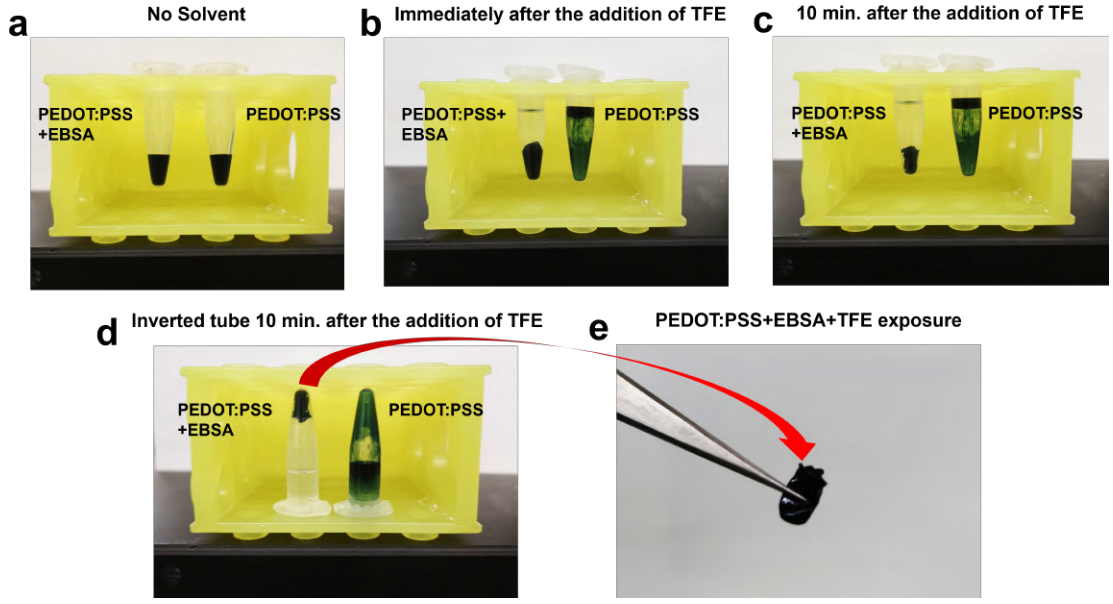

Figure 2.3. The combination of EBSA and TFE facilitates the formation of solid, sponge-like pieces of PEDOT:PSS. **a**, Comparison of PEDOT:PSS+EBSA and PEDOT:PSS before TFE addition. No obvious difference is observed. **b**, Comparison immediately after TFE addition. With EBSA, PEDOT:PSS solidifies. Without EBSA, TFE sinks, and the PEDOT:PSS suspension floats to the top difference due to the difference in density compared to water (1.39 g/cm3 vs. 0.997 g/cm3). **c**, Comparison 10 min. after TFE addition. The PEDOT:PSS+EBSA solid shrinks with time. **d**, Comparison after the tubes are inverted. PEDOT:PSS+EBSA does not flow down because it solidified, but PEDOT:PSS without EBSA the mixture flows down. **e**, PEDOT:PSS+EBSA solid picked up with a tweezer.

Based on the aforementioned criteria, poly(sulfobetaine methacrylate) (PSB) was chosen as the zwitterionic component. Sulfobetaine-based small molecules have been reported to increase the conductivity of PEDOT:PSS films[48]. Furthermore, due to the strong intra- and inter-chain electrostatic attraction, PSB hydrogels swell the least compared to other zwitterionic hydrogels[13,49]. We use it to form double-network ZIPH with PEDOT:PSS by firstly dissolving SB monomer, crosslinker (N,N'-methylenebisacrylamide), initiator (ammonium persulfate or 2-hydroxy-2-methylpropiophenone), and 4-ethylbenzenesulfonic acid (EBSA) as an additive in the aqueous PEDOT:PSS dispersion, and then polymerizing the mixture in bulk (thermal initiation) or thin-film (UV initiation) states. In particular, the addition

of EBSA is hypothesized to facilitate the formation of rod-like structures (Fig. 2.2) for the PEDOT phase, through the destabilization of the micellar structure of PEDOT:PSS. Small-angle X-ray scattering (SAXS) revealed that the addition of EBSA to the PEDOT:PSS dispersion causes the PEDOT:PSS nanoparticles to transition from spheroidal to rod-like conformations, as indicated by the transition from a power law slope of 0 to -1 in the mid-q regime (Fig. 2.2).

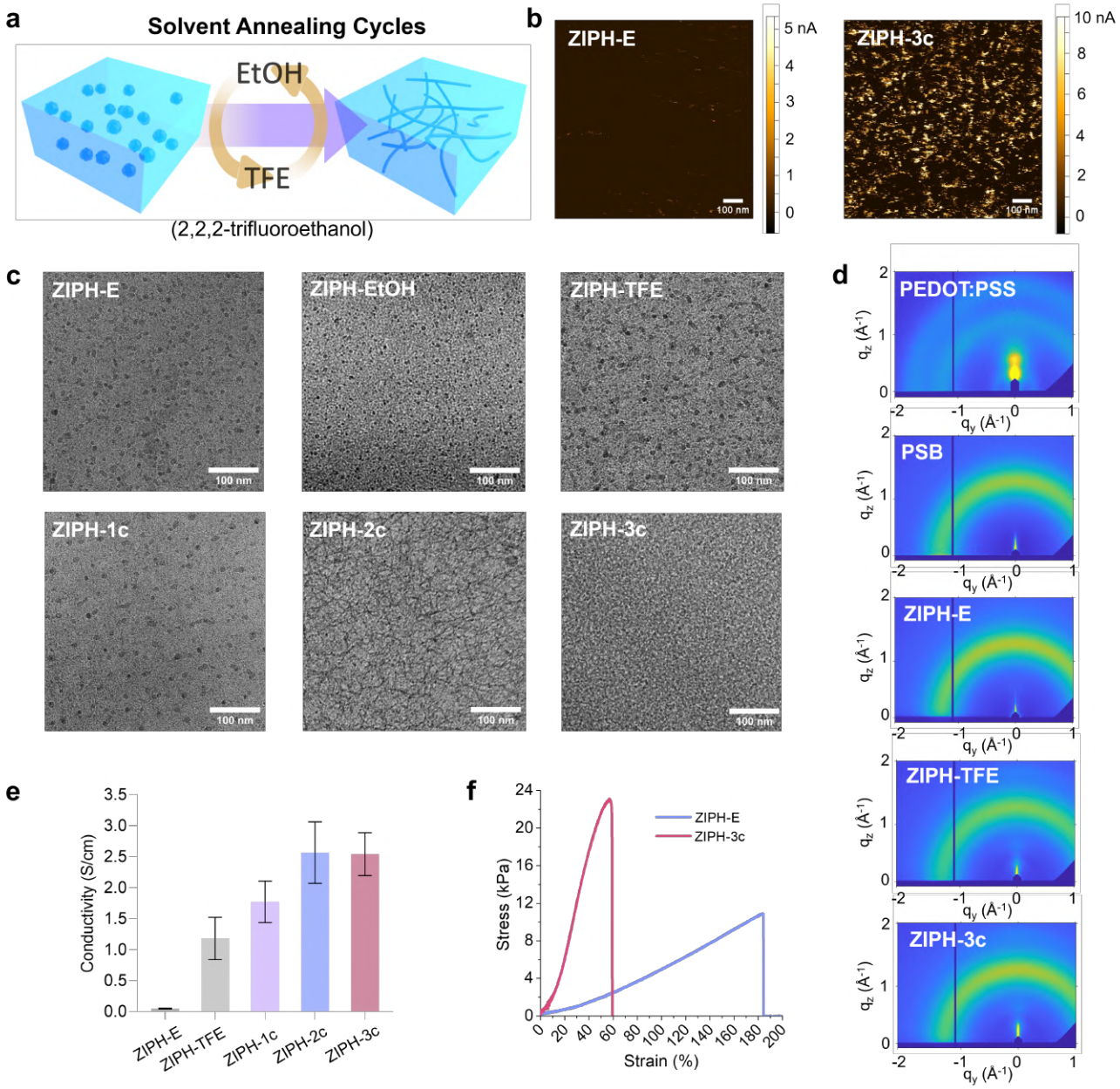

Figure 2.4. Solvent annealing treatment on ZIPH facilitate the formation of percolated PEDOT:PSS networks and higher conductivity. **a**, Schematic illustration of the morphological changes that occur to ZIPH after ethanol-TFE annealing cycles. **b**, Cryo-TEM images of ZIPH subjected to various solvent annealing conditions. With each ethanol-TFE cycle, the PEDOT:PSS particles transition to a more interconnected fibrillar morphology. **c**, C-AFM images of ZIPH before (ZIPH-E) and after (ZIPH-3c) 3 cycles of ethanol-TFE annealing cycles. **d**, GIXD diffraction patterns of PSB hydrogel and ZIPH subjected to various solvent annealing conditions. **e**, Conductivity values of non-implanted ZIPH samples prepared with various solvent annealing conditions obtained with a standard four-point measurement. All hydrogels were pre-equilibrated in PBS and autoclaved before being measured in a state fully hydrated with PBS. **f**, Tensile curves of ZIPH before (ZIPH-E) and after (ZIPH-3c) 3 cycles of ethanol-TFE annealing cycles.

To further promote the aggregation and interconnectivity of the PEDOT phase in ZIPH, we devised a novel solvent annealing method that involves alternatively exposing ZIPH to ethanol and 2,2,2-trifluoroethanol (TFE) with a certain number of cycles (ZIPH-nc for n cycles). Because TFE is a good solvent for uncrosslinked PSB while having poor chemical compatibility with PEDOT:PSS, we hypothesize that TFE could penetrate into the PSB hydrogel matrix to further destabilize the PEDOT:PSS phase, thereby promoting the formation of larger PEDOT:PSS aggregates in the PSB hydrogel matrix (Fig. 2.3). The combination of EBSA and TFE was observed to cause the PEDOT:PSS to collapse into a sponge-like solid, but TFE alone did not (Fig. 2.3). Before each TFE treatment, ZIPH is treated with ethanol in each cycle to deswell the hydrogel, thereby preemptively counteracting the excessive swelling of ZIPH by TFE. In addition, the deswelling by ethanol causes the PEDOT:PSS phases to be in closer proximity to each other, which increases the likelihood of adjacent PEDOT:PSS phases to connect (Fig. 2.4a).

2.2.2 Morphology and conductivity evolution of ZIPH during solvent annealing

The hypothesized effect of the solvent annealing process in facilitating the formation of PEDOT nanofibrous morphology is validated by cryogenic transmission electron microscopy (cryo-TEM) on ZIPH samples that went through different solvent annealing processes (Fig.

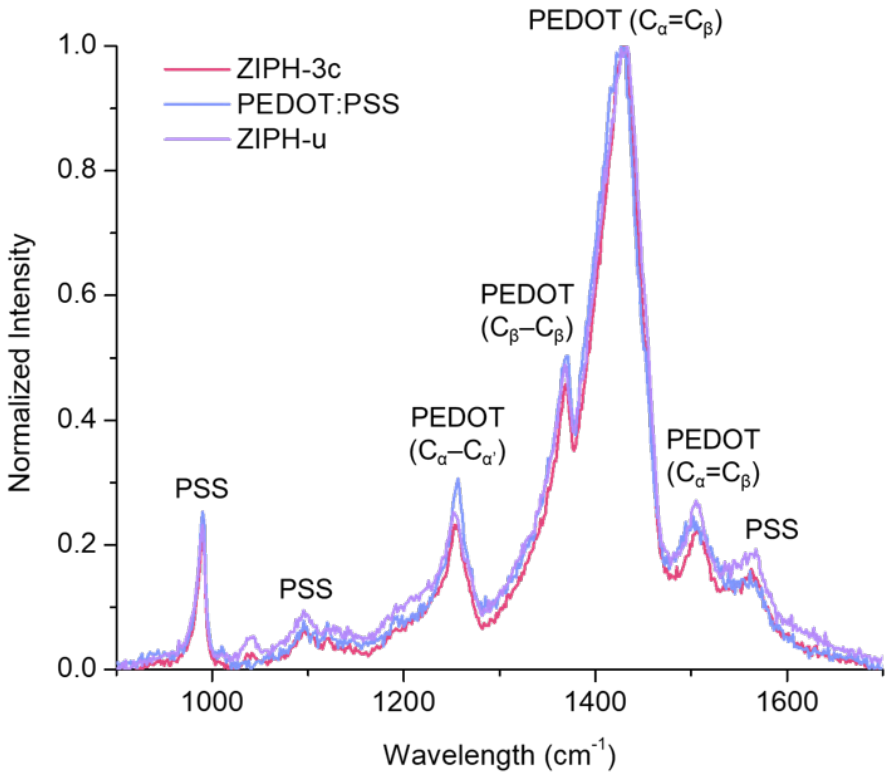

Figure 2.5. Comparison of Raman spectra of ZIPH-3c, PEDOT:PSS hydrogel, and ZIPH-u.

2.4b). For ZIPH blended with EBSA for promoting aggregation but without any solvent annealing steps (referred as ZIPH-E), dispersed PEDOT:PSS nanoparticles of 5-15 nm in diameter were observed. This shows that the favorable chemical compatibility between PSB and PEDOT:PSS does not provide enough driving force for PEDOT:PSS to grow nanoparticles into larger aggregates. After the solvent treatments in only ethanol or TFE, or 1 cycle of ethanol-TFE, there is minimal change in the nanoparticle morphology for PEDOT:PSS. After 2 to 3 solvent annealing cycles, the interconnected nanofibers started to emerge. The formation of the PEDOT:PSS fibrous structures from the solvent treatment processes can also be observed using conductive atomic force microscopy (C-AFM), as shown by the comparison of ZIPH-E and ZIPH-3c in Figure 2.4c.

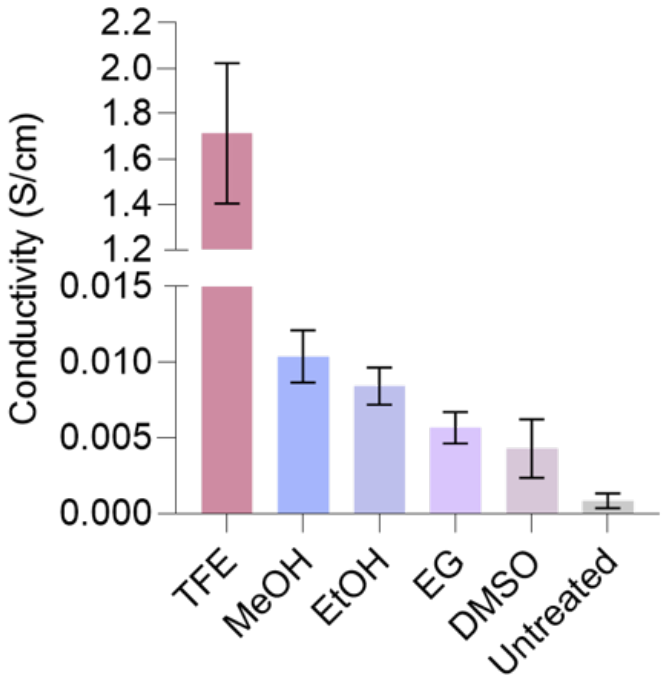

Figure 2.6. The conductivities of ZIPH-E bulk samples treated with excess amounts of various solvents for 30 minutes. EG, ethylene glycol; DMSO, dimethyl sulfoxide.

Grazing-incidence X-ray diffraction (GIXD) revealed that in contrast to the crystalline structure of pristine PEDOT:PSS, ZIPH suppresses the long-range crystallization of PEDOT (Fig. 2.4d). The solvent treatment processes have little effect in changing such amorphous structure. The diffraction pattern was nearly identical to that of PSB hydrogel (Fig. 2.4d). The PSS to PEDOT ratio also remained largely unchanged (Fig. 2.5).

As a result of the solvent annealing-induced formation of the interconnected nanofibrous morphology of PEDOT:PSS, the conductivity of non-implanted, hydrated ZIPH samples improved substantially from $\sim 10^{-4}$ S/cm for ZIPH-E to $\sim$2.5 S/cm for ZIPH-2c and ZIPH-3c (Fig. 2.4e), which is much higher increase than other reported treatment methods utilized on ZIPH samples (Fig. 2.6).The formulations were optimized for conductivity. Crosslinking density and solvent annealing method had a significant effect on conductivity (Fig. 2.7). For dry, thin film samples, the conductivity of ZIPH-3c reached 80 S/cm. The effective capacitance of ZIPH-3c was similar to that of PEDOT:PSS (Fig.2.8). For TFE-only or 1

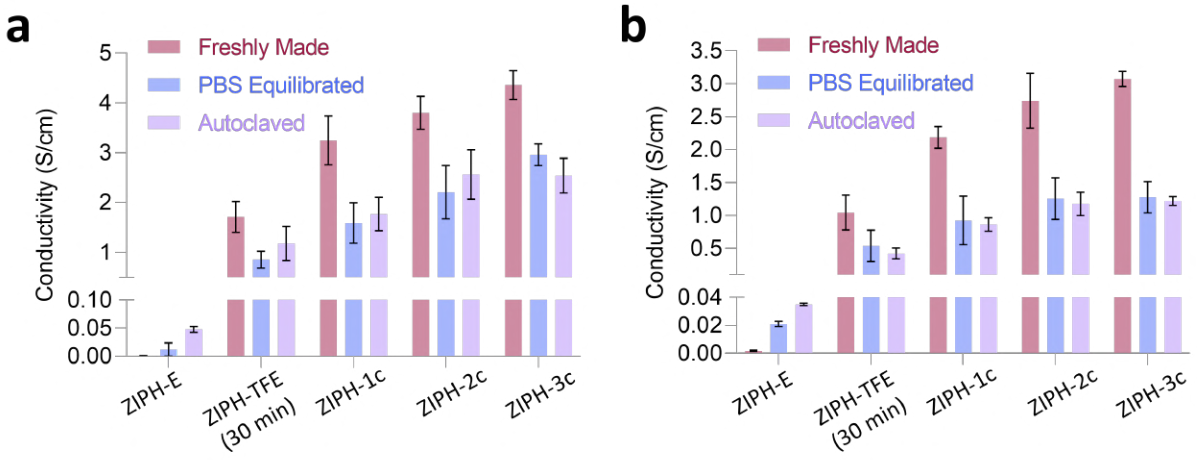

Figure 2.7. Crosslinking densities, solvent annealing, and post-treatments affects the conductivity of ZIPH. **a**, Conductivity comparisons of ZIPH made with 1.0 mol% crosslinking density. **b**, Conductivity comparison of ZIPH made with 1.8 mol% crosslinking density. Crosslinking mol% values were calculated with respect to the monomer concentration.

cycle of ethanol-TFE annealing, even though little changes were observed in the morphology, increases in conductivity have already started to take effect. The solvent treatment process also led to the increase in Young's modulus, from 1.4 kPa for ZIPH-E to 9.9 kPa for ZIPH-3c (Fig. 2.4f). This is also due to the formation of an interconnected network by the more rigid phase of PEDOT:PSS.

Table 2.1. Young's moduli of all materials used in in vivo experiments. Young's moduli were calculated from tensile tests.

Material	Young's Modulus (kPa)
PEDOT:PSS Hydrogel	720
ZIPH-3c	9.9
ZIPH-E	1.4
ZIPH-u	8.7
PSB	9.0
PSS	9.7
PDMS	9.8
Dex-PDMS	10

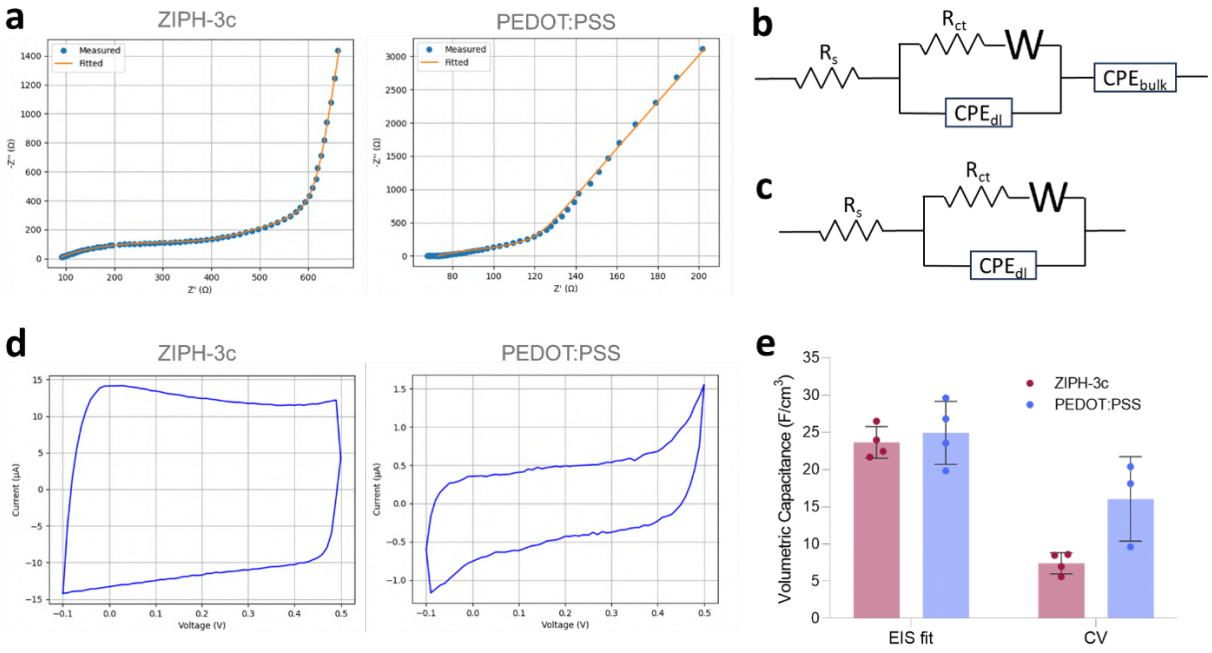

Figure 2.8. Comparisons of electrochemical properties. **a**, Nyquist plot and fitting results. **b**, Equivalent circuit model for ZIPH-3c. **c**, Equivalent circuit model for PEDOT:PSS. R_s is the solvent resistance, R_{ct} is the charge transfer resistance, W is the finite-space Warburg element, CPE_{dl} is the double-layer constant phase element, and CPE_{bulk} is the bulk constant phase element. **d**, CV curves conducted at 0.1 V/s. **e**, Comparison of capacitances calculated from the EIS fits and the CV curves.

2.2.3 ZIPH-3c is associated with the lowest collagen density among non-drug eluting implants

Next, we studied the FBR behaviors against ZIPH by subcutaneously implanting disc-shaped samples into mice. We assumed that the surface properties of PEDOT:PSS are largely governed by PSS since PSS forms a hydrophilic shell around the PEDOT core. For this assumption to be valid, the PSS shell around PEDOT needs to be largely intact. Water contact angle measurements show that the water contact angle of PEDOT:PSS hydrogel (11 °) is similar to PSS (6.5 °) and is substantially different compared to PEDOT-TMA (115 °), confirming our assumption that PSS mostly dictates the surface properties of PEDOT:PSS hydrogel (Fig. 2.11).

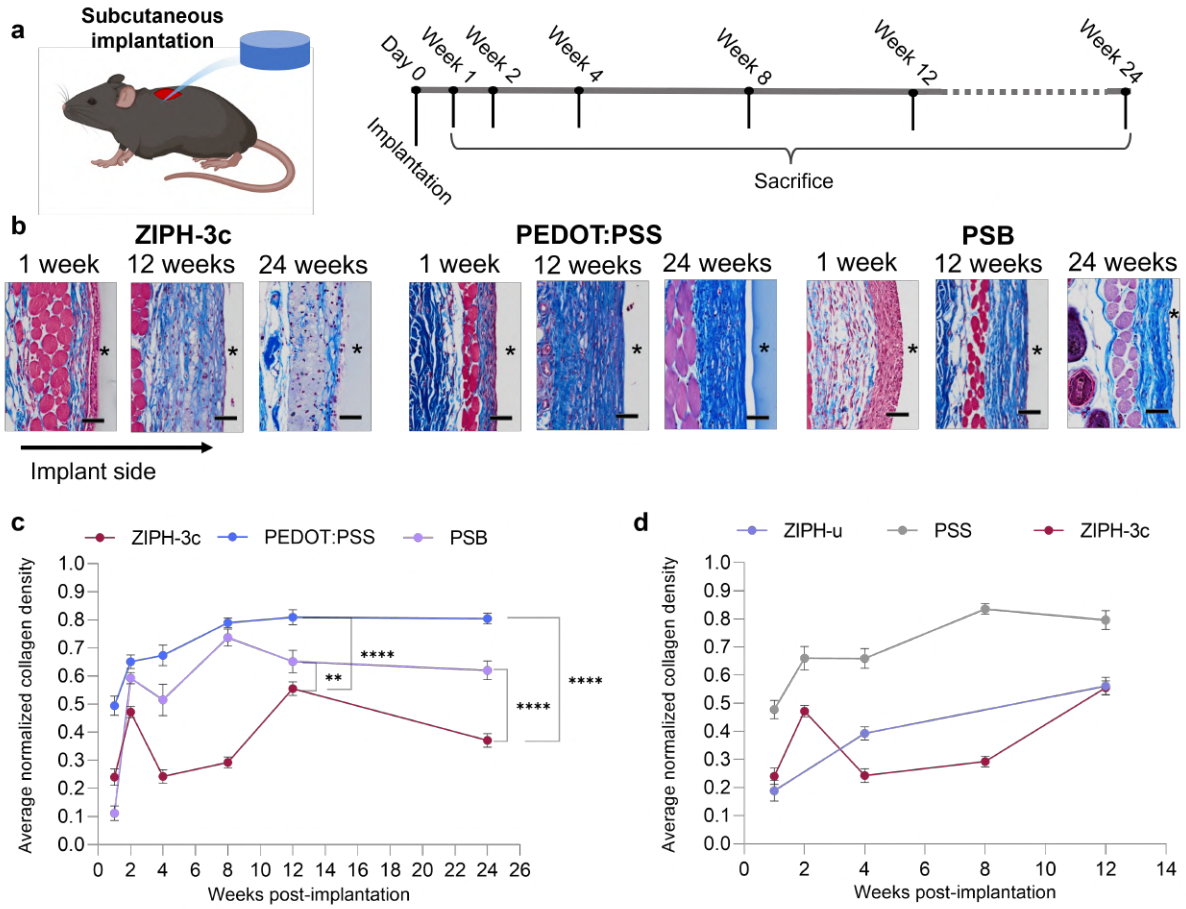

Figure 2.9. Measurement of FBR-induced collagen deposition shows that ZIPH-3c has one of the lowest collagen density. **a**, Schematic illustration of the subcutaneous implantation timeline. **b**, Representative MTS-stained tissues from 3 types of implants 1-, 4-, 12-, and 24-weeks post-implantation. Locations of implants appear clear and are indicated by asterisks. **c-d**, Average collagen density (blue pixel density) of the fibrotic capsule over time, determined from MTS-stained tissue. Scale bars, 50 µm. Error bars, mean ± s.d. N=5-6 mice per treatment. One-way ANOVA was used to compare collagen densities between treatments. **, $P < 0.001$; ****, $P < 0.0001$.

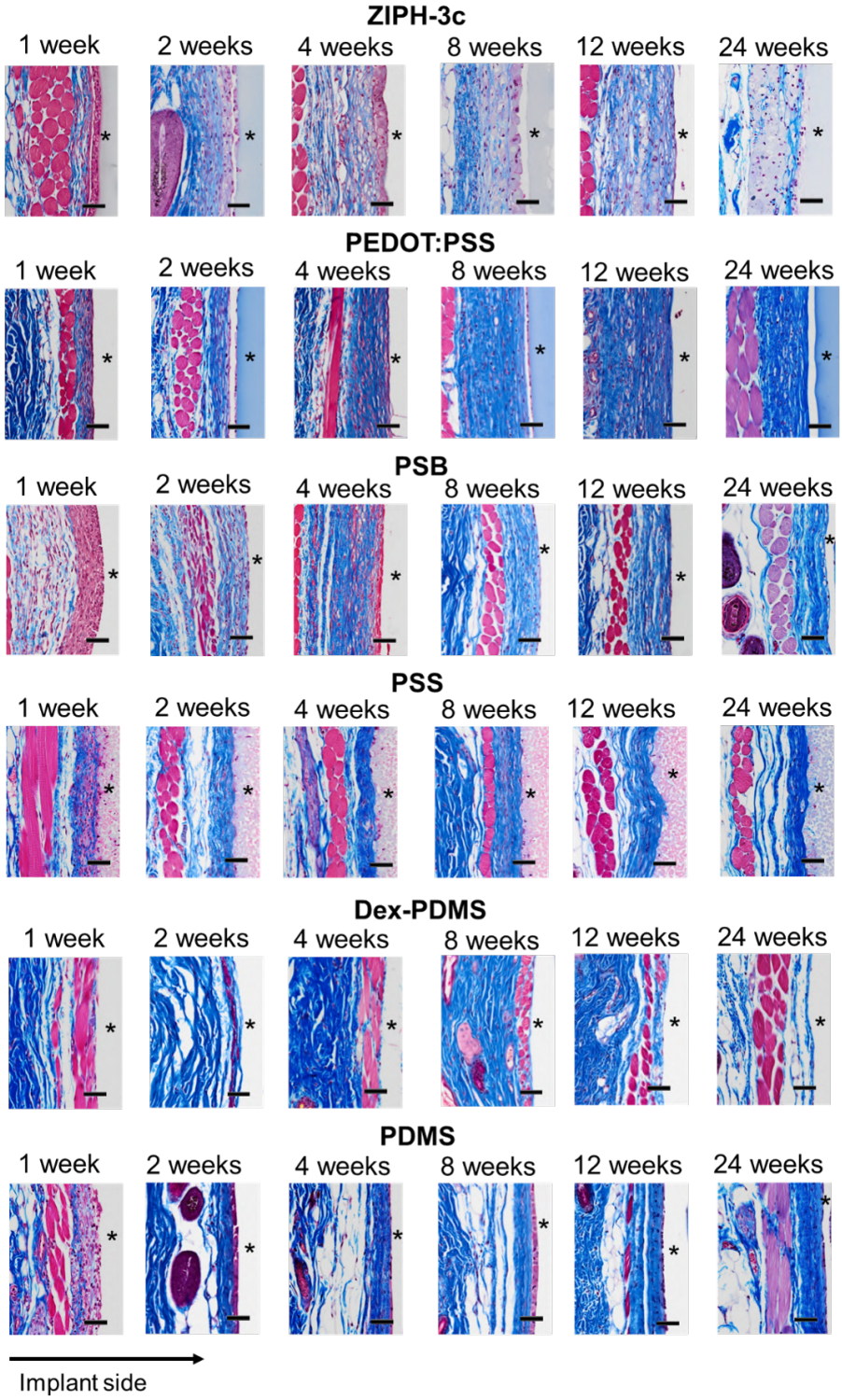

Figure 2.10. Representative Masson's trichrome stained tissues of ZIPH-3c, PEDOT:PSS, PSB, PSS, Dex-PDMS, and PDMS at 1-, 2-, 4-, 8-, 12-, 24-week post-implantation. Locations of implants are marked by asterisks. Scale bar, 50 /textmu m.

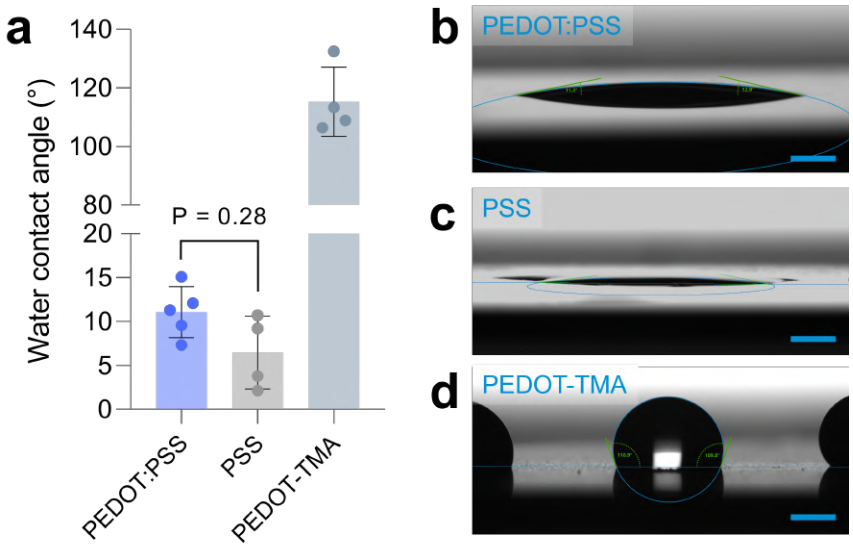

Figure 2.11. Static water contact angle measurements of PEDOT:PSS, PSS, and PEDOT-TMA. **a**, Static water contact angle measurements on dry, thin films of PEDOT:PSS, PSS, and PEDOT tetramethacrylate (PEDOT-TMA) on silicon. **b-d**, Representative photographs of static water contact angle measurements for PEDOT:PSS, PSS, and PEDOT-TMA. Scale bar, 1 mm. The contact angle for PEDOT:PSS was much more similar to PSS than that of PEDOT-TMA, demonstrating that the surface chemistry of PSS can mimic that of PEDOT:PSS.

After pre-determined timepoints, the mice were sacrificed at 1-, 2-, 4-, 8-, 12-, and 24-weeks post-implantation and histological analyses of explanted tissues around the implants were conducted (Fig. 2.9a & b and Fig. 2.10). Using MTS, the density of the collagen layer formed as a result of the FBR was quantified. Young's moduli for all implants tested were kept at around 10 kPa except for PEDOT:PSS to account for mechanical effects (Table 2.1), and the surface roughness for all implants were kept at the nanometer scale by using glass and plastic molds with a surface roughness on the order of a few nanometers to account for topographical effects. As shown by the average collagen density of the fibrotic capsule over time (Fig. 2.9c & d), ZIPH-3c indeed had substantially decreased collagen density than the PEDOT:PSS hydrogel at all timepoints, which validated that the incorporation of the zwitterionic hydrogel PSB effectively suppresses the FBR. Surprisingly, ZIPH-3c had a much lower collagen density than the PSB hydrogel at all timepoints as well (Fig. 2.9b & c).

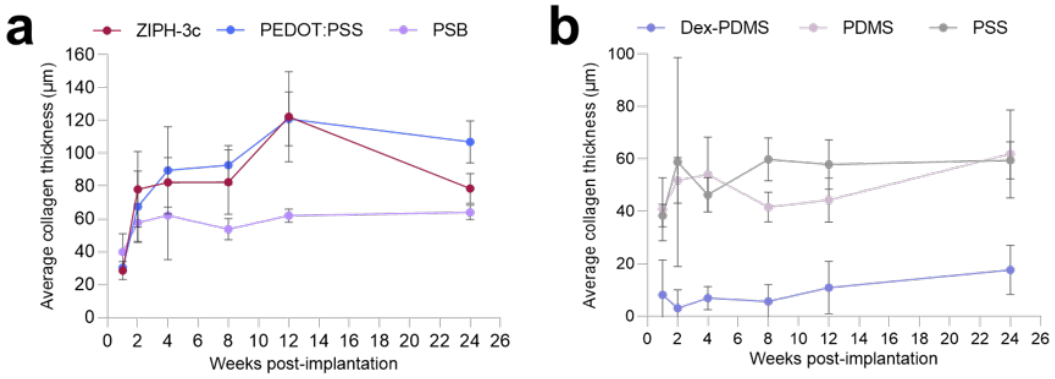

Figure 2.12. Collagen densities as a function of distance away from the surface of the implants for ZIPH-u. Representative Masson's trichrome stained tissues at 1-, 4-, and 12-weeks post-implantation (**a**). Collagen density comparisons of ZIPH-u and ZIPH-3c at 1-, 4-, and 12-week post-implantation (**b-d**).

For the thickness of the fibrotic capsule, ZIPH-3c was associated with the second thickest, behind only PEDOT:PSS, at most timepoints (Fig. 2.12). This indicates that the double-network morphology might be having some unique effect in helping to decrease the collagen density of FBR-associated fibrosis without necessarily decreasing the thickness. Along this line, the higher collagen density of ZIPH without the addition of EBSA or solvent treatment (ZIPH-u) compared to ZIPH-3c implies that the interconnected nanofibrous morphology of PEDOT:PSS in ZIPH-3c is also favorable for suppressing the FBR (Fig. 2.13). To the best of our knowledge, such effects of double-network morphology on the FBR have never been reported before in other biomaterials studies.

For PEDOT:PSS hydrogel, the high FBR-induced fibrosis could largely come from the negatively charged PSS[38–42]. To test this, we also prepared and tested PSS hydrogels, which, indeed, gave the highest collagen density at the surface of the implant (Fig. 2.9d).

Although the immunocompatible properties of zwitterionic polymers mostly come from the antifouling properties, protein adsorption assays indicate that this may not be the case for the ZIPH designs. Among all the tested samples (Fig. 2.14), both ZIPH-3c and ZIPH-u have some of the highest levels of protein adsorption. This suggests that the embedment of

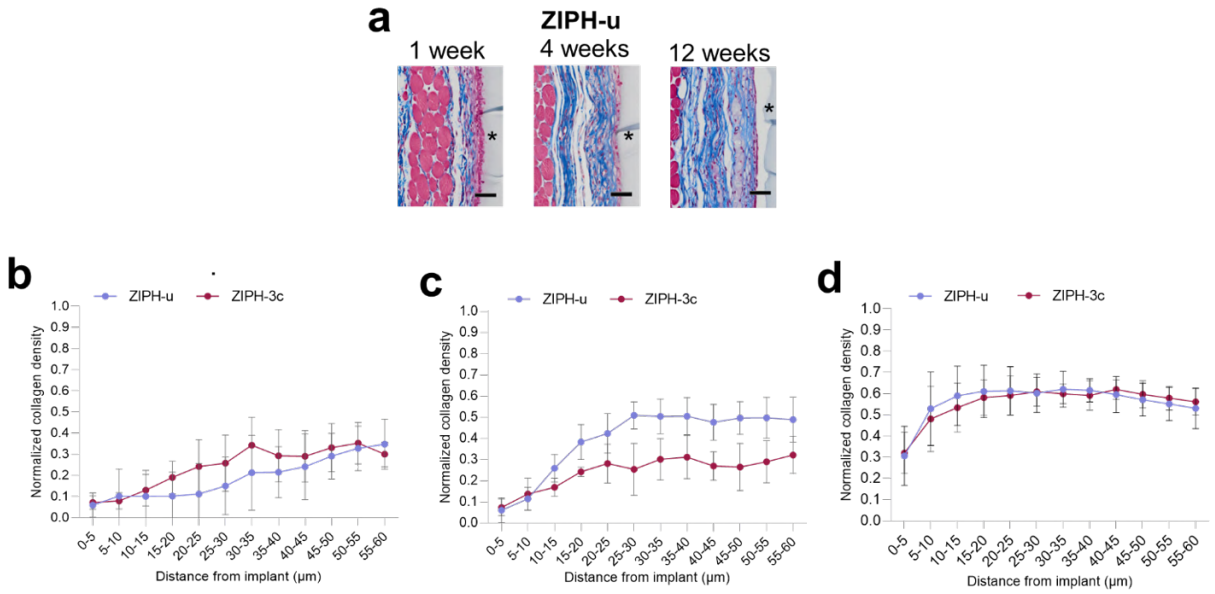

Figure 2.13. Fibrotic capsule thicknesses over time for ZIPH-3c, PEDOT:PSS, and PSB (**a**) and Dex-PDMS, PDMS, and PSS (**b**).

PEDOT:PSS in the PSB matrix may not be enough to negate the high protein adsorptive behavior of PEDOT:PSS. Our result also shows that PSS is indeed responsible for the high protein adsorptive behavior of PEDOT:PSS (Fig. 2.14), which is consistent with the in vivo collagen density results. Overall, the trend from these protein adsorption results does not fully agree with the in vivo histology results discussed above, which indicates that in our designs, protein adsorption only has a loose correlation with the fibrosis associated with each implant type.

2.2.4 Immune response for ZIPH-3c diverges from its parent materials

In the FBR, macrophages are known to play a central role in the final outcome[33,38,50]. To gain a deeper understanding of the different immune responses induced by different hydrogel designs, we used both flow cytometry (FC) and immunofluorescence (IF) to analyze the population size and phenotypes of macrophages surrounding each implant at 1-, 4-, and 12-weeks post-implantation (Fig. A.1-A.5). FC data (Fig. 2.15a and Fig. A.1-

A.3) indicated that ZIPH-3c was associated with the greatest number of Ly-6C$^{-/lo}$ F4/80^{hi} macrophages compared to other samples including PEDOT:PSS, PSB, PSS, and sham for all timepoints. Furthermore, the polarization states of Ly-6C$^{-/lo}$ F4/80^{hi} macrophages, M1 and M2 macrophages, were analyzed. M1 and M2 macrophages are thought to be pro- and anti-inflammatory, respectively, but studies have shown that an imbalance in macrophage polarization in either direction compared to sham can be a primary driver for poor FBR and fibrosis outcomes[33,51]. Macrophage polarization states exist on a continuum, and the M1/M2 classification can vary significantly depending on the markers used[51,52]. To gain a clear understanding on the average polarization states of macrophages, iNOS (M1) / Arg-1 (M2) and CD86 (M1) / CD206 (M2) single positive ratios were quantified using FC at 4 weeks. Both macrophage polarization classification methods indicated that the immunological milieu of ZIPH-3c was biased towards M1 polarization (Fig. 2.154b & c and Fig. A.2, A.3). Immunofluorescence (IF) microscopy confirmed that the Ly-6C$^{-/lo}$ F4/80^{hi} macrophages analyzed using FC were localized at the surface of the implants (Fig. 2.15d). Since an M1 bias suggests a polarization to type 1 immunity, T cell phenotypes were also assessed, and the fraction of cells expressing T-bet, a master regulator of Type 1 T helper cells (T_h1) and a marker for type 1 immunity, among CD3$^+$ T cells was found to be the highest for ZIPH-3c (Fig. 2.15e), consistent with the observed M1 bias. To check if markers for type 1 immunity necessarily imply an inflammatory response, FoxP3$^+$ T regulatory cells (T_{reg}s) were also quantified. It was found that ZIPH-3c was associated with the highest fraction of T_{reg}s among CD4$^+$ T helper cells (T_h cells), indicating the co-existence of an anti-inflammatory regulatory response (Supplementary Discussion). Consistent with previous results for zwitterionic hydrogels[14], PSB exhibited a preference towards M2 polarization and type 2 immunity (Fig. 2.15b,c,e and Fig. A.2), an indication that the immune response to ZIPH-3c has significantly diverged from PSB. Even though, in our case, the material with the lowest fibrosis, ZIPH-3c, is associated with more M1-like macrophages, these two observations may not

be directly causally linked. Prior work[51] has suggested that macrophage polarization state alone does not consistently predict FBR severity and fibrosis outcomes, which are highly context-dependent. The interesting observation in this work is that ZIPH-3c has an opposite macrophage polarization state compared to PSB and warrants investigative efforts on the underlying reasons in future studies.

Cytokines secreted during the FBR also provide in-depth information on the different

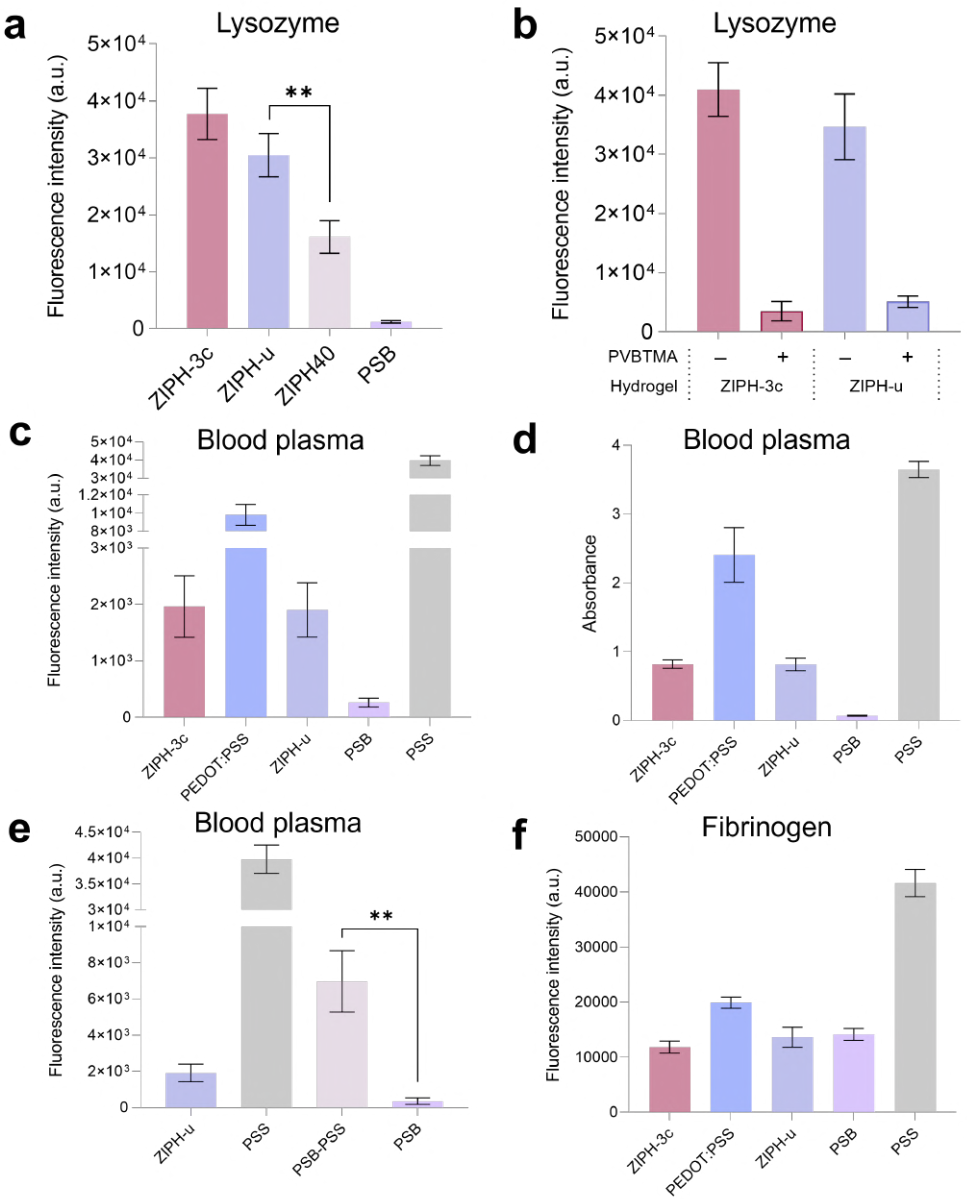

Figure 2.14. Comparison of protein adsorption amount.**a**, Comparison of positively charged lysozyme protein adsorption on ZIPH-3c, ZIPH-u, ZIPH40 (40% PSB), and PSB. Increasing PSB leads to decrease in lysozyme adsorption. **b**, Comparison of positively charged lysozyme protein adsorption on ZIPH-3c and ZIPH-u not neutralized or neutralized with PVBTMA. The neutralization of PSS by PBTMA leads to lower protein adsorption. **c**, Comparison of blood plasma protein adsorption on ZIPH-u, PSS hydrogel, PSB-PSS hydrogel, and PSS non-neutralized or neutralized with PVBTMA determined via CBQCA assay. Adding PSS to PSB hydrogel leads to higher protein adsorption. Neutralization of PSS with PVBTMA leads to lower protein adsorption. **d**, Comparison of blood plasma protein adsorption on ZIPH-3c, PEDOT:PSS hydrogel, ZIPH-u, PSB, and PSS with or without surface-assembled PSB polymer brushes determined via CBQCA assay. **e**, Confirmation of the results from (**d**) by using BCA instead of CBQCA. **f**, Comparison of fibrinogen (1 mg/mL) adsorption on ZIPH-3c, PEDOT:PSS hydrogel, ZIPH-u, PSB, and PSS with or without surface-assembled PSB polymer brushes determined via CBQCA assay. All data were acquired using CBQCA assay except for (**e**).

immune responses. We used a 14-cytokine LegendPlex panel to quantify cytokine concentrations at 1-, 2-, 4-, 8-, and 12-weeks post-implantation (Fig. 2.15g-j and Fig. B.1-B.5). IFN-γ, a crucial cytokine for type 1 immunity, was found to be expressed at similar levels for all implants, including ZIPH-3c, suggesting that T_{reg}s may be counteracting the inflammatory effects of type 1 immunity (Fig. B.1-B.5). However, IL-10, a T_{reg}-associated cytokine, was not significantly upregulated (Fig. B.1-B.5), suggesting an IL-10-independent regulatory mechanism. In addition, other cytokine expression profiles of ZIPH-3c and ZIPH-u are found to significantly diverge from their parent materials, PEDOT:PSS and PSB. In particular, ZIPH-3c and ZIPH-u were found to be associated with significantly higher concentrations of MCP-1 at all timepoints tested and higher concentrations of VEGF at the 1-, 2-, and 4-week timepoints compared to the rest of the implants (Fig. 2.15g & i and Fig. B.1-B.5). The significant upregulation of MCP-1 is a potential explanation for why ZIPH-3c is associated with the greatest number of macrophages. Interestingly, even though MCP-1 and VEGF are known to be powerful arteriogenic and angiogenic cytokines, respectively[53,54], vascularization in the surrounding areas did not match the high levels of MCP-1 and VEGF at 4-weeks post-implantation (Fig. 2.16). Another important cytokine is IL-1β, which is one of the first

cytokines released during tissue injury[55]. All the hydrogels except for PSB had suppressed IL-1β levels, and ZIPH-3c had one of the lowest IL-1β levels for all time points (Fig. 2.15g & i and Fig. 2.17a). This difference between ZIPH-3c and PSB may explain the lower fibrotic tendency of ZIPH-3c. For PEDOT:PSS and PSS hydrogels, significant upregulation of TNF-α was found after 1 week, suggesting an inflammatory response (Fig. 2.15h). Such

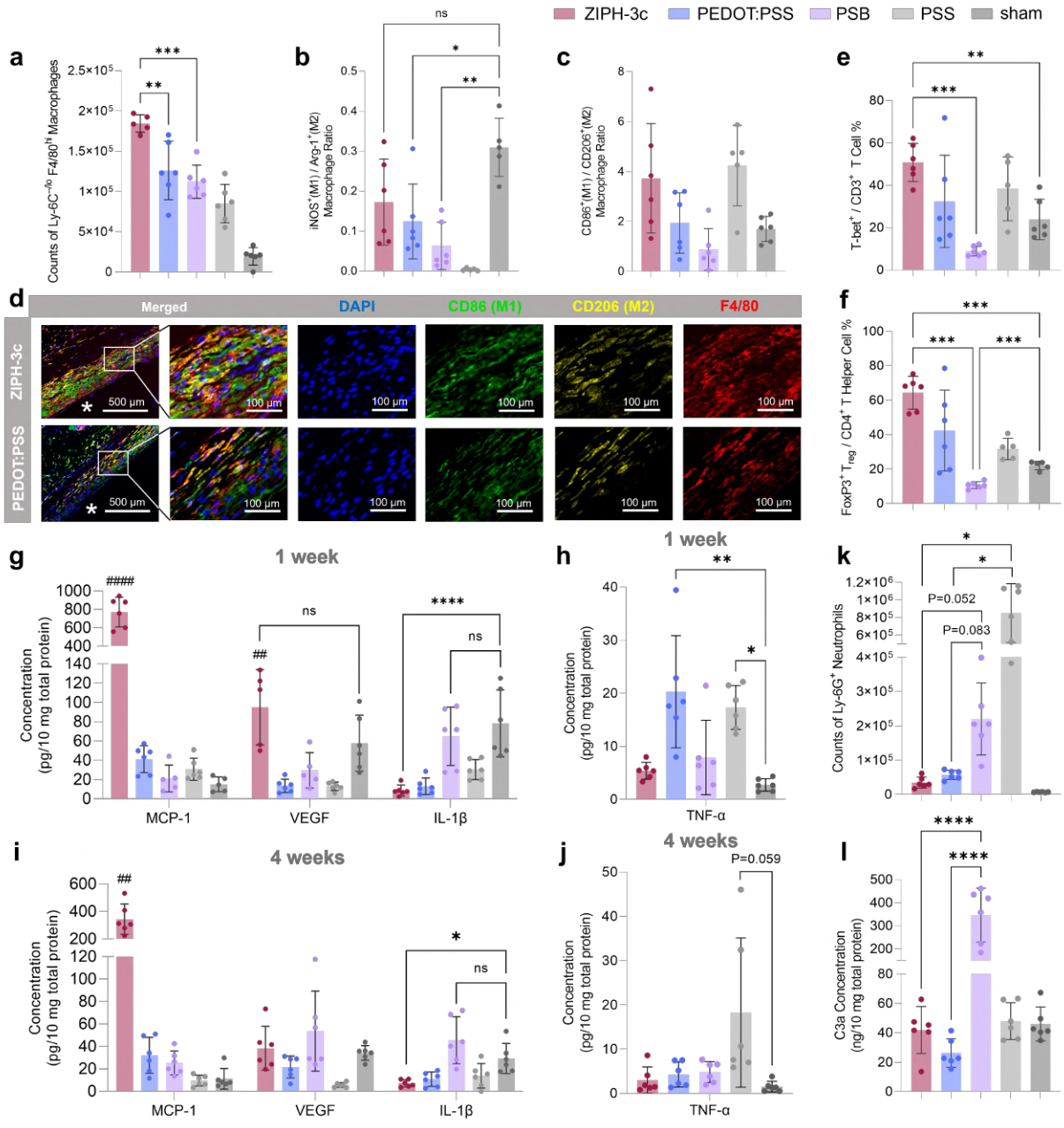

Figure 2.15. Comparisons of key immune cell populations and cytokine concentration from different implants show that ZIPH-3c induces a distinct immune response compared to its parent materials. **a**, Total counts of macrophages associated with each type of implant, determined by flow cytometry and 4-week post-implantation. Macrophages were defined as F4/80+ cells. ZIPH-3c is consistently associated with the greatest number of macrophages. **b**, iNOS$^+$ Arg-1$^-$ / iNOS$^-$ Arg-1$^+$ macrophage ratios associated with each implant, determined by flow cytometry at 4 weeks post-implantation. iNOS$^+$ Arg-1$^-$ macrophages are considered to be M1-like and iNOS$^-$ Arg-1$^+$ macrophages are considered to be M2-like. ZIPH-3c is associated with the most M1-like macrophages. **c**, CD86$^+$ CD206$^-$ / CD86$^-$ CD206$^+$ macrophage ratios associated with each implant, determined by flow cytometry at 4 weeks post-implantation. CD86$^+$ CD206$^-$ macrophages are considered to be M1-like and CD86$^-$ CD206$^+$ macrophages are considered to be M2-like. ZIPH-3c is associated with the most M1-like macrophages. **d**, Representative immunofluorescence microscopy images of tissues stained with F4/80 (macrophage), CD86 (M1), and CD206 (M2). Locations of implants appear clear and are marked by asterisks. **e**, Percentage of CD3$^+$ T cells that are T-bet$^+$. T cells associated with ZIPH-3c have a high fraction of T-bet$^+$ cells. **f**, Percentage of CD4$^+$ T helper cells that are FoxP3$^+$ Tregs. CD4+ T helper cells associated with ZIPH-3c have a high fraction of FoxP3$^+$ Tregs. **g-j**, Key cytokines associated with each implant, determined via LegendPlex assay at 1-week ($^{g\text{-}h}$) and 4-week ($^{i\text{-}j}$) post-implantation. MCP-1 is consistently upregulated for both ZIPH-3c and ZIPH-u. **k**, Total counts of neutrophils associated with each implant, determined by flow cytometry 1-week post-implantation. Neutrophils were defined as Ly-6G$^+$ cells. **l**, Complement C3a concentration associated with each implant, determined by ELISA 1-week post-implantation. The high number of neutrophils is correlated with the generation of C3a. PSB has a distinctly higher neutrophil number and C3a concentration than the rest of the hydrogels that contain PSS. Error bars, mean ± s.d. N = 5-6 mice per treatment. One-way ANOVA was used for statistical comparison of multiple means. *, $P < 0.05$; **, $P < 0.01$; ****, $P < 0.0001$; , $P < 0.01$ compared to rest; , $P < 0.0001$ compared to rest.

upregulation persisted at 4 weeks for PSS (Fig. 2.15j). Because TNF-α is a powerful pro-inflammatory cytokine leading to fibrosis, this may partially explains the fibrotic response against PEDOT:PSS and PSS. Cytokine concentration evolved significantly over time, and some key cytokines were observed to be in sync with the evolution of collagen density and thickness over time (Fig. 2.9c and Fig. 2.17b).

Another important type of cell in the FBR is neutrophils, which act as the first responders to the implants. We used flow cytometry to quantify Ly-6G$^+$ neutrophils. At 1-week post-implantation, the number of Ly-6G$^+$ neutrophils associated with PSB and PSS was found to

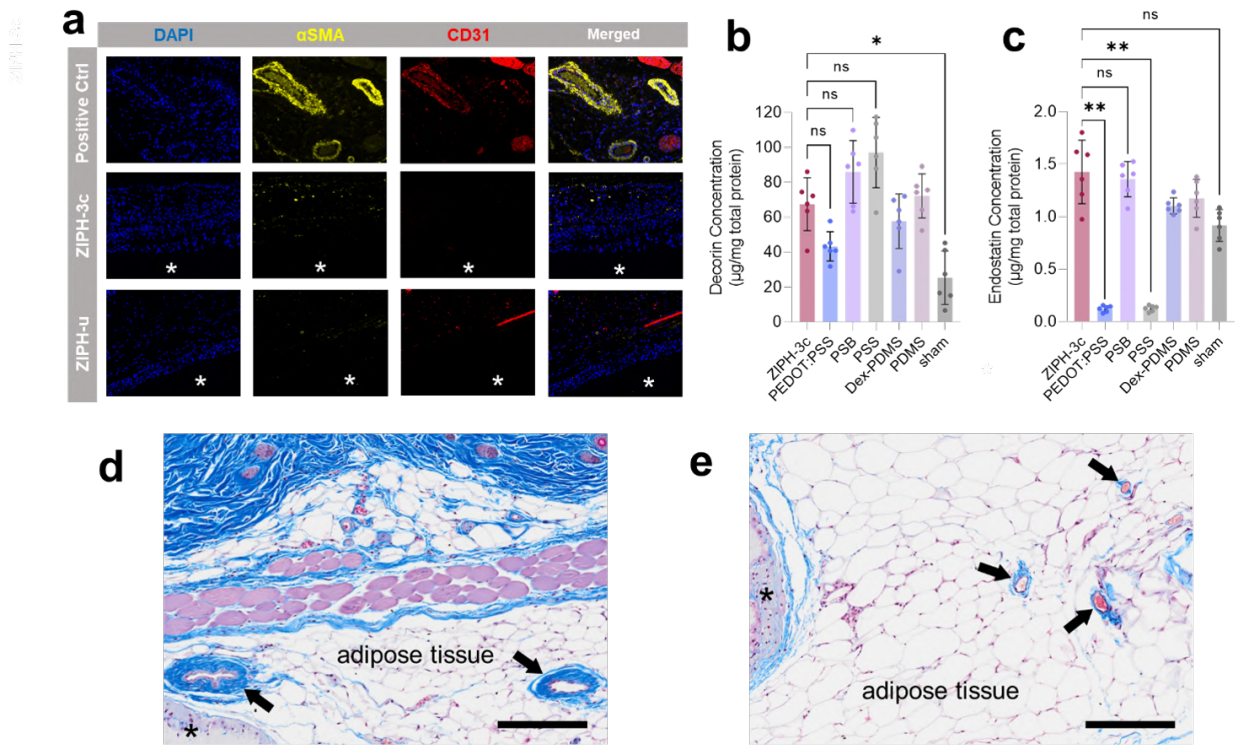

Figure 2.16. Angiogenesis was not initially observed but becomes prominent at 24-weeks post-implantation. **a**, Immunofluorescence microscopy images of ZIPH-3c and ZIPH-u stained with αSMA and CD31 at 4-weeks post-implantation. No angiogenesis is observed in the peri-implant region. The papillary dermis was used as the positive control. Implant locations are marked with asterisks. **b-c**, Concentrations of endogenous angiogenesis inhibitors decorin (**b**) and endostatin (**c**) determined with ELISA 2-weeks post-implantation, when the concentrations of MCP-1 and VEGF were at their peaks. ZIPH-3c is associated with some of the highest concentrations of decorin and endostatin. **d-e**, Masson's trichrome stained tissues from the peri-implant region of ZIPH-3c at 24-weeks post-implantation. Blood vessels are marked with arrows. Implant locations are marked with asterisks. Scale bar, 200 μm.

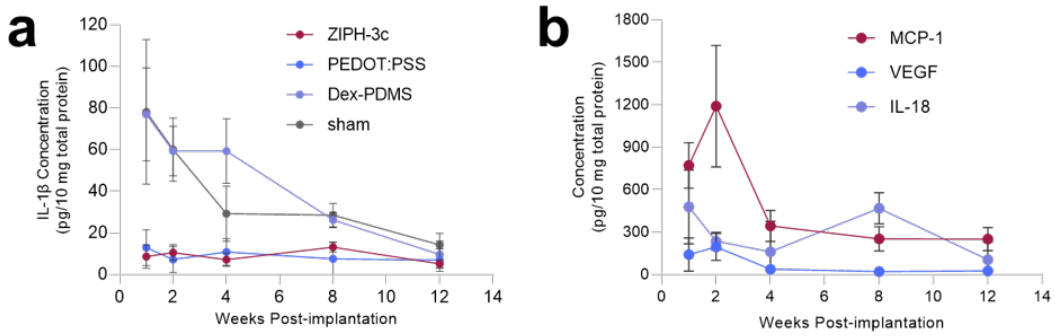

Figure 2.17. Peri-implant concentrations of key cytokines. **a**, Concentration of IL-1β over time for ZIPH-3c, PEDOT:PSS, Dex-PDMS, and sham. **b**, Concentrations of MCP-1, VEGF, and IL-18 over time for ZIPH-3c.

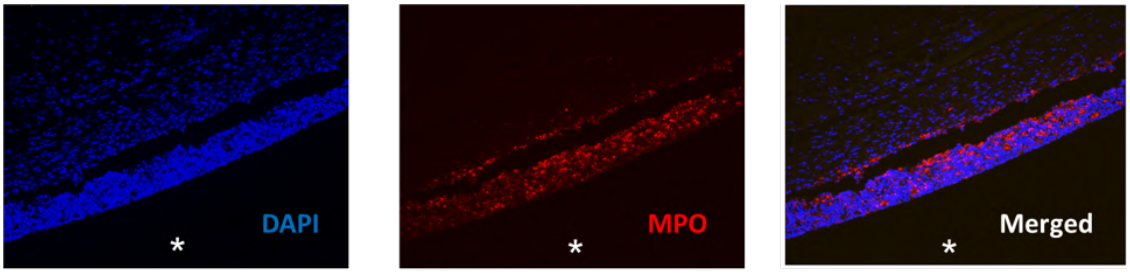

Figure 2.18. Tissue section of PSB 1-week post-implantation stained for DAPI and myeloperoxidase (MPO). MPO is a marker for neutrophils, confirming that the high number of neutrophils associated with PSB 1-week post-implantation are associated with the implant. Implant location is marked with an asterisk.

be greater compared to rest (Fig. 2.15k and Fig. A.1 & 2.18). It is known that the recruitment of neutrophils can be facilitated by the activation of the complement system3. Therefore, we further compared complement activation of different samples by quantifying protein C3a, which is generated as a result of complement activation. At the 1-week timepoint, PSB had substantially higher C3a concentrations in the peri-implant tissue than the rest (Fig. 2.15l), suggesting that PSB is activating the complement cascade. This finding is consistent with a previous study showing that a zwitterionic polymer, poly(2-metharyloyloxyethyl phosphorylcholine), facilitates complement activation[56]. For PSS, neutrophil recruitment may primarily be facilitated by TNF-α. For the ZIPH samples, despite having PSB as a significant fraction, the lower trafficking of neutrophils and complement activation (Fig. 2.15k & l and Fig. A.1) could come from PSS, which has been shown to suppress complement activation[57,58]. This difference between ZIPH and PSB could also be part of the reason for the lower collagen density from ZIPH.

2.2.5 ZIPH-3c is associated with a unique gene expression pattern

To gain further insight into the mechanisms of the FBR against ZIPH-3c, the tissues associated with the implant materials were analyzed with a 50-gene NanoString panel 4- and 12-weeks post-implantation (Fig. C.1-C.4). The most difference in gene expression occurred at 4-weeks post-implantation. Principal component analysis (PCA) was used to analyze the data. When the data are plotted on a vector space defined by the first (PC1) and third (PC3) principal components, there is a loose separation between the mildly fibrotic implants, consisting of ZIPH-3c and ZIPH-u, and the more severe fibrotic implants, consisting of PEDOT:PSS and PSB (Fig. 2.19a).

Compared to the other implants, the gene expression pattern for ZIPH-3c is unique. ZIPH-3c forms a tight, unique cluster on the PC1-PC3 vector space and is one of the main drivers of variance for PC3 (Fig. 2.19a). Among all the representative PC3 genes, the gene

with the most distinct expression level for ZIPH-3c is *Tbx21*, a gene for T-bet. Although not statistically significant ($P = 0.054$), *Tbx21* was upregulated for ZIPH-3c, consistent with FC results. T-bet is the master regulator for Type 1 T helper cells (T_h1), which, under certain circumstances, is implicated in the suppression of fibrosis[59–61]. But for T_h2 and T_h17, which are implicated in the induction[62–64], their master regulators, Gata3 (T_h2) and Rorc (T_h17), from ZIPH-3c were found to be indistinguishable from the baseline sham control (Fig. 2.19b and Supplementary Fig. 47b). On the other hand, PC1 is composed of genes that have the

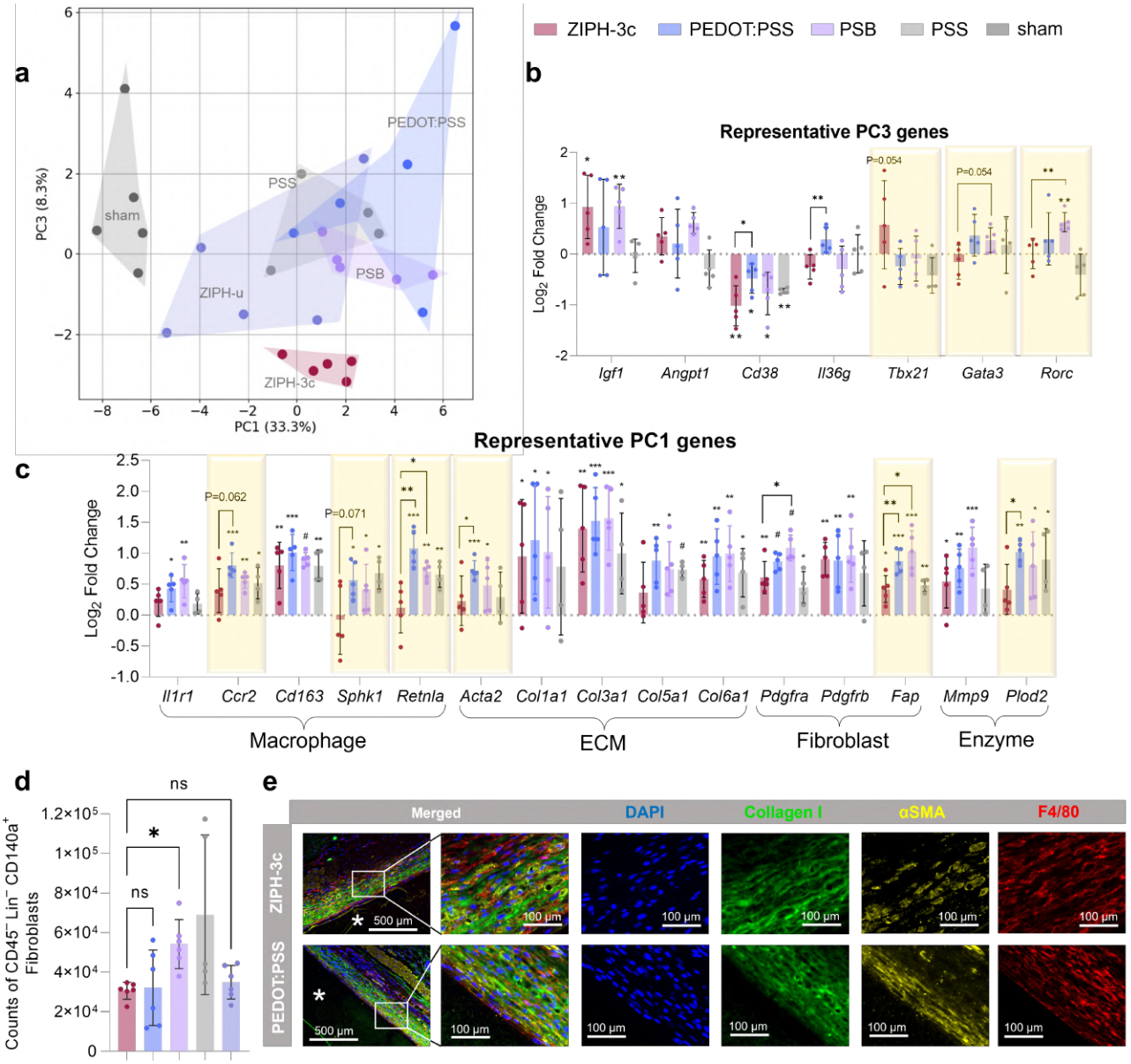

Figure 2.19. Gene expression analysis coupled with characterization of fibroblast and myofibroblast populations show that ZIPH-3c is associated with a unique, mildly fibrotic gene expression pattern. **a**, Principal component analysis (PCA) of a 50-gene panel from 4-week post-implantation samples plotted against each other. **b**, Genes associated with the negative direction of the third principal component (PC3). The expression of *Tbx21* (T-bet) makes ZIPH-3c unique among the samples in the experiment. T helper cell-related genes are highlighted. **c**, Differentially expressed genes associated with the positive direction of the first principal component (PC1). All the genes have some connection to fibrotic diseases. Genes that are statistically significantly different from sham control and have a strong connection with fibrosis are highlighted. **d**, Total counts of fibroblasts associated with each implant, determined by flow cytometry 4 weeks post-implantation. Fibroblasts are defined as CD45– Lin– CD140a+, in which Lin consists of CD31, Ep-CAM, Tie-2, and Ter-119. **e**, Representative immunofluorescence microscopy images of tissues stained with collagen I, αSMA (myofibroblast), and F4/80 (macrophage). Locations of implants are marked by asterisks. Error bars, mean ± s.d. N=5-6 mice per treatment. One-way ANOVA was used for statistical comparison of multiple means. *, $P < 0.05$; **, $P < 0.01$; ***, $P < 0.001$; , $P < 0.00001$.

biggest correlation with fibrosis[65–70], including *Ccr2, Sphk1, Retnla, Acta2, Fap*, and *Plod2*. Strong upregulations of these fibrotic genes are consistently observed for PEDOT:PSS, PSB, and ZI-SAM-PH, but not for ZIPH-3c or ZIPH-u (Fig. 2.19c). Not surprisingly, collagen genes also contribute strongly to PC1. Their expression patterns overall follow the trend of collagen deposition on different implants (Fig. 2.19c). However, given that the differences between implants are not statistically significant, there should be other genes and pathways important for the FBR outcome.

Fibroblasts and myofibroblasts are responsible for collagen deposition, with the increasing presence of myofibroblasts associated with increasing FBR severity[70]. *Acta2*, a gene expressed by myofibroblasts, was found to be upregulated with statistical significance for PEDOT:PSS and PSB implants, while ZIPH-3c maintained a similar level with sham (Fig. 2.19c). This agrees with IF imaging using αSMA (Acta2), which shows concentrated myofibroblasts at the surface of PEDOT:PSS but not for ZIPH-3c (Fig. 2.19e). In addition, $CD45^-$ Lin^- $CD140a^+$ cells, which encompass both fibroblasts and myofibroblasts, were quantified via FC. ZIPH-3c, was associated with the one of the least number of $CD45^-$ Lin^- $CD140a^+$

cells across all timepoints (Fig. 2.19d and Fig. A.1-A.3). IF imaging also confirmed that collagen I, αSMA, and F4/80 were all co-localized at the implant surface, confirming that the fibrotic response was directed against the implants and both F4/80$^+$ macrophages and CD45$^-$ Lin$^-$ CD140a$^+$ cells are part of the same immunological milieu (Fig. 2.19e). In contrast to the FC result for CD45$^-$ Lin$^-$ CD140a$^+$ cells, the αSMA expression on ZIPH-3c indicates a low number of myofibroblasts, which is consistent with the current understanding of the FBR[70].

2.3 Conclusion

To suppress the FBR against PEDOT:PSS by imparting intrinsic immunocompatibility, we report a double-network design of in situ formed PEDOT:PSS nanofibers embedded in a zwitterionic hydrogel matrix. By tuning the phase separation morphology, this design not only achieved higher conductivity, but also substantially reduced the FBR by 64% (as measured by the collagen density) compared to pristine PEDOT:PSS hydrogels (Supplementary Table 2). Most interestingly, its FBR severity is markedly lower than its parent zwitterionic polymer, PSB, which suggests some unique synergistic effects between PSB and PEDOT:PSS.

Along with these functional and morphological findings, our systematic immunological experiments combining histology, immunofluorescence, flow cytometry, RNA profiling, cytokine assays, and in vitro protein adsorption experiments have provided deeper insights. First, the poor immunocompatibility of PEDOT:PSS may be due to the high protein adsorptive properties of negatively charged PSS. Second, the higher immunocompatibility of ZIPH-3c compared to PSB may be related to its bias towards type 1 immunity while maintaining a high T_{reg} population and unique gene expression patterns, both of which deviate significantly from the parent materials of ZIPH-3c. These effects could come from the interplay between a unique combination of polymers and the resulting morphological structure. Although no causal relationships can be established based on the available data, the interest-

ing biological observations obtained from ZIPH-3c, mainly related to the emergent biological response that is not seen in either of its parent materials, lead to questions that could give way to new research directions for deepening our understanding of the FBR.

Overall, this work suggests that chemical heterogeneity, which has been rarely explored, could be another design parameter for enabling facile "mix-and-match" approaches for imparting immunocompatibility to functional materials without changing the chemical structure. Also, for deepening the immunological understanding of the FBR mechanism, creating model systems with controlled chemical heterogeneity could be a useful tool and is one of our ongoing efforts.

2.4 Experimental Details

2.4.1 Materials

PEDOT:PSS (PH1000) was purchased from Clevios and was filtered through a 0.7 µm glass fiber filter (Tisch Scientific) before use. The following chemicals were purchased from Sigma-Aldrich: [2-(Methacryloyloxy)ethyl]dimethyl-(3-sulfopropyl)ammonium hydroxide (SBMA, 95%), *N,N'*-Methylenebisacrylamide (MBAA, ≥98%), ammonium persulfate (APS, ≥98%), *N,N,N',N'*-tetramethylethylenediamine (TEMED, 99%), 2-hydroxy-2-methylpropiophenone (HMPP, 97%), 4-ethylbenzenesulfonic acid (EBSA, 95%), sodium styrene sulfonate (NaSS, Sigma-Aldrich, ≥90%), divinylbenzene (DVB, 80%), (3-aminopropyl)triethoxysilane (APTES, 99%), acrylic acid (AAc, 99%), (vinylbenzyl)trimethyl ammonium chloride (VBTMAC, 99%), sodium dodecylbenzene sulfonate (SDS, ≥98.5%), 2-cyano-2-propyl benzodithioate (CPBD, >97%), and tetramethacrylate end-capped PEDOT (PEDOT-TMA, 0.5 wt% in nitromethane, doped with p-toluenesulfonate). 2,2,2-trifluoroethanol (TFE, ≥99%) was purchased from Sigma-Aldrich and Tokyo Chemical Industries. Poly(allylamine) (PAH, 15% aq. soln.) was purchased from Polysciences. PDMS Sylgard 184 was purchased

from Dow-Corning. The acetate buffer was prepared with 0.1 M acetic acid (glacial, Sigma-Aldrich, ≥99.85%), 0.1 M sodium acetate trihydrate (Sigma-Aldrich, >99%), and 0.5 M NaCl at pH 5.2. Styrene-ethylene-butadiene-styrene H1062 elastomer (SEBS) was purchased from Asahi Kasei.

2.4.2 Preparation of hydrogels

For preparing ZIPH-E hydrogels, 250 mg of [2-Methacryloyloxy)-ethyl]dimethyl-(3-sulfopropyl)ammonium hydroxide and 1.4 mg (1 mol%) of MBAA were dissolved in 1.0 mL of PEDOT:PSS dispersion. Then, for the preparation of thermally initiated hydrogels, 10.21 µL (0.1 mol%) of APS (20 mg/mL) and 10.41 µL (0.2 mol%) of TEMED (20 mg/mL) aqueous solutions were added dropwise to the PEDOT:PSS mixture under continuous agitation. For the preparation of UV initiated hydrogels, 7.5 µL (0.1 mol%) of HMPP (20 mg/mL) aqueous solution was added. This was followed by the dropwise addition of 62.5 µL of EBSA aqueous solution (20 wt%) while the mixture is continuously agitated and vortexed for an additional minute. For thermal polymerization, the final mixture was placed under vacuum for 15 minutes, injected into a sandwich sheet mold, and placed in an 80°C oven for 1 hour. For UV polymerization, the final mixture was sparged with nitrogen for 10 minutes, spin coated and exposed to UV irradiation (365 nm wavelength, 4 mW/cm $_2$) for 5 minutes. To prepare ZIPH-u hydrogels, the above procedures were carried out without the addition of EBSA. To prepare annealing cycle treated bulk ZIPH hydrogels, ZIPH-E hydrogels were briefly rinsed in ethanol. Subsequently, the hydrogels were immersed in a volume of ethanol three times the volume of the ZIPH sample. Thereafter, the ethanol was discarded, and the hydrogels were immersed in a volume of TFE three times the volume of the ZIPH sample. The TFE was discarded, and the hydrogels were briefly rinsed in water. The whole annealing process was repeated two more times to obtain ZIPH-3c. To prepare annealing cycle treated thin film ZIPH hydrogels, the films were immersed in ethanol for 1 minute and immersed in

TFE for 1 minute.

To prepare PSB hydrogels, 1.5 g of SBMA (55 wt%), 4.2 mg of MBAA (0.5 mol%), and 0.882 mg of HMPP (0.1 mol%) were dissolved in PBS. The solution was vortexed for 1 minute and sparged with nitrogen for 10 minutes. The sparged solution was injected into a sandwich sheet mold and irradiated with UV light (365 nm wavelength, 4 mW/cm ^{2}) for 30 minutes per side.

To prepare PSS hydrogels, 700 mg of NaSS (28 wt%) was dissolved in 1694 µL of DMSO by stirring overnight. To the NaSS solution, 22.6 µL of DVB (4 mol%), 43.4 µL (0.1 mol%) of APS DMSO solution (20 mg/mL), and 44.2 µL (0.2 mol%) of TEMED DMSO solution (20 mg/mL) were added and vortexed for 1 minute. Thereafter, the solution was placed under vacuum for 15 minutes, injected into a sandwich sheet mold, and placed in an 80°C oven for 3 hours. The resulting PSS gel was rinsed twice in PBS.

For the preparation of PEDOT:PSS bulk hydrogels, 16% v/v of DMSO was added to PEDOT:PSS. Then, 10 mg/mL of EMIM OTf was added dropwise while the solution was continuously agitated. The resultant mixture was vortexed for 1 minute, placed under vacuum for 15 minutes, and injected into a sandwich sheet mold with silicone lining on top. The mold was placed on a hotplate, heated to 90 °C, for 90 minutes with the silicone lining side up. Then, the top piece with the silicone lining was removed, and the PEDOT:PSS gel was exposed to air. The PEDOT:PSS gel was dried at 40 °C for 16 hours, followed by another round of drying at 50 °C for 16 hours, at which point the thickness and lateral dimensions of the gel was approximately a third and a half of the original dimensions, respectively. The resulting PEDOT:PSS gel was rinsed twice in PBS.

All gels were washed in PBS for three days with changes of fresh PBS every 12 hours. All hydrogels used in in vivo experiments were autoclaved at 121 °C for 30 minutes in PBS. To ensure that most of the EMIM OTf was washed out of the PEDOT:PSS hydrogel and that most of the organic solvents and EBSA was washed out of ZIPH-3c during the PBS

washing steps, freshly made PEDOT:PSS or ZIPH-3c hydrogel was soaked in D $_2$ O-PBS at 30 times the volume of the hydrogel. 3 mg/mL of 1,3,5-trioxane was dissolved in D $_2$ O-PBS to serve as an internal standard for calculating the residual concentrations of various chemical species in the discarded wash. Fresh changes of D2O were made every 12 hours, and the discarded wash was analyzed via 1H NMR.

2.4.3 Preparation of PDMS

To prepare PDMS discs, 45 parts of base was mixed with 1 part of curing agent and poured in a petri dish. To prepare 1 mm thick samples, the uncured PDMS was leveled in the petri dish and cured at 80 °C for 3 hours. To prepare Dex-PDMS, 2% w/v of dexamethasone was dissolved in THF. 1 volume of the resultant THF solution was mixed with 1 volume of PDMS base, and the THF was slowly removed in a rotary evaporator. The resultant mixture was placed in vacuum overnight to completely remove the remaing THF and to obtain a PDMS base mixture with 1% w/w dexamethasone. To prepare 1 mm thick samples, 44 parts of the dexamethasone-PDMS base mixture was mixed with 1 part curing agent and poured into a petri dish. The uncured mixture was leveled in the petri dish and cured at 80 °C for 3 hours. To prepare ∼100 µm thick films, dextran (10% in DI H2O, 0.05% w/v Tween-20) was spin coated at 2000 RPM on O2 plasma treated glass and baked at 80 °C for 1 minute. Then, a mixture of 10 parts of dexamethasone-PDMS base and 1 part of curing agent was spin coated at 1000 RPM for 2 minutes and baked at 80 °C for 30 minutes.

All in vivo PDMS samples were sterilized with ethylene oxide.

2.4.4 Synthesis of PGMA

Poly(glycidyl methacrylate) (PGMA) (Fig. 2.20) was synthesized by dissolving 10.0 g GMA (70.3 mmol), 23 mg AIBN (0.14 mmol), and 156 mg CPBD (0.703 mmol) were dissolved in 30 mL DMF. The solution was sparged with nitrogen gas for 30 minutes and reacted at 65

°C for 18 hours. The polymer was precipitated in over 10 times the volume of cold methanol and re-dissolved in DCM. The polymer was precipitated twice more and dried under vacuum for two days.

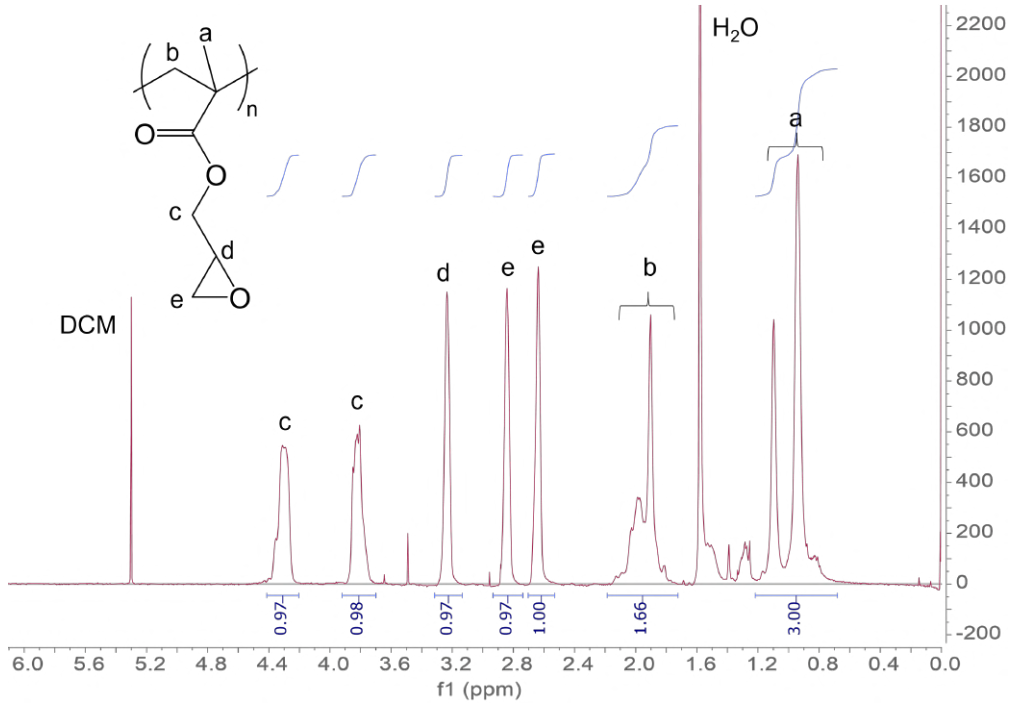

Figure 2.20. NMR spectrum of PGMA.

2.4.5 Multilayer functionalization

To achieve stable adhesion of conducting hydrogels, monolayers of PGMA and PAH (PGMA-PAH method) was deposited. For the PGMA-PAH method, the substrate was first O_2 plasma treated and PGMA (5 mg/mL in 19:1 $CHCl_3$:chlorobenzene) was spin coated at 2000 RPM, followed by baking at 120°C for 30 minutes. The baked substrate was washed in CHCl3 for 2 minutes and blow dried to form a PGMA monolayer. PAH (5 mg/mL 29:1 isopropanol:DI H_2O) was spin coated at 2000 RPM on top of the PGMA monolayer and baked at 80°C for 10 minutes. The baked substrate was washed in DI H2O (+0.05% Tween-20) for 2 minutes, rinsed in DI H_2O, and blow dried to form a PAH monolayer.

2.4.6 Measurement of material properties

Conductivity measurements were conducted using a standard four-point geometry (Supplementary Fig. 4a & b). Bulk hydrogels were prepared into discs (10 mm in diameter and 1 mm in thickness) using a biopsy punch, and solvent treatments were applied to the discs. Any changes in physical dimensions that resulted from the solvent treatments were accounted for when determining the conductivity values. Probes were put in direct contact with the non-implanted hydrogels fully hydrated in PBS (Fig. 2.4e). Conductivity measurements were also carried out for dry spin-coated thin films.

The electrochemical measurements were made using the PalmSens electrochemical workstation. To fabricate Au electrodes, physical vapor deposition of 10/50 nm of Ti/Au using the EvoVac (Angstron Engineering) was carried out with a shadow mask on glass substrates. For PEDOT:PSS, PGMA monolayers were deposited on the glass substrates, followed by spin coating PEDOT:PSS (13% 1:13 Triton X-100:DMSO) at 1000 RPM through a PET mask. The PET mask was peeled off, the substrate was baked at 120°C for 30 minutes, and rinsed with DI H2O. For ZIPH-3c, multilayer functionalization was carried out with PGMA and PAH. The resultant free amines were reacted in a tetrachloroethane solution of 2% triethylamine and 2% methacryloyl chloride. The ZIPH-3c precursor solution was spin coated at 1000 RPM for 10 seconds through a PET mask, followed by exposure to UV light (365 nm wavelength, 4 mW/cm2) for 30 minutes under a humidified atmosphere. The PET mask was peeled off, and three 1 minute cycles of ethanol-TFE solvent annealing was conducted to obtain ZIPH-3c films on Au electrodes. For electrochemical measurements, PDMS wells were used to hold 1x PBS. The Au electrode served as the working electrode, and a Ag/AgCl reference electrode and a platinum electrode were held in contact with PBS. Electrochemical impedance spectroscopy (EIS) spectra were obtained over a range of 100 kHz to 0.1 Hz with an AC 10 mV sine wave and with no DC offset. Cyclic voltammetry was conducted at a scan rate of 0.1 V/s and with a voltage window of -0.1 V to +0.5 V with respect to Ag/AgCl

(Supplementary Fig. 9).

The tensile properties of hydrogels were tested on a universal testing machine (zwickiLine Z0.5, Zwick Roell Group, Ulm, Germany) with 500-N load cell at room temperature. Hydrogels were cut into JIS K6251-8 industrial standard dumbbells. For ZIPH-3c, ZIPH-u, pSB, and pSS hydrogels, the crosshead speed was set to 30 mm/s. For PEDOT:PSS hydrogel, the crosshead speed was set to 5 mm/s. Cyclic tests were also conducted.

2.4.7 Characterization of material microstructure

For cryo-TEM imaging, UV polymerized ZIPH films were prepared following a modified version of the procedures described earlier. The precursor solutions were spin-coated at 2000 RPM for 10 seconds on oxygen plasma-treated copper Quantifoil grids (200 mesh, R1.2/1.3; Electron Microscopy Sciences) supported on PDMS. A portion of the gel was scraped away to expose the mesh pattern of the grid. The hydrogel films were kept in a humidified chamber until further processing. The gels were then back blotted (force = 1, 20 s) and plunge frozen into liquid ethane on a Thermo Scientific Vitrobot Mark IV. The Aquilos 2 cryo-FIB/SEM (Thermo Scientific) was used to prepare the lamella. Using the in-column sputter coater the grid was coated with platinum at 1 kV and 10 mA current for 15 seconds. The grid was SEM imaged and then atlased using Maps 3.26 (Thermo Scientific) at 10kV accelerating voltage and 13 pA current to find suitable areas for milling. Prior to milling the grids were coated with a layer of organometallic platinum using a gas injection system for 10 sec. The milling process was automated into 4 steps (all at 30kV accelerating voltage): Rough Milling, Medium Milling, Fine Milling, and Thinning using 500, 300, 100, 30 pA current, respectively. The final lamella thickness was targeted between 100-150 nm. Lamella were imaged on the Thermo Scientific Titan Krios 3Gi at 300 kV at cryogenic temperature equipped with a Gatan K3 direct electron detector and BioContinuum in counting CDS mode.

Conductive AFM (C-AFM) measurements were performed by using the C-AFM mode

of Cypher ES Environmental AFM with ASTELEC-01 probe and the dual gain C-AFM probe holder (gain=1µA/1nA/V). UV polymerized ZIPH-E and ZIPH-3c films were prepared following the procedures described earlier. The precursor solutions were spin-coated at 6000 RPM for 10 seconds on oxygen plasma-treated Au films on SiO2 substrates and dried on a hotplate. Magnets were placed separately on Au and sample film, and were sealed with Ag paste to realize ideal contact. Before measurement, the sample bias was zeroed by applying an offset voltage from the AFM hardware. During the measurement, 1 mV bias was applied across samples and the current was converted to a voltage and then amplified and recorded by the AFM hardware. Scans were acquired using scan rates of 2 µm/s.

2.4.8 X-ray scattering and diffraction

Small-angle X-ray scattering (SAXS) was performed at the Advanced Photon Source at Argonne National Laboratory on beamline 12-ID-B. Pristine PEDOT:PSS and PEDOT:PSS with 10 mg/mL of EBSA were loaded into capillary tubes (Charles Supper) and sealed. The sample-to-detector distance was 2 m, corresponding to a q-range of 0.003-0.5 $Å^{-1}$.

Grazing-incidence X-ray diffraction (GIXD) was performed at the Advanced Photon Source at Argonne National Laboratory on beamline 8-ID-E. UV-initiated ZIPH samples were spin-coated at 1500 RPM for 10 seconds. Thermally initiated ZIPH samples were prepared by sandwiching 10 µL of the precursor solution between a piece of silicon (O_2-plasma treated) and PET laminated coverslip (10 mm x 17 mm) and heating to 80°C for 15 minutes. PSB hydrogel samples were prepared similarly by sandwiching 3 µL of the precursor solution between a piece of silicon (O_2-plasma treated) and PET laminated coverslip (10 mm x 17 mm) and exposing to UV light for 10 minutes. The coverslip was gently removed while submerged in water. All samples were dried on a hotplate after polymerization of solvent annealing.

2.4.9 Spectroscopy for chemical characterization

Scanning electron microscopy – energy dispersive X-ray spectroscopy (SEM-EDX) was conducted using the TESCAN LYRA3 field-emission SEM with Oxford X-Max detectors for EDX. UV-initiated ZIPH samples were spin-coated at 2000 RPM for 10 seconds. An accelerating voltage of 4 kV was used to locate and analyze the samples.

Raman spectroscopy was conducted using the HORIBA LabRAM HR Evolution Confocal Raman Microscope. Thermally initiated ZIPH and PEDOT:PSS hydrogels were sealed between a glass slide and coverslip to prevent dehydration during measurement. An objective magnification of 10x was used to focus the 532 nm laser beam on the sample. The scattered light was analyzed using a grating of 600 lines/mm (Fig. 2.5).

2.4.10 Static water contact angle measurement

Measurements were taken using the KRÜSS DSA100 Drop Shape Analyzer. Each measurement was taken using ultrapure DI water from Milli-Q®, and the dispensed volume was below 10 µL to minimize the influence of gravity on the contact angle. The dispensing rate was 2.67 µL/min. The contact angles were measured from +2° tilt and calculated using elliptical fit approximation.

Dry films of the PEDOT:PSS hydrogel control was prepared by, first, incubating a piece of silicon treated with O2 plasma in APTES (2% in ethanol) for 1 hour. Then, HPU (4% in 95/5 ethanol/water) was spin coated as an adhesion layer at 3000 RPM, baked at 90 °C for a minute, and treated with O_2 plasma. On top of the HPU, PEDOT:PSS (16 v/v% DMSO, 10 mg/mL EMIM OTf) was spin coated at 2000 RPM. Immediately, the PEDOT:PSS film was placed in a partially sealed, humidified container and heated to 90 °C for 5 minutes. Thereafter, the film was baked for 90°C in open air for a minute, rinsed thoroughly with DI H2O, blow dried, and baked again at 90°C for a minute. For the preparation of the PSS film, PGMA (5 mg/mL in 19:1 $CHCl_3$:chlorobenzene) was spin coated on O_2 plasma treated

silicon at 2000 RPM and baked at 120 °C for 30 minutes. The silicon was thoroughly rinsed with CHCl3 and blow dried. Next, PSS (200 kDa, 12% in 4:1 H2O:IPA) was spin coated at 2000 RPM, baked at 120 °C for 30 minutes, thoroughly rinsed with DI H_2O, and blow driesd. For the preparation of the PEDOT control, SEBS (10 mg/mL in toluene) was spin coated at 1000 RPM on a piece of O_2 plasma treated silicon and baked at 120°C to serve as the adhesion layer. Then, a pre-sonicated mixture of PEDOT-TMA and HMPP (0.05 wt%) was spin coated at 500 RPM for 15 seconds, followed by 1500 RPM for 30 seconds. The film was baked for a minute at 120°C, exposed to UV irradiation (365 nm wavelength, 4 mW/cm^2) for 3 minutes, and baked at 180°C for 10 minutes. The PEDOT-TMA spin coating step to the 180 °C bake step was repeated 3 more times to ensure full coverage of the substrate underneath.

2.4.11 In vitro protein adsorption test

Human plasma adsorption on the hydrogels was evaluated using the 3-(4-Carboxybenzoyl)quinoline-2-carboxaldehyde (CBQCA) assay and bicinchoninic acid (BCA) assay. Hydrogel samples (5 mm in diameter and 1 mm in thickness) were incubated in 150 µL of human plasma (Innovative Research, Inc.) in 48-well plates at 37°C for 2 hours. The hydrogels were washed with 1 mL of PBS 5 times and transferred to 96-well U-bottom plates. 150 µL of 1% SDS-PBS solution was added and shaken for 1 hours. 75 µL of the protein-SDS solution was transferred to 96-well flat bottom plates and diluted with 60 µL of PBS. Then, CBQCA assay was directly carried out to determine the relative amount of proteins adsorbed on the hydrogels. The fluorescence intensities at 550 nm (excitation/emission of 465/550 nm) were recorded using the TECAN Inifinite M200 Pro plate reader. For the BCA assay, 30 µL of the protein-SDS solution was transferred to 96-well flat-bottom plates and standard BCA procedures were applied. The absorbance at 562 nm was recorded using the TECAN Inifinite M200 Pro plate reader.

2.4.12 Cytotoxicity assay

NIH-3T3 fibroblasts were cultured in DMEM medium (Gibco) supplemented with 10% fetal bovine serum (FBS, Gibco) and 1% penicillin/streptomycin (Gibco). Cytotoxicity of the hydrogels was determined by directly culturing fibroblasts on the hydrogels and using the LIVE/DEAD Viability Cytotoxicity Kit (Invitrogen). Hydrogel discs (5 mm in diameter and 1 mm in thickness) in 96-well flat bottom plates were pre-conditioned in 200 µL DMEM, and cells were directly seeded at a density of 1300 cells per well. After 96 hours, 5 µL of SDS solution (2 wt%) per 100 µL media were added to half of the wells and incubated at room temperature for 10 minutes to establish dead controls. 100 µL of working solution (4 µM calcein AM and 4 µM ethidium homodimer) was added to the experimental wells, and 100 µL of calcein AM solution (4 µM) or ethidium homodimer solution (4 µM) was added to the dead control wells. The cells were incubated at room temperature for 45 minutes and immediately evaluated (LIVE: 494/517 nm, DEAD: 528/617 nm) using the TECAN Infinite M200 Pro plate reader.

2.4.13 Implantation surgeries

6- to 8-week-old male C57BL/6 mice were purchased from Jackson Laboratories. Preoperatively, all mice received subcutaneous injections of 5 mg/kg of Meloxicam for pre-surgery analgesia. All mice were anesthetized using 2-4% isoflurane in oxygen, and the backs of all mice were shaved. All mice received eye lubricants to prevent dehydration-induced blindness. Then, the shaved backs of all mice were sterilized by scrubbing with betadine and alcohol pads in an alternating fashion, repeated two times.

Implantation of discs. Two longitudinal incisions, 1 cm in length, were made in the upper and lower backs. The blade tips of a pair of scissors were inserted into the subcutaneous space through the incisions, and two subcutaneous pockets, flanking each incision, were made via blunt tissue dissection using the blunt sides of a pair of scissors. Two implants (5 mm in

diameter and 1 mm in thickness) were inserted in the subcutaneous pockets on both sides of each incision, towards the limbs of the mice, for a total of four implants per mouse. For sham control, subcutaneous pockets were made but no implants were placed. The incisions were closed via wound clips. Following surgery, all mice were given subcutaneous injections of 5 mg/kg of Meloxicam once every 24 hours for two days. Wound clips were removed after 10 days.

2.4.14 Histological processing, staining, and analysis

After 1-, 4-, or 12-weeks post-implantation, all mice were euthanized by CO2 asphyxiation, followed by cervical dislocation. Afterward, the backs of all the mice were shaved. The implants and the surrounding tissues were explanted and fixed in 10% neutral buffered formalin for 24 hours. After fixation, the implants and tissues were transferred to 70% ethanol. The materials were then paraffin-embedded, sectioned (5 µm), and stained for H&E using standard procedures by the Human Tissue Resource Center at the University of Chicago. Masson's trichrome staining (MTS) was carried out in-house using standard procedures. Whole-section scans of H&E and MTS-stained tissue sections were conducted using the Olympus VS200 Slideview Slide Scanner.

ImageJ software was used to analyze the collagen density and thickness of the fibrotic capsule from MTS-stained sections. Fibrotic capsules were measured at approximately the first, second, and third quarters along the length of the widths of two halves of the implant facing the dermis, for a maximum of six measurements per biological replicate. Care was taken to omit the basement membrane, upon which the panniculus carnosus sits, from the analysis. Three to six technical replicate measurements were taken per biological replicate, depending on the quality of the tissue section. For locations where artifacts prevented accurate measurements, the measurement was either not made for the location or was taken instead at the nearest location without artifact obstruction. For collagen density calcula-

tions, the blue pixel brightness was measured with 100 µm wide slices from the surface of the implant to a distance of at least 80 µm as a function of the distance away from the surface of the implant. The technical replicate values at corresponding distances were averaged within the same biological replicate. Subsequently, from the same biological replicate, the data points within each 5 µm increment moving away from the surface of the implant were averaged to obtain pixel brightness values every 5 µm. The pixel brightness values were normalized with respect to the maximum possible pixel brightness value of 255. For measuring the thickness, layers formed only from cells were omitted from the measurements. Technical replicates were averaged to obtain individual biological replicates.

2.4.15 Immunofluorescence

Materials were fixed, embedded, and sectioned as described above. Tissue sections were deparaffinized in xylene and rehydrated using an ethanol-to-water gradient. Antigen retrieval was conducted in citrate buffer (pH 5) for 45 minutes at 55°C. Samples were then rinsed in water, permeabilized by incubating in 10% DMSO in PBS for 5 minutes, washed in PBS-tween 20 (PBS-T), and rinsed in water again. Thereafter, the samples were blocked for 1 hour using a 1% bovine serum albumin (BSA) solution. The blocking buffer was removed, and the sections were incubated in either the macrophage panel or fibrosis panel antibodies overnight at 4°C. The macrophage panel antibodies included: rat anti-mouse F4/80 (1:100 dilution, Abcam, Cat. #ab6640), rabbit anti-mouse CD86 (1:200 dilution, Biorbyt, Cat. #orb49101), and goat anti-mouse CD206 (1:100 dilution, R&D Systems, Cat. #AF2535). The fibrosis panel antibodies included: rat anti-mouse F4/80 (1:100 dilution, Abcam, Cat. #ab6640), rabbit anti-mouse collagen I (1:100 dilution, Bio-Rad, Cat. #2150-1410), and goat anti-mouse αSMA (1:100 dilution, Novus Biologicals, Cat. #NB300-978). The next day, the sections were washed twice in PBS-T and once in PBS. The washed sections were incubated for 2 hours at room temperature in a secondary antibody cocktail,

consisting of donkey anti-rat IgG AlexaFluor 647 (1:200 dilution, Southern Biotech, Cat. #OB643031), donkey anti-rabbit IgG AlexaFluor 488 (1:500 dilution, Fisher Scientific, Cat. #A21206), and donkey anti-goat IgG AlexaFluor 555 (1:500 dilution, Fisher Scientific, Cat. #A21432). Afterward, the sections were washed twice with PBS-T and once with PBS. The washed sections were counterstained with 4',6-diamidino-2-phenylindole (DAPI, 1:1000 dilution, Thermo Scientific) for 2 minutes and washed with PBS. Prolong Antifade Gold mounting medium (Invitrogen) was added, and the sections were sealed with coverslips and nail polish. Images were acquired using either Zeiss Axiovert 200m inverted epifluorescence microscope with a Hamamatsu Flash 4.0 camera run by SlideBook 6.0 software (Intelligent Imaging Innovations). Background fluorescence was determined by tissue sections stained only with secondary antibodies and with no primary antibodies.

2.4.16 Cytokine analysis

Cytokine quantifications were performed using a 14-cytokine LegendPlex custom panel (BioLegend). After 1- or 4-weeks post-implantation, all mice were euthanized by CO_2 asphyxiation, followed by cervical dislocation. Afterward, the backs of all the mice were shaved. The explanted implant and associated tissues were frozen immediately on dry ice and stored in a -80°C freezer for later use. The frozen tissues were thawed at room temperature and minced with scissors. The minced implants and tissues were transferred to lysis matrix tubes (MP Biomedicals) with 300 µL of T-PER solution (Thermo Scientific), consisting of 5 mM EDTA and protease inhibitor (Thermo Scientific). Three cycles of homogenization were conducted on the FastPrep-24 5G homogenizer (MP Biomedicals) with three minutes on ice between cycles. Subsequently, the tubes were centrifuged for 20 minutes at 10,000 g's at 4°C, after which a fat layer, a protein layer, and a debris layer formed. Avoiding the fat layer, the protein layer was transferred to low-bind tubes (Fisher Scientific) and centrifuged again for 10 minutes at 10,000 g's at 4°C. Similar to the first centrifugation step, the protein layer

was transferred to fresh low-bind tubes. The centrifugation and protein layer transfer step were conducted once more. The protein solutions were stored in a -80°C freezer for future analysis. The protein solutions were thawed at room temperature, and LegendPlex assay was conducted using the un-diluted protein solutions, following manufacturer's protocol on the Agilent Penteon 5-30 flow cytometer. A C3a ELISA kit (Novus Biologicals), a decorin ELISA kit (R&D Systems), and an endostatin ELISA kit (Abcam) were used following manufacturer's instructions. The protein solution was diluted 20-fold in PBS for C3a ELISA, 5000-fold for decorin ELISA, and 1000-fold for endostatin ELISA. The absorbancees for the ELISAs were recorded at a wavelength of 450 nm using the TECAN Inifinte M200 Pro plate reader.

2.4.17 Flow cytometry

After 1- or 4-weeks post-implantation, all mice were euthanized by CO2 asphyxiation, followed by cervical dislocation. The backs of all the mice were shaved, and subsequently, a depilatory cream was applied for one minute. Afterward, the cream and the hair were washed off with water and 70% ethanol. Approximately 2 cm^2 of skin, including the implant, was extracted from the back and placed on ice. The implants and associated tissues were finely minced with scissors and digested by adding 200 µL of RPMI-1640 (Sigma), supplemented with Liberase TL (0.5 mg/mL, Roche) and DNase I (0.5 mg/mL, Grade II, Roche). The samples were shaken for 90 minutes at 37°C. Immediately, 200 µL of ice-cold dissociation buffer (1x PBS, 10 mM EDTA, 2% FBS) were added to halt digestion. The digested tissues were pestled through 70-µm cell strainers (Fisher Scientific) and rinsed with 2 mL of ice-cold dissociation buffer. Then, the washed digested tissues were centrifuged for 8 minutes at 400 g's at 4°C and resuspended in 200 µL of FACS buffer (eBiosciences). The enriched single-cell suspension was transferred to 96-well U-bottom plates, centrifuged, and resuspended in 200 µL of FACS buffer another time.

Aliquots of the single-cell suspension were then stained with propidium iodide (1:200 dilution, BD Bioscences) and counted on an Agilent Penteon 5-30 flow cytometer. Subsequently, 106¬ cells were incubated in LIVE/DEAD Fixable Blue Dead Cell Stain Kit (1:500 dilution, Invitrogen) for 20 minutes on ice followed by washing with FACS buffer. The cells were treated with Fc block (1:50 dilution, TruStain FcX Plus, BioLegend) for 10 minutes on ice followed by washing with FACS buffer. Then, the cells were stained with the flow cytometry panel shown below. The cells were stained with CCR2 at 37 °C for 1 hour, and the cell surface stains were carried out on ice for 20 minutes. The cells were fixed with Cytofix/Cytoperm buffer (BD Bioscences), intracellular stains were carried out at room temperature, and run on the Cytek Aurora flow cytometer the next day. All analyses were performed in FlowJo Flow Cytometry Analysis Software (Treestar) using the gating strategy shown in Figure A.5. PE was used as the exclusionary channel for CD31, Tie-2, Ter-119, and Ep-CAM, which are collectively abbreviated as Lin. Macrophages were defined as $CD45^{+}$ $CD11b^{+}$ $Ly\text{-}6G^{-}$ $Ly\text{-}6C^{-/lo}$ $F4/80^{hi}$, monocytes were defined as $CD45^{+}$ $CD11b^{+}$ $Ly\text{-}6G^{-}$ $Ly\text{-}6C^{hi}$ $F4/80^{lo}$, neutrophils were defined as $CD45^{+}$ $CD11b^{+}$ $Ly\text{-}6G^{+}$, T cells were defined as $CD45^{+}$ $CD3^{+}$, and fibroblasts were defined as $CD45^{-}$ Lin^{-} $CD140a^{+}$.

2.4.18 Nanostring analysis

Gene expression was evaluated using a custom-built multiplexed 50-gene FBR panel (NanoString Technologies). After 4-weeks post-implantation, all mice were euthanized by CO2 asphyxiation, followed by cervical dislocation. Afterward, the backs of all the mice were shaved. The explanted material and associated tissues were soaked in RNAlater solution (Invitrogen) overnight at 4 °C. The next day, the excess RNAlater solution was discarded, and the tissue samples were stored at -80 °C. For RNA isolation, the tissues were thawed, finely diced, and 600 µL of Trizol reagent (Invitrogen) with 10 µL/mL of 2-mercaptoethanol was added to approximately 100 mg of tissue. The tissues were mechanically ground down

and incubated for 5 minutes at room temperature. After the addition of 120 µL of chloroform, the tube was shaken vigorously for 15 seconds and incubated for 2 minutes at room temperature. The tubes were centrifuged at 12,000 xg for 15 minutes at 4°C. 350 µL of the aqueous phase was transferred to columns from the RNeasy mini kit (Qiagen), and the RNA isolation was completed using the manufacturer's instructions. All samples were checked for a 260/280 ratio of 2 before proceeding to further steps. 100 ng of RNA was processed according to NanoString manufacturer protocols, and RNA levels (absolute copy numbers) were obtained via nCounter (NanoString Technologies). Group samples were analyzed using nSolver analysis software (NanoString Technologies). *GUSB*, *ACTB*, *B2M*, and *TBP* were used as reference genes.

2.5 References

1. Jansen, L. E. *et al.* Zwitterionic PEG-PC Hydrogels Modulate the Foreign Body Response in a Modulus-Dependent Manner. *Biomacromolecules* **19,** 2880–2888. ISSN: 1525-7797. (2026) (July 2018).
2. Carnicer-Lombarte, A. *et al. Foreign body reaction is triggered in vivo by cellular mechanosensing of implants stiffer than host tissue* en. Pages: 829648 Section: New Results. Dec. 2022. (2026).
3. Zhang, D. *et al.* Dealing with the Foreign-Body Response to Implanted Biomaterials: Strategies and Applications of New Materials. en. *Advanced Functional Materials* **31,** 2007226. ISSN: 1616-3028. (2026) (2021).
4. Vegas, A. J. *et al.* Combinatorial hydrogel library enables identification of materials that mitigate the foreign body response in primates. en. *Nature Biotechnology* **34,** 345–352. ISSN: 1546-1696. (2026) (Mar. 2016).
5. Xie, X. *et al.* Reduction of measurement noise in a continuous glucose monitor by coating the sensor with a zwitterionic polymer. en. *Nature Biomedical Engineering* **2,** 894–906. ISSN: 2157-846X. (2026) (Dec. 2018).
6. Wu, J. *et al.* Adhesive anti-fibrotic interfaces on diverse organs. en. *Nature* **630,** 360–367. ISSN: 1476-4687. (2026) (June 2024).
7. Deng, J. *et al.* A bioadhesive pacing lead for atraumatic cardiac monitoring and stimulation in rodent and porcine models. *Science Translational Medicine* **16,** eado9003. (2026) (June 2024).
8. Hasselgren, P.-O. Glucocorticoids and muscle catabolism. en-US. *Current Opinion in Clinical Nutrition & Metabolic Care* **2,** 201. ISSN: 1363-1950. (2026) (May 1999).
9. Schakman, O., Kalista, S., Barbé, C., Loumaye, A. & Thissen, J. P. Glucocorticoid-induced skeletal muscle atrophy. *The International Journal of Biochemistry & Cell Biology. Molecular Basis of Muscle Wasting* **45,** 2163–2172. ISSN: 1357-2725. (2026) (Oct. 2013).
10. Zani, F. *et al.* Sterilization of corticosteroids for ocular and pulmonary delivery with supercritical carbon dioxide. *International Journal of Pharmaceutics* **450,** 218–224. ISSN: 0378-5173. (2026) (June 2013).
11. Matter, B. *et al.* Dexamethasone Degradation in Aqueous Medium and Implications for Correction of In Vitro Release from Sustained Release Delivery Systems. en. *AAPS PharmSciTech* **20,** 320. ISSN: 1530-9932. (2026) (Oct. 2019).
12. Jiang, S. & Cao, Z. Ultralow-Fouling, Functionalizable, and Hydrolyzable Zwitterionic Materials and Their Derivatives for Biological Applications. en. *Advanced Materials* **22,** 920–932. ISSN: 1521-4095. (2026) (2010).
13. Dong, D. *et al.* High-strength and fibrous capsule–resistant zwitterionic elastomers. *Science Advances* **7,** eabc5442. (2026) (Jan. 2021).

14. Zhang, L. *et al.* Zwitterionic hydrogels implanted in mice resist the foreign-body reaction. en. *Nature Biotechnology* **31,** 553–556. ISSN: 1546-1696. (2026) (June 2013).

15. Ishihara, K. Biomimetic materials based on zwitterionic polymers toward human-friendly medical devices. *Science and Technology of Advanced Materials* **23,** 498–524. ISSN: 1468-6996. (2026) (Dec. 2022).

16. Keiler, J. *et al.* Neointimal fibrotic lead encapsulation – Clinical challenges and demands for implantable cardiac electronic devices. *Journal of Cardiology. Topics in implantable medical devices* **70,** 7–17. ISSN: 0914-5087. (2026) (July 2017).

17. McClatchey, P. M. *et al.* Fibrotic Encapsulation Is the Dominant Source of Continuous Glucose Monitor Delays. *Diabetes* **68,** 1892–1901. ISSN: 0012-1797. (2026) (Aug. 2019).

18. Wrzeszcz, A. *et al.* Hydrogel coated and dexamethasone releasing cochlear implants: Quantification of fibrosis in guinea pigs and evaluation of insertion forces in a human cochlea model. en. *Journal of Biomedical Materials Research Part B: Applied Biomaterials* **103,** 169–178. ISSN: 1552-4981. (2026) (2015).

19. Lacour, S. P., Courtine, G. & Guck, J. Materials and technologies for soft implantable neuroprostheses. en. *Nature Reviews Materials* **1,** 16063. ISSN: 2058-8437. (2026) (Sept. 2016).

20. Inal, S., Rivnay, J., Suiu, A.-O., Malliaras, G. G. & McCulloch, I. Conjugated Polymers in Bioelectronics. *Accounts of Chemical Research* **51,** 1368–1376. ISSN: 0001-4842. (2026) (June 2018).

21. Kayser, L. V. & Lipomi, D. J. Stretchable Conductive Polymers and Composites Based on PEDOT and PEDOT:PSS. en. *Advanced Materials* **31,** 1806133. ISSN: 1521-4095. (2026) (2019).

22. Rivnay, J. *et al.* Structural control of mixed ionic and electronic transport in conducting polymers. en. *Nature Communications* **7,** 11287. ISSN: 2041-1723. (2026) (Apr. 2016).

23. Khodagholy, D. *et al.* NeuroGrid: recording action potentials from the surface of the brain. en. *Nature Neuroscience* **18,** 310–315. ISSN: 1546-1726. (2026) (Feb. 2015).

24. Liu, Y. *et al.* Soft and elastic hydrogel-based microelectronics for localized low-voltage neuromodulation. en. *Nature Biomedical Engineering* **3,** 58–68. ISSN: 2157-846X. (2026) (Jan. 2019).

25. Jiang, Y. *et al.* Topological supramolecular network enabled high-conductivity, stretchable organic bioelectronics. *Science* **375,** 1411–1417. (2026) (Mar. 2022).

26. Song, Y. *et al.* Wireless battery-free wearable sweat sensor powered by human motion. *Science Advances* **6,** eaay9842. (2026) (Sept. 2020).

27. Saraf, N., Woods, E. R., Peppler, M. & Seal, S. Highly selective aptamer based organic electrochemical biosensor with pico-level detection. *Biosensors and Bioelectronics* **117,** 40–46. ISSN: 0956-5663. (2026) (Oct. 2018).

28. Yang, M. *et al.* Robust Neural Interfaces with Photopatternable, Bioadhesive, and Highly Conductive Hydrogels for Stable Chronic Neuromodulation. *ACS Nano* **17,** 885–895. ISSN: 1936-0851. (2026) (Jan. 2023).

29. Wang, X. *et al.* Bioadhesive and conductive hydrogel-integrated brain-machine interfaces for conformal and immune-evasive contact with brain tissue. English. *Matter* **5,** 1204–1223. ISSN: 2590-2393, 2590-2385. (2026) (Apr. 2022).

30. Liu, Y. *et al.* Morphing electronics enable neuromodulation in growing tissue. en. *Nature Biotechnology* **38,** 1031–1036. ISSN: 1546-1696. (2026) (Sept. 2020).

31. Zhou, T. *et al.* 3D printable high-performance conducting polymer hydrogel for all-hydrogel bioelectronic interfaces. en. *Nature Materials* **22,** 895–902. ISSN: 1476-4660. (2026) (July 2023).

32. Khatib, M. *et al.* High-density soft bioelectronic fibres for multimodal sensing and stimulation. en. *Nature* **645,** 656–664. ISSN: 1476-4687. (2026) (Sept. 2025).

33. Martin, K. E. & García, A. J. Macrophage phenotypes in tissue repair and the foreign body response: Implications for biomaterial-based regenerative medicine strategies. *Acta Biomaterialia. Immunomodulatory Biomaterials* **133,** 4–16. ISSN: 1742-7061. (2026) (Oct. 2021).

34. Jones, J. A. *et al.* Proteomic analysis and quantification of cytokines and chemokines from biomaterial surface-adherent macrophages and foreign body giant cells. en. *Journal of Biomedical Materials Research Part A* **83A.** _eprint: https://onlinelibrary.wiley.com/doi/pdf/10.1002/jbm.a.31221, 585–596. ISSN: 1552-4965. (2026) (2007).

35. Anderson, J. M. & Jones, J. A. Phenotypic dichotomies in the foreign body reaction. *Biomaterials. Festschrift honouring Professor David F. Williams* **28,** 5114–5120. ISSN: 0142-9612. (2026) (Dec. 2007).

36. Saleh, L. S. *et al.* Mapping Macrophage Polarization and Origin during the Progression of the Foreign Body Response to a Poly(ethylene glycol) Hydrogel Implant. en. *Advanced Healthcare Materials* **11,** 2102209. ISSN: 2192-2659. (2026) (2022).

37. Shi, H., Liu, C., Jiang, Q. & Xu, J. Effective Approaches to Improve the Electrical Conductivity of PEDOT:PSS: A Review. en. *Advanced Electronic Materials* **1,** 1500017. ISSN: 2199-160X. (2026) (2015).

38. Klopfleisch, R. & Jung, F. The pathology of the foreign body reaction against biomaterials. en. *Journal of Biomedical Materials Research Part A* **105,** 927–940. ISSN: 1552-4965. (2026) (2017).

39. Chen, X. *et al.* Ordered adsorption of coagulation factor XII on negatively charged polymer surfaces probed by sum frequency generation vibrational spectroscopy. en. *Analytical and Bioanalytical Chemistry* **388,** 65–72. ISSN: 1618-2650. (2026) (May 2007).

40. Sanders, J. E. *et al.* Relative influence of polymer fiber diameter and surface charge on fibrous capsule thickness and vessel density for single-fiber implants. en. *Journal of Biomedical Materials Research Part A* **65A.** _eprint: https://onlinelibrary.wiley.com/doi/pdf/10.1002/jbm.a.10525, 462–467. ISSN: 1552-4965. (2026) (2003).

41. Gessner, A., Lieske, A., Paulke, B.-R. & Müller, R. H. Functional groups on polystyrene model nanoparticles: Influence on protein adsorption. en. *Journal of Biomedical Materials Research Part A* **65A,** 319–326. ISSN: 1552-4965. (2026) (2003).

42. Chen, Y. & Luo, S.-C. Synergistic Effects of Ions and Surface Potentials on Antifouling Poly(3,4-ethylenedioxythiophene): Comparison of Oligo(Ethylene Glycol) and Phosphorylcholine. *Langmuir* **35,** 1199–1210. ISSN: 0743-7463. (2026) (Feb. 2019).

43. Mukherjee, S. *et al.* Screening hydrogels for antifibrotic properties by implanting cellularly barcoded alginates in mice and a non-human primate. en. *Nature Biomedical Engineering* **7,** 867–886. ISSN: 2157-846X. (2026) (July 2023).

44. Li, N. *et al.* Immune-compatible designs of semiconducting polymers for bioelectronics with suppressed foreign-body response. en. *Nature Materials* **25,** 124–132. ISSN: 1476-4660. (2026) (Jan. 2026).

45. Xiang, Y. *et al.* A Zwitterionic Conductive Hydrogel Interface for Enhanced Electrocorticography Signal Fidelity via High Conductivity, Antifouling, and Brain-Matched Mechanics. *Biomacromolecules* **26,** 7959–7973. ISSN: 1525-7797. (2026) (Nov. 2025).

46. Chen, S. *et al.* Characterization of Topographical Effects on Macrophage Behavior in a Foreign Body Response Model. *Biomaterials* **31,** 3479–3491. ISSN: 0142-9612. (2026) (May 2010).

47. Crispin, X. *et al.* The Origin of the High Conductivity of Poly(3,4-ethylenedioxythiophene)-Poly(styrenesulfonate) (PEDOT-PSS) Plastic Electrodes. *Chemistry of Materials* **18,** 4354–4360. ISSN: 0897-4756. (2026) (Sept. 2006).

48. Xia, Y., Zhang, H. & Ouyang, J. Highly conductive PEDOT:PSS films prepared through a treatment with zwitterions and their application in polymer photovoltaic cells. en. *Journal of Materials Chemistry* **20,** 9740–9747. ISSN: 1364-5501. (2026) (Nov. 2010).

49. Zhao, W. *et al.* A comprehensive study and comparison of four types of zwitterionic hydrogels. en. *Journal of Materials Science* **53,** 13813–13825. ISSN: 1573-4803. (2026) (Oct. 2018).

50. Anderson, J. M., Rodriguez, A. & Chang, D. T. Foreign body reaction to biomaterials. *Seminars in Immunology. Innate and Adaptive Immune Responses in Tissue Engineering* **20,** 86–100. ISSN: 1044-5323. (2026) (Apr. 2008).

51. Witherel, C. E., Abebayehu, D., Barker, T. H. & Spiller, K. L. Macrophage and Fibroblast Interactions in Biomaterial-Mediated Fibrosis. en. *Advanced Healthcare Materials* **8,** 1801451. ISSN: 2192-2659. (2026) (2019).

52. Klopfleisch, R. Macrophage reaction against biomaterials in the mouse model – Phenotypes, functions and markers. *Acta Biomaterialia* **43,** 3–13. ISSN: 1742-7061. (2026) (Oct. 2016).

53. Ferrara, N. Vascular Endothelial Growth Factor: Basic Science and Clinical Progress. *Endocrine Reviews* **25,** 581–611. ISSN: 0163-769X. (2026) (Aug. 2004).

54. Hong, K. H., Ryu, J. & Han, K. H. Monocyte chemoattractant protein-1–induced angiogenesis is mediated by vascular endothelial growth factor-A. *Blood* **105,** 1405–1407. ISSN: 0006-4971. (2026) (Feb. 2005).

55. Barrientos, S., Stojadinovic, O., Golinko, M. S., Brem, H. & Tomic-Canic, M. PERSPECTIVE ARTICLE: Growth factors and cytokines in wound healing. en. *Wound Repair and Regeneration* **16,** 585–601. ISSN: 1524-475X. (2026) (2008).

56. Goda, T., Ishihara, K. & Miyahara, Y. Critical update on 2-methacryloyloxyethyl phosphorylcholine (MPC) polymer science. en. *Journal of Applied Polymer Science* **132.** _eprint: https://onlinelibrary.wiley.com/doi/pdf/10.1002/app.41766. ISSN: 1097-4628. (2026) (2015).

57. Murakami, Y., Iwata, H., Kitano, E., Kitamura, H. & Ikada, Y. Interaction of poly(styrene sulfonic acid) with the alternative pathway of the serum complement system. *Journal of Biomaterials Science, Polymer Edition* **16.** _eprint: https://doi.org/10.1163/1568562053654095, 381–395. ISSN: 0920-5063. (2026) (Jan. 2005).

58. Murakami, Y., Iwata, H., Kitano, E., Kitamura, H. & Ikada, Y. Interaction of poly(styrene sulfonic acid) with the classical pathway of the serum complement system. *Journal of Biomaterials Science, Polymer Edition* **16.** _eprint: https://doi.org/10.1163/1568562053992469, 685–697. ISSN: 0920-5063. (2026) (Jan. 2005).

59. Wynn, T. Cellular and molecular mechanisms of fibrosis. en. *The Journal of Pathology* **214,** 199–210. ISSN: 1096-9896. (2026) (2008).

60. Gowdy, K. M. *et al.* Protective Role of T-bet and Th1 Cytokines in Pulmonary Graft-versus-Host Disease and Peribronchiolar Fibrosis. *American Journal of Respiratory Cell and Molecular Biology* **46,** 249–256. ISSN: 1044-1549. (2026) (Feb. 2012).

61. Lakos, G., Melichian, D., Wu, M. & Varga, J. Increased Bleomycin-Induced Skin Fibrosis in Mice Lacking the Th1-Specific Transcription Factor T-bet. *Pathobiology* **73,** 224–237. ISSN: 1015-2008. (2026) (Feb. 2007).

62. Barron, L. & Wynn, T. A. Fibrosis is regulated by Th2 and Th17 responses and by dynamic interactions between fibroblasts and macrophages. *American Journal of Physiology - Gastrointestinal and Liver Physiology* **300,** G723–G728. ISSN: 0193-1857. (2026) (May 2011).

63. Gieseck, R. L., Wilson, M. S. & Wynn, T. A. Type 2 immunity in tissue repair and fibrosis. en. *Nature Reviews Immunology* **18,** 62–76. ISSN: 1474-1741. (2026) (Jan. 2018).

64. Chung, L. *et al.* Interleukin 17 and senescent cells regulate the foreign body response to synthetic material implants in mice and humans. *Science Translational Medicine* **12,** eaax3799. (2026) (Apr. 2020).

65. Seki, E. *et al.* CCR2 promotes hepatic fibrosis in mice#. en-US. *Hepatology* **50,** 185. ISSN: 0270-9139. (2026) (July 2009).

66. Milara, J. *et al.* Sphingosine-1-phosphate is increased in patients with idiopathic pulmonary fibrosis and mediates epithelial to mesenchymal transition. en. *Thorax* **67,** 147–156. ISSN: 0040-6376, 1468-3296. (2026) (Feb. 2012).

67. Liu, T. *et al.* FIZZ1 Stimulation of Myofibroblast Differentiation. *The American Journal of Pathology* **164,** 1315–1326. ISSN: 0002-9440. (2026) (Apr. 2004).

68. Acharya, P. S., Zukas, A., Chandan, V., Katzenstein, A.-L. A. & Puré, E. Fibroblast activation protein: a serine protease expressed at the remodeling interface in idiopathic pulmonary fibrosis. *Human Pathology* **37,** 352–360. ISSN: 0046-8177. (2026) (Mar. 2006).

69. Van der Slot, A. J. *et al.* Identification of *PLOD2* as Telopeptide Lysyl Hydroxylase, an Important Enzyme in Fibrosis*. *Journal of Biological Chemistry* **278,** 40967–40972. ISSN: 0021-9258. (2026) (Oct. 2003).

70. Noskovicova, N., Hinz, B. & Pakshir, P. Implant Fibrosis and the Underappreciated Role of Myofibroblasts in the Foreign Body Reaction. en. *Cells* **10,** 1794. ISSN: 2073-4409. (2026) (July 2021).

CHAPTER 3

SUPPRESSED FOREIGN BODY RESPONSE TO ZWITTERIONIC PEDOT:PSS HYDROGEL ENABLE LOW SIGNAL-LOSS CHRONIC ELECTROPHYSIOLOGICAL RECORDINGS

3.1 Introduction

In the previous chapter, the material properties, the material structure, the extent of FBR-induced fibrosis, and the biological response to zwitterionic PEDOT:PSS hydrogel (ZIPH-3c) was thoroughly characterized. However, for demonstrating practical applicability and the benefits of suppressing the FBR, it is essential to test ZIPH-3c in an implantable device. In order to do so, we must choose a device type that can give us un-ambiguous performance metrics. Since ZIPH-3c is an electrically conductive material, electrophysiological devices are ideal. Out of the many types of electrophysiological devices, we chose electrocardiography (ECG) because of three reasons. First, signals from passive recording processes most accurately reflects the change in interfacial impedance caused by insulating fibrotic capsules. In contrast, active recording and stimulation processes involve the application of external power, which does not reflect the intrinsic insulating effects of the fibrotic capsule. Second, ECG provides consistent, reliable signals, making comparisons between devices more reliable[1]. Third, ECG electrodes can be implanted subcutaneously, which most closely reflects the subcutaneous implantation model that was used to collect all the biological data in the previous chapter.

The design of the ECG electrode needed to un-ambiguously show the benefits of suppressing the FBR. This means that confounding effects need to be eliminated as much as possible. There are three main criteria for this. First, the electrode needs to have intimate,

conformal contact with tissue. Instability of the electrode-tissue interface can degrade the signal. Second, the adhesion of the PEDOT:PSS-based material needs to be robust enough to survive the implantation period. Delamination and damage to the electronic material can also lead to signal loss and expose the substrate which can alter the results. Third, the exposed surface area of the PEDOT:PSS-based material needs to be equal to or greater than the surface area of one side of the disc implant used in the previous chapter. This is because it is currently unknown at what length scale nearby materials can start to effect the FBR, especially in a device in which it is often unavoidable to have multiple types of material adjacent to each other, and it is unclear if the surface area can be a confounding factor.

The third criterion rules out designs that encapsulate a large portion of the PEDOT:PSS-based material for stable adhesion since the exposed surface area is too small[2–5]. The methods reported to fulfill the second criterion are not compatible with the preparation and fabrication process of ZIPH-3c devices. PEDOT:PSS is often electrodeposited on metal electrodes, but this requires changing the formulation of the ZIPH-3c precursor solution[6–8]. (3-glycidyloxypropyl)trimethoxysilane (GOPS) is a popular option to crosslink PEDOT:PSS and achieve stable adhesion of PEDOT:PSS on a variety of substrates, but this requires adding GOPS to the ZIPH-3c precursor solution[9,10]. Another reported method is to use hydrophilic polyurethane (HPU) as the adhesion layer for PEDOT:PSS[11], but HPU is soluble in the solvents used in the solvent annealing process for ZIPH-3c.

Out of the three listed criteria for the design of the ECG electrode, achieving robust adhesion is by far the biggest challenge, especially combined with the criterion of a relatively large exposed area of the PEDOT:PSS-based material. ZIPH-3c is highly hydrophilic and naturally has bad adhesion on all conventional electronic substrates, especially under aqueous conditions. To overcome this challenge, we report a polymeric multilayer (PML) strategy, consisting of poly(glycidyl methacrylate) (PGMA) and polyallylamine (PAH), for introducing a high density of surface primary amines for high density surface functionalization. This

enabled robust adhesion of ZIPH-3c on a variety of substrates.

With the new polymeric multilayer strategy, ZIPH-3c ECG electrodes were used to obtain chronic ECG recordings in mice over a 12-week period. The recordings were compared to those obtained from PEDOT:PSS ECG electrodes and PEDOT:PSS electrodes with dexamethasone-eluting PDMS backings (PEDOT:PSS-Dex). The results clearly show that ZIPH-3c electrodes have much less signal degradation than PEDOT:PSS electrodes over a 12-week period, have comparable signal degradation compared to PEDOT:PSS-Dex electrodes, and lead to no side effects that is seen in mice implanted with PEDOT:PSS-Dex electrodes.

3.2 Results and Discussions

3.2.1 Design and fabrication of electrocardiographic electrodes

Several adhesion strategies were attempted, including benzophenone treated elastomers[12] and substrates with GOPS surface functionalization[13]. However, the hydrophilicity and sensitivity to changes in water content of ZIPH-3c made these strategies non-viable. We propose that there are four main criteria for achieving robust adhesion of ZIPH-3c on substrates. First, the covalent linkages between ZIPH-3c and the substrate needs to be resistant to hydrolytic cleavage, which was shown to be the case for esters and silyl ether bonds used to anchor hydrophilic polymer brushes on surfaces[14–17]. Second, these hydrolysis resistant covalent linkages need to be present at a high density to ensure maximum interfacial strength. Third, non-covalent interactions need to be present at the interface to dissipate stress. Fourth, the surface needs to be remain hydrophilic after surface functionalization to enable spin coating of the ZIPH-3c precursor solution.

Based on the aforementioned criteria, we devised the PML strategy (Fig. 3.1). In the first step, the substrate is oxygen plasma treated to introduce hydroxyl groups. Then, PGMA

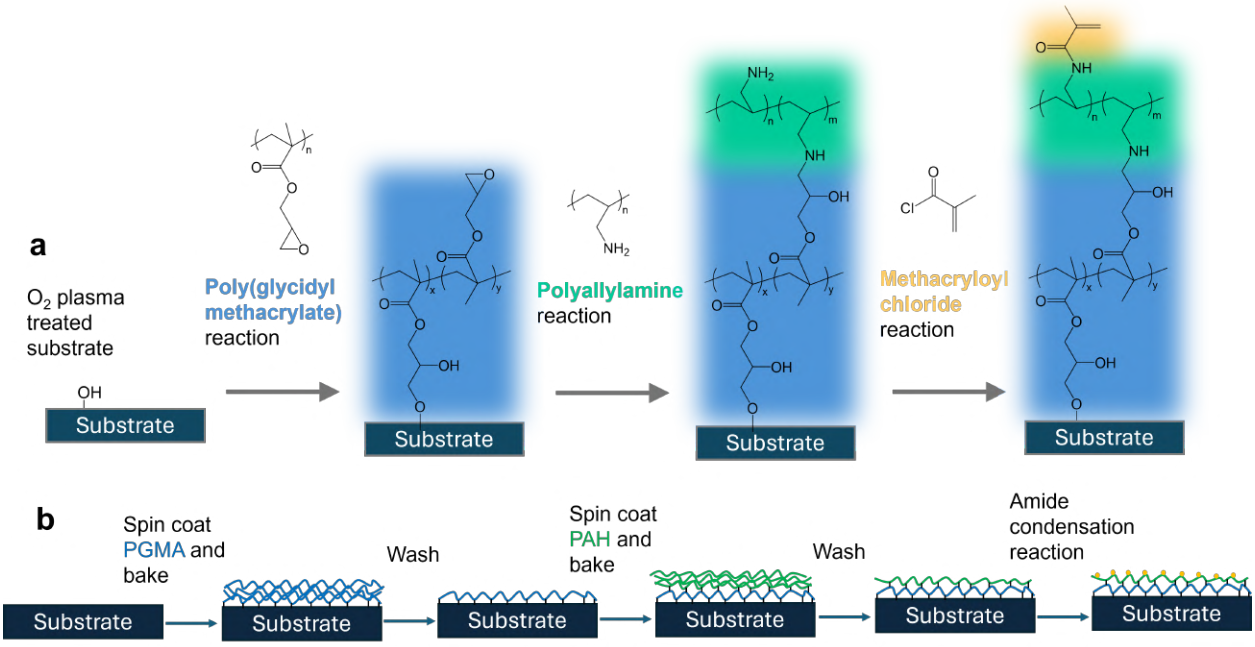

Figure 3.1. Procedures for surface PML functionalization of methacrylates. **a**, Chemical structures of polymeric monolayers after every step of the PML functionalization process. **b**, Schematic of the evolution of polymer films and monolayers after every step of the PML functionalization process.

is spin coated and baked, so the PGMA is covalently bound to the surface via ring-opening reaction of the epoxy groups by hydroxyl groups. After the excess PGMA is rinsed off to form a monolayer, PAH is spin coated and baked. The primary amines on PAH attack the epoxy groups on PGMA to form covalent linkages between the PAH and PGMA. The excess PAH is rinsed off to form a monolayer with a high density of primary amines presented on the surface. A variety of surface functional groups can be introduced from here. For the adhesion of ZIPH-3c, methacryloyl chloride is reacted with the amines to introduce a high density of methacrylate groups on the surface. When the ZIPH-3c precursor solution is spin coated and polymerized the surface methacrylate groups copolymerizes with the zwitterionic monomers, creating interfacial covalent linkages. This strategy fulfills the criteria for robust adhesion because (1) the surface methacrylates are anchored with hydrolysis-resistant amide bonds, (2) the monolayer of PAH ensures a high density of primary amines on the surface for amide

bond formation, (3) the residual amines on the surface electrostatically bind to the sulfonate groups on PSB and PSS in ZIPH-3c to dissipate stress, and (4) the high density of surface amines guarantees that there will always be plenty of residual amines to keep the surface hydrophilic. PGMA monolayers by itself can facilitate robust adhesion of PEDOT:PSS to a variety of substrates, so we decided to use them for the fabrication of PEDOT:PSS ECG electrodes.

The disadvantage of using the PML strategy is that it does not work so well on gold, which is used to connect ZIPH-3c to the soldered wire connection. Gold can be surface functionalized with hydroxy thiols, but thiol-gold bonds are known to be labile[18]. To get around this issue, the gold contacts were patterned into a comb shape to introduce interleaved gold and non-gold regions, in which the non-gold regions have PML functionalization. The area with gold is covered in thermoplastic polyurethane encapsulation to insulate and protect the area from abrasion. With parylene C being one of the most robust flexible substrates for conformal contact with tissues, the fabrication process with a parylene C substrate and the PML strategy is illustrated in Figure 3.2.

3.2.2 Design of a high gain amplifier and ECG recording setup

The amplitude of the ECG signal recorded with subcutaneous electrodes in mice can be on the order of single µV, depending on the quality of the electrodes and the extent of fibrosis. Since many signal acquisition equipment have wideband noise values of a couple mV, the single µV ECG signal needs to be amplified by at least three orders of magnitude for it to register consistently on the equipment. ECG recording in mice require bandwidths of a couple kHz, and instrumentation amplifiers typically have a gain bandwidth product of around 1 MHz, making gains on the order of a few thousand unfeasible. Furthermore, amplifying such small signals can also lead to the amplification of trace amounts of noise. To solve this issue, we built a two stage amplifier (Fig. 3.3), in which both instrumentation amplifier stages have

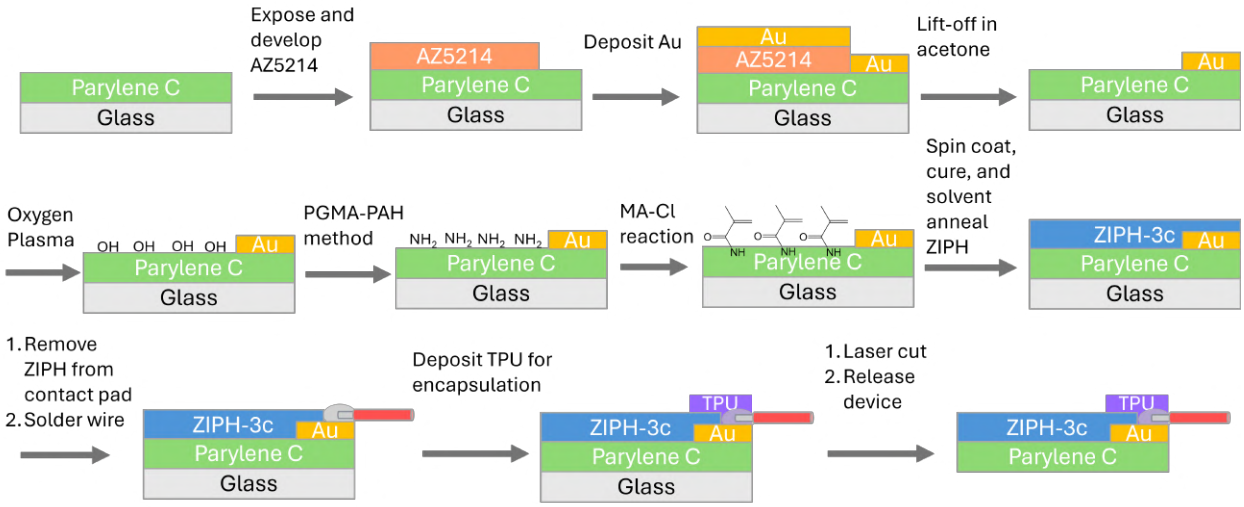

Figure 3.2. Fabrication procedures for ZIPH-3c electrodes. Starting with a parylene C substrate, Au contact pads are patterned using photolithography. Next, the PML functionalization strategy is used to introduce surface methacrylate groups. ZIPH-3c precurosor solution is spin coated and polymerized on top to form a robustly adhered ZIPH-3c on parylene C. A wire is soldered on the Au contact pad, and the solder joint and contact pad is encapsulated with TPU. PGMA, poly(glycidyl methacrylate); PAH, polyallylamine; MA-Cl, methacryloyl chloride; TPU, thermoplastic polyurethane.

gains of around 100 for a total gain of around 10,000. Between the two stages, a second order high pass Butterworth filter with a cutoff frequency of 0.1 Hz was placed to prevent offsets from the first stage from saturating the second stage. The combination of instrumentation amplifier and Butterworth filter is already enough to eliminate most of the noise. To get a cleaner signal, batteries were used instead of DC power sources to drive the op-amps in the amplifier circuit.

Even with a high gain, ultra-low noise amplifier, the ECG recording can be noisy if the recording setup is not put together well. Unless the room that the recording is taking place is built to be free of electrical noise, the room will need to be thoroughly checked for sources of electrical noise. Practically, this means that any large pieces of metal in the room will need to be grounded. For electrode placements, other than the two electrodes for differential signal acquisition, a third electrode will need to be placed on the mouse to prevent the potential of the mouse from floating. In our setup, we implanted the acquisition electrodes

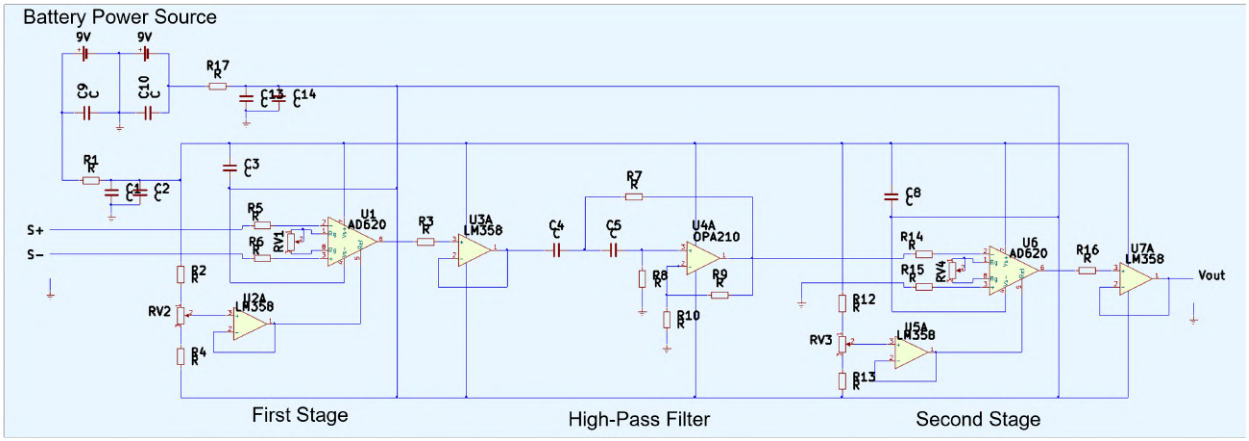

Figure 3.3. Circuit schematic of the two stage amplifier. A high pass filter is placed between the first and second stage to prevent the amplificiation of the offset from the first stage from saturating the second stage. Battery power sources are used for all op-amps to keep the noise level low.

but did not implant the ground electrode. To record, the mouse was put under anesthesia, and the ground electrode was placed on the base of the tail. We find the tail to be convenient because it is hairless and smooth.

3.2.3 ZIPH-3c benefits electrophysiological recordings by decreasing signal loss over time

To demonstrate that the lower collagen density of the fibrotic capsule associated with ZIPH-3c benefits electrophysiological recordings, we implanted passive electrocardiography (ECG) recording devices (Fig. 3.4a, Supplementary Discussion) in the subcutaneous space of mice over the course of 12 weeks. The electrodes were fixed to the dorsal muscles by overlaying a piece of polyacrylate-NHS ester tissue adhesive on the backs of the electrodes. Because the tissue adhesives were made to be slightly larger than the electrodes, some amount of the tissue adhesive forms an overhang, allowing it to adhere with the tissue underneath. Modified vascular access buttons were installed transdermally in mice and connected with two separate ECG electrodes, and the external ports were used to connect to peripheral electronics and to enable chronic recording (Fig. 3.4b and Fig. 3.5). ECG recordings from ZIPH-3c electrodes were compared with those from pristine PEDOT:PSS electrodes, as well as the

PEDOT:PSS electrodes (PEDOT:PSS-Dex) incorporating a dexamethasone elution layer as the gold standard for suppressing FBR (Fig. 3.4c, d). Because of the lower collagen density associated with ZIPH-3c, we expect it to have less signal decay compared to PEDOT:PSS, which is associated with a dense collagen layer. For PEDOT:PSS-Dex, the controlled release of dexamethasone from the Dex-PDMS layer should eliminate the growth of a fibrotic

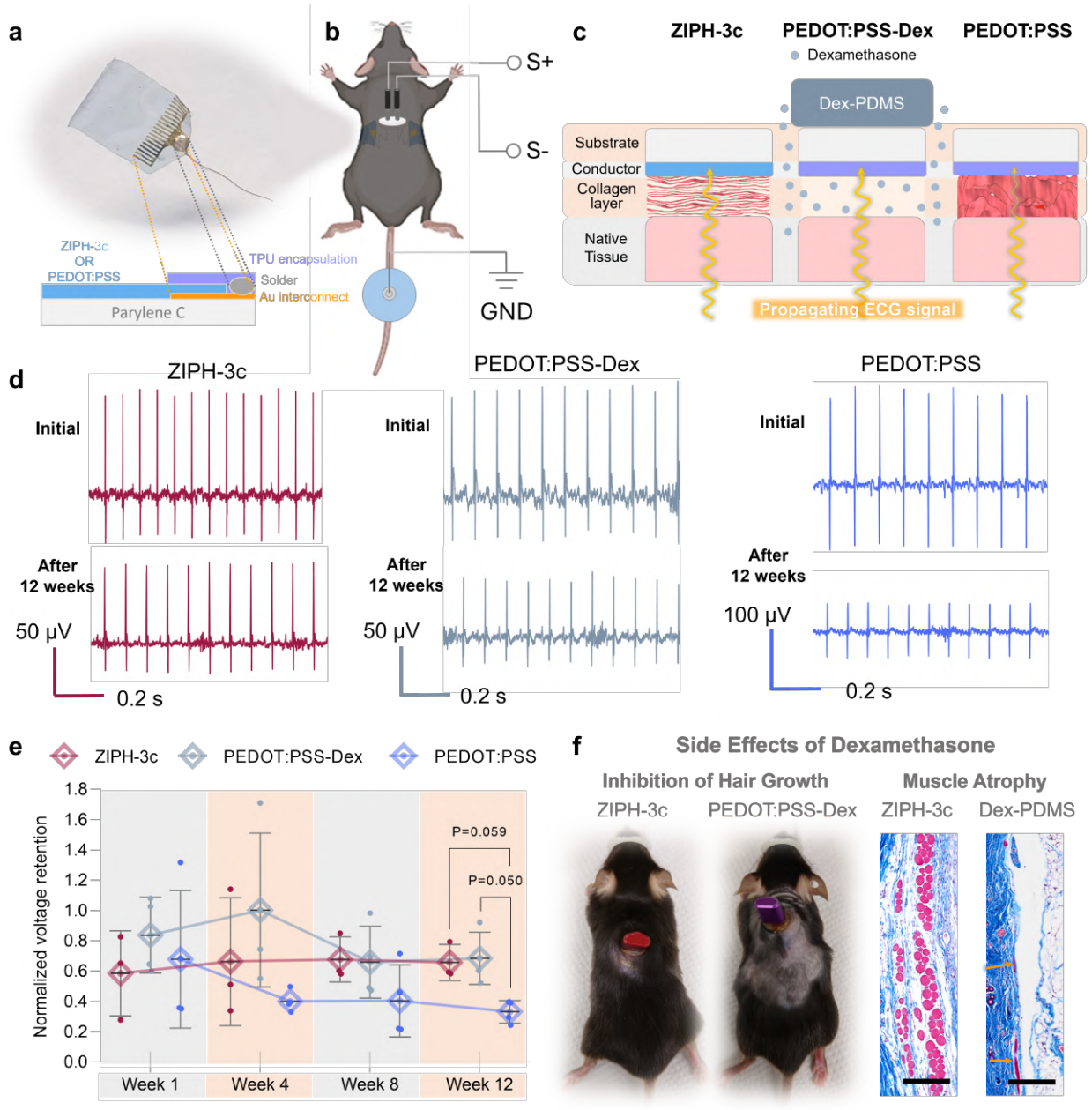

Figure 3.4. ZIPH-3c electrocardiographic electrodes experience less signal loss compared to PEDOT:PSS electrodes. **a**, Device structure of ECG electrodes used to test the effect of the FBR on electrophysiological recordings. **b**, Electrical connection on anesthetized mouse for ECG recording. Created with BioRender.com. **c**, Schematic illustration of the effects of the fibrotic capsule on ECG signal propagation for different electrode types. **d**, Examples of ECG traces immediately after surgery (top) and 12-weeks post-implantation (bottom). **e**, Peak R-wave voltages at various timepoints normalized to peak R-wave voltages immediately after surgery. **f**, Side effects of dexamethasone 12-weeks post-implantation, as demonstrated by photographs showing the inhibition of hair growth in mice implanted with PEDOT:PSS-Dex electrodes (left) and MTS-stained tissues showing the atrophy of the panniculus carnosus in mice implanted with Dex-PDMS discs (right). Orange arrows indicate the locations of the remaining panniculus carnosus for the Dex-PDMS-implanted mouse. Scale bar, 200 µm. Error bars, mean ± s.d. N = 3-4 mice per treatment. One-way ANOVA was used for statistical comparison of multiple means.

capsule, also leading to less signal decay (Fig. 3.4c). These are indeed supported by the statistical results shown in Figure 3.4e, with 3-4 device replicates in each group. As expected, both ZIPH-3c and PEDOT:PSS-Dex retained more of the initial signal than PEDOT:PSS by week 4. By week 12, the signal retentions of ZIPH-3c (66%) and PEDOT:PSS-Dex (68%) were twice that of PEDOT:PSS (33%) (Fig. 3.4e and Supplementary Discussion). These results show that ZIPH-3c can decrease FBR-induced electrophysiological signal decay just as well as dexamethasone.

Notably, the mice with PEDOT:PSS-Dex electrode implants did not grow back the fur shaved for surgery even after 12 weeks, as opposed to the mice implanted with the other electrodes pairs, which mostly grew their fur back after 12 weeks (Fig. 3.4f and Supplementary Fig. 56). In combination with the muscle atrophy caused by dexamethasone (Fig. 3.4f and Supplementary Fig. 57), a side effect that has been reported previously[19,20]. this shows that ZIPH-3c electrodes can perform just as well as dexamethasone-eluting electrodes for chronic, electrophysiological implantation without causing the side effects associated with dexamethasone.

The large variation in voltage retention at early timepoints may originate from the shifting of the electrodes and the dynamic nature of the extracellular matrix and cell population in

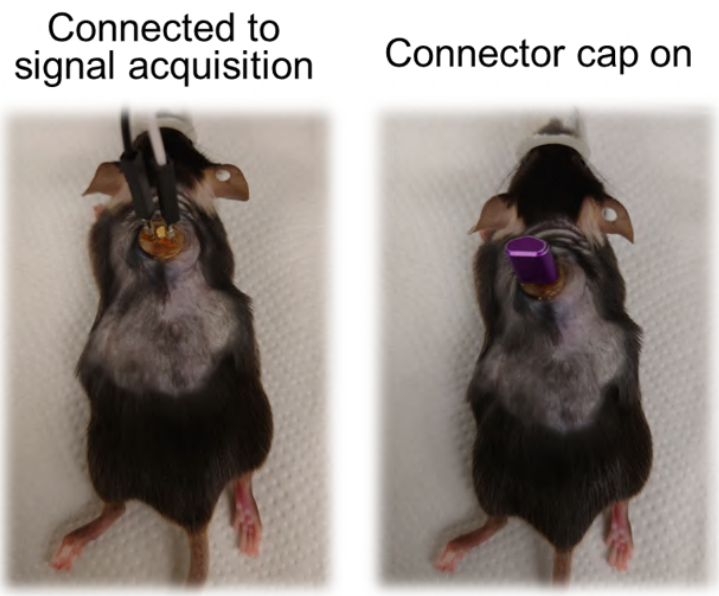

Figure 3.5. Modified vascular access button for ECG recording in mice. Anesthetized mouse with electrodes connected to peripheral electronics (left) and disconnected mouse with a cap on to protect the connector ports (right).

the peri-implant region. Even though the electrodes are fixed to the surface of the muscles on the lower rib cage with tissue adhesives, they may shift until tissues grow in to stabilize the electrode location and orientation. For PEDOT:PSS-Dex, even though no fibrotic tissue forms, loose layers of adipose and miscellaneous tissue types can form around the edges to stabilize the electrode, as can be seen from the histological sections of Dex-PDMS implants. The reason there is a big initial drop in voltage retention in week 1 may also be due to the shift in the electrode location and orientation. Lastly, ZIPH-3c and PEDOT:PSS-Dex electrodes have similar voltage retention at later timepoints, possibly because the diffusion and migration of ions in hydrogel matrices are dictated by water content, as suggested by some hydrogel diffusion models86. The lower collagen density for ZIPH-3c leads to a fibrotic capsule with a higher water content compared to that of PEDOT:PSS, improving signal quality.

3.3 Conclusion

The previous section focused on the material design, material characterization, and the biological response to the material. This section provided evidence that the findings from the previous section can be translated to real, practical electrophysiological devices. Before ZIPH-3c can be used in a device, a major adhesion challenge needed to be overcome, which was solved by a novel PML functionalization strategy. In addition, careful design and fabrication of ZIPH-3c electrodes and careful design of the ECG recording setup have led to the collection of reliable ECG data. Our results show that ZIPH-3c electrodes perform two times better than PEDOT:PSS electrodes and just as well as PEDOT:PSS-Dex electrodes without the side effects over a 12-week implantation period. For the future uses of PEDOT:PSS in electrically biointerfaced devices, as exemplified by our chronic, *in vivo* ECG tests, our work on ZIPH-3c provides a thoroughly tested solution for addressing the most challenging problem of the foreign body response.

3.4 Experimental Details

3.4.1 Materials

PEDOT:PSS (PH1000) was purchased from Clevios and was filtered through a 0.7 µm glass fiber filter (Tisch Scientific) before use. The following chemicals were purchased from Sigma-Aldrich: [2-(Methacryloyloxy)ethyl]dimethyl-(3-sulfopropyl)ammonium hydroxide (SBMA, 95%), *N,N'*-Methylenebisacrylamide (MBAA, ≥98%), 2-hydroxy-2-methylpropiophenone (HMPP, 97%), 4-ethylbenzenesulfonic acid (EBSA, 95%), acrylic acid (AAc, 99%), 2-cyano-2-propyl benzodithioate (CPBD, >97%), and tetramethacrylate end-capped PEDOT (PEDOT-TMA, 0.5 wt% in nitromethane, doped with p-toluenesulfonate). 2,2,2-trifluoroethanol (TFE, ≥99%) was purchased from Sigma-Aldrich and Tokyo Chemical Industries. Poly(allylamine) (PAH, 15% aq. soln.) was purchased from Polysciences. PDMS

Sylgard 184 was purchased from Dow-Corning. The acetate buffer was prepared with 0.1 M acetic acid (glacial, Sigma-Aldrich, ≥99.85%), 0.1 M sodium acetate trihydrate (Sigma-Aldrich, >99%), and 0.5 M NaCl at pH 5.2. Hydromed D4 Hydrophilic Thermoplastic Polyurethane (HPU) was purchased from AdvanSource Biomaterials. Elastollan 1185A10 Polyether Type Polyurethane (TPU) was purchased from BASF.

3.4.2 Preparation of tissue adhesive

Dextran (10% in DI H2O, 0.05% w/v Tween-20) was spin coated at 2000 RPM on O2 plasma treated glass and baked at 80 °C for 1 minute. PDMS (10:1 base:curing agent, 50% in heptane) was spin coated at 2000 RPM for 2 minutes and baked at 120 °C for 10 minutes. The spin coated PDMS was treated with O_2 plasma and incubated in APTES (2% in ethanol) for 1 hour. Then, the tissue adhesive precursor solution was prepared by dissolving 5 wt% HPU, 30 wt% AAc, 1 wt% AAc-NHS ester, 0.3 wt% MBAA, and 0.2 mol% (vs. AAc) HMPP in 95/5 ethanol/DI H_2O and sparged in nitrogen for 10 minutes. The sparged precursor solution was sandwiched between a piece of glass with APTES-treated PDMS and a piece of glass with PTFE coating with a ∼130 µm PET spacer. The precursor solution was cured under UV (365 nm wavelength, 4 mW/cm^2) for 30 minutes. After curing, the mold was opened, rinsed with DI H2O, and blow dried. Before surgical implantion, the tissue adhesive was sterilized with UV-C.

3.4.3 Preparation of dexamethasone-eluting PDMS

To prepare Dex-PDMS, 2% w/v of dexamethasone was dissolved in THF. 1 volume of the resultant THF solution was mixed with 1 volume of PDMS base, and the THF was slowly removed in a rotary evaporator. The resultant mixture was placed in vacuum overnight to completely remove the remaing THF and to obtain a PDMS base mixture with 1% w/w dexamethasone. 44 parts of the dexamethasone-PDMS base mixture was mixed with 1 part

curing agent. To prepare ∼100 µm thick films, dextran (10% in DI H2O, 0.05% w/v Tween-20) was spin coated at 2000 RPM on O_2 plasma treated glass and baked at 80 °C for 1 minute. Then, a mixture of 10 parts of dexamethasone-PDMS base and 1 part of curing agent was spin coated at 1000 RPM for 2 minutes and baked at 80 °C for 30 minutes. Before surgical implantation, Dex-PDMS films were sterilized with ethylene oxide.

3.4.4 Synthesis of PGMA

Poly(glycidyl methacrylate) (PGMA) (Fig. 2.20) was synthesized by dissolving 10.0 g GMA (70.3 mmol), 23 mg AIBN (0.14 mmol), and 156 mg CPBD (0.703 mmol) were dissolved in 30 mL DMF. The solution was sparged with nitrogen gas for 30 minutes and reacted at 65 °C for 18 hours. The polymer was precipitated in over 10 times the volume of cold methanol and re-dissolved in DCM. The polymer was precipitated twice more and dried under vacuum for two days.

3.4.5 Multilayer functionalization

To achieve stable adhesion of conducting hydrogels, monolayers of PGMA and PAH (PGMA-PAH method) was deposited. For the PGMA-PAA method, the substrate was first O_2 plasma treated and PGMA (5 mg/mL in 19:1 $CHCl_3$:chlorobenzene) was spin coated at 2000 RPM, followed by baking at 120°C for 30 minutes. The baked substrate was washed in CHCl3 for 2 minutes and blow dried to form a PGMA monolayer. PAH (5 mg/mL 29:1 isopropanol:DI H_2O) was spin coated at 2000 RPM on top of the PGMA monolayer and baked at 80°C for 10 minutes. The baked substrate was washed in DI H2O (+0.05% Tween-20) for 2 minutes, rinsed in DI H_2O, and blow dried to form a PAH monolayer.

3.4.6 Fabrication of electrodes

ZIPH-3c electrodes were fabricated using procedures shown in Figure 3.2. First, an oxygen plasma-treated 2"x3" glass slides were thoroughly washed with acetone, water, and isopropanol. To the washed slides, 2% solution of Micro-90 was spin coated at 1000 RPM and dried at 90 °C for a minute. On the glass slides, 5 µm thick layers of Parylene C was deposited using the PDS 2010 LabcoterTM 2 (Specialty Coating Systems). AZ 5214-E photoresist (MicroChemicals) was spin coated on the Parylene C and patterned using the Maskless Aligner MLA 150 (Heidelberg Instruments), followed by a photoresist descum process with O_2 plasma. Then, physical vapor deposition of 10/50 nm of Ti/Au using the EvoVac (Angstron Engineering) was carried out. The photoresist-Ti/Au stack was lifted off in acetone at 40 °C for 1 hour.

To achieve stable adhesion of conducting hydrogels, multilayer functionalization using PGMA and PAH was carried out. The resultant amines on the surface were functionalized by soaking in a tetrachloroethane solution of 2% triethylamine and 2% methacryloyl chloride for 2 hours at room temperature. The functionalized substrate was rinsed with chloroform and DI H_2O. UV initiatable ZIPH precursor solution was spin coated on the functionalized substrate at 1000 RPM for 10 seconds, followed by exposure to UV light (4 mW/cm^2) for 30 minutes under a humidified atmosphere. Immediately, the hydrogel film was subjected to three cycles of the solvent annealing process and dried at 60°C on a hotplate. The hydrogel film was rinsed with DI H_2O and blow dried.

For PEDOT:PSS electrodes, PEDOT:PSS (13% 1:13 Triton X-100:DMSO) was spin coated at 300 RPM. Then, the film was baked at 120 °C for 30 minutes. The baked film was rinsed with DI H_2O and blow dried.

Once the hydrogel films were prepared, the outlines of the electrodes were cut with a laser cutter. To enable wired connections to the electrodes, a wet swab was used to remove the hydrogel films on top of the Au contact pads, and 0.005" Ag wires with 0.007" PFA

insulation (A-M Systems) were attached to the contact pads with lead-free low temperature solder (Sn42Bi57Ag1, ChipQuik). 50 mg/mL TPU in THF was manually pipetted to cover the Au areas and dried under ambient conditions. Devices were peeled off, rinsed in DI H_2O, and dried on a polystyrene surface under ambient conditions.

3.4.7 Electrode-housing assembly

The ends of the Ag wires not soldered to the electrodes were attached to jumper wire female connectors via lead-free solder (Sn99.3Cu0.7, Yihua). The connectors were threaded through the holes of modified two-channel vascular access buttons (Instech) and were secured with a combination of Red Epoxy (Highside Chemicals) and super glue. The full assembly was sterilized in an autoclave at 121°C for 30 minutes before implantation.

3.4.8 Electrode implantation surgeries

6- to 8-week-old male C57BL/6 mice were purchased from Jackson Laboratories. Preoperatively, all mice received subcutaneous injections of 5 mg/kg of Meloxicam for pre-surgery analgesia. All mice were anesthetized using 2-4% isoflurane in oxygen, and the backs of all mice were shaved. All mice received eye lubricants to prevent dehydration-induced blindness. Then, the shaved backs of all mice were sterilized by scrubbing with betadine and alcohol pads in an alternating fashion, repeated two times.

One longitudinal incision, 2 cm in length, was made in the mid-back region. The blade tips of a pair of scissors were inserted into the subcutaneous space through the incisions, and two subcutaneous pockets, flanking the incision, were made via blunt tissue dissection using the blunt sides of a pair of scissors. After carefully exposing the subcutaneous musculature by pulling back the skin on one flank, an electrode was placed on the lower, lateral side of the latissimus dorsi. For PEDOT:PSS-Dex, a Dex-PDMS backing (∼100 µm thickness) was placed on top of the electrodes. A tissue adhesive (∼100 µm thickness) was placed on

top of the electrodes so that a slight overhang around the edges of the electrode adhered to the tissue underneath. The electrode placement procedure was repeated for the other subcutaneous pocket. Then, the felt attached to the vascular access button was tucked underneath the skin, and the remaining incisions longitudinally flanking the vascular access button were closed with wound clips. Following surgery, all mice were given subcutaneous injections of 5 mg/kg of Meloxicam once every 24 hours for two days. Wound clips were removed after 10 days.

"From the moment I understood the weakness of my flesh, it disgusted me. I craved the strength and certainty of steel. I aspired to the purity of the blessed machine. Your kind cling to your flesh as if it will not decay and fail you. One day the crude biomass that you called a temple will wither and you'll beg my kind to save you. But I am already saved. For the machine is immortal. Even in death I serve the Omnissiah." — Magos Dominus Reditus*

*Bulwark Studios. (2018). Warhammer 40,000: Mechanicus [Video game]. Kasedo Games.

3.4.9 Chronic electrocardiographic recording

First, a mouse was anesthetized using 2-4% isoflurane in oxygen. The protective cap for the external connectors were removed, and the female jumper wire connectors were connected to a custom-built amplifier. An adhesive electrocardiography patch was attached to the tail and connected to ground. Signal acquisition was carried out using the Keithley 2450 (Tektronix).

3.5 References

1. Mirvis, D. M. & Goldberger, A. L. en. in *Heart Disease* 82–128 (2001).
2. Liu, Y. *et al.* Soft and elastic hydrogel-based microelectronics for localized low-voltage neuromodulation. en. *Nature Biomedical Engineering* **3,** 58–68. ISSN: 2157-846X. (2026) (Jan. 2019).
3. Liu, Y. *et al.* Morphing electronics enable neuromodulation in growing tissue. en. *Nature Biotechnology* **38,** 1031–1036. ISSN: 1546-1696. (2026) (Sept. 2020).
4. Yang, M. *et al.* Robust Neural Interfaces with Photopatternable, Bioadhesive, and Highly Conductive Hydrogels for Stable Chronic Neuromodulation. *ACS Nano* **17,** 885–895. ISSN: 1936-0851. (2026) (Jan. 2023).
5. Chong, J. *et al.* Highly conductive tissue-like hydrogel interface through template-directed assembly. en. *Nature Communications* **14,** 2206. ISSN: 2041-1723. (2026) (Apr. 2023).
6. Mousavi, H., Ferrari, L. M., Whiteley, A. & Ismailova, E. Kinetics and Physicochemical Characteristics of Electrodeposited PEDOT:PSS Thin Film Growth. en. *Advanced Electronic Materials* **9,** 2201282. ISSN: 2199-160X. (2026) (2023).
7. Koutsouras, D. A. *et al.* Impedance Spectroscopy of Spin-Cast and Electrochemically Deposited PEDOT:PSS Films on Microfabricated Electrodes with Various Areas. en. *ChemElectroChem* **4.** _eprint: https://chemistry-europe.onlinelibrary.wiley.com/doi/pdf/10.1002/celc.201700297, 2321–2327. ISSN: 2196-0216. (2026) (2017).
8. Feig, V. R. *et al.* An Electrochemical Gelation Method for Patterning Conductive PEDOT:PSS Hydrogels. en. *Advanced Materials* **31,** 1902869. ISSN: 1521-4095. (2026) (2019).
9. Håkansson, A. *et al.* Effect of (3-glycidyloxypropyl)trimethoxysilane (GOPS) on the electrical properties of PEDOT:PSS films. en. *Journal of Polymer Science Part B: Polymer Physics* **55.** _eprint: https://onlinelibrary.wiley.com/doi/pdf/10.1002/polb.24331, 814–820. ISSN: 1099-0488. (2026) (2017).
10. Oldroyd, P. *et al.* Fabrication of thin-film electrodes and organic electrochemical transistors for neural implants. en. *Nature Protocols* **20,** 2100–2124. ISSN: 1750-2799. (2026) (Aug. 2025).
11. Inoue, A., Yuk, H., Lu, B. & Zhao, X. Strong adhesion of wet conducting polymers on diverse substrates. *Science Advances* **6,** eaay5394. (2026) (Mar. 2020).
12. Yuk, H., Zhang, T., Parada, G. A., Liu, X. & Zhao, X. Skin-inspired hydrogel–elastomer hybrids with robust interfaces and functional microstructures. en. *Nature Communications* **7,** 12028. ISSN: 2041-1723. (2026) (June 2016).

13. Osazuwa, P. O. *et al.* Surface Functionalization with (3-Glycidyloxypropyl)trimethoxysilane (GOPS) as an Alternative to Blending for Enhancing the Aqueous Stability and Electronic Performance of PEDOT:PSS Thin Films. *ACS Applied Materials & Interfaces* **15,** 54711–54720. ISSN: 1944-8244. (2026) (Nov. 2023).

14. Quintana, R., Gosa, M., Jańczewski, D., Kutnyanszky, E. & Vancso, G. J. Enhanced Stability of Low Fouling Zwitterionic Polymer Brushes in Seawater with Diblock Architecture. *Langmuir* **29,** 10859–10867. ISSN: 0743-7463. (2026) (Aug. 2013).

15. Yu, Y., Vancso, G. J. & de Beer, S. Substantially enhanced stability against degrafting of zwitterionic PMPC brushes by utilizing PGMA-linked initiators. *European Polymer Journal* **89,** 221–229. ISSN: 0014-3057. (2026) (Apr. 2017).

16. Chen, W.-L. *et al.* Reduced Lateral Confinement and Its Effect on Stability in Patterned Strong Polyelectrolyte Brushes. *Langmuir* **33,** 3296–3303. ISSN: 0743-7463. (2026) (Apr. 2017).

17. Brió Pérez, M., Cirelli, M. & de Beer, S. Degrafting of Polymer Brushes by Exposure to Humid Air. *ACS Applied Polymer Materials* **2,** 3039–3043. (2026) (Aug. 2020).

18. Karpovich, D. S. & Blanchard, G. J. Direct Measurement of the Adsorption Kinetics of Alkanethiolate Self-Assembled Monolayers on a Microcrystalline Gold Surface. en. *Langmuir* **10,** 3315–3322. ISSN: 0743-7463, 1520-5827. (2026) (Sept. 1994).

19. Hasselgren, P.-O. Glucocorticoids and muscle catabolism. en-US. *Current Opinion in Clinical Nutrition & Metabolic Care* **2,** 201. ISSN: 1363-1950. (2026) (May 1999).

20. Schakman, O., Kalista, S., Barbé, C., Loumaye, A. & Thissen, J. P. Glucocorticoid-induced skeletal muscle atrophy. *The International Journal of Biochemistry & Cell Biology. Molecular Basis of Muscle Wasting* **45,** 2163–2172. ISSN: 1357-2725. (2026) (Oct. 2013).

CHAPTER 4

POLYELECTROLYTE MULTILAYER-MEDIATED SELF-ASSEMBLY OF ZWITTERIONIC POLYMER BRUSHES ON PEDOT:PSS ENABLES ANTIFOULING BIOELECTRONICS THAT SUPPRESSES THE FOREIGN BODY RESPONSE

4.1 Introduction

In the previous two chapters, using ZIPH, we showed that chemical heterogeneity can potentially be a different route for achieving FBR suppression for electronic materials. However, ZIPH did not have antifouling properties. In this chapter, we explored how self-assembled monolayers of zwitterionic antifouling polymer brushes on PEDOT:PSS can suppress the FBR. There have been many works that report the synthesis of functionalized PEDOT derivatives that have pre-installed zwitterionic moeities[1,2] or have moeities that enable the grafting of zwitterionic polymers[3,4] for conferring antifouling properties to PEDOT. Out of all the PEDOT derivatives, works on commercially available PEDOT:PSS, such as Clevios PH1000, have produced the highest electrical conductivity values[5–7]. Thus, if the goal is to maximize electrical conductivity and FBR-suppressive properties, commercial PEDOT:PSS is the ideal choice. However, the surface properties of PEDOT:PSS are dictated by the PSS shell that encapsulates PEDOT[5,8,9], limiting functionalization options for PEDOT:PSS to direct chemical modifications of PSS. The strong electron withdrawing properties of sulfonate makes aromatic substitution difficult. Activating the benzene ring by removing the sulfonate group requires reaction conditions that can damage PEDOT:PSS. Aromatic substitution reactions in general have harsh reaction conditions that can also damage PEDOT:PSS.

Zwitterionic polymer brushes have regularly been grafted on a variety of surfaces by using zwitterionic polymer-hydrophobic polymer block copolymers[10–12]. Self assembly strategies

that rely on hydrophobic forces are not effective since PEDOT:PSS swells under aqueous conditions, which causes the coating to detach. Therefore, we need a new strategy for stably modifying PEDOT:PSS surfaces using mild conditions. Zwitterionic polymer brushes have also been grafted on surfaces by adsorbing a base layer of polydopamine[13]. However, polydopamine coatings are usually several nanometers thick, dense structures[14], which could greatly increase the interfacial impedance of PEDOT:PSS. Given that established methods are compatible with PEDOT:PSS, we needed a new strategy for assembling polymer brushes on PEDOT:PSS.

PSS is a polyanion, which means that it can electrostatically bind to polycations in a process called polyelectrolyte complexation. Polyelectrolyte complexation happens spontaneously when dissolved polyelectrolyte pairs are mixed under ambient conditions[15], making it ideal for fabrication processes that require mild conditions, such as the processing of PEDOT:PSS. Polyelectrolyte complexation has been used to assembled polyelectrolyte multilayers, in which oppositely charged polyelectrolytes are coated layer by layer on a variety of surfaces, giving rise to a variety of surface properties and functions[16–18]. The complexation strength of polyelectrolyte complexes can vary, and weaker polyelectrolyte pairs can dissociate in aqueous environments with weak ionic strengths[15]. It has been reported that the polyelectrolyte pairs of PSS and poly((4-vinylbenzyl)trimethylammonium chloride) (PVBT) have exceptionally high salt resistance, with complete dissolution of the PEC occuring at ionic strengths higher than 5 M[19]. Given that it has been reported before that polyzwitterion-polyelectrolyte block copolymer can self assemble on charged surfaces to give rise to antifouling surfaces[20,21], we hypothesized that the same method can be utilized to assemble zwitterionic polymer brushes on PEDOT:PSS through polyelectrolyte complexation and form a durable coating that can survive *in vivo* conditions, in which the ionic strength is around 0.15 M.

We demonstrated that the self assembly of zwitterionic polymer brushes on PEDOT:PSS

can significantly reduce protein adsorption. The zwitterionic polymer brush appears to not substantially interfere with electrophysiological recording capabilities of electrocardiographic PEDOT:PSS electrodes. Furthermore, there is almost no signal degradation over a 12-week implantation period, a highly promising result for the application of self assembled zwitterionic polymer brushes on PEDOT:PSS-based implantable medical devices.

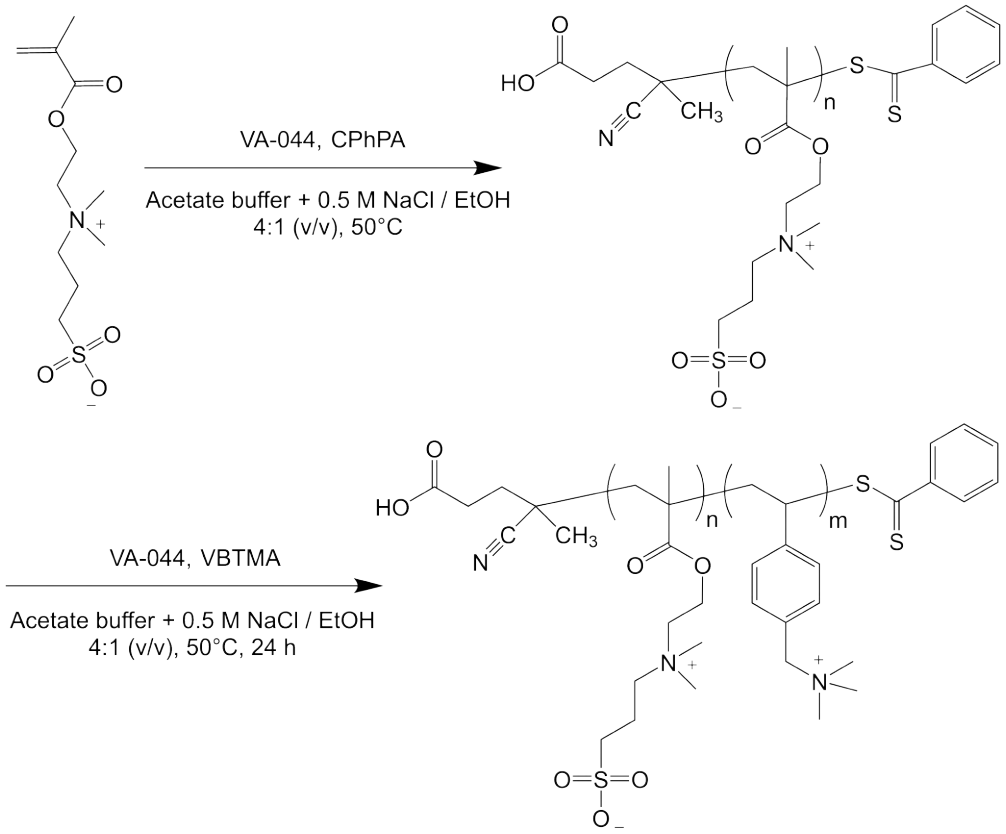

Figure 4.1. Synthesis route for PSB-b-PVBT.

4.2 Results and Discussions

4.2.1 Synthesis of polyzwitterion-polyelectrolyte block copolymers

We synthesized block copolymers with poly(sulfobetaine methacrylate) (PSB) and poly(2-methacryloyloxyethyl phosphorylcholine) (PMPC) as the zwitterionic block. For the polyelectrolyte block, PVBT was used because of the high salt resistance of PSS-PVBT polyelec-

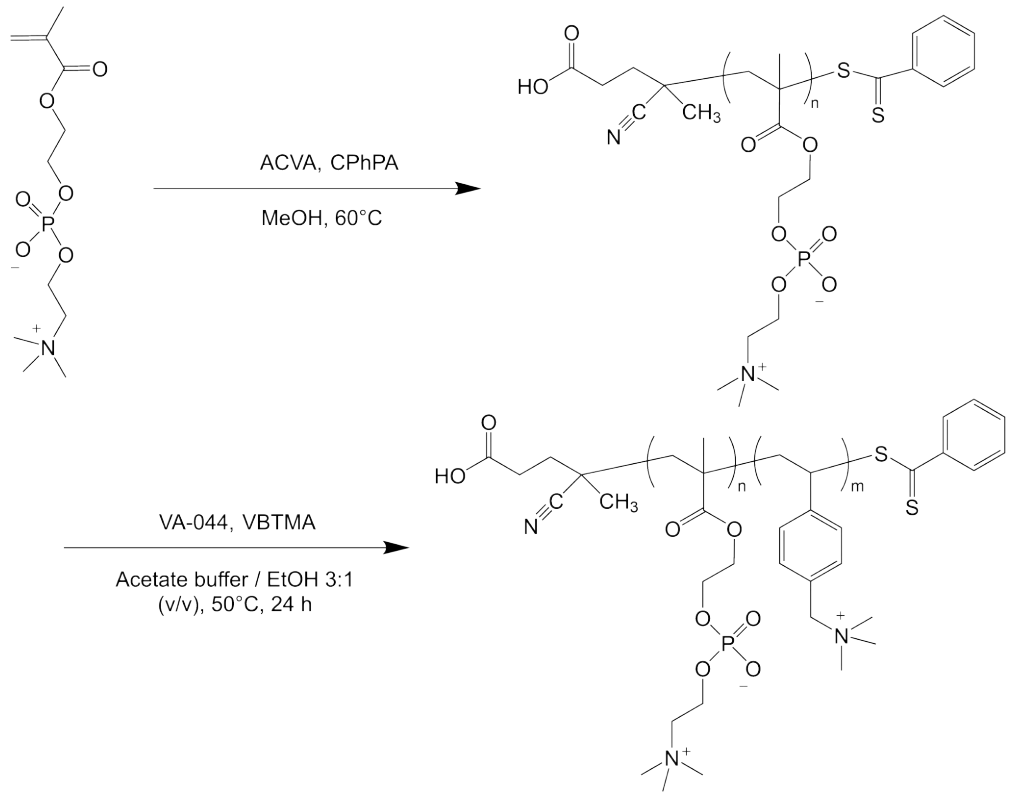

Figure 4.2. Synthesis route for PMPC-b-PVBT.

trolyte complexes[19]. Based on a previous report[21], the target degree of polymerization (DP) for the polyzwitterion was chosen to be 100. For the PVBT block, target DPs of 20 and 40 were chosen. The synthesis routes of PSB-PVBT block copolymer (PSB-b-PVBT) and PMPC-PVBT block copolymer (PMPC-PVBT) via reverse addition-fragmentation chain-transfer (RAFT) polymerization are as shown in Figures 4.1 and 4.2. The main consideration for the PVBT block lengths was to find the optimal length to maximize both the binding strength and polymer brush density since making the block lengths longer increases the binding strength at the expense of polymer brush density.

4.2.2 Optimization of self-assembly conditions of zwitterionic polymer brushes

The self-assembly conditions of the zwitterionic polymer brushes were optimized using protein adsorption assays. Some of these experiments were originally conducted with the goal

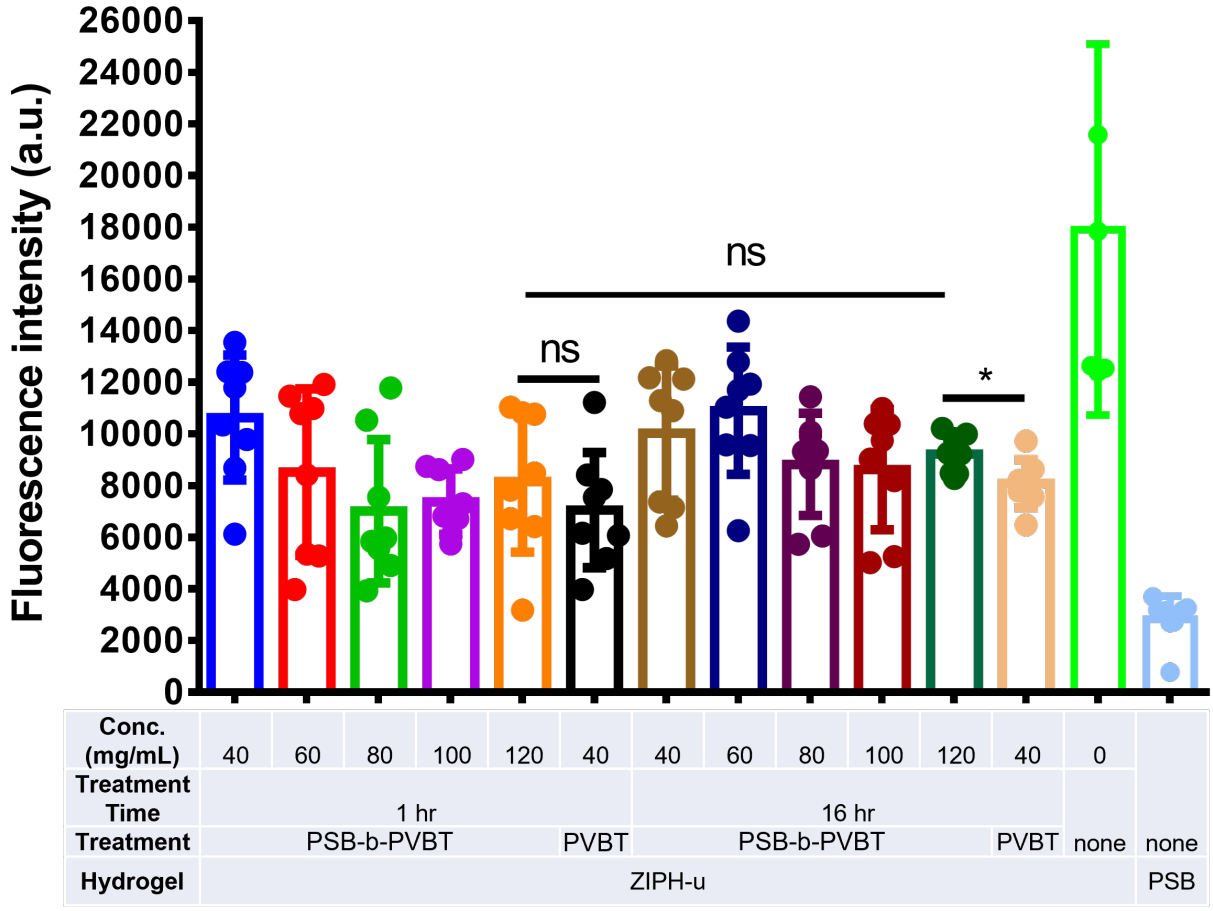

Figure 4.3. Initial optimization data for self-assembly conditions for PSB-b-PVBT. ZIPH-u was used for all the samples that had surface self assembly. Concentration of PSB-b-PVBT in the self-assembly solution and the incubation time in the self-assembly solution were tested. As controls, PSB hydrogel and ZIPH-u adsorbed with PVBT homopolymer were used.

of making ZIPH antifouling, so the optimization experiments were conducted with ZIPH-u and ZIPH-3c. Regardless, the conclusions of the experiments should hold for PEDOT:PSS as well. All protein adsorption studies were conducted with 5 mm discs submerged in human blood plasma. After it was found that there were no difference in protein adsorption between the block copolymers with a $PVBT_{20}$ and a $PVBT_{40}$ block, concentration of PSB-b-PVBT with $PVBT_{20}$ blocks in the self-assembly solution and the incubation time in the self assembly solution were tested (Fig. 4.3. There were no difference between the 1 and 16 hour incubation conditions, and the protein adsorption amount decreased with increasing concen-

tration of PSB-b-PVBT until it started to plateau at 100 mg/mL. The PSB hydrogel control had the lowest protein adsorption level. What could not be explained, however, was that the samples treated with only PVBT had protein adsorption levels that were comparable to samples treated with PSB-b-PVBT. The first hypothesis to explain this was that PSB might be aggregating in solution, causing it to not self-assemble correctly. PSB is known to have the strongest self-associative interaction out of all the zwitterionic polymers[22,23].

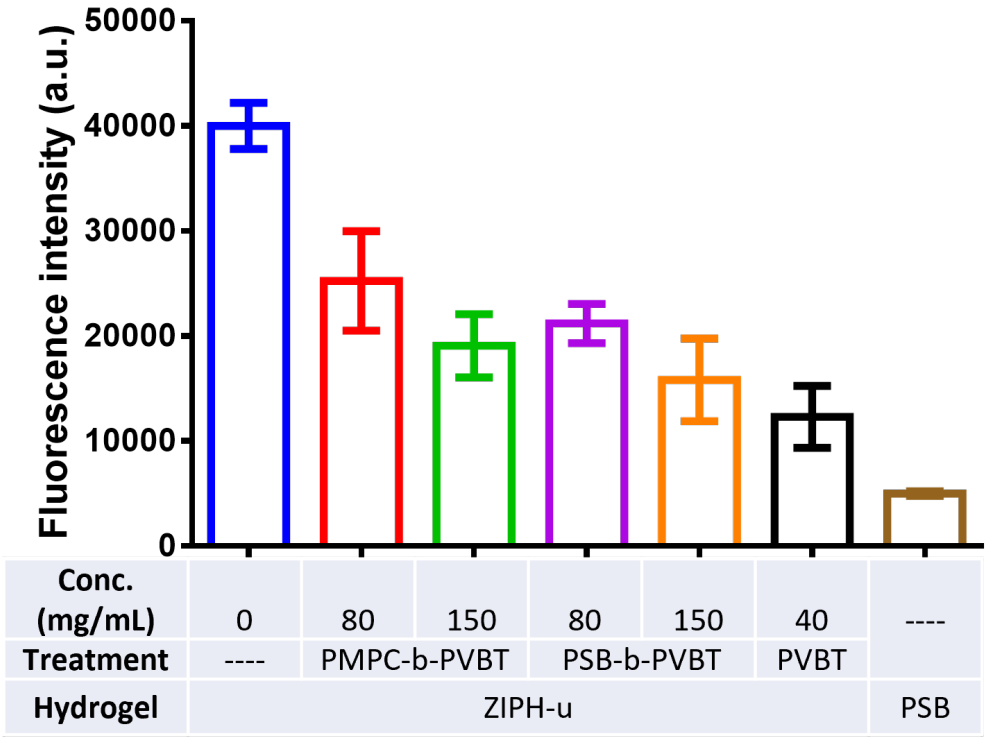

Figure 4.4. Comparison of protein adsorption levels between samples treated with PSB-b-PVBT and PMPC-b-PVBT. Different concentrations of PSB-b-PVBT and PMPC-b-PVBT in the self-assembly solution was tested. Samples treated with the PVBT homopolymer and the PSB hydrogel were used as controls.

To test this hypothesis, protein adsorption to samples treated with PMPC-b-PVBT, PSB-b-PVBT, or PVBT homopolymer were compared (Fig. 4.4. PMPC-b-PVBT treated samples had higher protein adsorption than PSB-b-PVBT, and samples treated with PVBT still had comparable protein adsorption to the best performing polymer brush self-assembly conditions. The PSB hydrogel control still had the lowest protein adsorption level. Since

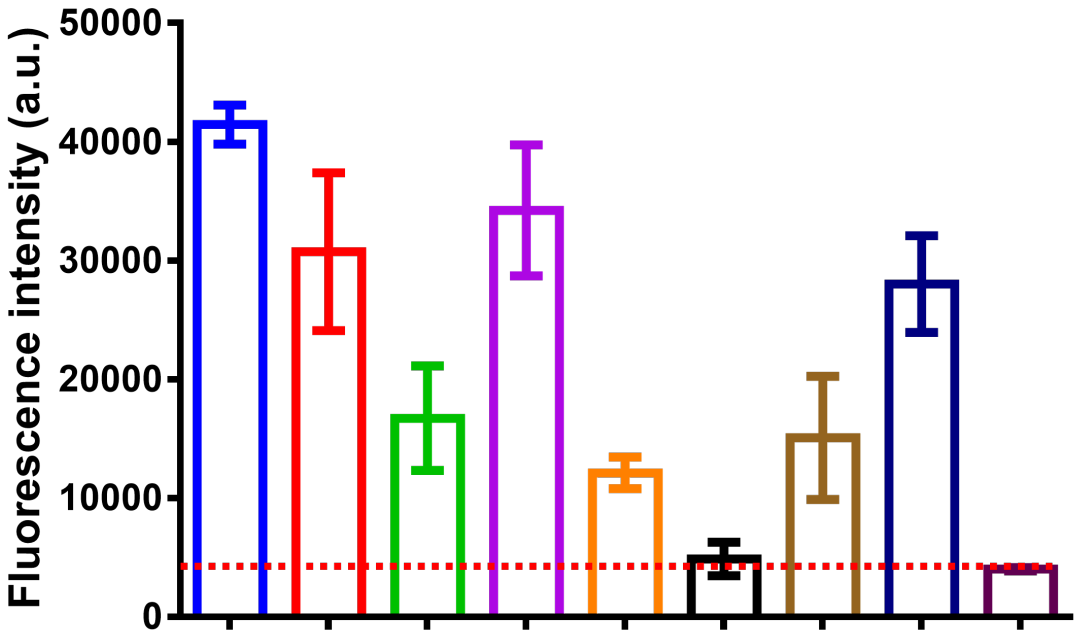

Layer 3	-----	-----	-----	-----	PVBT	PSB-b-PVBT	-----	-----	PSB
Layer 2	-----	-----	PSB-b-PSS	PSS			-----	PSB-b-PSS	
Layer 1	-----	PVBT					PSB-b-PVBT		
Hydrogel	ZIPH-u								

Figure 4.5. Comparison of protein adsorption levels among samples coated with different combinations of alternating oppositely charged polymers. Samples had between one and three layers of polymer coatings. Cells in the table with dash lines indicate that further layers were not deposited. PSB hydrogels served as controls. The horizontal red dash line marks the protein adsorption level of the PSB hydrogel control, which is at almost the same level as the condition coated with the PVBT/PSS/PSB-b-PVBT trilayer.

samples treated with PVBT homopolymer had the lowest protein adsorption out of all the testec conditions except for the PSB hydrogel, we tested if polyelectrolyte multilayers terminated with or without self-assembled zwitterionic polymer brushes would lead to lower protein adsorption (Fig. 4.5. Because there were no difference in protein adsorption levels between PSB-b-PVBT and PMPC-b-PVBT and PSB-b-PVBT polymer brushes should be more stable due to stronger self-associative interactions, we chose to use PSB-b-PVBT for all rest of the study. Up to three layers of alternating oppositely charged polymers were coated in various combinations. The condition with PVBT, PSS, and PSB-b-PVBT trilayer had

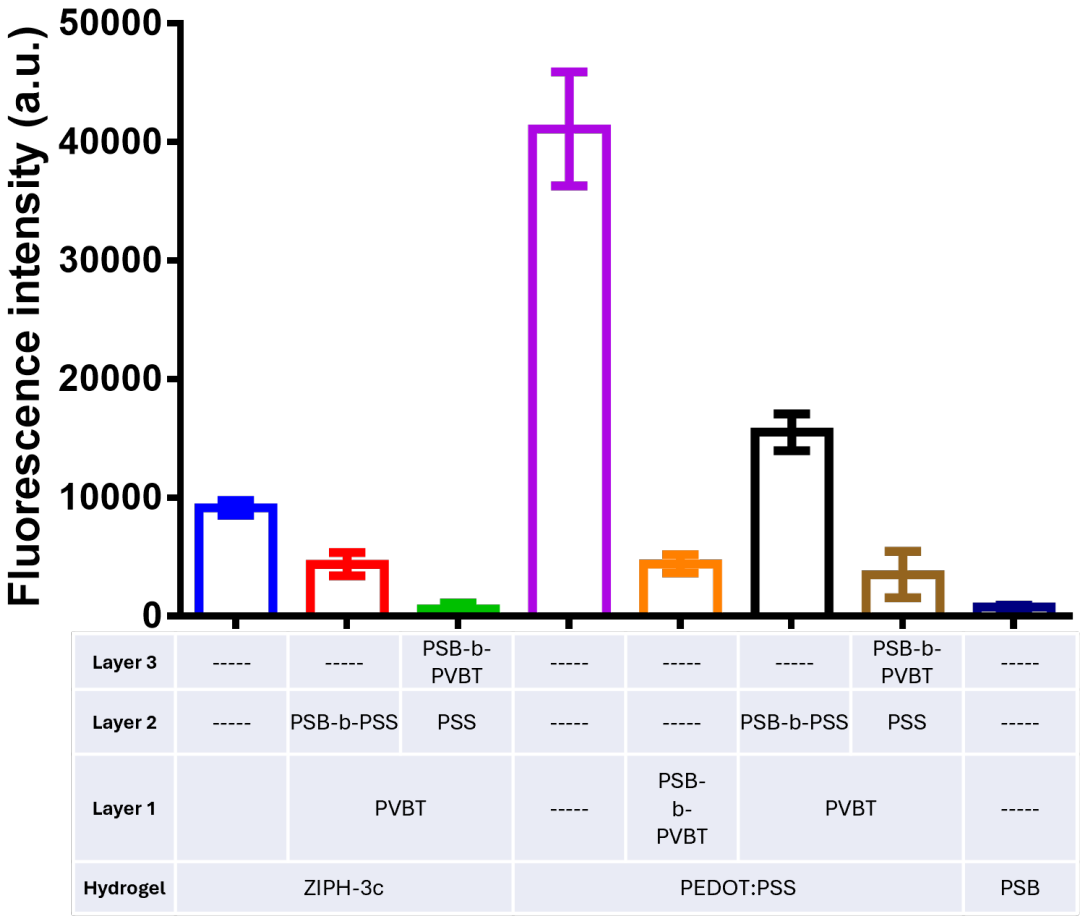

Figure 4.6. Comparison of protein adsorption levels among ZIPH-3c and PEDOT:PSS samples coated with different combinations of alternating oppositely charged polymers. Samples had between one and three layers of polymer coatings. Cells in the table with dash lines indicate that further layers were not deposited. PSB hydrogels served as controls.

comparable protein adsorption levels to the PSB hydrogel control. PEDOT:PSS hydrogels were also tested using similar conditions and had similar results (Fig. 4.6). The biggest difference was that PEDOT:PSS had substantially higher protein adsorption levels compared to ZIPH-3c, and PEDOT:PSS coated with the PVBT/PSS/PSB-b-PVBT trilayer had a slightly higher protein adsorption level compared to ZIPH-3c with the same coating. Because it is the best performing coating method, the PVBT/PSS/PSB-b-PVBT trilayer coating will be the main focus for the remainder of the chapter and will be referred to as polyelectrolyte trilayer zwitterionic polymer brush (PET-ZIP) for the remainder of the chapter.

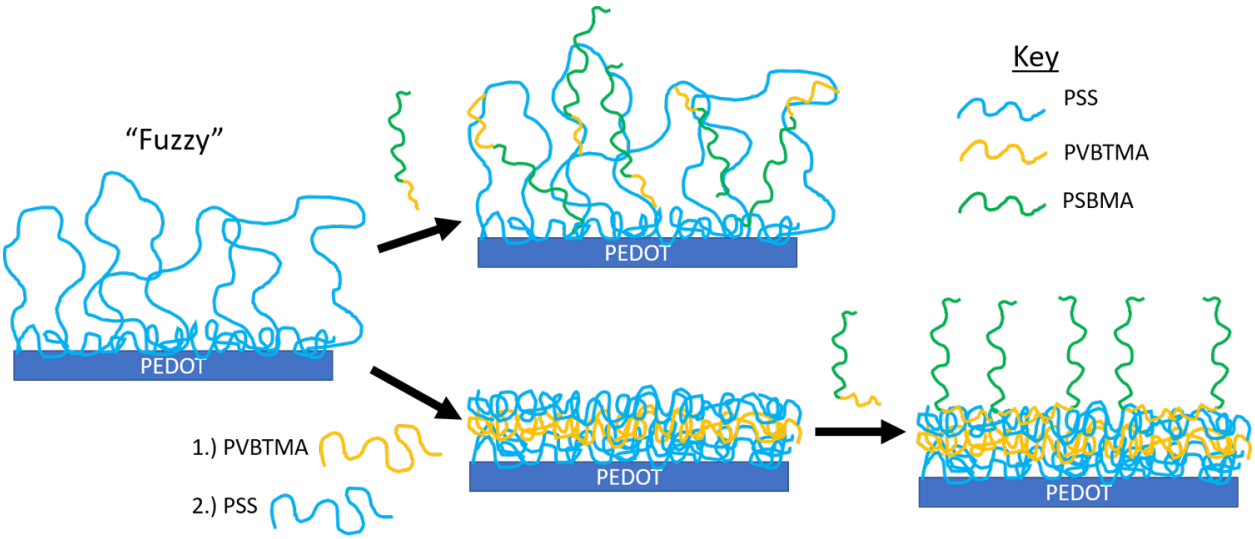

Figure 4.7. Schematic illustrating the potential explanation for why zwitterionic polymer brushes assembled with a trilayer has much lower protein adsorption compared to the ones assembled with a monolayer.

Characterizing PEDOT:PSS samples with self-assembled zwitterionic polymer brushes is challenging because the total coating is only a few nanometers thick and the PEDOT:PSS underneath interferes with spectroscopy, microscopy, and light scattering techniques. We do not have any evidence to prove the reason why the PET-ZIP approach works better than the monolayer approach due to this, but we believe we have a highly plausible explanation (Fig. 4.7). The PSS in PEDOT:PSS is not tightly bound to PEDOT under aqueous conditions. The PSS forms a "fuzzy" permeable polymer layer at the surface of PEDOT instead of forming an impermeable, hard solid-liquid interface. This allows PSB-b-PVBT chains to orient itself in any direction once the PVBT block complexes with PSS, which causes only a small fraction of the zwitterionic blocks to point away from the PEDOT:PSS surface to act as an antifouling barrier. The permeability of the PSS layer also allows PSB-b-PVBT chains to diffuse into the PSS layer before the PVBT block complexes with the PSS, potentially leading to the PSB-b-PVBT chains to be buried in the PSS layer. If polyelectrolyte multilayers are applied to the PEDOT:PSS surface, the "fuzzy" PSS layer collapses due to polyelectrolyte complexation, forming an impermeable, hard solid-liquid

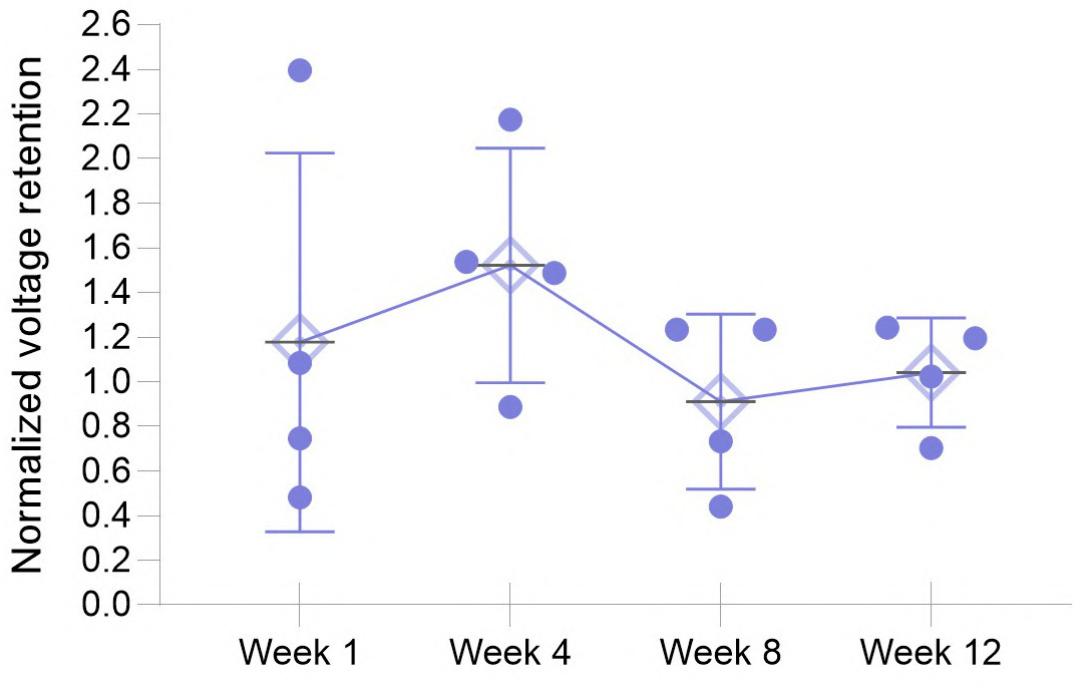

Figure 4.8. Normalized voltage retention of ECG recorded using PEDOT:PSS electrodes with PET-ZIP coatings. Normalized voltage retention is defined as peak R-wave voltages at specific timepoint normalized to peak R-wave voltages immediately after surgery.

interface. This facilitates the polymer brushes to assembled in the correct orientations.

4.2.3 Chronic electrocardiography in mice with zwitterionic polymer brush-coated PEDOT:PSS electrodes

To test if PET-ZIP on PEDOT:PSS can enable low signal-loss, chronic electrophysiological recording, the same electrocardiography (ECG) setup used in Chapter 3 was utilized for PET-ZIP. Before the ECG electrodes can be fabricated, it was essential to determine if sterilization techniques, such as autoclaving, can damage the PET-ZIP layer. We found that autoclaving degrades the antifouling properties of the PET-ZIP layer. Therefore, the self-assembly solution and PEDOT:PSS ECG electrodes were autoclaved separately. Then, the PET-ZIP self-assembly procedures were conducted in a biosafety cabinet to ensure sterility.

ECG recordings were recorded in mice over a 12-week period, and it was observed that,

on average, there was very little to no signal degradation over time (Fig. 4.8). The recorded voltage stayed above the initial recording at all timepoints except for the 8-week timepoint. The signal loss experienced by PET-ZIP PEDOT:PSS ECG electrodes is much less than the signal loss experienced by ZIPH and PEDOT:PSS-Dex ECG electrodes from Chapter 3 (Fig. 3.4e).

4.3 Conclusion

Achieving stable coatings on PEDOT:PSS under physiological conditions is challenging because PEDOT:PSS lacks useful functional groups, and the hydrophilicity causes it to swell in water. Here, we report a new method, involving polyelectrolyte multilayers, to achieve a stable, self-assembled zwitterionic polymer brush coating. ZIPH and PEDOT:PSS coated with PET-ZIP achieve antifouling properties comparable to PSB hydrogels. Furthermore, PEDOT:PSS ECG electrodes coated with PET-ZIP experience little to no signal loss over a 12-week implantation period. However, there are still several questions un-answered with this work. Electrical and electrochemical characterizations are still lacking, and the degree of fibrosis PEDOT:PSS coated with PET-ZIP will experience in mice is still unknown.

4.4 Experimental Details

4.4.1 Materials

PEDOT:PSS (PH1000) was purchased from Clevios and was filtered through a 0.7 µm glass fiber filter (Tish Scientific) before use. The following chemicals were purchased from Sigma-Aldrich: [2-(Methacryloyloxy)ethyl]dimethyl-(3-sulfopropyl)ammonium hydroxide (SBMA, 95%), sodium styrene sulfonate (NaSS, ≥90%), 4,4'-azobis(4-cyanovaleric acid) (ACVA, ≥98%), (vinylbenzyl)trimethyl ammonium chloride (VBTMAC, 99%), sodium dodecylbenzene sulfonate (SDS, ≥98.5%), and 4-cyano-4-(phenylcarbonothioylthio) pen-

tanoic acid (CPhPA). 2,2'-azobis[2-(2-imidazolin-2-yl)propane]dihydrochloride (VA-044) was purchased from Wako Chemicals (USA). 2-methacryloyloxyethyl phosphorylcholine (MPC, ≥96%) was purchased from Tokyo Chemical Industries and purified by washing it with diethyl ether. The acetate buffer was prepared with 0.1 M acetic acid (glacial, Sigma-Aldrich, ≥99.85%), 0.1 M sodium acetate trihydrate (Sigma-Aldrich, >99%), and 0.5 M NaCl at pH 5.2.

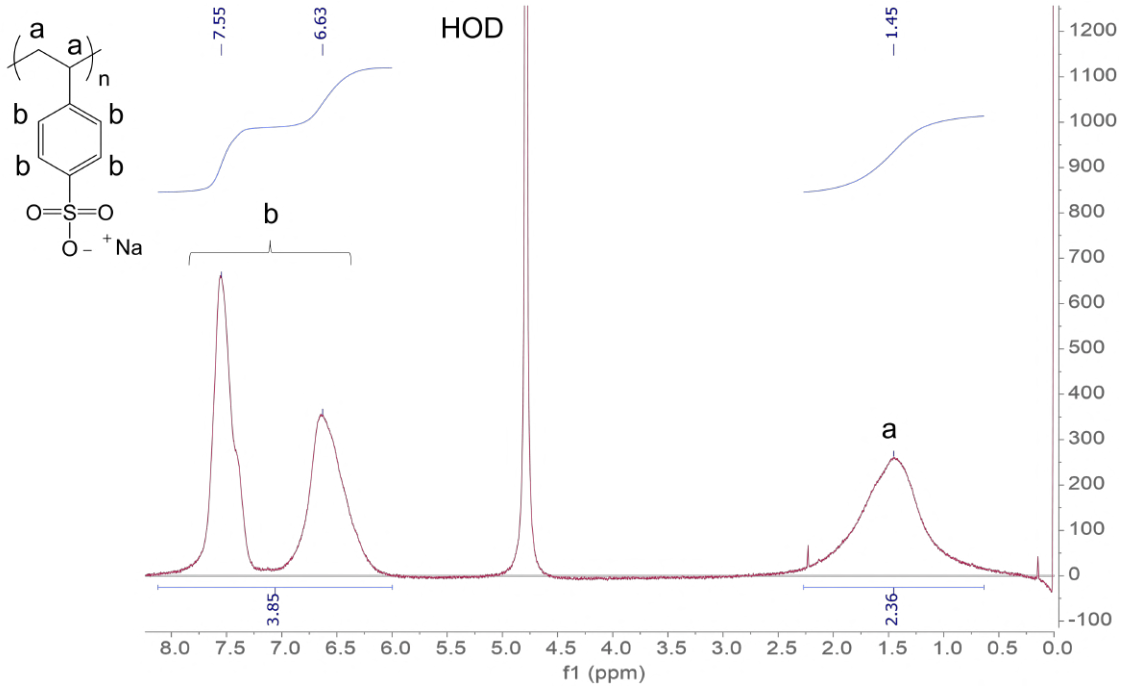

Figure 4.9. NMR spectrum of PSS.

4.4.2 Synthesis of polymers

Poly(styrene sulfonate) (PSS) (Fig. 4.9) was synthesized by dissolving 150 g of NaSS (727 mmol, 150 g) and 70 mg of ACVA (0.25 mmol, 70 mg) in 1.5 L of deionized (DI) H_2O. The solution was sparged with argon gas at a high flow rate for 45 minutes before being heated to 65 °C for 12 hours. A portion of the resulting solution was dialyzed using 10k dialysis tubes from (Thermo Scientific, SnakeSkin, 3.5k molecular weight cut-off) for 5 days against an excess of pure DI water which was changed every 12 hours. After purification, the solution

containing polymer was collected, frozen with liquid nitrogen and lyophilized to give PSS as a dry white powder.

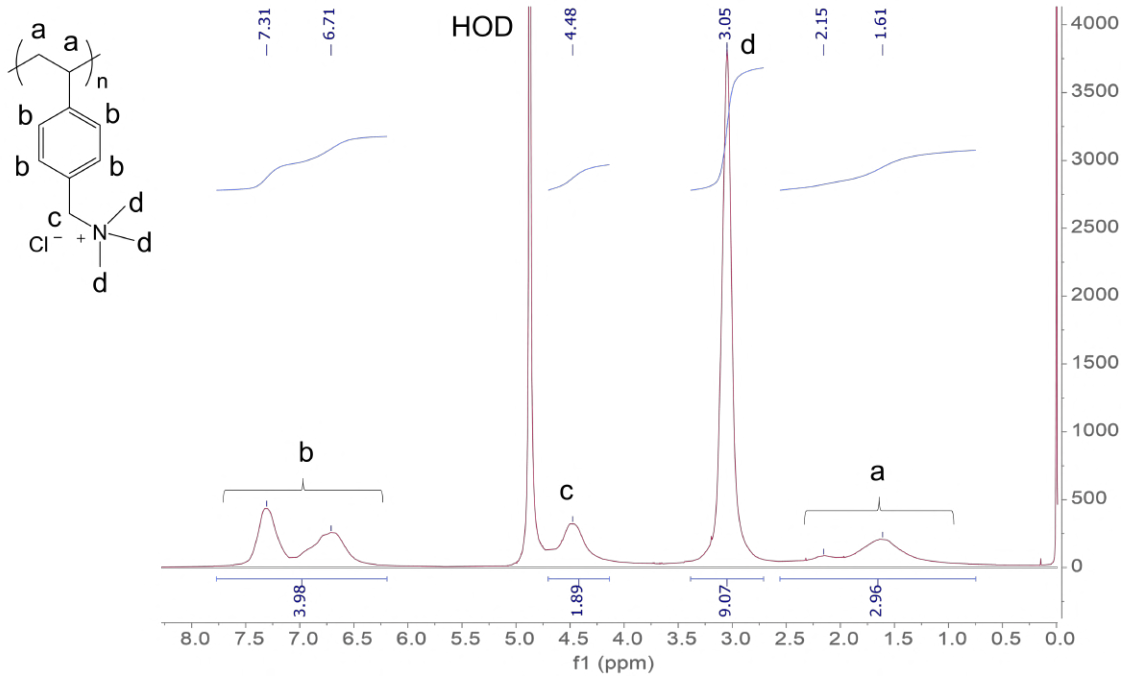

Figure 4.10. NMR spectrum of PVBT.

Poly((vinylbenzyl)trimethyl ammonium chloride) (PVBT) (Fig. 4.10) was synthesized by dissolving VBT (945 mmol, 200 g) and ACVA (0.33 mmol, 93 mg) in 1.5 L of DI H_2O. The solution was sparged with argon at a high flow rate for 45 minutes before being heated to 65 °C for 12 hours. The reaction solution was purified the same way as PSS, resulting in pure PVBT as a white powder.

Poly(sulfobetaine methacrylate)-b-poly((vinybenzyl)trimethylammonium chloride) (PSB_{100}-b-$PVBT_{20}$) was synthesized according to the synthesis route depicted in Figure 4.1. First, poly(sulfobetaine methacrylate) (PSB_{100}) (Fig. 4.11) was synthesized by dissolving SBMA (71.6 mmol, 20.0g), VA-044 (0.0500 mmol, 16.2 mg), and CPhPA (0.5000 mmol, 139.9 mg) in 100 ml of 4:1 (v/v) acetate buffer/ethanol cosolvent. The solution was sparged with nitrogen gas for 30 minutes, heated to 50 °C for 6.5 hours, and quenched in liquid nitrogen. The polymer was precipitated in 20 times the volume of methanol and

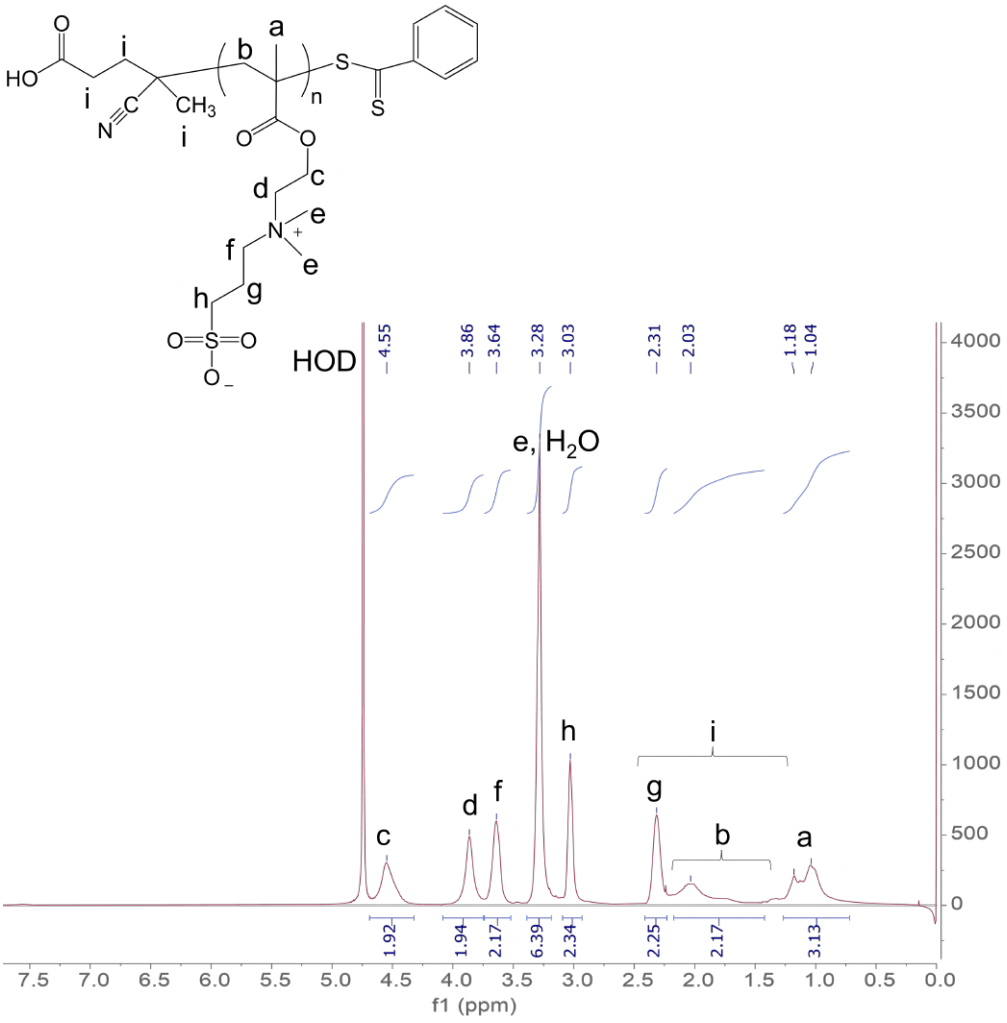

Figure 4.11. NMR spectrum of PSB.

redissolved in 0.5 M NaCl a total of three times. The polymer was dried under vacuum. Conversion: 70%.

To synthesize PSB_{100}-b-$PVBT_{20}$ (Fig. 4.12), PSB_{100} (5.00 g), VBT (4.46 mmol, 945.2 mg), and VA-044 (0.0179 mmol, 5.78 mg) were dissolved in 11.3 mL of 4:1 (v/v) acetate buffer/ethanol cosolvent. The solution was sparged with nitrogen gas for 20 minutes and heated to 50 °C for 18 hours. The polymer was precipitated in 20 times the volume of methanol and redissolved in 30 mL of 7:1 (v/v) acetate buffer/ethanol cosolvent. The polymer was re-precipitated in 10 times the volume of methanol, and the supernatant was cen-

trifuged at 4000 g's for 30 minutes. The precipitates were collected and washed with excess acetone. The polymer was lyophilized for 24 hours.

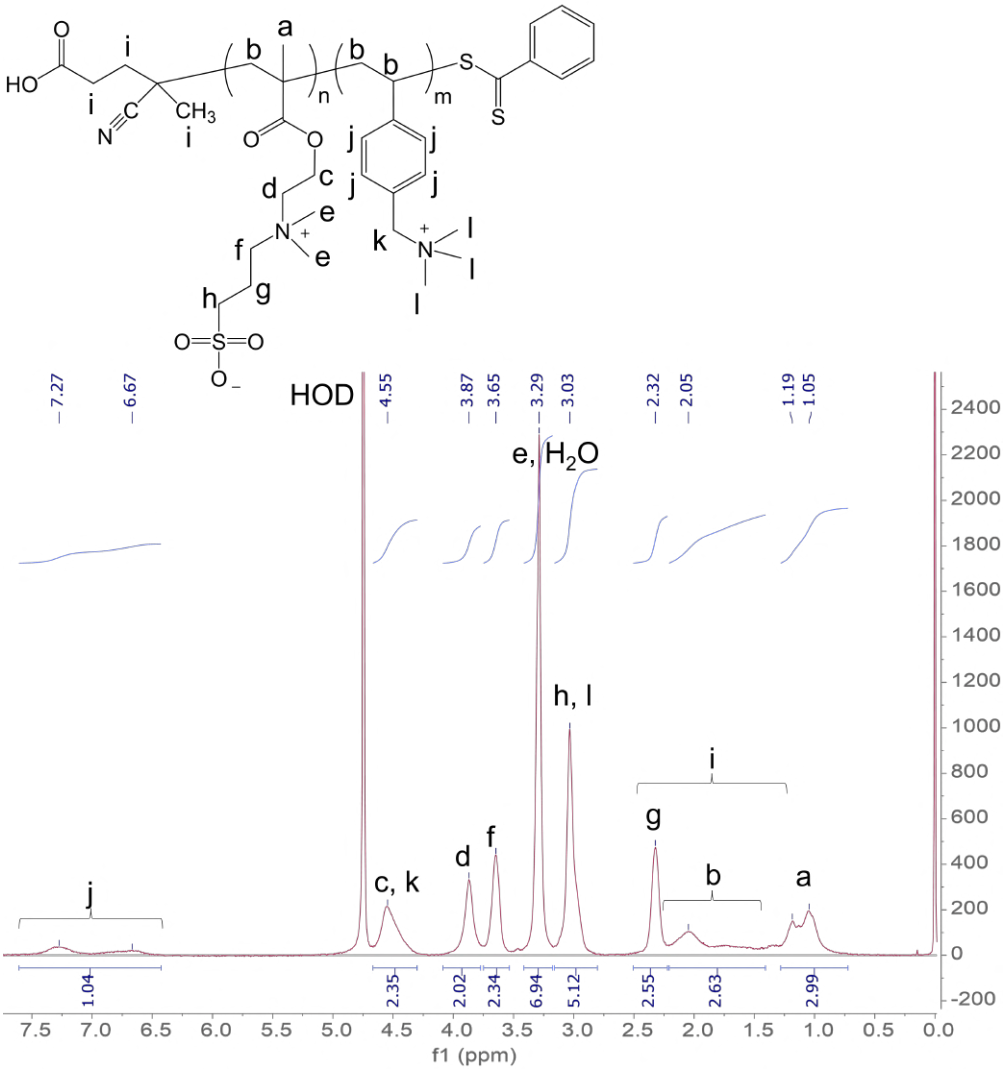

Figure 4.12. NMR spectrum of PSB-b-PVBT.

Poly(2-methacryloyloxyethyl phosphorylcholine)-b-poly((vinylbenzyl)trimethylammonium chloride) ($PMPC_{100}$-b-$PVBT_{20}$) was synthesized according to the synthesis route depicted in Figure 4.2. To synthesize poly(2-methacryloyloxyethyl phosphorylcholine) ($PMPC_{100}$), MPC (5.11 mmol, 1.51 g), ACVA (0.00407 mmol, 1.14 mg), and CPhPA (0.0408 mmol, 11.4 mg) were dissolved in 6.42 mL of methanol. The solution was sparged with nitrogen gas for 20 minutes, heated to 60 °C for 22.5 hours, and quenched in liquid nitrogen. The polymer

was precipitated in 20 times the volume of acetone and redissolved in methanol a total of three times. The polymer was collected by dissolving it in methanol. Then, the solution was dried via rotary evaporator and under vacuum overnight. Conversion: 75%.

To synthesize $PMPC_{100}$-b-$PVBT_{20}$ (Fig. 4.13), $PMPC_{100}$ (601 mg), VBTMA (0.540 mmol, 114.4 mg), and VA-044 (0.00216 mmol, 0.697 mg) were dissolved in 1.4 mL of 3:1 (v/v) acetate buffer/ethanol cosolvent and purged with nitrogen gas for 20 minutes. The solution was heated to 50 °C for 18 hours, and the reaction was stopped by opening the flask to air under room temperature. The polymer was precipitated in 20 times the volume of acetone and redissolved in methanol a total of three times. The polymer was collected by dissolving it in methanol. Then, the solution was dried via rotary evaporator and under vacuum overnight.

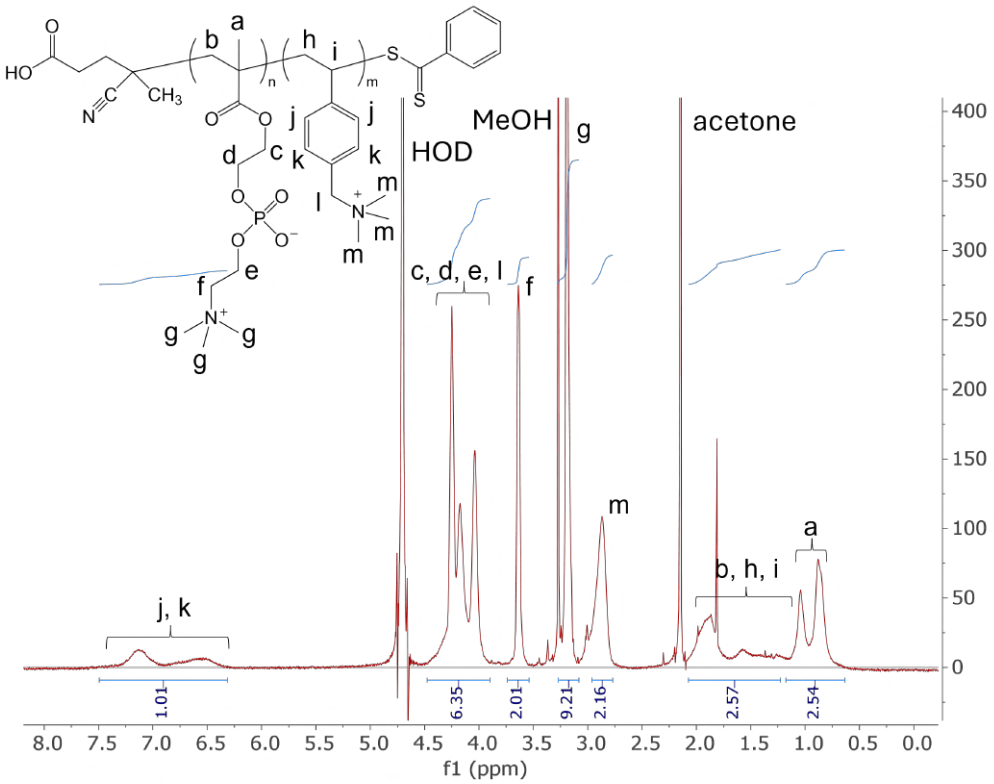

Figure 4.13. NMR spectrum of PMPC-b-PVBT.

Poly(glycidyl methacrylate) (PGMA) (Fig. 2.20) was synthesized by dissolving 10.0

g GMA (70.3 mmol), 23 mg AIBN (0.14 mmol), and 156 mg CPBD (0.703 mmol) were dissolved in 30 mL DMF. The solution was sparged with nitrogen gas for 30 minutes and reacted at 65 °C for 18 hours. The polymer was precipitated in over 10 times the volume of cold methanol and re-dissolved in DCM. The polymer was precipitated twice more and dried under vacuum for two days.

4.4.3 Zwitterionic self-assembled monolayer

For assembling zwitterionic polymer brush on hydrogels, hydrogel discs were transferred to 48-well plates. 150 µL of PVBTMA solution (30 mg/mL in PBS) was added, and the hydrogel in solution was shaken for 1 hour. The PVBTMA solution was discarded, and the hydrogels were washed with 1 mL of PBS three times. The previous steps were repeated except PSS solution (30 mg/mL in PBS) was used instead of PVBTMA solution. Then, 150 µL of PSB_{100}-b-$PVBT_{20}$ solution (13 wt% in PBS with 0.5 M total NaCl) was added and shaken for 1 hour. The solution was discarded, and the hydrogels were washed three times in PBS with 0.5 M total NaCl. Then, the hydrogels were washed once with regular PBS and soaked in PBS overnight.

4.4.4 In vitro protein adsorption test

Human plasma adsorption on the hydrogels was evaluated using the 3-(4-Carboxybenzoyl) quinoline-2-carboxaldehyde (CBQCA) assay. Hydrogel samples (5 mm in diameter and 1 mm in thickness) were incubated in 150 µL of human plasma (Innovative Research, Inc.) in 48-well plates at 37°C for 2 hours. The hydrogels were washed with 1 mL of PBS 5 times and transferred to 96-well U-bottom plates. 150 µL of 1% SDS-PBS solution was added and shaken for 1 hours. 75 µL of the protein-SDS solution was transferred to 96-well flat bottom plates and diluted with 60 µL of PBS. Then, CBQCA assay was directly carried out to determine the relative amount of proteins adsorbed on the hydrogels. The fluorescence

intensities at 550 nm (excitation/emission of 465/550 nm) were recorded using the TECAN Inifinite M200 Pro plate reader.

4.4.5 Fabrication of electrodes

ECG electrodes were fabricated using procedures shown in Supplementary Fig. 53. First, an oxygen plasma-treated 2"x3" glass slides were thoroughly washed with acetone, water, and isopropanol. To the washed slides, 2% solution of Micro-90 was spin coated at 1000 RPM and dried at 90 °C for a minute. On the glass slides, 5 µm thick layers of Parylene C was deposited using the PDS 2010 LabcoterTM 2 (Specialty Coating Systems). AZ 5214-E photoresist (MicroChemicals) was spin coated on the Parylene C and patterned using the Maskless Aligner MLA 150 (Heidelberg Instruments), followed by a photoresist descum process with O_2 plasma. Then, physical vapor deposition of 10/50 nm of Ti/Au using the EvoVac (Angstron Engineering) was carried out. The photoresist-Ti/Au stack was lifted off in acetone at 40 °C for 1 hour.

To achieve stable adhesion of PEDOT:PSS, PGMA (5 mg/mL in 95/5 $CHCl_3$/chlorobenzene) was spin coated at 2000 RPM and baked at 120 °C for 30 minutes, followed by rinsing with $CHCl_3$ to form a monolayer. Then, PEDOT:PSS (13% 1:13 Triton X-100:DMSO) was spin coated at 300 RPM. Then, the film was baked at 120 °C for 30 minutes. The baked film was rinsed with DI H_2O and blow dried.

Once the hydrogel films were prepared, the outlines of the electrodes were cut with a laser cutter. To enable wired connections to the electrodes, a wet swab was used to remove the hydrogel films on top of the Au contact pads, and 0.005" Ag wires with 0.007" PFA insulation (A-M Systems) were attached to the contact pads with lead-free low temperature solder (Sn42Bi57Ag1, ChipQuik). 50 mg/mL TPU in THF was manually pipetted to cover the Au areas and dried under ambient conditions. Devices were peeled off, rinsed in DI H_2O, and dried on a polystyrene surface under ambient conditions.

The devices and self-assembly solutions were autoclaved at 121 °C for 30 minutes. The devices were not peeled off the glass supporting substrate before autoclaving. The polymer self-assembly was carried out in a biosafety cabinet. The devices were covered with PVBT solution (30 mg/mL in PBS) and incubated for 30 minutes. The PVBT solution was discarded, and the devices were thoroughly rinsed with sterile PBS and blow dried. The previous steps were repeated except PSS solution (30 mg/mL in PBS) was used instead of PVBT solution. Next, the devices were covered with PSB_{100}-b-$PVBT_{20}$ solution (13 wt% in PBS with 0.5 M total NaCl) and incubated for 30 minutes. The solution was discarded, and the devices were rinsed thoroughly in sterile PBS with 0.5 M total NaCl and blow dried. Then, the hydrogels were washed once with regular sterile PBS and blow dried.

4.4.6 Electrode-housing assembly

The ends of the Ag wires not soldered to the electrodes were attached to jumper wire female connectors via lead-free solder (Sn99.3Cu0.7, Yihua). The connectors were threaded through the holes of modified two-channel vascular access buttons (Instech) and were secured with a combination of Red Epoxy (Highside Chemicals) and super glue. The full assembly was sterilized in an autoclave at 121°C for 30 minutes before implantation.

4.4.7 Electrode implantation surgeries

6- to 8-week-old male C57BL/6 mice were purchased from Jackson Laboratories. Preoperatively, all mice received subcutaneous injections of 5 mg/kg of Meloxicam for pre-surgery analgesia. All mice were anesthetized using 2-4% isoflurane in oxygen, and the backs of all mice were shaved. All mice received eye lubricants to prevent dehydration-induced blindness. Then, the shaved backs of all mice were sterilized by scrubbing with betadine and alcohol pads in an alternating fashion, repeated two times.

One longitudinal incision, 2 cm in length, was made in the mid-back region. The blade

tips of a pair of scissors were inserted into the subcutaneous space through the incisions, and two subcutaneous pockets, flanking the incision, were made via blunt tissue dissection using the blunt sides of a pair of scissors. After carefully exposing the subcutaneous musculature by pulling back the skin on one flank, an electrode was placed on the lower, lateral side of the latissimus dorsi. For PEDOT:PSS-Dex, a Dex-PDMS backing (∼100 µm thickness) was placed on top of the electrodes. A tissue adhesive (∼100 µm thickness) was placed on top of the electrodes so that a slight overhang around the edges of the electrode adhered to the tissue underneath. The electrode placement procedure was repeated for the other subcutaneous pocket. Then, the felt attached to the vascular access button was tucked underneath the skin, and the remaining incisions longitudinally flanking the vascular access button were closed with wound clips. Following surgery, all mice were given subcutaneous injections of 5 mg/kg of Meloxicam once every 24 hours for two days. Wound clips were removed after 10 days.

"From the moment I understood the weakness of my flesh, it disgusted me. I craved the strength and certainty of steel. I aspired to the purity of the blessed machine. Your kind cling to your flesh as if it will not decay and fail you. One day the crude biomass that you called a temple will wither and you'll beg my kind to save you. But I am already saved. For the machine is immortal. Even in death I serve the Omnissiah." — Magos Dominus Reditus*

*Bulwark Studios. (2018). Warhammer 40,000: Mechanicus [Video game]. Kasedo Games.

4.4.8 Chronic electrocardiographic recording

First, a mouse was anesthetized using 2-4% isoflurane in oxygen. The protective cap for the external connectors were removed, and the female jumper wire connectors were connected to a custom-built amplifier. An adhesive electrocardiography patch was attached to the

tail and connected to ground. Signal acquisition was carried out using the Keithley 2450 (Tektronix).

4.5 References

1. Cao, B. *et al.* Integrated zwitterionic conjugated poly(carboxybetaine thiophene) as a new biomaterial platform. *Chemical Science* **6,** 782–788. ISSN: 2041-6520. (2026) (Jan. 2015).
2. Cao, B. *et al.* Electroactive poly(sulfobetaine-3,4-ethylenedioxythiophene) (PSBEDOT) with controllable antifouling and antimicrobial properties. *Chemical Science* **7,** 1976–1981. ISSN: 2041-6520. (2026) (Mar. 2016).
3. Zhao, H. *et al.* Controlled Protein Absorption and Cell Adhesion on Polymer-Brush-Grafted Poly(3,4-ethylenedioxythiophene) Films. *ACS Applied Materials & Interfaces* **5,** 4536–4543. ISSN: 1944-8244. (2026) (June 2013).
4. Lin, C.-H. & Luo, S.-C. Combination of AFM and Electrochemical QCM-D for Probing Zwitterionic Polymer Brushes in Water: Visualization of Ionic Strength and Surface Potential Effects. *Langmuir* **37,** 12476–12486. ISSN: 0743-7463. (2026) (Oct. 2021).
5. Kim, N. *et al.* Highly Conductive PEDOT:PSS Nanofibrils Induced by Solution-Processed Crystallization. *Advanced Materials* **26,** 2268–2272. ISSN: 1521-4095. (2026) (2014).
6. Wang, Y. *et al.* A highly stretchable, transparent, and conductive polymer. *Science Advances* **3,** e1602076. (2026) (Mar. 2017).
7. Jiang, Y. *et al.* Topological supramolecular network enabled high-conductivity, stretchable organic bioelectronics. *Science* **375,** 1411–1417. (2026) (Mar. 2022).
8. Lang, U., Müller, E., Naujoks, N. & Dual, J. Microscopical Investigations of PEDOT:PSS Thin Films. en. *Advanced Functional Materials* **19.** _eprint: https://advanced.onlinelibrary.wiley.com/doi/pdf/10.1002/adfm.200801258, 1215–1220. ISSN: 1616-3028. (2026) (2009).
9. Takano, T., Masunaga, H., Fujiwara, A., Okuzaki, H. & Sasaki, T. PEDOT Nanocrystal in Highly Conductive PEDOT:PSS Polymer Films. *Macromolecules* **45,** 3859–3865. ISSN: 0024-9297. (2026) (May 2012).
10. Ishihara, K. Biomimetic materials based on zwitterionic polymers toward human-friendly medical devices. *Science and Technology of Advanced Materials* **23,** 498–524. ISSN: 1468-6996. (2026) (Dec. 2022).
11. Ueda, T., Oshida, H., Kurita, K., Ishihara, K. & Nakabayashi, N. Preparation of 2-Methacryloyloxyethyl Phosphorylcholine Copolymers with Alkyl Methacrylates and Their Blood Compatibility. en. *Polymer Journal* **24,** 1259–1269. ISSN: 1349-0540. (2026) (Nov. 1992).
12. Chu, M. *et al.* A soft and flexible biosensor using a phospholipid polymer for continuous glucose monitoring. en. *Biomedical Microdevices* **11,** 837–842. ISSN: 1572-8781. (2026) (Aug. 2009).

13. Xie, X. *et al.* Reduction of measurement noise in a continuous glucose monitor by coating the sensor with a zwitterionic polymer. en. *Nature Biomedical Engineering* **2,** 894–906. ISSN: 2157-846X. (2026) (Dec. 2018).

14. Lee, H., Dellatore, S. M., Miller, W. M. & Messersmith, P. B. Mussel-Inspired Surface Chemistry for Multifunctional Coatings. *Science* **318,** 426–430. (2026) (Oct. 2007).

15. Srivastava, S. & Tirrell, M. V. en. in *Advances in Chemical Physics* _eprint: https://onlinelibrary.wiley.com/doi/pdf/10.1002/9781119290971.ch7, 499–544 (John Wiley & Sons, Ltd, 2016). ISBN: 978-1-119-29097-1. (2026).

16. Dubas, S. T. & Schlenoff, J. B. Factors Controlling the Growth of Polyelectrolyte Multilayers. *Macromolecules* **32,** 8153–8160. ISSN: 0024-9297. (2026) (Nov. 1999).

17. Zhai, L., Cebeci, F. Ç., Cohen, R. E. & Rubner, M. F. Stable Superhydrophobic Coatings from Polyelectrolyte Multilayers. *Nano Letters* **4,** 1349–1353. ISSN: 1530-6984. (2026) (July 2004).

18. Berg, M. C., Zhai, L., Cohen, R. E. & Rubner, M. F. Controlled Drug Release from Porous Polyelectrolyte Multilayers. *Biomacromolecules* **7,** 357–364. ISSN: 1525-7797. (2026) (Jan. 2006).

19. Meng, S., Ting, J. M., Wu, H. & Tirrell, M. V. Solid-to-Liquid Phase Transition in Polyelectrolyte Complexes. *Macromolecules* **53,** 7944–7953. ISSN: 0024-9297. (2026) (Sept. 2020).

20. Virga, E., Žvab, K. & de Vos, W. M. Fouling of nanofiltration membranes based on polyelectrolyte multilayers: The effect of a zwitterionic final layer. *Journal of Membrane Science* **620,** 118793. ISSN: 0376-7388. (2026) (Feb. 2021).

21. Kalasin, S., Letteri, R. A., Emrick, T. & Santore, M. M. Adsorbed Polyzwitterion Copolymer Layers Designed for Protein Repellency and Interfacial Retention. *Langmuir* **33,** 13708–13717. ISSN: 0743-7463. (2026) (Nov. 2017).

22. Shao, Q. *et al.* Differences in Cationic and Anionic Charge Densities Dictate Zwitterionic Associations and Stimuli Responses. *The Journal of Physical Chemistry B* **118,** 6956–6962. ISSN: 1520-6106. (2026) (June 2014).

23. Zhao, W. *et al.* A comprehensive study and comparison of four types of zwitterionic hydrogels. en. *Journal of Materials Science* **53,** 13813–13825. ISSN: 1573-4803. (2026) (Oct. 2018).

CHAPTER 5

CONCLUSION

The foreign body response continues to be a major hurdle for achieving long term stability and function for implantable medical devices. There have been several reported strategies to suppress the FBR, but many of them only partially suppress the FBR, have unclear prospects when translated to humans, and have questionable applicability and effectiveness for broader device types. In particular, there have been a lack of research on FBR-suppression for electronic materials. Zwitterionic polymers are a promising class of antifouling and FBR-suppressing materials. As electronic materials, PEDOT:PSS has been a popular choice because it is chemically stable, highly electrically conductive, easily processable, and non-cytotoxic. However, PEDOT:PSS has historically been challenging to chemically modify and apply coatings on for endowing it with additional useful properties, such as FBR suppression. In the first part of this dissertation, we use PEDOT:PSS and zwitterionic polymers to expand the number of FBR-suppressing strategies by exploring chemical heterogeneity as a potentially new category of strategies. Chemical heterogeneity is an important property to study because electronic IMDs rarely have chemically homogeneous surfaces due to various electronic components present on the surface. In the second part of the dissertation, we directly address the difficulty associated with chemically modifying and coating PEDOT:PSS by exploring a novel approach for achieving stable tethering of zwitterionic polymer brushes on PEDOT:PSS surfaces.

In Chapter 2, we report a new type of FBR-suppressing electronic material, zwitterionic PEDOT:PSS hydrogel (ZIPH). We devised a new solvent annealing method, consisting of ethanol and 2,2,2-trifluoroethanol, to facilitate the formation of PEDOT:PSS nanofibers in a poly(sulfobetaine methacrylate) PSB hydrogel matrix, significantly increasing the conductivity. The electrical, electrochemical, mechanical, and chemical properties were thoroughly characterized. Next, ZIPH was implanted, along with other controls, into the subcutaneous

space of mice. The fibrotic response and the immune response were thoroughly characterized. It was observed that ZIPH was associated with lower collagen densities compared to its parent materials, PEDOT:PSS and PSB. Moreover, the immune response to ZIPH was unique, significantly differing from any other material tested and diverging from its parent materials. This is the first work to demonstrate that chemical heterogeneity can lead to emergent FBR-suppressing and biointerfacing properties and could inspire the development of more FBR-suppressing materials using similar principles.

In Chapter 3, we demonstrate that the high conductivity and FBR-suppressing properties of ZIPH confers major advantages in electrophysiological applications through electrocardiography (ECG) in mice. To realize this, we solved the highly challenging problem of poor adhesion of ZIPH on a variety of substrates by devising a new strategy consisting of two monolayers of polymers. The base layer consists of poly(glycidyl methacrylate), and the top layer consists of polyallylamine. The primary amine-rich top layer was functionalized with methacrylates. Spin coated ZIPH was polymerized on top to create a robust interface. We also discussed in detail on how the ECG recordings were conducted on mice and how we designed an amplifier for this purpose. *In vivo*, ZIPH ECG electrodes experienced half the signal loss compared to PEDOT:PSS ECG electrodes over a 12 week period. Furthermore, ZIPH ECG electrodes experienced comparable signal loss compared to PEDOT:PSS ECG electrodes with dexamethasone-eluting silicone backings, an industrial gold standard for FBR suppression, without causing any of the side effects associated with dexamethasone. The work in this chapter demonstrated that ZIPH has great potential in achieving long term stability and function for IMDs.

In Chapter 4, we addressed the difficulty associated with functionalizing and coating PEDOT:PSS due to a lack of useful functional groups and its hydrophilic properties. Specifically, we solved this issue by coating PEDOT:PSS with polyelectrolyte multilayers, in which oppositely charged polymers bind to each other in a process called polyelectrlyte complex-

ation. After a base coat of polyelectrolytes, poly(sulfobetaine methacrylate)-*block*-poly((4-vinylbenzyl)trimethylammonium chloride) (PSB-b-PVBT) formed a zwitterionic polymer brush coating through self-assembly. The whole coating consisting of polyelectrolyte multilayers and PSB-b-PVBT (PET-ZIP) lowered protein adsorption levels in PEDOT:PSS to a level that is comparable to that of PSB hydrogels. Moreover, ECG recording with PEDOT:PSS electrodes coated with PET-ZIP in mice over a 12-week implantation period exhibited little to no signal loss.

Collectively, these works have addressed two problems. First, it solves the problem of PEDOT:PSS being difficult to confer FBR-suppressing properties because it is difficult to chemically modify and applying coatings to. ZIPH achieved this by physically blending PEDOT:PSS and a zwitterionic polymer. PET-ZIP achieved this by taking advantage of the electrostatic interactions PSS can have with polycations, enabling the self-assembly of zwitterionic polymer brushes on PEDOT:PSS surfaces. Second, the work on ZIPH addressed the problem of a limited existing repertoire of categories of FBR-suppressing material strategies by introducing chemical heterogeneity as a novel material strategy.

APPENDIX A

FLOW CYTOMETRY DATA

The following are additional flow cytometry data for Chapter 2.

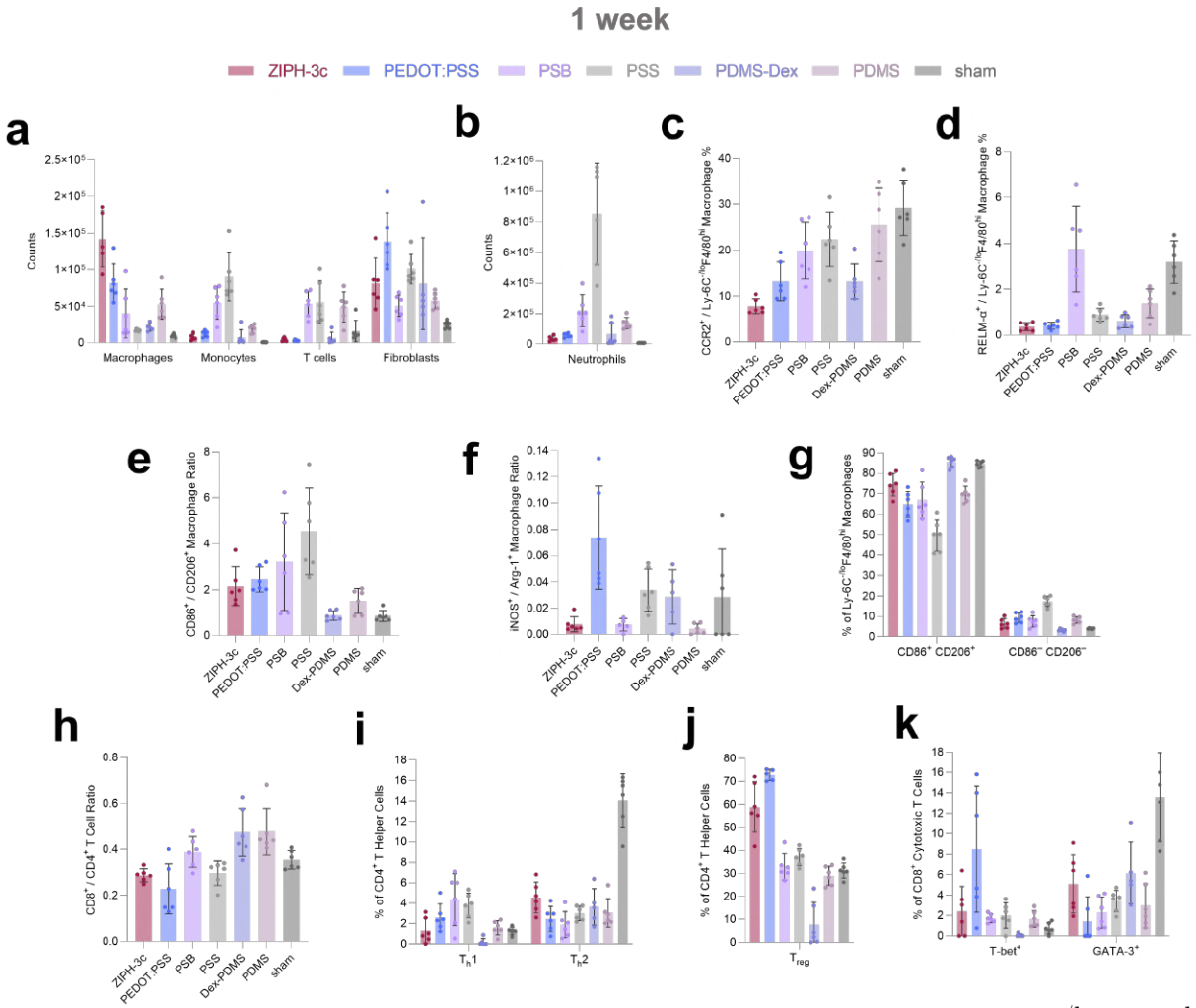

Figure A.1. Flow cytometry data for 1-week post-implantation. **a**, Total Ly-6C$^{-/\mathrm{lo}}$ F4/80$^{\mathrm{hi}}$ macrophage, Ly-6C$^{\mathrm{hi}}$ F4/80$^{\mathrm{lo}}$ monocyte, CD3^{+} T cell, and CD45$_{-}$ Lin$_{-}$ CD140a^{+} fibroblast counts. **b**, Total Ly-6G^{+} neutrophil counts. **c**, Percentage of Ly-6C$^{-/\mathrm{lo}}$ F4/80$^{\mathrm{hi}}$ macrophages that are CCR2^{+}. **d**, Percentage of Ly-6C$^{-/\mathrm{lo}}$ F4/80$^{\mathrm{hi}}$ macrophages that are RELM-α^{+}. **e**, CD86^{+} / CD206^{+} ratios among Ly-6C$^{-/\mathrm{lo}}$ F4/80$^{\mathrm{hi}}$ macrophages. **f**, iNOS^{+} / Arg-1^{+} ratios among Ly-6C$^{-/\mathrm{lo}}$ F4/80$^{\mathrm{hi}}$ macrophages. **g**, Percentages of Ly-6C$^{-/\mathrm{lo}}$ F4/80$^{\mathrm{hi}}$ macrophages that are CD86^{+} CD206^{+} (double positive) and CD86$_{-}$ CD206$_{-}$ (double negative). **h**, CD8^{+} / CD4^{+} ratios among CD3^{+} T cells. **i**, Percentage of CD3^{+} CD4^{+} T helper cells that are $\mathrm{T_h}1$ (T-bet^{+}) and $\mathrm{T_h}2$ (GATA-3^{+}). **j**, Percentage of CD3^{+} T cells that are $\mathrm{T_{reg}}$ (FoxP3^{+}). **k**, Percentage of CD3^{+} CD8^{+} cytotoxic T cells that are T-bet^{+} and GATA-3^{+}.

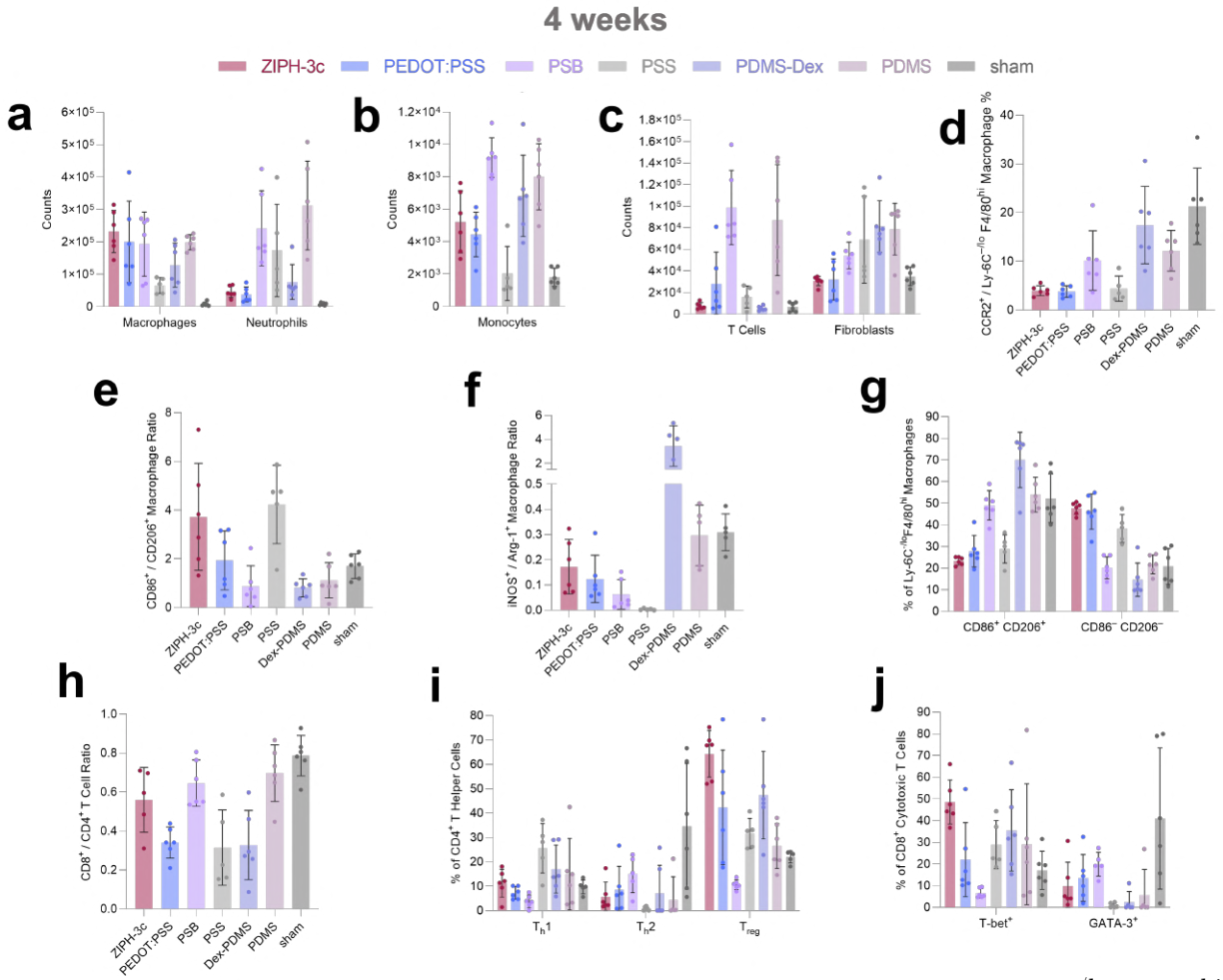

Figure A.2. Flow cytometry data for 4-week post-implantation. **a**, Total Ly-6C$^{-/lo}$ F4/80^{hi} macrophage and Ly-6G^{+} neutrophil counts. **b**, Total Ly-6C^{hi} F4/80^{lo} monocyte counts. **c**, Total CD3^{+} T cell and CD45$_{-}$ Lin$_{-}$ CD140a^{+} fibroblast counts. **d**, Percentage of Ly-6C$^{-/lo}$ F4/80^{hi} macrophages that are CCR2^{+}. **e**, CD86^{+} CD206^{+} ratios among Ly-6C$^{-/lo}$ F4/80^{hi} macrophages. **f**, iNOS^{+} / Arg-1^{+} ratios among Ly-6C$^{-/lo}$ F4/80^{hi} macrophages. **g**, Percentages of Ly-6C$^{-/lo}$ F4/80^{hi} macrophages that are CD86^{+} CD206^{+} (double positive) and CD86$_{-}$ CD206$_{-}$ (double negative). **h**, CD8^{+} / CD4^{+} ratios among CD3^{+} T cells. **i**, Percentage of CD3^{+} CD4^{+} T helper cells that are T_h1 (T-bet^{+}), T_h2 (GATA-3^{+}), and T_{reg} (FoxP3^{+}). **j**, Percentage of CD3^{+} CD8^{+} cytotoxic T cells that are T-bet^{+} and GATA-3^{+}.

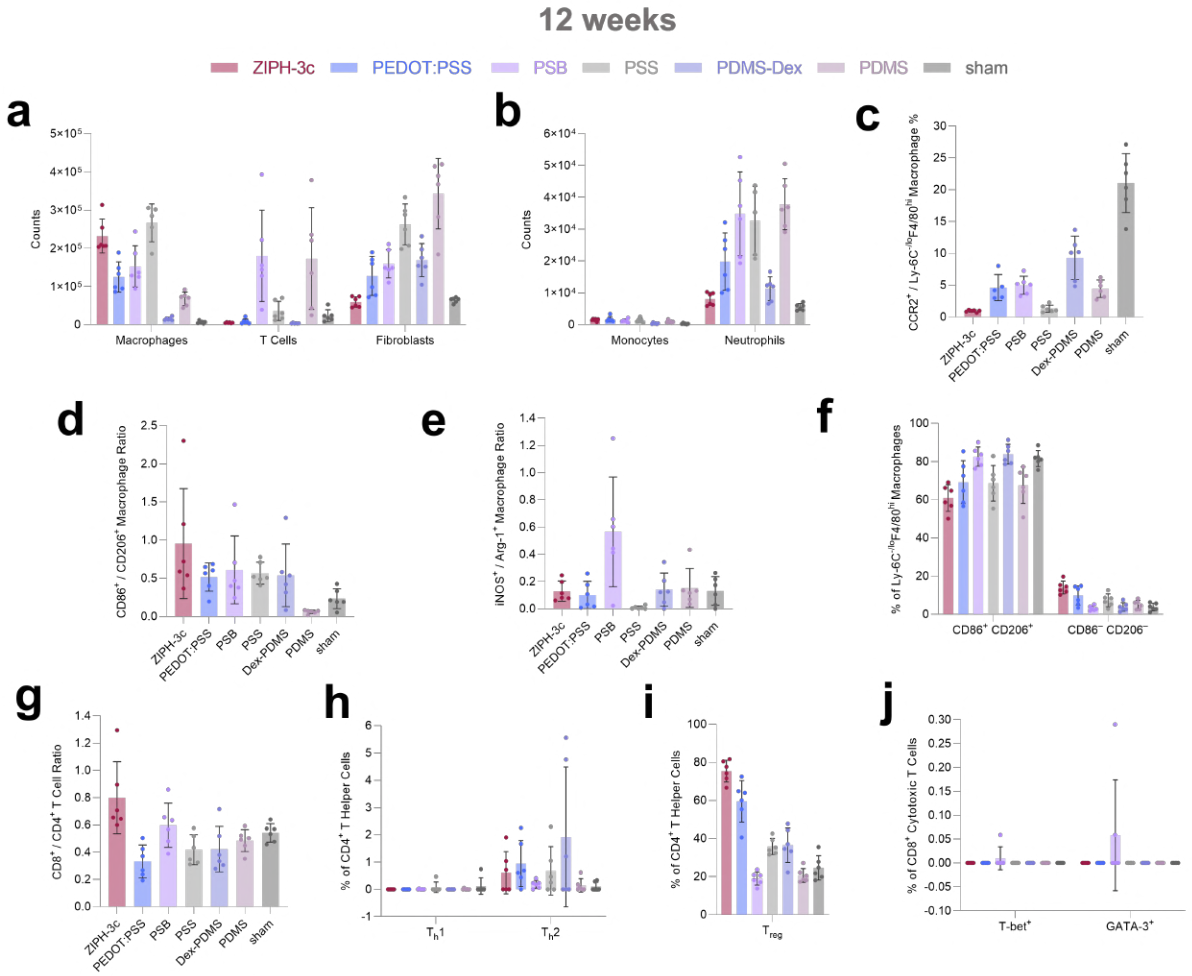

Figure A.3. Flow cytometry data for 12-week post-implantation. **a**, Total Ly-6C$^{-/lo}$ F4/80^{hi} macrophage, CD3^{+} T cell, and CD45$_{-}$ Lin$_{-}$ CD140a^{+} fibroblast counts. **b**, Total Ly-6C^{hi} F4/80^{lo} monocyte Ly-6G^{+} neutrophil counts. **c**, Percentage of Ly-6C$^{-/lo}$ F4/80^{hi} macrophages that are CCR2^{+}. **d**, CD86^{+} CD206^{+} ratios among Ly-6C$^{-/lo}$ F4/80^{hi} macrophages. **e**, iNOS^{+} / Arg-1^{+} ratios among Ly-6C$^{-/lo}$ F4/80^{hi} macrophages. **f**, Percentages of Ly-6C$^{-/lo}$ F4/80^{hi} macrophages that are CD86^{+} CD206^{+} (double positive) and CD86$_{-}$ CD206$_{-}$ (double negative). **g**, CD8^{+} / CD4^{+} ratios among CD3^{+} T cells. **h**, Percentage of CD3^{+} CD4^{+} T helper cells that are T_h1 (T-bet^{+}), T_h2 (GATA-3^{+}). **i**, Percentages of CD3^{+} CD4^{+} that are T_{reg} (FoxP3^{+}). **j**, Percentage of CD3^{+} CD8^{+} cytotoxic T cells that are T-bet^{+} and GATA-3^{+}.

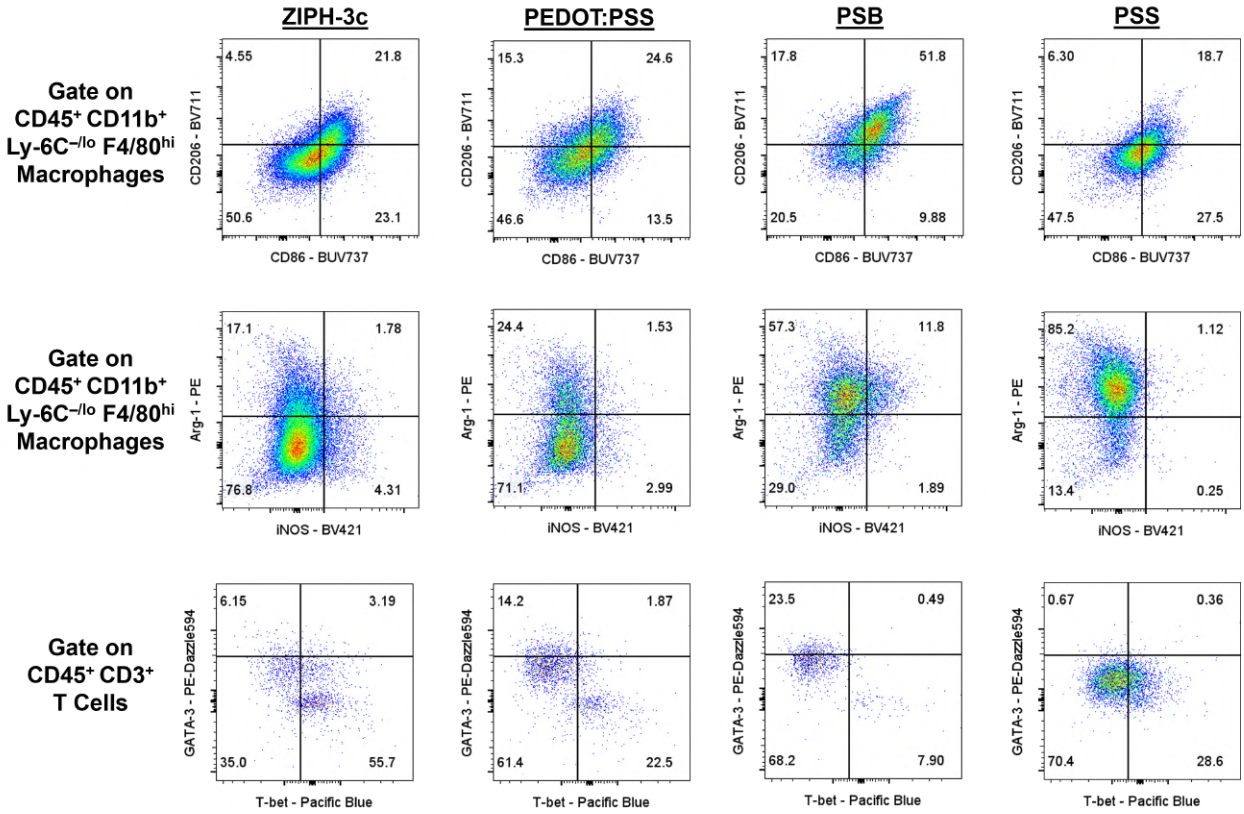

Figure A.4. Representative flow cytometry plots of CD86/CD206, iNOS/Arg-1, and T-bet/GATA-3 cross gates for ZIPH-3c, PEDOT:PSS, PSB, and PSS 4-weeks post-implantation.

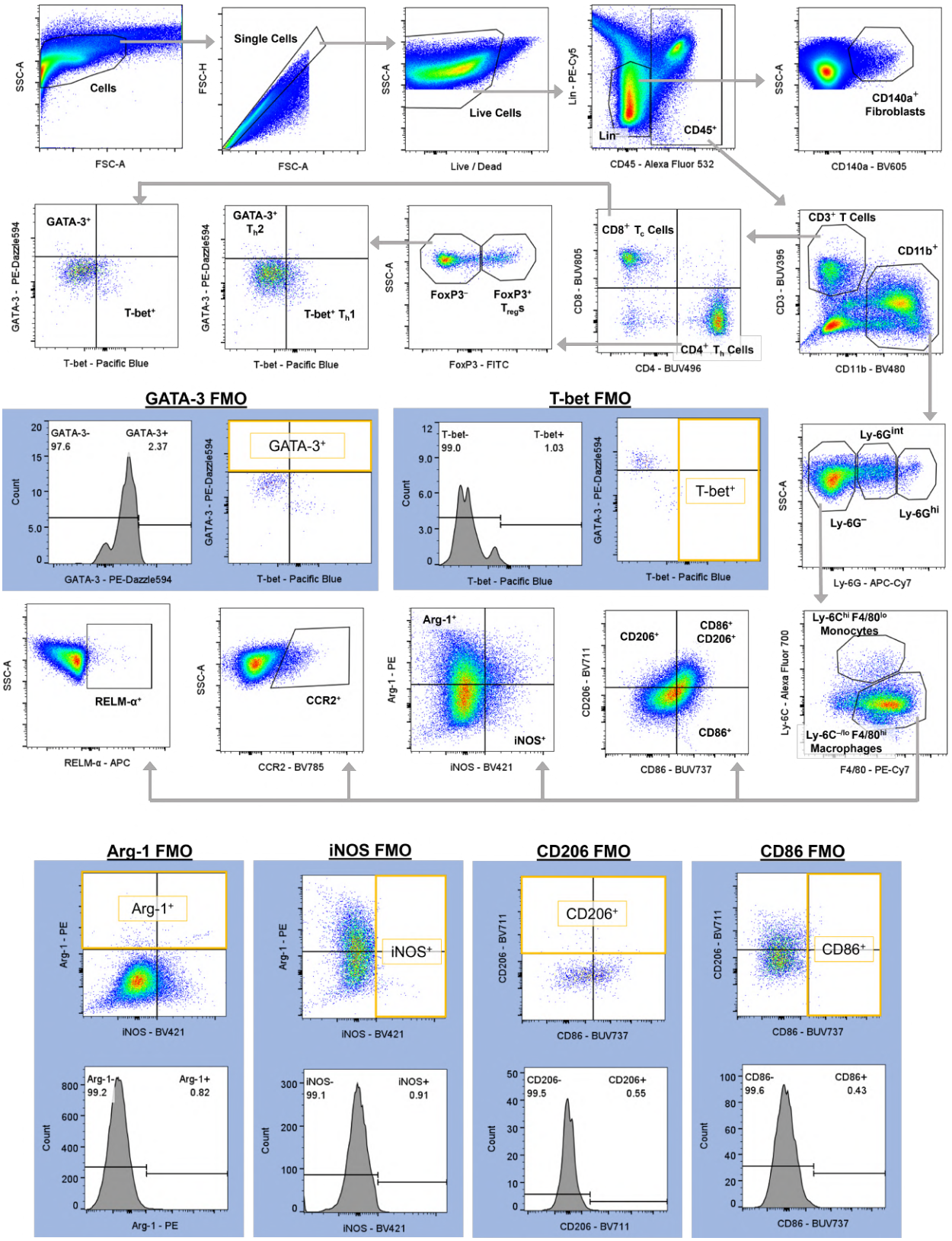

Figure A.5. Flow cytometry gating strategy for all flow cytometry experiments conducted in Chapter 2

APPENDIX B

CYTOKINE DATA

The following are additional cytokine data for Chapter 2.

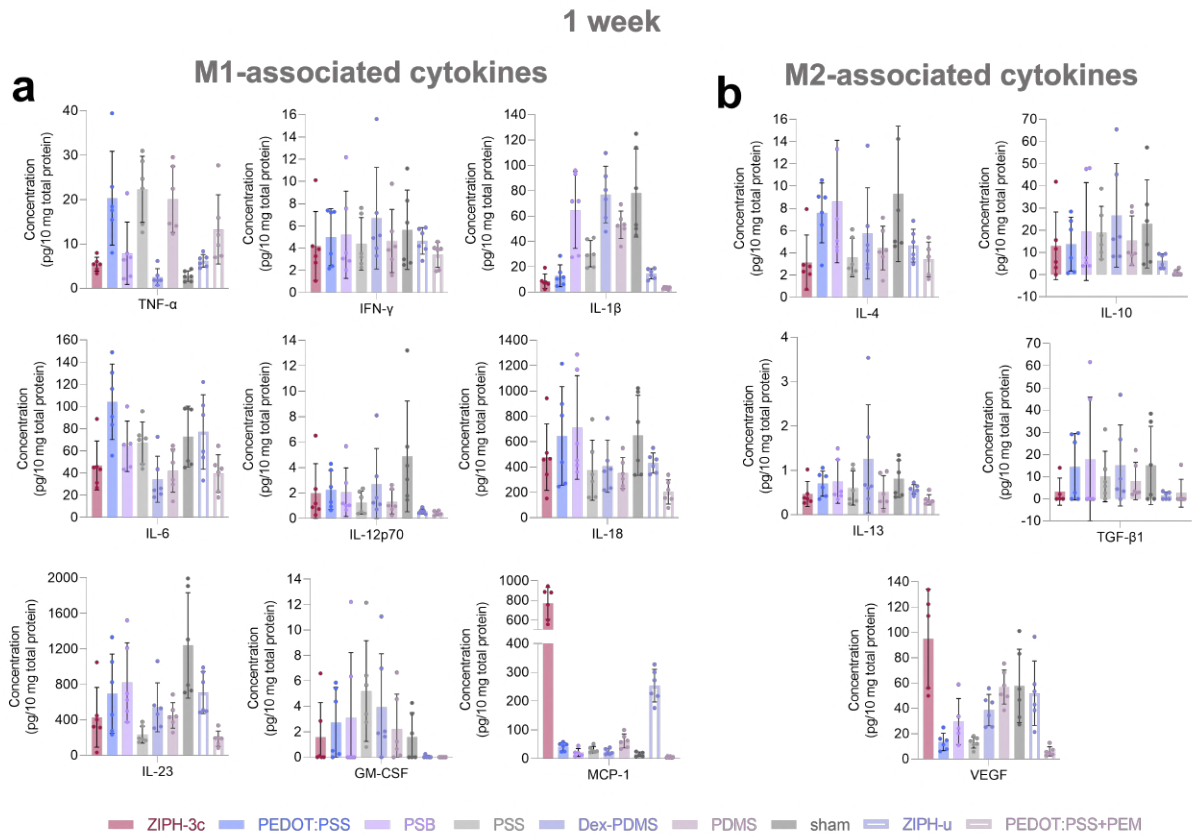

Figure B.1. Cytokine data from 1-week post-implantation. Cytokine concentrations determined via Legendplex assay divided into a, M1-associated cytokines and b, M2-associated cytokines.

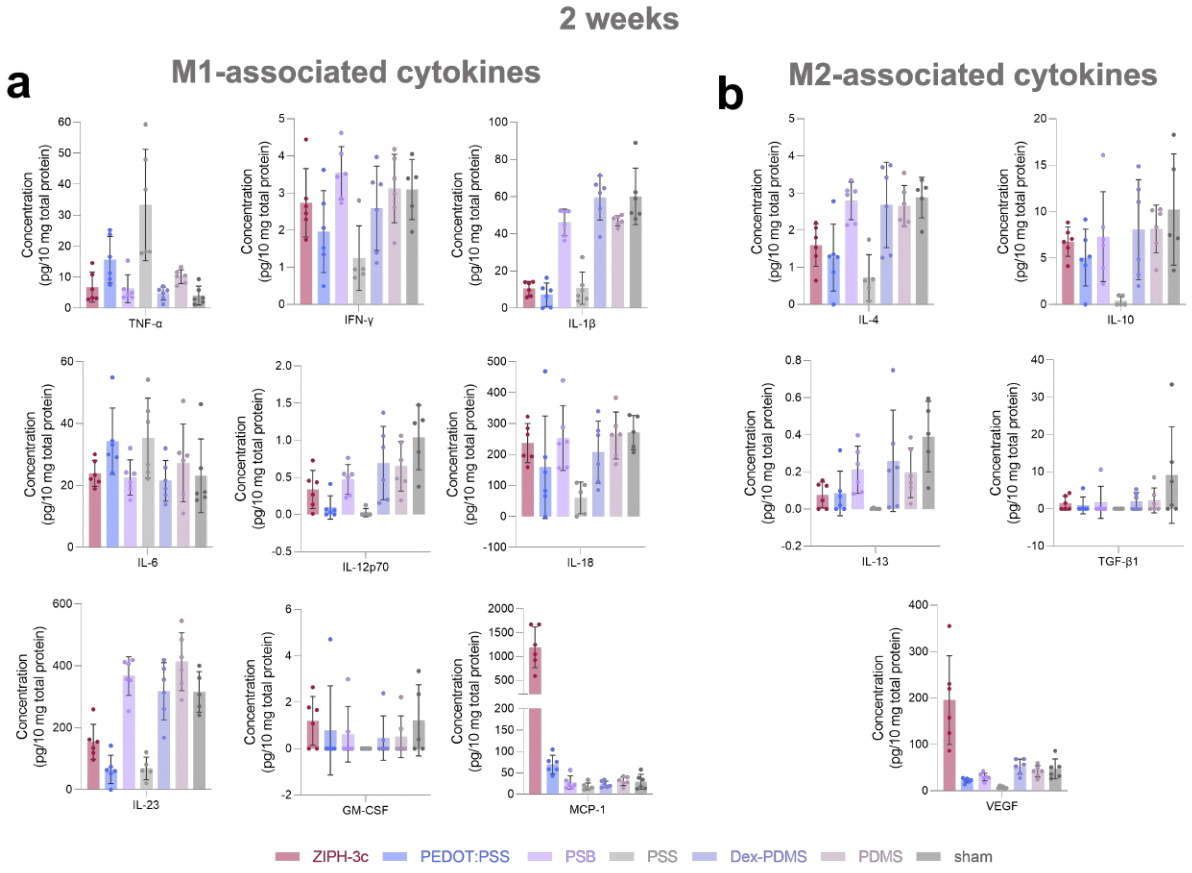

Figure B.2. Cytokine data from 2-week post-implantation. Cytokine concentrations determined via Legendplex assay divided into a, M1-associated cytokines and b, M2-associated cytokines.

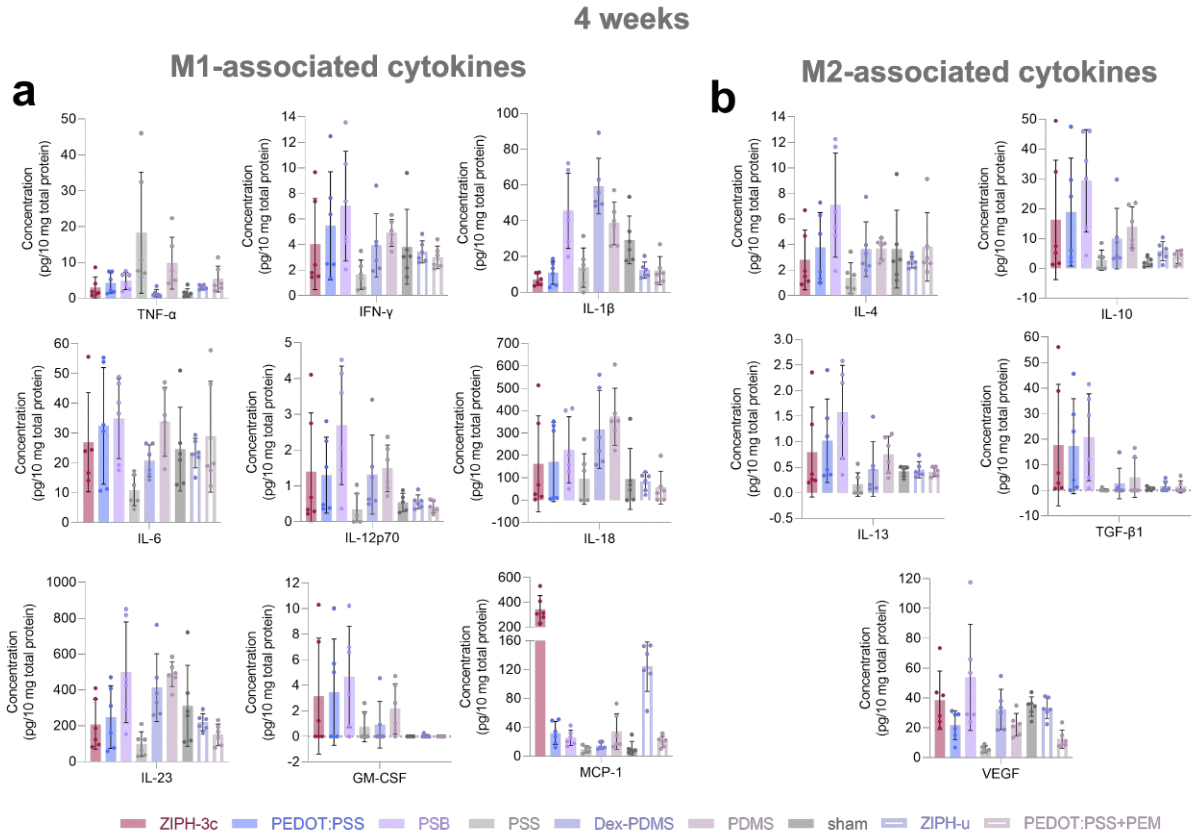

Figure B.3. Cytokine data from 4-week post-implantation. Cytokine concentrations determined via Legendplex assay divided into a, M1-associated cytokines and b, M2-associated cytokines.

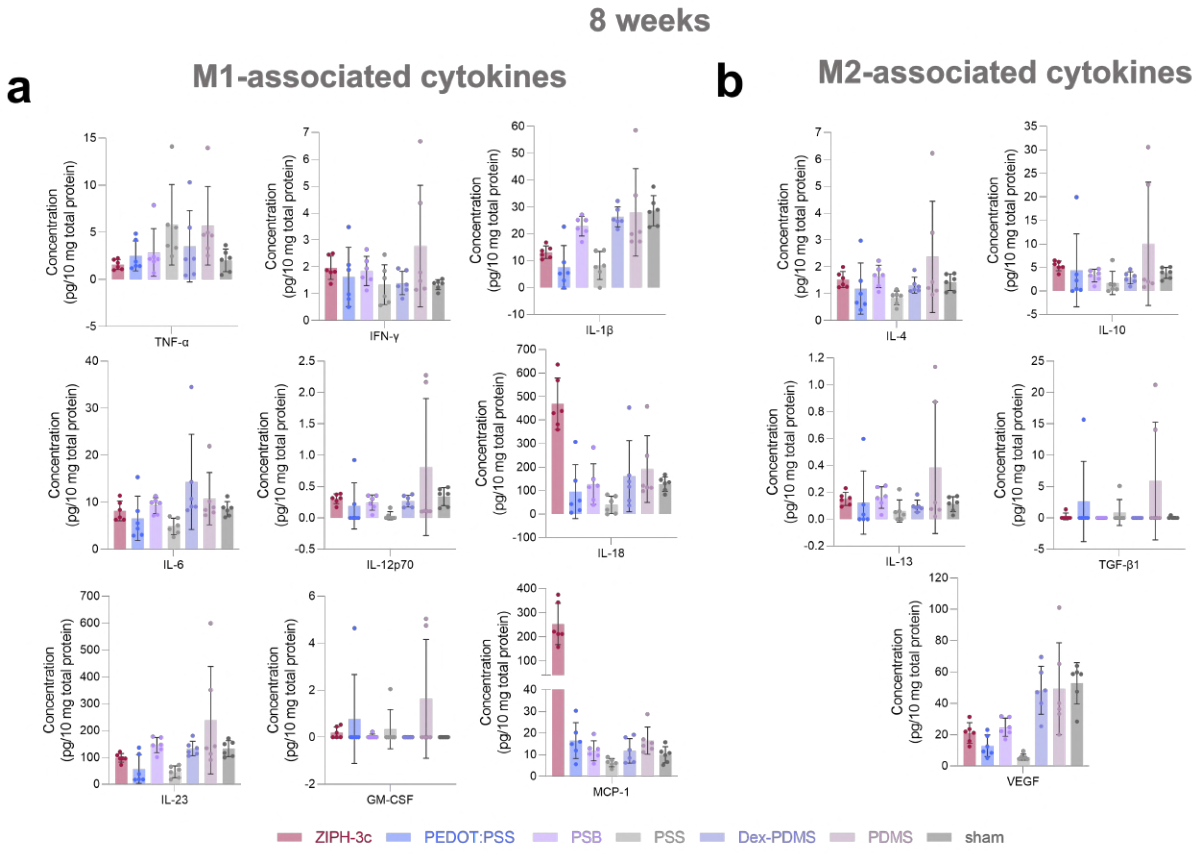

Figure B.4. Cytokine data from 8-week post-implantation. Cytokine concentrations determined via Legendplex assay divided into a, M1-associated cytokines and b, M2-associated cytokines.

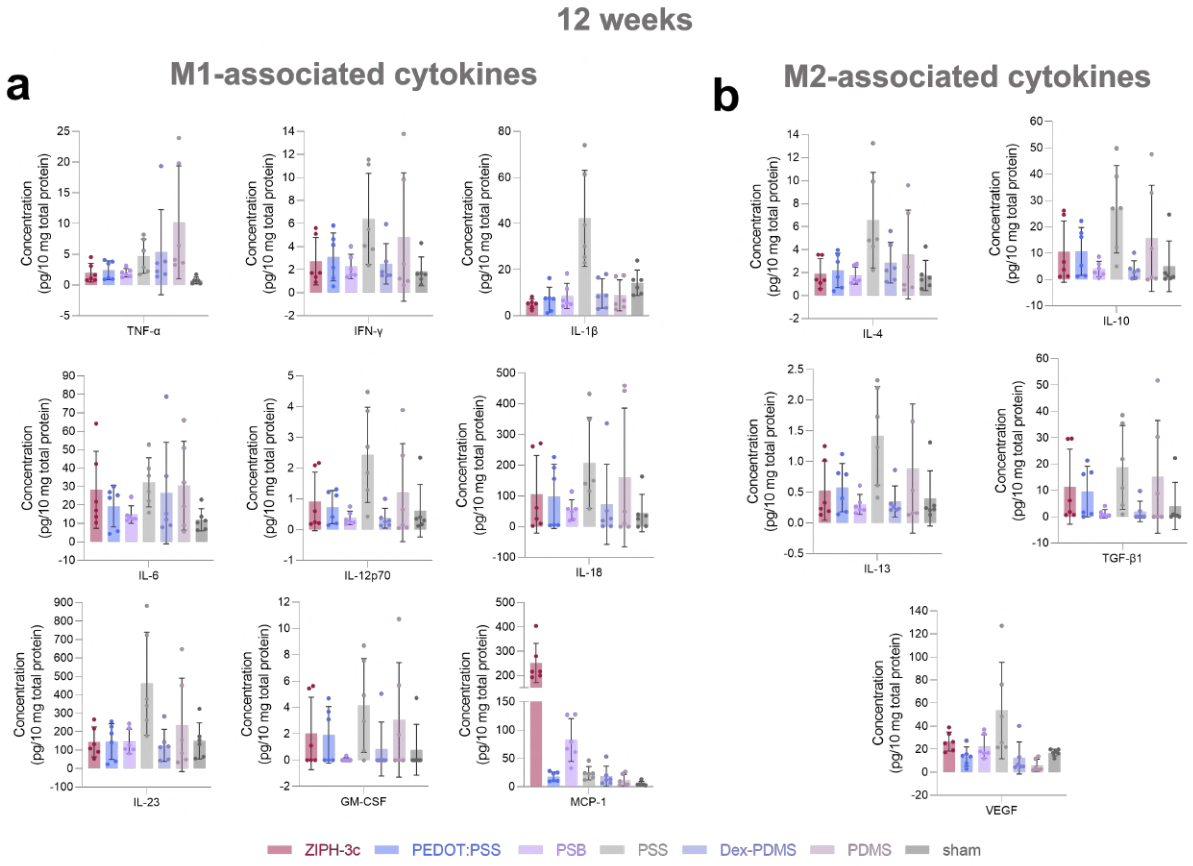

Figure B.5. Cytokine data from 12-week post-implantation. Cytokine concentrations determined via Legendplex assay divided into a, M1-associated cytokines and b, M2-associated cytokines.

APPENDIX C

RNA PROFILING DATA

The following are additional RNA profiling for Chapter 2.

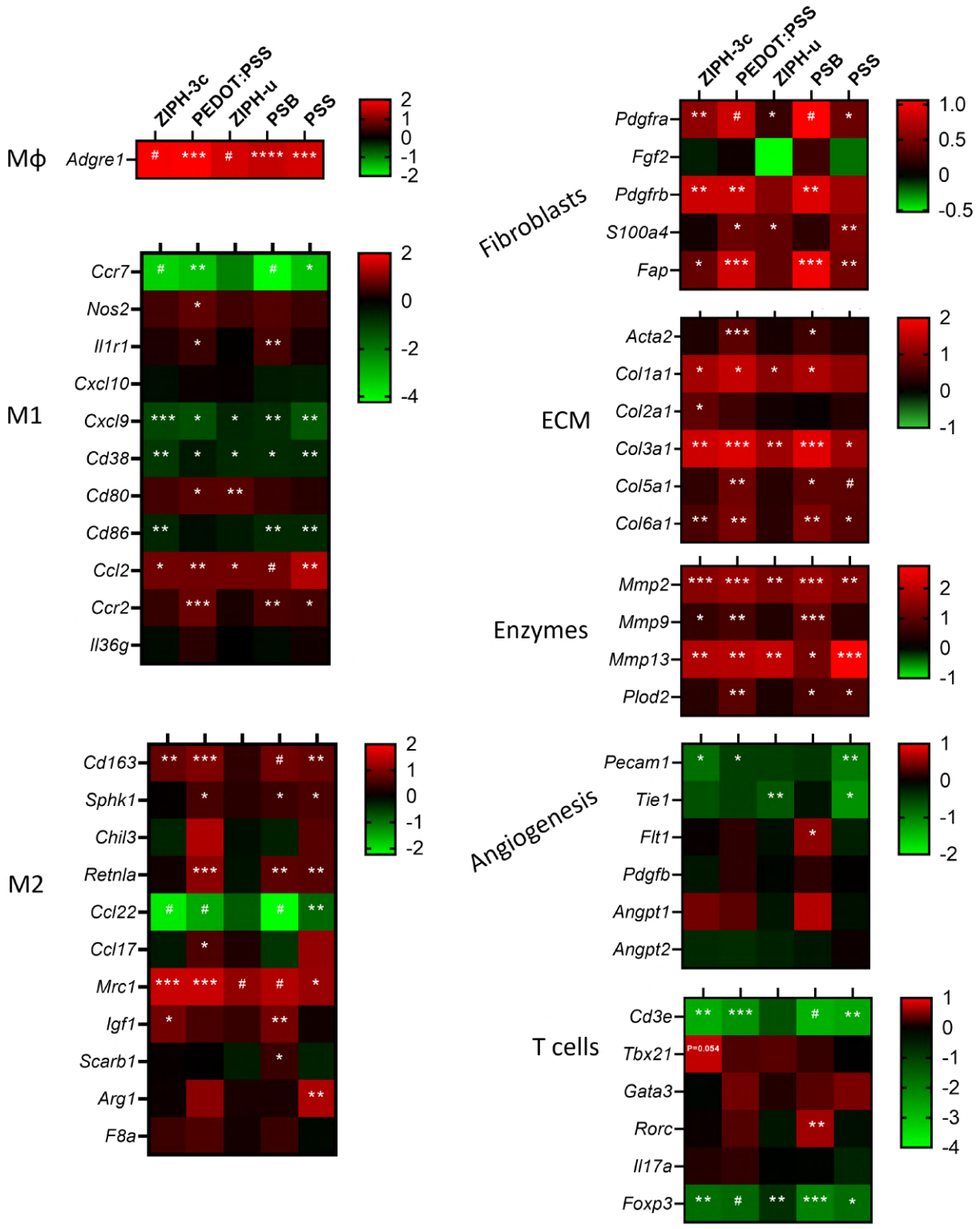

Figure C.1. Heat maps of RNA expression normalized to sham control 4-weeks post-implantation. Data were acquired using NanoString. N=4-5 mice per treatment. *, $P < 0.05$; **, $P < 0.01$; ***, $P < 0.001$; , $P < 0.0001$ compared to sham.

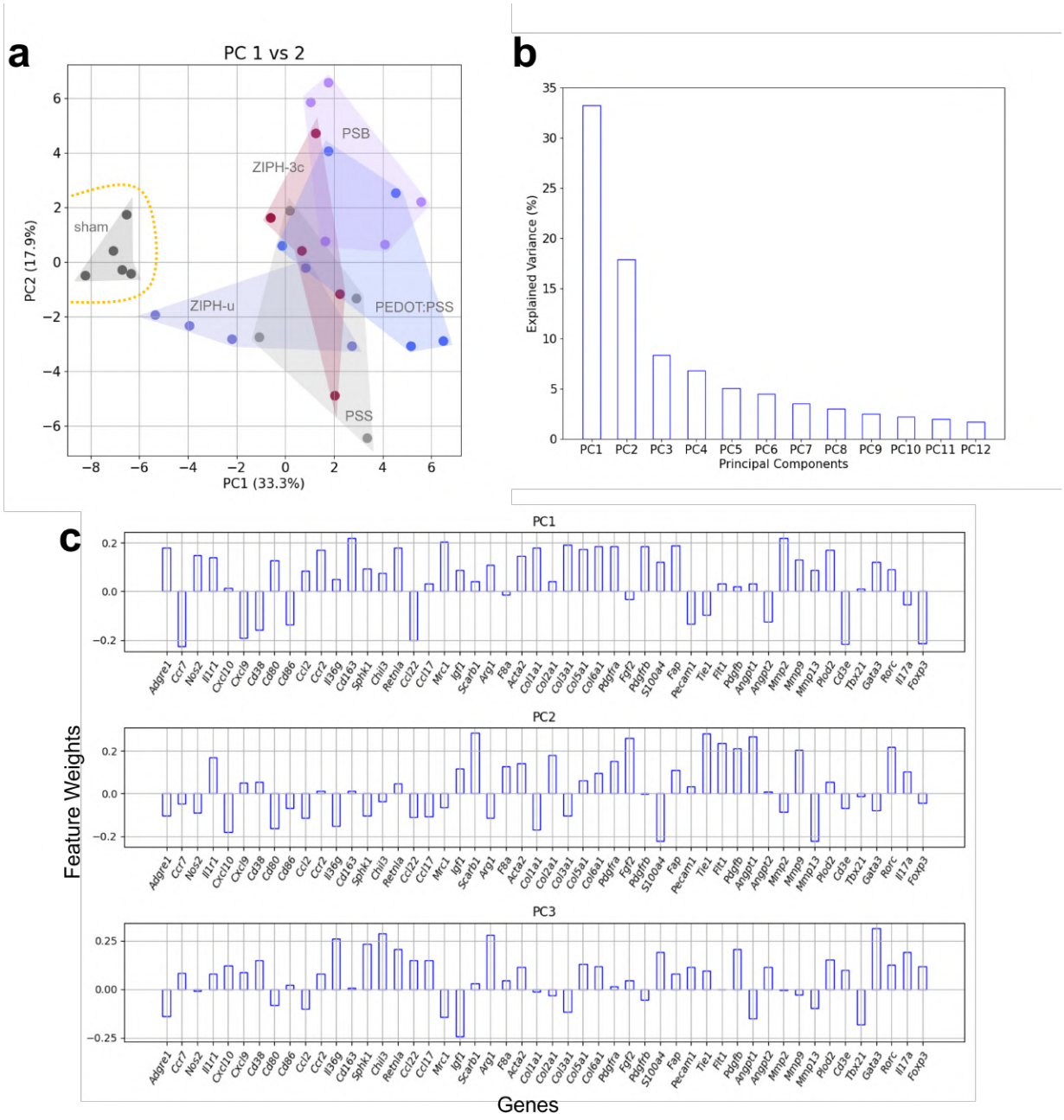

Figure C.2. Principle component analysis (PCA) of 50-genes, acquired via NanoString, 4-weeks post-implantation. **a**, Each sample plotted on PC1-PC2 vector space. **b**, Top 12 PCs and their explained variances. **c**, Genes and their associated weights for each PC.

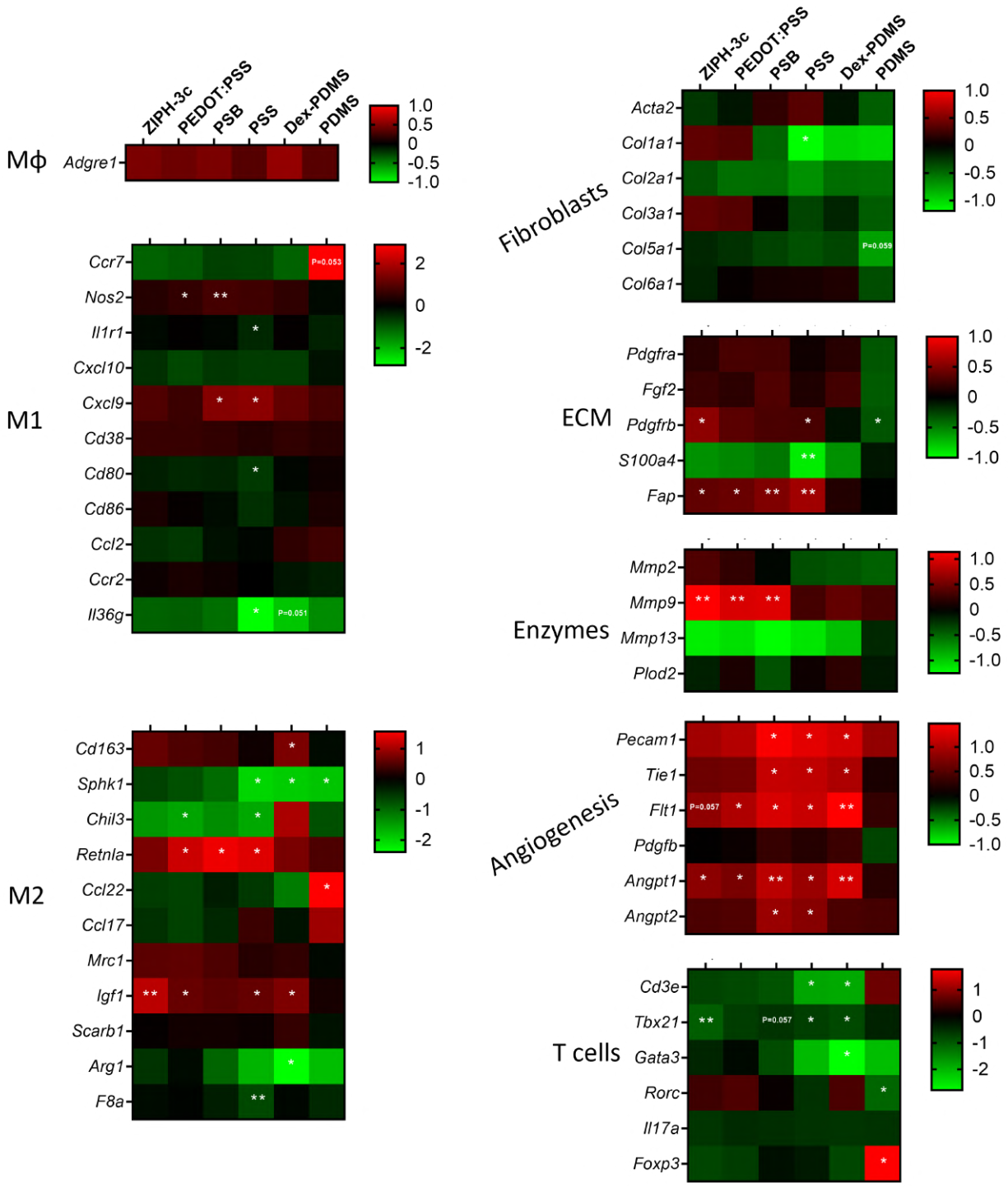

Figure C.3. Heat maps of RNA expression normalized to sham control 12-weeks post-implantation. Data were acquired using NanoString. N=4-5 mice per treatment. *, $P < 0.05$; **, $P < 0.01$ compared to sham.

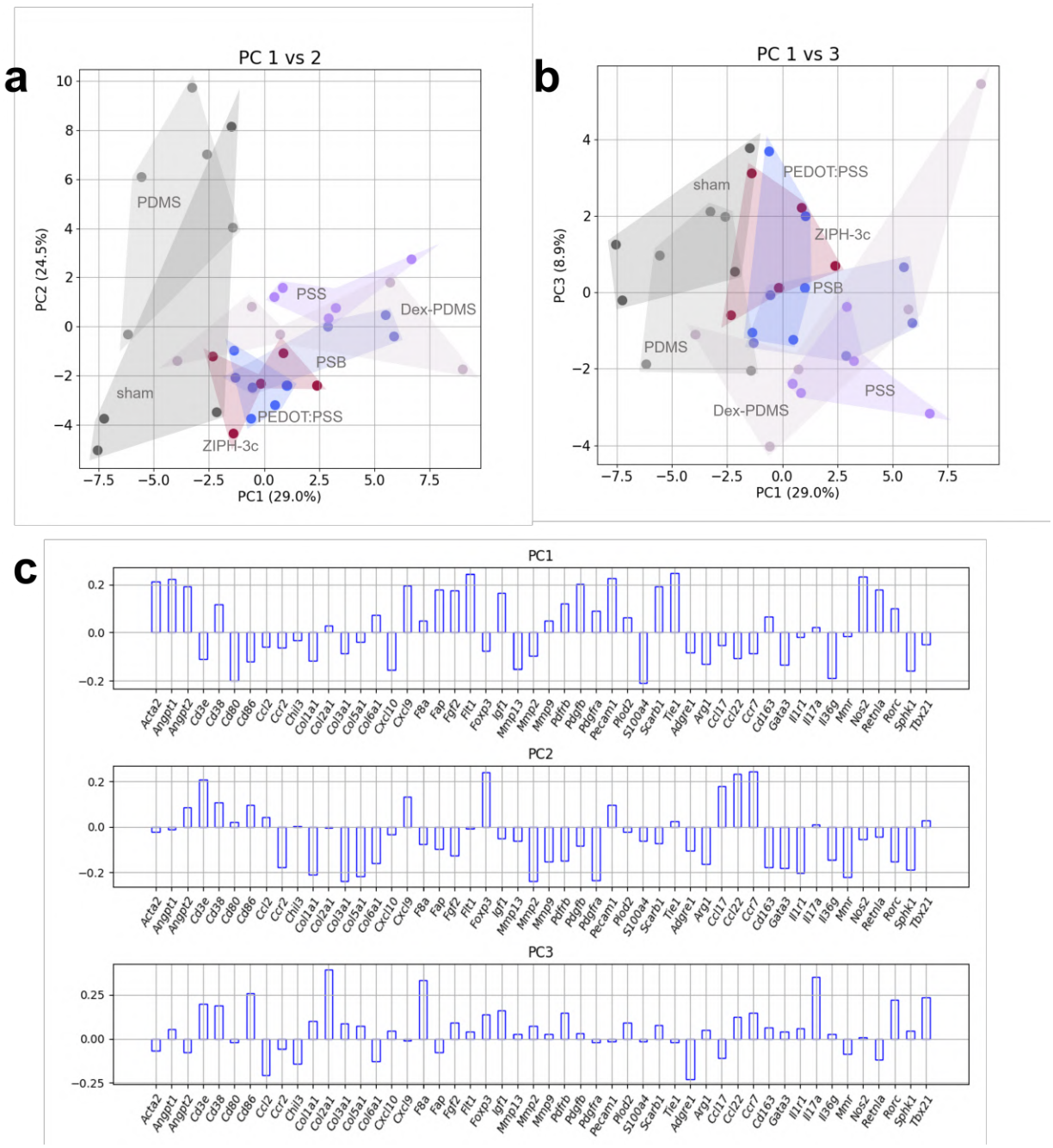

Figure C.4. Principle component analysis (PCA) of 50-genes, acquired via NanoString, 12-weeks post-implantation. **a**, Each sample plotted on PC1-PC2 vector space. **b**, Each sample plotted on PC1-PC3 vector space. **c**, Genes and their associated weights for each PC.